

The selective catalytic reduction of NO by NH₃ at Brønsted and Lewis acid sites of vanadium oxide surfaces: Density functional theory studies

**im Fachbereich Physik
der Freien Universität Berlin eingereichte
Dissertation zur Erlangung des akademischen Grades
DOCTOR RERUM NATURALIUM**

von
Dipl. Ing.
Mathis Gruber

Berlin 2011



MAX-PLANCK-GESELLSCHAFT

Erster Gutachter (Betreuer): Prof. Dr. Klaus Hermann

Zweiter Gutachter: Prof. Dr. Eberhard K.U. Gross

Disputationstermin: 8. Februar 2012

Table of Contents

1	Introduction	6
2	Literature survey: the selective catalytic reduction of NO by NH₃.....	9
2.1.1	The catalysts	9
2.1.2	Reactions and reactant stoichiometry	10
2.1.3	Adsorption of NH ₃ and NO	11
2.1.4	SCR reaction mechanisms	12
2.1.5	General requirements and findings for the SCR reaction.....	15
3	Theoretical foundations	16
3.1	Density functional theory.....	16
3.1.1	Born-Oppenheimer approximation.....	16
3.1.2	Hohenberg-Kohn theorem	18
3.1.3	The Kohn-Sham scheme.....	19
3.1.4	Local density and generalized gradient approximation.....	21
3.2	Methods to identify minima, minimum energy paths, and saddle points of the potential energy surface	26
3.2.1	Broyden-Fletcher-Goldfarb-Shanno method.....	26
3.2.2	Nudged elastic band method	28
3.2.3	The dimer method.....	33
4	Perfect and reduced vanadium pentoxide, V₂O₅.....	40
4.1	The perfect V ₂ O ₅ (010) surface	40
4.1.1	Crystal structure of V ₂ O ₅	40
4.1.2	Cluster models for the V ₂ O ₅ (010) surface.....	43
4.1.3	Electronic structure of the V ₂ O ₅ (010) surface.....	49
4.2	The reduced V ₂ O ₅ (010) surface, oxygen vacancies.....	53
4.2.1	Results for surface O(1), O(2), O(3) and sub-surface O(1') vacancies....	56
4.3	Oxygen vacancy diffusion at the V ₂ O ₅ (010) surface.....	66

5	H, NH_x, (x = 0,...,4), and NO adsorption at the V₂O₅(010) surface	74
5.1	Adsorption of H, NH _x , (x = 0,...,4), and NO at the perfect V ₂ O ₅ (010) surface	75
5.1.1	Hydrogen adsorption at the perfect V ₂ O ₅ (010) surface	75
5.1.2	NH _x , (x = 0,1,2), adsorption at the perfect V ₂ O ₅ (010) surface.....	80
5.1.3	Ammonia adsorption at the perfect V ₂ O ₅ (010) surface	85
5.1.4	NH ₄ adsorption at the perfect V ₂ O ₅ (010) surface.....	86
5.1.5	NO adsorption at the perfect V ₂ O ₅ (010) surface	89
5.2	Adsorption of H, NH _x , (x = 0,...,4), and NO at the reduced V ₂ O ₅ (010) surface	90
5.2.1	Substitutional adsorption near oxygen vacancy sites of the V ₂ O ₅ (010) surface.....	93
5.2.2	Ammonia adsorption near oxygen vacancy sites of the V ₂ O ₅ (010) surface	100
5.2.3	NH ₄ adsorption near oxygen vacancy sites of the V ₂ O ₅ (010) surface...	102
5.3	Ammonia adsorption at V ₂ O ₅ (010) surface, theory and experiment	104
6	Diffusion of adsorbates at the V₂O₅(010) surface	109
6.1	Hydrogen diffusion and H ₂ O formation at the perfect V ₂ O ₅ (010) surface ...	110
6.1.1	Hydrogen diffusion at the V ₂ O ₅ (010) surface	110
6.1.2	H ₂ O formation at the V ₂ O ₅ (010) surface	117
6.2	NH ₄ diffusion at the perfect V ₂ O ₅ (010) surface.....	120
6.2.1	NH ₄ diffusion on the vanadyl ridge	121
6.2.2	NH ₄ diffusion between ridge and valley.....	124
6.2.3	NH ₄ diffusion in the valley	125
7	(De)hydrogenation of NH_x, (x = 0,...,4) at the V₂O₅(010) surface.....	127
7.1	The Born-Haber cycle	127
7.2	Energetics for (de)hydrogenation of NH _x , at the V ₂ O ₅ (010) surface.....	127
7.2.1	Gas phase reactions.....	129
7.2.2	Reactions at the V ₂ O ₅ (010) surface	130

8	Selective catalytic reduction of nitric oxide by ammonia at vanadium oxide surfaces	133
8.1	Preliminary considerations for modeling the SCR reaction based on the initial ammonia adsorption.....	134
8.2	Surface and particle models	135
8.3	Initial adsorption, nitrosamide (NH ₂ NO) formation, and diffusion near Brønsted and Lewis acid sites.....	137
8.3.1	Reaction near Brønsted acid sites.....	137
8.3.2	Reaction near Lewis acid sites	144
8.4	Nitrosamide (NH ₂ NO) decomposition.....	152
8.5	Comparison of Brønsted and Lewis acid site based mechanisms	154
9	Conclusions	156
	Appendices	160
A.	Correlation energy of the Perdew-Burke-Ernzerhof functional	160
B.	Computational details and basis set definitions.....	162
C.	Cluster models for diffusion calculations.....	171
D.	SCR reaction path at the particle and the small cluster	180
	Abstract	188
	Zusammenfassung	189
	Lebenslauf	192
	Bibliography.....	193

1 Introduction

Metal oxides are fascinating materials that are both of high scientific interest and great technological importance. This includes many applications in fields that can be as different as superconductivity or gas sensing [1]. For the majority of metals, their oxides are the most stable phase under ambient conditions and, therefore, the understanding of oxides and corrosion is of great importance [1]. In catalysis, oxides including metal oxides are acting as support material. In fact, most of the commercial catalysts are dispersed on oxide particles, where porous oxides such as SiO_2 , Al_2O_3 , or TiO_2 are used [1, 2]. Notably, metal oxides can be catalytically active themselves [1, 3].

The transition metal vanadium is of particular interest as it can form many different oxides, covering a large variety of crystal structures with diverse physical/chemical properties [4, 5]. They are distinguished by the formal valence charge of the vanadium atom ranging from +II to +V for VO , V_2O_3 , VO_2 and V_2O_5 . In addition, vanadium oxide phases with mixed oxidation states exist, e.g., the Magnéli-phases $\text{V}_n\text{O}_{2n-1}$ or the Wadsley-phases $\text{V}_{2n}\text{O}_{5n-2}$ [6]. The number of applications of the V_xO_y is as large as their variety. Many vanadium oxides show a metal - insulator transition as a function of pressure, temperature, or doping. Examples are VO , VO_2 , or V_2O_3 , where the electrical resistance changes over orders of magnitude at phase transitions [7, 8]. Hence, these materials are interesting for electronic applications or fast optical switches [9]. VO_2 has been found to yield a promising thermochromic material with a transition temperature close to the room temperature and, therefore, suitable for applications in ‘smart windows’ [10].

Vanadium oxides are also widely used in the field of catalysis. This can be related to various properties such as the mobility of the surface/lattice oxygen atoms, the existence of Lewis acid-base sites, and the different reactivity of different crystal faces [11]. VO_x based catalysts are widely used or represent promising candidates for many catalytic reactions, e.g., the oxidation and dehydrogenation of hydrocarbons [12], the oxidation of sulfur dioxide [13], the ammoxidation reaction to produce acrylonitrile [14, 15], or the selective catalytic reduction (SCR) of NO_x with NH_3 [16, 17]. In general, supported vanadium oxides [12, 13, 16, 17], or vanadia that is incorporated in complex mixed metal oxides [14, 15], are catalytically more active than pure vanadium oxide and such catalysts are widely used in industry.

The focus of the present work is the SCR reaction, one of the most important applications to remove nitric oxides from the waste gas of stationary sources such as utility plants [17]. More than half of the worldwide electricity is produced by burning fossil fuels and, considering the increasing demand for energy, it will be important for many years. Although, the reaction is widely used and heavily investigated many

details are still under debate [17]. However, knowledge of the reaction details and catalyst properties is crucial to improve and design better catalysts. The complex crystallography of vanadium oxides accompanied by a complex variety of properties, makes the understanding of these systems a very challenging scientific task. Even worse, considering surface reaction processes raises the complexity. Therefore, further combined theoretical and experimental efforts are necessary to analyze the reaction mechanism and to understand how the catalyst operates.

This study is organized as follows. At the beginning, the SCR reaction will be introduced in an overview of previous experimental and theoretical research in Chapter 2. In addition to summarizing the established knowledge this also highlights the open questions.

Chapter 3 presents the theoretical concepts that are applied in this study. The investigation of geometric, electronic, and energetic properties is based on electronic structure calculations. These are performed with the StoBe package [18] employing density functional theory (DFT) [19, 20]; the fundamental principles of DFT are summarized briefly in Chapter 3. In addition, the algorithms that were used to locate stable geometric structures, transition states of diffusion, and reaction paths will be outlined. For the latter the nudged elastic band (NEB) [21] and the dimer [22] methods were implemented and, therefore, will be discussed in greater detail.

After this introductory part, the results of the investigation of vanadium oxide as a catalyst in the SCR reaction will be presented in Chapters 4 - 8. Catalytic reactions are very complex and include additional processes such as adsorption, desorption, or diffusion at the catalyst surface. Therefore, at the beginning, the most fundamental task, the description of the catalyst surface, will be discussed followed by an analysis of basic surface processes (adsorption, diffusion, and dehydrogenation). Finally, based on these results specific reaction scenarios will be suggested and examined.

Chapter 4 starts with a discussion of the perfect $V_2O_5(010)$ surface. Since detailed structural properties of real catalysts are unknown, a model catalyst, the well characterized $V_2O_5(010)$ surface [11] is studied instead. The surface is modeled by hydrogen saturated V_2O_5 clusters that will be introduced and their geometric, energetic, and electronic properties will be compared with experimental and theoretical work. Special emphasis will be put on the results of previous cluster studies [23, 24] that provide the basis for the cluster models applied in this work. Surface reduction and the formation of oxygen vacancies on the catalyst surface are important processes in the SCR reaction [17]. Therefore, in addition to the perfect, the reduced $V_2O_5(010)$ surface modeled by the presence of oxygen vacancies is investigated. In order to understand how the geometric structure changes after oxygen removal and how the electronic structure is affected, geometric structures, corresponding atom charges, and atom-projected density of states (DOS) of the perfect and the reduced surface models are analyzed. As stated above the ability of vanadium oxides to provide lattice oxygen is important for catalytic applications. This indicates that, besides the oxygen vacancy

formation, also the mobility of oxygen vacancies may become important. Thus, oxygen vacancy diffusion processes will be discussed at the end of Chapter 4, presenting selected diffusion paths and corresponding transition states and energy barriers.

In Chapter 5 the results obtained for the adsorption properties of H, NH_x, (x = 0, ..., 4), and NO at perfect and reduced V₂O₅(010) surfaces are outlined. Here, the cluster models established in the previous chapter are used. Besides the adsorption energies for different adsorption sites at the surface, the corresponding structural details, and local electronic rearrangements as represented by the atom charges will be discussed. Following ammonia adsorption, two strongly adsorbed NH_x surface species have been identified by infrared (IR) spectroscopy experiments [25, 26]. Therefore, at the end of this chapter, the calculated vibrational properties for selected surface species will be presented and compared with experimental IR data.

After analyzing adsorption at the V₂O₅(010) surface in the previous chapter, surface diffusion of the adsorbates at the surface are examined in Chapter 6. Here, the surface diffusion properties of two adsorbates, atomic hydrogen and NH₄, will be discussed. This is motivated by the fact that both adsorbates bind strongly to the surface, indicating that desorption and re-adsorption is energetically unfavorable. Moreover, hydrogen with its small mass can diffuse more easily compared to other adsorbates and the diffusion of OH groups may participate in the water formation during the SCR reaction. NH₄ is an interesting example as it adsorbs at the V₂O₅(010) surface with strong electrostatic binding contributions.

Ammonia hydrogenation or dehydrogenation processes are assumed to participate in the SCR reaction [17]. Therefore, in Chapter 7, the (de)hydrogenation reaction energies of NH_x in gas phase and at the perfect as well as at the reduced V₂O₅(010) surfaces are examined. A Born-Haber cycle [27] is employed to calculate the surface reaction energies based on adsorption energies (presented in Chapter 5) and gas phase binding energies.

In Chapter 8 two SCR reaction schemes involving different active sites of the catalyst surface, Brønsted acid (surface OH groups) and Lewis acid (vanadium centers) sites, are examined and compared. These mechanisms are based on the results obtained from the analysis of the catalyst surface properties and basic surface processes presented in Chapters 3 - 7 as well as the knowledge from previous experimental and theoretical work that is summarized in Chapter 2. In addition to the V₂O₅(010) surface model, a small V₂O₅ cluster and a silica-supported particle are considered as alternative catalyst models illustrating how the presence of an extended surface or an oxide support influences the reaction. A detailed analysis of the reaction paths including the transition states and the corresponding energy barriers for all three catalyst models will be presented.

Further technical details of the calculations can be found in the appendices at the end of this thesis.

2 Literature survey: the selective catalytic reduction of NO by NH₃

The selective catalytic reduction (SCR) process was invented in the United States in the late 1950s to remove nitric oxides from waste gas, a process which is called DeNOxing [28]. In the SCR reaction nitric oxide, molecular oxygen, and ammonia react to form molecular nitrogen and water according to



This reaction was first implemented for both industrial and utility plants in the 1970s in Japan where it was further developed. More recently, the majority of DeNOxing applications for stationary sources in industry employ the SCR process. Although this process is widely used and extensively studied, the detailed reaction mechanism has not yet been unveiled. An elaborate and useful overview of the scientific findings examining the SCR reaction was published by Busca et al. in 1998 [17]. The present survey follows this overview. More recent reviews were published by Calatayud et al., emphasizing theoretical aspects [29] and by Liu et al. providing a compact overview [30].

2.1.1 The catalysts

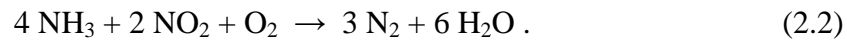
Most of the catalysts used for the SCR reaction are based on metal oxides. After reviewing the available data, Busca et al. [17] conclude that metal oxides that are active in oxidation catalysis are also active in the SCR reaction. The standard catalysts for industrial applications are TiO₂-supported V₂O₅-WO₃ and TiO₂-supported V₂O₅-MO₃ [31-36]. Various other materials, such as iron, copper, chromium, and cerium oxides supported on metal oxides or zeolites, have been synthesized and tested [17, 29]. Nevertheless, vanadium based, mixed metal oxide catalysts are predominant in industrial applications and continue to be developed further.

The amount of vanadium oxide in industrial catalysts is very small (< 1% w/w) [31]. The best catalysts have less than a monolayer of vanadium plus tungsten (or molybdenum) on a TiO₂ anatase support [17]. There is general agreement that vanadium oxide species provides the active sites as removing V₂O₅ reduces the activity and selectivity significantly [34]. In contrast, pure V₂O₅ supported on TiO₂ anatase is still active and quite selective [34]. TiO₂ anatase itself is a metastable phase while the

thermodynamically stable form is rutile. The presence of V_2O_5 favors the anatase-to-rutile phase transition [37, 38] while WO_3 [38-40] and MO_3 [41] hinder this phase transition. Thus, besides promoting the SCR reaction, the presence of WO_3 and MO_3 also stabilize the anatase phase. Some researchers claim also that tungsten oxide could affect the catalytic performance by offering a second active site or interacting electronically through the TiO_2 with the vanadium oxide [17].

2.1.2 Reactions and reactant stoichiometry

In the 1980s, there was some debate on whether NO_2 or NO is the reactant in the SCR reaction. One proposal [42] claimed that NO reacts with O_2 in gas phase to NO_2 and that NO_2 is the actual reactant at the catalyst surface yielding the reaction



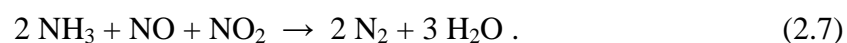
It has been shown that under dilute gas conditions, such as those present in stationary industrial applications, NO is the reactant because it is not oxidized by gaseous oxygen [43-45]. In addition, molecular oxygen participates in the reaction [46-48], hence, the main reaction is described by equation (2.1).

Isotopic labeling studies have shown that N_2 is formed by one nitrogen from NO and one from NH_3 [49-54]. Two conceptually different types of water are formed during the reaction: water containing oxygen from the NO , and water containing oxygen from the catalyst surface [49, 50]. The addition of gaseous oxygen accelerates the reaction and it is generally accepted that O_2 re-oxidizes the reduced catalyst. The enhancement caused by the addition of O_2 is attributed to the fact that it is a better oxidizing agent than NO .

As pointed out by Busca et al. [17], good SCR catalysts should promote reaction (2.1), but they should also suppress unwanted repercussions, such as undesirable reactions (2.3-2.6), described as



While previous studies showed that under dilute gas conditions, NO is the reactant [43-45], a reaction including NO_2 as a reactant has gained interest [55]. The so-called ‘fast SCR’ process,



This process has the advantages of higher reaction rates in the lower temperature range of 200 - 350°C [55] while the working window for standard SCR is between 250 - 450°C [56]. However, a reaction as described in equation (2.7) needs equimolar amounts of NO and NO₂. As exhaust gas mainly contains NO and not NO₂, an additional oxidation catalyst is positioned upstream to increase the amount of NO₂. The ‘fast SCR’ is mainly used for automotive DeNO_x systems such as Diesel engines of heavy duty vehicles, where urea acts as a source of NH₃ [55].

In agreement with the work of Inomata et al. [43-45] it is generally accepted that NH₃ reacts from a strongly adsorbed state, while NO reacts from the gas phase or a weakly adsorbed state [17, 29, 30] (and references therein). For the re-oxidation cycle, most researchers in this area agree that oxygen is involved in the re-oxidation of the catalyst in a Mars van Krevelen or ‘redox’ type mechanism [57].

2.1.3 Adsorption of NH₃ and NO

Adsorption of ammonia on the SCR catalysts was studied mainly by temperature programmed desorption (TPD) [58], Fourier transform infrared spectroscopy (FTIR) [25, 26, 59] and combined TPD-FTIR experiments [60, 61]. Most of the studies have been performed on TiO₂ supported V₂O₅ [17], however some studies also have investigated pure V₂O₅ [25, 26]. The results for both systems are basically the same. They show the existence of two different surface species after NH₃ adsorption could be identified [17, 29, 30]. Ammonia can adsorb at the vanadium center that provides a Lewis acid site [25, 26, 59]; this species is also often denoted as coordinated ammonia. The second species is a surface ammonium ion, NH₄⁺, that is formed by NH₃ adsorption at OH groups which act as Brønsted acid sites [25, 26, 59]. Two studies [25, 26] find that NH₃ adsorbed at Lewis acid sites is more stable than surface NH₄⁺ since the IR bands assigned to surface NH₄⁺ disappeared after heating the sample. Several TPD experiments on V₂O₅/TiO₂ have been performed, confirming the findings of two adsorbed species with different thermal stability [58, 60, 61]. The adsorption energies were estimated to be in the range of -0.8 eV up to -1.1 eV [60]. Some of the studies find spectroscopic features on pure V₂O₅, as well as TiO₂ supported VO_x samples, which could be assigned to an amide, -NH₂, species [26, 62, 63]. Ramis et al. [26, 62] claim that these species could be precursors in the formation of N₂. Further, an nuclear magnetic resonance (NMR) study [64] confirmed the presence of the two surface species, coordinated ammonia and NH₄⁺, and also found NH₂ surface species due to dehydrogenation processes after adsorption.

The NH₃ adsorption/desorption could be described by invoking a non-activated adsorption process and a Temkin-type desorption kinetics (linear dependency of the heat of adsorption on the coverage) [65, 66]. These studies suggest that a ‘reservoir’ of

adsorbed ammonia species is present and available for the reaction. In contrast to the active site, which could be assigned to vanadium atoms, titanium or tungsten could play a role in NH_3 storage. The adsorption of NO has also been investigated experimentally [17] showing that NO interacts weakly with pure and supported V_2O_5 but adsorbs at reduced vanadium oxide surfaces.

The adsorption of ammonia and nitric oxide on vanadium oxide based catalyst surface was also studied by theory [67-76]. Most of these studies have been performed for the perfect $\text{V}_2\text{O}_5(010)$ surface. They include calculations using periodic as well as cluster models at the semi-empirical (MSINDO), DFT, or DFT-hybrid level of theory. In contrast to experimental work discussed above [25, 26], theoretical studies investigating NH_3 adsorption at the $\text{V}_2\text{O}_5(010)$ surface only identify one strongly adsorbed species on the surface, NH_4^+ that is formed by ammonia adsorption at surface OH groups (Brønsted acid sites) [67-72] yielding adsorption energies between -0.5 eV and -1.4 eV [67-72]. Only two studies found that NH_3 can bind near a vanadium atom (Lewis acid site) but the adsorption energies are very small, -0.1 eV [70] and -0.3 eV [68]. Thus, there is a clear gap between theoretical and experimental findings for ammonia adsorption at the $\text{V}_2\text{O}_5(010)$ surface and a possible explanation will be discussed in Section 5.3 of the present work.

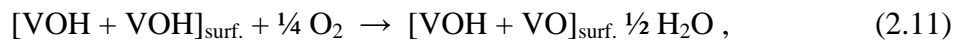
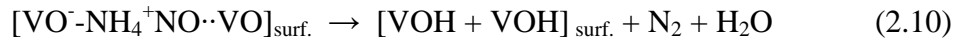
Fewer theoretical studies have been performed on NH_3 adsorption at TiO_2 supported VO_x [73-76]. There, researchers have concentrated on adsorption at Lewis acid sites. The adsorption energies are found to be significantly larger and vary from -0.6 eV to -1.3 eV [73-76]. One study [76] evaluates the adsorption energy of NH_3 at Lewis- and Brønsted acid sites of TiO_2 supported VO_x . For both sites, an NH_3 adsorption energy of -0.6 eV has been found. Theoretical studies investigating the NO adsorption find very weak interaction of NO with pure V_2O_5 [68, 71] and TiO_2 anatase supported V_2O_5 [75].

2.1.4 SCR reaction mechanisms

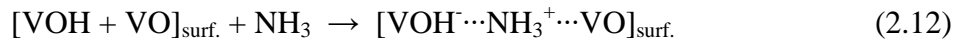
For the SCR reaction, according to equation (2.1), various detailed reaction schemes describing individual steps on the catalyst surface have been proposed. The most extensive review can be found in [17]. The present overview concentrates on the most important reaction mechanisms and steps. Most of the reaction schemes suggested by researchers can be divided into two groups: Lewis- [62] and Brønsted acid site [43] based mechanisms. This categorization is mainly motivated by two findings. First, it is generally accepted that adsorbed ammonia reacts with NO from gas phase or with NO that is weakly adsorbed at the surface [17]; and second, two different surface species were found after ammonia adsorption that could be assigned to NH_3 adsorbed at Lewis- and Brønsted acid sites [25, 26, 59]. Mechanisms considering neither of these two

surface species have been presented [49, 50], but are more controversial and will not be discussed here any further.

The Brønsted acid site mechanisms are based on the work of Inomata et al. [43] who proposed as reaction steps

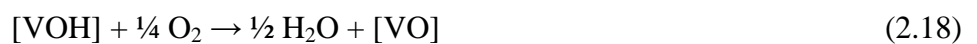
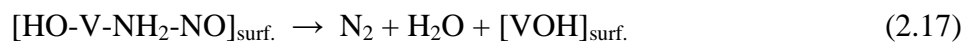
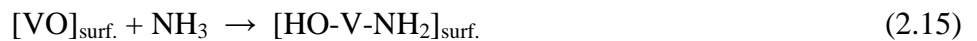


implying that NH_4^+ is the reactive surface species (step 2.8). It forms an activated complex NH_4NO (step 2.9) with gaseous NO that decomposes into two surface OH groups, N_2 , and H_2O (step 2.10). The excessive hydrogen can react with oxygen to form an H_2O molecule (step 2.11). This process was further developed by Topsøe et al. [77, 78]. Their reaction scheme is represented by the following steps



They propose that ammonia adsorbs as NH_3^+ connected to the OH group, which reflects the NH_4^+ species (step 2.12). After reaction with NO , an NONH_3^+ intermediate is formed (step 2.13). This intermediate species decomposes into N_2 and H_2O (step 2.13). The remaining surface hydrogen reacts with oxygen to form H_2O , as proposed by Inomata (step 2.11). Various modifications of this mechanism have been reported and can be found in [17].

The most prominent reaction mechanism that considers Lewis acid sites for the SCR reaction is a so-called ‘amide-nitrosamide’ type mechanism [62]. It consists of the following steps (2.15-2.18)



Ammonia adsorbs at the Lewis acid site and is activated by dehydrogenation (step 2.15). The resulting amide species can react with NO and forms the key intermediate nitrosamide (NH_2NO) (step 2.16). The nitrosamide decomposes into N_2 and H_2O (step 2.17). This is followed by the re-oxidation of the catalyst with gas phase oxygen (step 2.18). Went et al. [61, 79, 80], proposed a similar mechanism. They also include two alternative reaction steps that form N_2O species and consider the re-oxidation of the catalyst by NO.

The majority of the theoretical studies focused on the Brønsted acid site mechanism [67, 69, 71, 72]. All researchers agree that after NH_4 and NO reacts, an NH_3NOH intermediate is formed. This follows the scheme suggested by Topsøe et al. [77, 78], see step (2.13). But, in contrast, it is claimed that an additional intermediate nitrosamide, NH_2NO , is formed and that this is the key intermediate, which gets further decomposed into N_2 and H_2O . Here, the rate limiting step with the largest barrier is the formation of the nitrosamide. Only one author [71] could locate the transition states and calculated an energy difference of 1.5 eV between the intermediate configuration with adsorbed NH_4^+ and NO in the gas phase and the transition state to form NH_2NO . This process is separated by a weakly stabilized NH_3NOH intermediate into two individual energy barriers of 1.1 eV and 0.4 eV. Studies of the reaction at Brønsted acid sites of TiO_2 supported V_2O_5 investigated only the formation of NH_2NO starting from a NONH_3 like intermediate and evaluated an energy barrier of 0.8 eV [76].

The reaction at the Lewis acid site of perfect V_2O_5 has been considered by one theoretical study [71]. The authors conclude that this mechanism is very unlikely because of the large exothermicity of step (2.15). The other studies [67, 69, 72] exclude the Lewis acid site mechanism because no strongly adsorbed ammonia at the perfect $\text{V}_2\text{O}_5(010)$ surface has been found, and, therefore, initial adsorption at the Brønsted acid site seems to be favorable. In contrast, investigations of NH_3 adsorption at TiO_2 supported VO_x could identify coordinated ammonia [73-76] and thus examined the Lewis acid site mechanism. The largest individual energy barriers of the calculated reaction paths are between 1.3 eV [76] to 1.5 eV [75]. A detailed analysis and discussion of the two mechanisms and a comparison with the present study can be found in Chapter 8.

2.1.5 General requirements and findings for the SCR reaction

In the conclusion of their review [17], Busca et al., give a list of general requirements and findings for a SCR reaction mechanism that are accepted by almost all researchers and are repeated here briefly.

- The reaction stoichiometry under dilute conditions as present in industrial applications for stationary sources is given by equation (2.1) where NO is the reactant.
- N₂O is not an intermediate.
- The reaction is a coupling reaction, i.e., one nitrogen atom of the N₂ product comes from NO and the other from NH₃.
- The mechanism is of the redox type, where O₂ oxidizes the surface sites that get reduced by other reactants during the reaction.

From both experiment and theory it is not clear, which mechanism is favorable and whether Brønsted-, Lewis acid sites, or a combination of both are active in the SCR reaction. Therefore, further combined efforts of experiment and theory are needed to clarify the details of the SCR reaction.

3 Theoretical foundations

3.1 Density functional theory

Density functional theory (DFT) is one of the most successful and important methods to calculate the electronic structure of many body systems. It is a cornerstone of contemporary theoretical solid-state physics, theoretical chemistry and theoretical material science. The rapid evolution of hard- and software has opened up completely new fields for DFT applications, e.g., complex catalytic surface reactions or the investigation of biological systems such as proteins. Nowadays, DFT is a standard tool and is extensively discussed in various sources. A short overview is presented here, following the work of Dreizler and Gross [19], as well as of Koch and Holthausen [20].

3.1.1 Born-Oppenheimer approximation

The starting point is the non-relativistic time-independent Hamiltonian,

$$\hat{H} = \hat{H}_{elec} + \hat{H}_{nuc} + \hat{H}_{elec/nuc} \quad (3.1)$$

where \hat{H}_{elec} is the Hamiltonian of the electron contributions; \hat{H}_{nuc} the Hamiltonian of the nuclei contributions and $\hat{H}_{elec/nuc}$ describes the interaction between electrons and nuclei.

In the following we will be using the system of atomic units, which is convenient when working with atoms and molecules because it yields equations in a compact form. Therefore, the values of fundamental physical constants, such as the electron mass m_e , electron charge e , reduced Planck's constant \hbar and the permittivity of vacuum $4\pi\epsilon_0$, are set to unity.

In order to calculate the electronic structure of a many body system, the electronic and nuclear motions of the system are often decoupled. This can be achieved by the Born-Oppenheimer approximation [81] that is motivated by the fact that the mass of the nuclei is much larger compared to the mass of the electron. Therefore, the electrons can be assumed to adapt instantaneously to movements of the nuclei and the electronic part can be solved for fixed nuclei positions leading to a potential for the nuclei. The separated electronic part of a system containing N_e electrons at $\underline{r}_1, \dots, \underline{r}_{N_e}$ is then described by the non-relativistic, time-independent Hamiltonian for electrons where the

positions $\underline{R}^{(i)} = \{\underline{R}_1^{(i)}, \dots, \underline{R}_{N_n}^{(i)}\}$ and the atomic numbers Z_1, \dots, Z_{N_n} of the N_n nuclei enter as parameters.

$$\widehat{H}_e^{(\underline{R}^{(i)})}(\underline{r}_1, \dots, \underline{r}_{N_e}) = \widehat{T}_e^{(\underline{R}^{(i)})}(\underline{r}_1, \dots, \underline{r}_{N_e}) + \widehat{V}_e^{(\underline{R}^{(i)})}(\underline{r}_1, \dots, \underline{r}_{N_e}) + \widehat{W}_e^{(\underline{R}^{(i)})}(\underline{r}_1, \dots, \underline{r}_{N_e}) \quad (3.2)$$

\widehat{T}_e is the kinetic energy of the electrons

$$\widehat{T}_e^{(\underline{R}^{(i)})}(\underline{r}_1, \dots, \underline{r}_{N_e}) = -\frac{1}{2} \sum_{j=1}^{N_e} \Delta_j, \quad (3.3)$$

\widehat{W}_e the Coulomb interaction between the electrons

$$\widehat{W}_e^{(\underline{R}^{(i)})}(\underline{r}_1, \dots, \underline{r}_{N_e}) = \sum_{j,k=1}^{N_e} \frac{1}{|\underline{r}_j - \underline{r}_k|} \quad (3.4)$$

and \widehat{V}_e is the external potential describing additional contributions, e.g., interactions with external fields. In the Born-Oppenheimer approximation, the external potential accounts for interactions of the electrons with the nuclei and, if no external fields are considered, is defined by

$$\widehat{V}_e^{(\underline{R}^{(i)})}(\underline{r}_1, \dots, \underline{r}_{N_e}) = -\sum_{k=1}^{N_n} \sum_{j=1}^{N_e} \frac{Z_k}{|\underline{r}_j - \underline{R}_k^{(i)}|}. \quad (3.5)$$

Putting this together within the Born-Oppenheimer approximation \widehat{H}_e can be written as

$$\widehat{H}_e^{(\underline{R}^{(i)})}(\underline{r}_1, \dots, \underline{r}_{N_e}) = -\frac{1}{2} \sum_{j=1}^{N_e} \Delta_j - \sum_{k=1}^{N_n} \sum_{j=1}^{N_e} \frac{Z_k}{|\underline{r}_j - \underline{R}_k^{(i)}|} + \sum_{j,k=1}^{N_e} \frac{1}{|\underline{r}_j - \underline{r}_k|}. \quad (3.6)$$

From the solution of the corresponding Schrödinger equation,

$$\widehat{H}_e^{(\underline{R}^{(i)})} \Psi_n^{(\underline{R}^{(i)})}(\underline{r}_1, \dots, \underline{r}_{N_e}) = E_n^{(\underline{R}^{(i)})} \Psi_n^{(\underline{R}^{(i)})}(\underline{r}_1, \dots, \underline{r}_{N_e}) \quad (3.7)$$

follow the electronic wave functions $\Psi_n^{(\underline{R}^{(i)})}(\underline{r}_1, \dots, \underline{r}_{N_e})$ and the corresponding energy eigenvalues E_n . Thus the total energy for a given set of atoms is determined by the atom positions $E_n^{tot}(\underline{R}^{(i)})$ only.

If the nuclei are treated classically, the total energy of the system is

$$E_n^{tot} = E_n(\underline{R}^{(i)}) + \frac{1}{2} \sum_{j,k}^{j \neq k} \frac{Z_j Z_k}{|\underline{R}_j^{(i)} - \underline{R}_k^{(i)}|}. \quad (3.8)$$

and $E_n^{tot}(\underline{R}^{(i)})$ defines the Born-Oppenheimer potential energy surface (PES).

3.1.2 Hohenberg-Kohn theorem

As can be seen in (3.2), the non-relativistic, time-independent electronic Hamiltonians for different systems differ only in their external potentials \hat{V}_e . The ground state wave function of the system, $\Psi_0^{(R^{(i)})}(\underline{r}_1, \dots, \underline{r}_{N_e})$, determines the ground state electron density $\rho_0(\underline{r})$ where

$$\rho_0(\underline{r}) = N_e \cdot \sum_{\alpha} \int d^3 x_2 \dots \int d^3 x_{N_e} \left| \Psi_0(\underline{r}, \underline{x}_2, \dots, \underline{x}_{N_e}) \right|^2. \quad (3.9)$$

A density that can be generated by a potential via equations (3.7) and (3.9) is called *pure-state v -representable*.

Through an indirect proof, Hohenberg and Kohn show [82] that the map,

$$\rho(\underline{r}) \longleftrightarrow \Psi(\underline{r}_1, \dots, \underline{r}_{N_e}) \longleftrightarrow \hat{V} \quad (3.10)$$

is bijective for all densities that belong to \mathcal{N} , the set *pure-state v -representable* densities. Thus the density $\rho(\underline{r})$ can be uniquely attributed to its corresponding wave function $\Psi_0^{(R^{(i)})}(\underline{r}_1, \dots, \underline{r}_{N_e})$ and a corresponding external potential \hat{V} . Therefore the ground state expectation value of any observable is a unique functional of the ground state density.

In the second step, after showing that the density contains all necessary information, Hohenberg and Kohn [82] discuss the variational character of the energy functional,

$$E_{v_0}(\rho) = \left\langle \Psi(\rho) \left| \hat{T} + \hat{V}_0 + \hat{W} \right| \Psi(\rho) \right\rangle \quad (3.11)$$

where \hat{V}_0 is a given external potential. Based on the Rayleigh-Ritz principle, they show that E_0 , the minimum of E_{v_0} , is generated by applying the ground state density $\rho_0(\underline{r})$ to equation (3.11).

$$E_0 = E_{v_0}(\rho_0) \quad (3.12)$$

Thus the ground state density $\rho_0(\underline{r})$ can be obtained by minimizing the energy over the set \mathcal{X} , i.e.,

$$E_0 = \min_{\rho \in \mathcal{X}} E_{v_0}(\rho). \quad (3.13)$$

Since the map $\Psi(\underline{r}_1, \dots, \underline{r}_{N_e}) \longleftrightarrow \rho$ does not depend on the external potential \hat{V}_0 , the equation (3.11) can be written as the sum of the Hohenberg-Kohn functional

$$F_{HK}(\rho) = \left\langle \Psi(\rho) \left| \hat{T} + \hat{W} \right| \Psi(\rho) \right\rangle, \quad (3.14)$$

and $\int d\underline{r} v_0(\underline{r})\rho(\underline{r})$ where v_0 is the local external potential.

$$E_{v_0}(\rho) = F_{HK}(\rho) + \int d^3r v_0(\underline{r})\rho(\underline{r}) \quad (3.15)$$

F_{HK} is universal for all systems, as different systems vary by their external potentials. This tells us that a universal functional exists, but we have no information about how to construct it. The challenge to applying DFT is to find good approximations for F_{HK} .

The three statements, the invertibility of the map (3.10), the variational character of the energy functional $E_{v_0}(\rho)$ (3.13) and the universality of the Hohenberg-Kohn functional F_{HK} (3.14), are manifest in the Hohenberg-Kohn theorem [82]. It demonstrates that the ground state properties of the complicated, many-electron problem are determined by the ground state electron density $\rho_0(\underline{r})$. This quantity depends on three coordinates of the vector \underline{r} and, thus, is much less complicated than the ground state many-particle wave function $\Psi_0^{(R^{(i)})}(\underline{r}_1, \dots, \underline{r}_{N_e})$, which is dependent on $3 \cdot N_e$ coordinates of the multi-dimensional vector $\underline{r}_1, \dots, \underline{r}_{N_e}$.

As mentioned above, the statements are only valid for densities $\rho(\underline{r})$ that belong to \mathcal{X} , the set of *pure-state v -representable* densities. The question as to whether a density is *pure-state v -representable* is very important for the variational access to the ground state density and is discussed in detail in [19].

3.1.3 The Kohn-Sham scheme

The Kohn-Sham scheme [83] was developed from the Hohenberg-Kohn theorem [82] and has become a standard scheme for DFT implementations. It is based on the assertion that the ground state density of an interacting electron system $\rho_0(\underline{r})$ can be generated by a non-interacting auxiliary electron system. Such a density is also denoted to be *non-interacting v -representable* [19].

The auxiliary system used for the Kohn-Sham scheme is defined by a non-relativistic time-independent Hamiltonian of non-interacting electrons \hat{H}_s .

$$\hat{H}_s^{(R^{(i)})}(\underline{r}_1, \dots, \underline{r}_{N_e}) = \hat{T}_s^{(R^{(i)})}(\underline{r}_1, \dots, \underline{r}_{N_e}) + \hat{V}_s^{(R^{(i)})}(\underline{r}_1, \dots, \underline{r}_{N_e}), \quad (3.16)$$

where $\hat{T}_s^{(R^{(i)})}(\underline{r}_1, \dots, \underline{r}_{N_e})$ is the kinetic energy of the non-interacting electrons and $\hat{V}_s^{(R^{(i)})}(\underline{r}_1, \dots, \underline{r}_{N_e})$ is the external potential. By applying the Hohenberg-Kohn theorem [82] to this system (3.15), the energy can be written as follows,

$$E_s(\rho) = T_s(\rho) + \int d^3r v_s(\underline{r})\rho(\underline{r}). \quad (3.17)$$

Combining the interacting and the non-interacting auxiliary system via equations (3.15) and (3.17) using the Hohenberg-Kohn theorem and the assumption of *non-interacting v -representability* it is possible to find an expression for the external local potential of the non-interacting auxiliary system $v_{s,0}(\underline{r})$ that generates exactly the ground state density of the interacting system [19, 83].

$$v_{s,0}(\underline{r}) = v_0(\underline{r}) + \int d^3r' \frac{\rho_0(\underline{r}')}{|\underline{r} - \underline{r}'|} + v_{xc}(\rho_0; \underline{r}), \quad (3.18)$$

with $v_0(\underline{r})$ the local external potential of the interacting system, the Hartree term $\int d\underline{r}' \frac{\rho_0(\underline{r}')}{|\underline{r} - \underline{r}'|}$ and the local exchange-correlation potential $v_{xc}(\rho_0; \underline{r})$. The exchange-correlation potential is defined to be the functional derivative of the exchange-correlation energy with respect to the density.

$$v_{xc}(\rho_0; \underline{r}) = \left. \frac{\partial E_{xc}(\rho)}{\partial \rho(\underline{r})} \right|_{\rho=\rho_0} \quad (3.19)$$

The exchange-correlation energy E_{xc} contains the corrections for the difference between the Hohenberg-Kohn functional of the real system of interacting electrons and its approximation via the sum of a Hartree term and the kinetic energy of the non-interacting electrons.

$$E_{xc}(\rho) = F_{HK}(\rho) - \frac{1}{2} \iint d^3r d^3r' \frac{\rho(\underline{r})\rho(\underline{r}')}{|\underline{r} - \underline{r}'|} - T_s(\rho) \quad (3.20)$$

By applying (3.18), $\rho_0(\underline{r})$ is the ground state density of both the interacting electron and the auxiliary system. Therefore $\rho_0(\underline{r})$ can be expressed by one-particle wave functions $\varphi_{i,0}(\underline{r})$ that are the solution to the non-interacting system corresponding to $v_{s,0}$, according to

$$\rho_0(\underline{r}) = \sum_i^{N_e} |\varphi_{i,0}(\underline{r})|^2. \quad (3.21)$$

Combining equations (3.16), (3.18) and (3.21) yields the Kohn-Sham scheme [83]:

$$\left(-\frac{1}{2}\Delta + v_{s,0}(\underline{r}) \right) \varphi_{i,0}(\underline{r}) = \varepsilon_i \varphi_{i,0}(\underline{r}), \quad \varepsilon_1 \leq \varepsilon_2 \leq \dots \quad (3.22)$$

$$v_{s,0}(\underline{r}) = v_0(\underline{r}) + \int d^3 r' \frac{\rho_0(\underline{r}')}{|\underline{r} - \underline{r}'|} + v_{xc}(\rho_0; \underline{r}) \quad (3.22a)$$

$$\rho_0(\underline{r}) = \sum_{i=1}^{N_e} |\varphi_{i,0}(\underline{r})|^2 \quad (3.22b)$$

Since the density appears in equations (3.22a) and (3.22b), the set of equations has to be solved in a self-consistent way. On the whole, by applying the Kohn-Sham scheme [83] the complexity of the many-particle problem is condensed in the exchange-correlation potential v_{xc} . If one were to know the exact local exchange-correlation potential, v_{xc} , one could obtain the exact solution, but determining the v_{xc} is as complicated as solving the original problem. The advantage of the Kohn-Sham scheme is that it is more suitable for approximations than equations (3.15) and will be briefly discussed in the following section.

3.1.4 Local density and generalized gradient approximation

The local density approximation (LDA) and the generalized gradient approximation (GGA) are the most commonly used approximations for the exchange-correlation functional.

In the following, we divide the exchange-correlation functional into the exchange part that accounts for the Pauli principle (anti-symmetrization of the wave function) and the correlation part.

$$E_{xc}(\rho) = E_x(\rho) + E_c(\rho). \quad (3.23)$$

In LDA, E_{xc} is described by $\varepsilon_{xc}^{\text{hom}}$, the exchange-correlation energy per particle of a homogenous electron gas with the density $\rho(\underline{r})$.

$$E_{xc}^{\text{LDA}}(\rho) = \int d^3r \rho(\underline{r}) \varepsilon_{xc}^{\text{hom}}(\rho(\underline{r})) = \int d^3r \rho(\underline{r}) \left(\varepsilon_x^{\text{hom}}(\rho(\underline{r})) + \varepsilon_c^{\text{hom}}(\rho(\underline{r})) \right) \quad (3.24)$$

The exchange energy per particle of the homogenous electron $\varepsilon_x^{\text{hom}}$ can be expressed analytically as derived by Bloch and Dirac [84, 85], i.e.,

$$\varepsilon_x^{\text{hom}} = -\frac{3}{4} \sqrt[3]{\frac{3\rho^{\text{hom}}}{\pi}}. \quad (3.25)$$

Apart from the pre-factor $3/2\alpha$ (typical values of the semi-empirical parameter α are between $2/3$ and 1 [20]), this agrees with Slater's approximation of the Hartree-Fock exchange [86], therefore it is often denoted as the Slater exchange.

In contrast to $\varepsilon_x^{\text{hom}}$, no explicit expression exists for correlation energy per particle $\varepsilon_c^{\text{hom}}$. Analytical expressions are often generated by fitting to numerical data. Most well-known numerical data are the results of highly accurate quantum Monte Carlo simulations for the homogenous electron gas that have been presented by Ceperley and Alder [87]. Based on this data, Vosko, Wilk, and Nusair [88], as well as Perdew and Zunger [89] derived their analytical expressions for $\varepsilon_c^{\text{hom}}$.

The exchange-correlation energy E_{xc} also includes the correction for the difference between the kinetic energy of the interacting system T_e and the non-interacting auxiliary system T_s , see equations (3.14) and (3.20). Since the exchange energy E_x accounts for the Pauli principle, the correlation energy E_c contains the correction of the kinetic energy.

A quantity that is closely related to E_{xc} is the exchange-correlation hole h_{xc} . In order to define h_{xc} , it is necessary to introduce the pair density $\rho_2(\underline{r}_1, \underline{r}_2)$ and the conditional probability $\Omega(\underline{r}_1, \underline{r}_2)$. The first is the probability of finding an electron at \underline{r}_1 and simultaneously another electron at \underline{r}_2 ,

$$\rho_2(\underline{r}_1, \underline{r}_2) = N_e \cdot (N_e - 1) \cdot \sum_{\alpha} \int d^3x_3 \dots \int d^3x_{N_e} \left| \Psi_{\alpha}(\underline{r}_1, \underline{r}_2, \underline{x}_3, \dots, \underline{x}_{N_e}) \right|^2. \quad (3.26)$$

The latter is the probability of finding one electron at \underline{r}_2 if there is another electron known to be at \underline{r}_1 ,

$$\Omega(\underline{r}_2, \underline{r}_1) = \frac{\rho_2(\underline{r}_1, \underline{r}_2)}{\rho(\underline{r}_1)}. \quad (3.27)$$

The exchange-correlation hole is defined as the difference between the conditional probability $\Omega(\underline{r}_2, \underline{r}_1)$ and the density $\rho(\underline{r}_2)$.

$$h_{xc}(\underline{r}_1, \underline{r}_2) = \Omega(\underline{r}_2, \underline{r}_1) - \rho(\underline{r}_2). \quad (3.28)$$

In other words, it is the difference between the probabilities of finding an electron at \underline{r}_2 if there is another electron at \underline{r}_1 for interacting electrons and for non-interacting electrons. Analogous to the exchange-correlation energy, h_{xc} can be divided into the exchange hole h_x and the correlation hole h_c as well.

The importance of the exchange-correlation hole is that E_{xc} can be expressed by the corresponding h_{xc} [20] and that these objects fulfill certain constraints that can be used to parameterize approximations for the exchange-correlation functional. The most important are presented in the following.

As $\rho(\underline{r})$ is normalized to the number of electrons N_e and $\rho_2(\underline{r}_1, \underline{r}_2)$ to $N_e \cdot (N_e - 1)$, the exchange-correlation hole contains the charge of one electron

$$\int d^3 r_2 h_{xc}(\underline{r}_1, \underline{r}_2) = -1. \quad (3.29)$$

Furthermore, it has been shown that [90-92]

$$\int d^3 r_2 h_x(\underline{r}_1, \underline{r}_2) = -1 \quad (3.30)$$

$$\int d^3 r_2 h_c(\underline{r}_1, \underline{r}_2) = 0, \quad (3.31)$$

as well as that the exchange hole, has to be negative everywhere.

$$h_x(\underline{r}_1, \underline{r}_2) < 0, \text{ for all } \underline{r}_1, \underline{r}_2 \quad (3.32)$$

The remarkably good performance of LDA can be understood if we consider that the exchange-correlation hole of the homogenous electron gas fulfills the physical constraints described above. Therefore it may be a very simple approximation that results in a poor description of the exact exchange-correlation hole, but that nonetheless results in a good approximation of the spherically averaged exchange-correlation hole [20, 93, 94], which determines the exchange-correlation energy.

It has been shown that the Kohn-Sham scheme can be generalized for spin-polarized systems [19]. There the density $\rho(\underline{r})$ is defined as the sum of the spin densities $\rho_\uparrow(\underline{r})$ ('spin up') and $\rho_\downarrow(\underline{r})$ ('spin down'), i.e.,

$$\rho(\underline{r}) = \rho_\uparrow(\underline{r}) + \rho_\downarrow(\underline{r}). \quad (3.33)$$

The resulting exchange-correlation functional of the local spin polarized density approximation (LSDA) is a functional of the spin densities,

$$E_{xc}^{LSDA}(\rho_{\uparrow}, \rho_{\downarrow}) = \int d^3r \rho(\underline{r}) \varepsilon_{xc}(\rho_{\uparrow}(\underline{r}), \rho_{\downarrow}(\underline{r})). \quad (3.34)$$

In their original publication, Kohn and Sham [83] proposed an extension of the LDA by using information from the density and the density gradient $\nabla\rho(\underline{r})$. This so-called gradient expansion approximation (GEA) assumes that the E_{xc} can be written in the form

$$E_{xc}^{GEA}(\rho) = \int d^3r (a(\rho(\underline{r})) + b(\rho(\underline{r})) |\nabla\rho(\underline{r})|^2 + \dots). \quad (3.35)$$

This GEA approach was not very successful and in many cases it performed poorly when compared to the LDA approach [20, 91, 92, 94]. This has been attributed mainly to the fact that the GEA exchange-correlation hole is a truncated expansion and, in contrast to the LDA exchange-correlation hole, violates important relations for the true hole, e.g., the sum rules (3.29 - 3.31) and the non-positivity constraint (3.32) [20, 91, 92, 94]. Therefore it provides a bad approximation of the exchange-correlation energy.

The generalized gradient approximation (GGA) is the result of attempts to restore the physical conditions for the GEA exchange-correlation hole. The first attempt was presented by Perdew [92] in 1985 by applying a cutoff procedure that terminates the GEA exchange-correlation hole in real-space, yielding the famous Perdew-Wang-91 (PW91) functional [95, 96]. By doing so, GGA functionals combine the advantages of a good description of the spherically averaged exchange-correlation hole (LDA) and the additional information of the density gradient (GEA).

A widely used GGA functional is the famous Perdew-Burke-Ernzerhof (PBE) functional [94, 97, 98]. It is the outcome of efforts to reproduce the properties of the PW91 functional [95, 96], but minimizes the number of parameters. This is achieved by constructing the PBE functional considering only those seven conditions that were identified to be energetically significant [97]. Based on the spin scaling relationship for the exact exchange [99], the GGA exchange energy can be written as

$$E_x^{GGA}(\rho_{\uparrow}(\underline{r}), \rho_{\downarrow}(\underline{r})) = \frac{1}{2} E_x^{GGA}(2\rho_{\uparrow}(\underline{r})) + \frac{1}{2} E_x^{GGA}(2\rho_{\downarrow}(\underline{r})) \quad (3.36)$$

with

$$E_x^{GGA}(\rho(\underline{r})) = \int d^3r (\rho(\underline{r}) \varepsilon_x^{\text{hom}}(\rho(\underline{r})) F_x(s)). \quad (3.37)$$

$F_x(s)$ is the exchange enhancement factor. Perdew et al. [94, 97, 98] defined F_x as a function of the reduced gradient

$$s = \frac{|\nabla\rho(r)|}{2k_F\rho(r)}, \quad (3.38)$$

which measures the change of the density $\rho(r)$ in the scale of the local Fermi wavelength $\frac{2\pi}{k_F}$ where $k_F = (3\pi^2\rho(r))^{\frac{1}{3}}$.

Based on specific conditions explained in [94, 97, 98], Perdew et al. determined their PBE enhancement factor of the following mathematical form:

$$F_x^{PBE}(s) = 1 + \kappa - \frac{\kappa}{1 + \frac{\mu s^2}{\kappa}} \quad (3.39)$$

with the parameters $\mu = 0.21951$ and $\kappa = 0.804$.

Zhang et al. [100] proposed a slight variation of the PBE functional. The so-called revPBE functional was generated by changing the value of the parameter κ from 0.804 to 1.245. They showed that their modified functional gives more accurate atomic total energies and molecule atomization energies. Later it was found that the revPBE significantly improves the description of the chemisorption energies of atomic and molecular bonding to surfaces [101]. By changing value of κ , the revPBE does not fulfill all constraints that have been used to construct the PBE functional [100]. Therefore, Hammer et al. [101] presented an alternative modification of the PBE functional that can reproduce the revPBE results and fulfills the same constraints as the PBE functional. For their RPBE [101] functional, instead of changing the parameter κ , they propose to use another mathematical form for the local exchange enhancement factor $F_x(s)$.

$$F_x^{RPBE}(s) = 1 + \kappa \left(1 - e^{-\frac{\mu s^2}{\kappa}} \right) \quad (3.40)$$

The same expression for the correlation energy is used for the PBE functional and its variations (revPBE and RPBE) it is presented in Appendix A.

3.2 Methods to identify minima, minimum energy paths, and saddle points of the potential energy surface

In the Born-Oppenheimer picture, many physical properties of the system are determined by electronic states along the potential energy surface (PES). An evaluation of the full multi-dimensional PES is not possible for computational reasons. However, specific points and paths of the PES and their vicinity contain most of the important information. These are minima, minimum energy paths (MEP) that connect these minima, and saddle points of the MEP's. The minima reflect stable or metastable geometric configurations. The knowledge of the minimum energy paths (MEP) and corresponding saddle points is needed to describe processes, such as diffusion, switching between different isomers, or chemical reactions.

The DFT formalism can be used to calculate total energies and forces for a given geometric configuration $\underline{R}^{(i)}$ of the system represented by the coordinates of the nuclei, $\underline{R}^{(i)} = \{\underline{R}_1^{(i)}, \dots, \underline{R}_{N_n}^{(i)}\}$, where the index i is used to differentiate between configurations. To locate minimum configurations at the lowest possible computational cost, efficient methods for minimizing the energy with respect to the atom positions are used. In principle, many of the optimization methods converge to a stationary point and hence could also converge to a saddle point. Nevertheless the algorithms are designed for minimization. Therefore, either modified [102] or additional, different algorithms are necessary for the localization of saddle points. This section gives an overview of the algorithms which are used in the present work. The implementation of methods to evaluate MEP's and saddle points for the StoBe DFT code [18] was part of this thesis.

3.2.1 Broyden-Fletcher-Goldfarb-Shanno method

The Broyden-Fletcher-Goldfarb-Shanno (BFGS) optimization method [103-106] is used for finding minima or maxima of an object function $f(\underline{x})$ where \underline{x} denotes a multi-dimensional vector. It is one of the most popular algorithms to find local minima of the Born-Oppenheimer PES that is defined by the object function $E(\underline{R})$, as defined in equation (3.8).

It is assumed that $f(\underline{x})$ can be represented by a quadratic form around \underline{x}

$$f(\underline{x} + \underline{p}) = f(\underline{x}) + \nabla f(\underline{x})^T \underline{p} + \frac{1}{2} \underline{p}^T \underline{\underline{B}} \underline{p} \quad (3.41)$$

where \underline{B} is an approximation of the Hessian matrix of second order partial derivatives of the object function, which will be updated iteratively. The Taylor series for the gradient itself,

$$\nabla f(\underline{x} + \underline{p}) = \nabla f(\underline{x}) + \underline{B} \underline{p}, \quad (3.42)$$

is used to define the search direction \underline{p} by setting the gradient to zero

$$\underline{p} = -\underline{B}^{-1} \nabla f(\underline{x}) \quad (3.43)$$

where \underline{B}^{-1} is the inverse Hessian matrix. The vector \underline{x} that minimizes the function $f(\underline{x})$ is evaluated in an iterative procedure as follows.

$$\underline{x}_{k+1} = \underline{x}_k + \alpha_k \underline{p}_k \quad (3.44)$$

The step length α_k is chosen to satisfy the condition that ensures a sufficient decrease of the object function, i.e.,

$$f(\underline{x}_k + \alpha_k \underline{p}_k) \leq f(\underline{x}_k) + c_1 \alpha_k \nabla f(\underline{x}_k)^T \underline{p}_k \quad (3.45)$$

and the curvature condition,

$$\nabla f(\underline{x}_k + \alpha_k \underline{p}_k)^T \underline{p}_k \geq c_2 \nabla f(\underline{x}_k)^T \underline{p}_k. \quad (3.46)$$

The curvature condition is motivated by the assumption that if the slope at the point \underline{x}_{k+1} is strongly negative $f(\underline{x})$, it can be reduced by going further along the search direction \underline{p}_k . These two conditions are collectively known as the Wolfe conditions [107]. The BFGS method belongs to the class of quasi-Newton methods [107]. For quasi-Newton methods, the Hessian matrix is approximated and updated at each step of the optimization based on the gradient. This avoids the expensive evaluation of Hessian matrices, i.e., of second order derivatives. The approximation of the inverse Hessian matrix at step k for the BFGS algorithm is defined as follows:

$$\underline{B}_{k+1}^{-1} = \left(I - \frac{\underline{y}_k \Delta \underline{x}_k^T}{\underline{y}_k^T \Delta \underline{x}_k} \right)^T \underline{B}_k^{-1} \left(I - \frac{\underline{y}_k \Delta \underline{x}_k^T}{\underline{y}_k^T \Delta \underline{x}_k} \right) + \frac{\Delta \underline{x}_k \Delta \underline{x}_k^T}{\underline{y}_k^T \Delta \underline{x}_k} \quad (3.47)$$

with

$$\Delta \underline{x}_k = \underline{x}_{k+1} - \underline{x}_k = \alpha_k \underline{p}_k \quad (3.48)$$

and

$$\underline{y}_k = \nabla f(\underline{x}_{k+1}) - \nabla f(\underline{x}_k). \quad (3.49)$$

With these definitions, the BFGS algorithm can be written as:

Step 1: define initial $\underline{\underline{B}}$ (usually the identity matrix) and calculate gradient $\nabla f(\underline{x}_1)$.

Step 2: evaluate Newton step $\Delta \underline{x}_k = -\alpha_k \underline{\underline{B}}_k^{-1} \nabla f(\underline{x}_k)$ and update $\underline{x}_{k+1} = \underline{x}_k + \Delta \underline{x}_k$

Step 3: calculate the gradient $\nabla f(\underline{x}_{k+1})$ and check for convergence.

Step 4: update $\underline{\underline{B}}^{-1}$ according to equation (3.47) and go to Step 2.

3.2.2 Nudged elastic band method

The nudged elastic band method (NEB) for finding the MEP connecting two stable configurations (local minima) of the PES was presented first by Mills and Jónsson [21, 108, 109]. The current summary follows their line of argument [21].

The two stable configurations that are connected by the MEP are also denoted as initial state $\underline{R}^{(I)}$ and final state $\underline{R}^{(P)}$ of the transition. The path along the PES that connects the two states is approximated by a discrete number of points $\underline{R}^{(i)}$. These so-called images refer to different geometric configurations of the system that are defined by the coordinates of the nuclei $\underline{R}^{(i)} = \{\underline{R}_1^{(i)}, \dots, \underline{R}_{N_n}^{(i)}\}$. The set of images that is used to describe the path $\underline{R}^{(I)}, \dots, \underline{R}^{(P)}$ is called the chain or band of images.

3.2.2.1 The concept of the plain elastic band

In the plain elastic band (PEB) approach, neighboring images are connected by springs. The purpose of the spring forces is to ensure that the images remain evenly distributed along the path. The object function of the PEB is defined as (κ_i refer to specific spring constants)

$$S^{PEB}(\underline{R}^{(1)}, \dots, \underline{R}^{(P)}) = \sum_{i=2}^{P-1} V(\underline{R}^{(i)}) + \sum_{i=2}^P \frac{\kappa_i}{2} (\underline{R}^{(i)} - \underline{R}^{(i-1)})^2. \quad (3.50)$$

Thus, the force acting on each image is the sum of the negative gradients of the potential V with respect to the nuclei coordinates $\underline{\mathbf{R}}^{(i)}$ and the spring forces at $\underline{\mathbf{R}}^{(i)}$,

$$\underline{\mathbf{F}}_i^{PBE} = -\nabla V(\underline{\mathbf{R}}^{(i)}) + \underline{\mathbf{F}}_i^s \quad (3.51)$$

where

$$\underline{\mathbf{F}}_i^s = \kappa_{i+1}(\underline{\mathbf{R}}^{(i+1)} - \underline{\mathbf{R}}^{(i)}) - \kappa_i(\underline{\mathbf{R}}^{(i)} - \underline{\mathbf{R}}^{(i-1)}). \quad (3.52)$$

The path between initial state $\underline{\mathbf{R}}^{(1)}$ and final state $\underline{\mathbf{R}}^{(P)}$ – obtained by minimizing the function S^{PEB} with respect to the images in between $\underline{\mathbf{R}}^{(2)}, \dots, \underline{\mathbf{R}}^{(P-1)}$ – approximates the minimum energy path. This basic concept has fundamental problems and it has been shown that it cannot provide the exact MEP [110]. As pointed out by Jónsson et al. [21], the failure of PEB can be analyzed by comparing two extreme cases of very large and very small spring constants.

If the spring constants are large, the contribution of the second term in the S^{PEB} (3.50) becomes important. The shortest connection between $\underline{\mathbf{R}}^{(1)}$ and $\underline{\mathbf{R}}^{(P)}$ minimizes this term. When the spring contribution dominates S^{PEB} , minimization can lead to paths going over larger barriers if the length of the path can be shortened. The springs were only introduced to distribute images evenly along the path, but the spring forces $\underline{\mathbf{F}}_i^s$ also contain components that are normal to the MEP. These components can move images away from the MEP. By reducing the spring constants, this contribution can become smaller than any given threshold. Nevertheless, the MEP cannot be approximated with the desired accuracy as is shown in the following section.

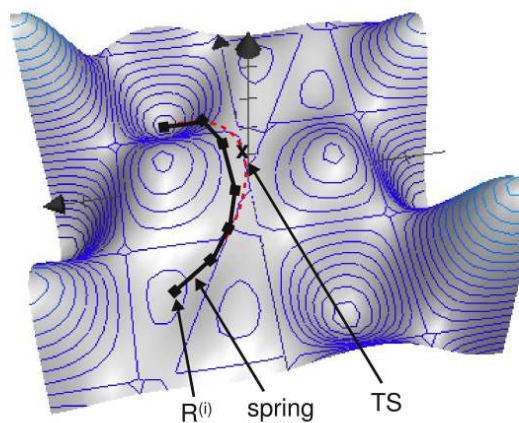


Figure 3.1: Sketch for a minimum energy path (MEP) obtained by a plain elastic band (PEB) with large springs constants (PEB path overestimates barrier). Images connected by springs are indicated by black squares connected by lines; MEP and transition state by red dotted line and black x, respectively.

For small spring constants, the spring forces and hence the component of \underline{F}_i^s normal to the MEP decreases and the images are closer to the MEP. But for small spring constants, the first term of S^{PEB} (3.50) becomes dominant and the object function is mainly minimized by the sum of $V(\underline{R}^{(i)})$ for the images $\underline{R}^{(2)}, \dots, \underline{R}^{(P-1)}$. Initial and final states $\underline{R}^{(1)}$ and $\underline{R}^{(P)}$ are by definition stable configurations referring to local minima of the PES. Therefore it may be energetically favorable that the images agglomerate in the vicinity of these two minima. The distribution of the images may become very uneven with a high density at the initial and final configurations but low density where V is largest. The latter is the interesting region as it contains the transition state of the MEP (for $\kappa = 0$ all images converge either in configuration $\underline{R}^{(1)}$ or $\underline{R}^{(P)}$).

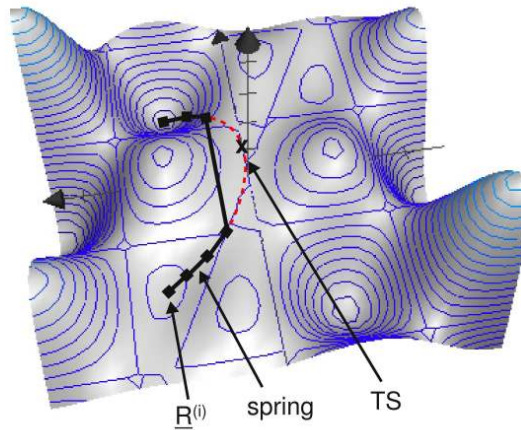


Figure 3.2: Sketch for a minimum energy path obtained by a plain elastic band with small spring constants (images agglomerate at initial and final configuration and cannot provide a good description of transition state region). Images that are connected by springs are indicated by black squares connected by lines; MEP and transition state by red dotted line and black x, respectively

This can be explained by the fact that the negative gradient of the potential $-\nabla V(\underline{R}^{(i)})$, which should only move the images towards the MEP, also has a component parallel to the MEP participating in the distribution of the images. Thus for very weak springs, this parallel component predominantly determines the distribution and inhibits an accurate description of the MEP in the region of the transition state.

It has been demonstrated that these problems are fundamental and cannot be solved by raising the number of images to the continuum limit [21].

3.2.2.2 Concept of the nudged elastic band

An improvement of the PEB formalism is the so-called nudged elastic band (NEB) method [21]. The critical behavior of the PEB approach described above could be related to two critical force components: the spring force components parallel to the MEP $\underline{F}_{i\parallel}^s$ and the components of the negative gradient of the potential $-\nabla V(\underline{R}^{(i)})_{\perp}$ normal to the MEP. Mills and Jónsson propose to simply subtract these critical components from the PEB force (3.51), yielding the NEB forces [21]

$$\underline{F}_i^{NEB} = -\nabla V(\underline{R}^{(i)}) + \underline{F}_i^s - (-\nabla V(\underline{R}^{(i)})_{\parallel} + \underline{F}_{i\perp}^s) = -\nabla V(\underline{R}^{(i)})_{\perp} + \underline{F}_{i\parallel}^s \quad (3.53)$$

$$\nabla V(\underline{R}^{(i)})_{\perp} = \nabla V(\underline{R}^{(i)}) - (\nabla V(\underline{R}^{(i)}) \cdot \underline{\tau}_i) \cdot \underline{\tau}_i \quad (3.54)$$

$$\underline{F}_{i\parallel}^s = \left[(\kappa_{i+1}(\underline{R}^{(i+1)} - \underline{R}^{(i)}) - \kappa_i(\underline{R}^{(i)} - \underline{R}^{(i-1)})) \cdot \underline{\tau}_i \right] \cdot \underline{\tau}_i \quad (3.55)$$

where $\underline{\tau}_i$ refers to the normalized local tangent at the image $\underline{R}^{(i)}$.

$$\underline{\tau}_i^* = \frac{\underline{R}^{(i)} - \underline{R}^{(i-1)}}{|\underline{R}^{(i)} - \underline{R}^{(i-1)}|} - \frac{\underline{R}^{(i+1)} - \underline{R}^{(i)}}{|\underline{R}^{(i+1)} - \underline{R}^{(i)}|} \quad (3.56)$$

$$\underline{\tau}_i = \underline{\tau}_i^* / |\underline{\tau}_i^*| \quad (3.57)$$

This correction guarantees that the approximation of the MEP only depends on the negative gradient of the potential, while the distribution of the images only depends on the spring forces. For sufficiently many images this ensures convergence of the NEB path towards the MEP. Mills and Jónsson refer to the force projection as ‘nudging’, (which is behind the name ‘nudged elastic band’) [21]. The NEB force no longer belongs to the object function S^{PEB} as defined in equation (3.50). S^{NEB} is not known, thus one is limited to minimization techniques that rely on the forces. In practice, this is not a restriction since most of the algorithms developed for geometry optimizations fulfill this condition.

For many images, the definition of the local tangent $\underline{\tau}_i$ from above (3.56) and (3.57) can lead to the formation of kinks in the path. In a subsequent publication [111], an improved definition for $\underline{\tau}_i$ was presented and will be mentioned in the following.

For images $\underline{R}^{(i)}$ with a corresponding potential energy $V(\underline{R}^{(i)})$ between the two neighboring images $\underline{R}^{(i+1)}$ and $\underline{R}^{(i-1)}$, only the adjacent image that is of higher energy is used to define the local tangent by choosing

$$\underline{\tau}_i^* = \begin{cases} \underline{\tau}^+ & \text{if } V(\underline{R}^{(i+1)}) > V(\underline{R}^{(i)}) > V(\underline{R}^{(i-1)}) \\ \underline{\tau}^- & \text{if } V(\underline{R}^{(i+1)}) < V(\underline{R}^{(i)}) < V(\underline{R}^{(i-1)}) \end{cases} \quad (3.58)$$

where

$$\underline{\tau}^+ = \underline{R}^{(i+1)} - \underline{R}^{(i)} \quad (3.59)$$

$$\underline{\tau}^- = \underline{R}^{(i)} - \underline{R}^{(i-1)}. \quad (3.60)$$

In addition, for images $\underline{R}^{(i)}$ that represent a maximum or a minimum along the approximated MEP, i.e., $V(\underline{R}^{(i+1)}) > V(\underline{R}^{(i)}) < V(\underline{R}^{(i-1)})$ or $V(\underline{R}^{(i+1)}) < V(\underline{R}^{(i)}) > V(\underline{R}^{(i-1)})$, the tangent is defined as a energy-weighted superposition of $\underline{\tau}_i^+$ and $\underline{\tau}_i^-$

$$\underline{\tau}_i^* = \begin{cases} \underline{\tau}^+ \Delta V_i^{\max} + \underline{\tau}^- \Delta V_i^{\min} & \text{if } V(\underline{R}^{(i+1)}) > V(\underline{R}^{(i-1)}) \\ \underline{\tau}^+ \Delta V_i^{\min} + \underline{\tau}^- \Delta V_i^{\max} & \text{if } V(\underline{R}^{(i+1)}) < V(\underline{R}^{(i-1)}) \end{cases} \quad (3.61)$$

with the weighing factors.

$$\Delta V_i^{\max} = \max(|V(\underline{R}^{(i+1)}) - V(\underline{R}^{(i)})|, |V(\underline{R}^{(i-1)}) - V(\underline{R}^{(i)})|) \quad (3.62)$$

$$\Delta V_i^{\min} = \min(|V(\underline{R}^{(i+1)}) - V(\underline{R}^{(i)})|, |V(\underline{R}^{(i-1)}) - V(\underline{R}^{(i)})|) \quad (3.63)$$

This ensures that there are no abrupt changes in the tangent when one image becomes higher in energy than another. Furthermore, a slightly modified definition of spring force has been given to provide an equidistant distribution of the images.

$$\underline{F}_{i\parallel}^s = (\kappa_{i+1} | \underline{R}^{(i+1)} - \underline{R}^{(i)} | - \kappa_i | \underline{R}^{(i)} - \underline{R}^{(i-1)} |) \cdot \underline{\tau}_i \quad (3.64)$$

This alternative definition of the local tangents significantly improved the original formalism and is generally used in NEB implementations and in the present work as well.

3.2.2.3 Climbing image extension of the NEB method

The NEB approximation of the MEP provides discrete images distributed along the MEP without explicit information about the saddle point itself. In many cases, one is especially interested in the saddle point of the MEP referring to the transition state. Climbing image NEB (CI-NEB) presented by Henkelman and Jónsson [112] is an extension of the NEB scheme that makes it possible to evaluate transition states.

For a given NEB path, the image with the highest energy, which is assumed to be the closest to the saddle point, is selected as a climbing image, $\underline{R}^{(climb)}$. For this image, a climbing force is defined as follows:

$$\underline{F}_{climb} = -\nabla V(\underline{R}^{(climb)}) + 2\nabla V_{\parallel}(\underline{R}^{(climb)}), \quad (3.65)$$

$$\underline{F}_{\text{climb}} = -\nabla V(\underline{R}^{(\text{climb})}) + 2(\nabla V(\underline{R}^{(\text{climb})}) \cdot \underline{\tau}_{\text{climb}}) \cdot \underline{\tau}_{\text{climb}}. \quad (3.66)$$

$\underline{F}_{\text{climb}}$ moves the climbing image uphill in energy along the direction parallel to the MEP (as described by the NEB path). Convergence is reached at the saddle point where the forces $\underline{F}_{\text{climb}}$ acting on the climbing image are zero.

The movement of the climbing image is coupled with the other images only via the definition of the local tangent $\underline{\tau}_{\text{climb}}$ (3.58 - 3.63) that defines the uphill direction. The other images are still connected with the climbing image by springs and will distribute left and right equidistantly if the same spring constant is chosen for all springs. The advantage of this formalism is that it is a simple extension of the NEB scheme. And since all images are relaxed simultaneously, there is no extra cost in applying the CI-NEB compared to NEB.

For complicated paths, the convergence behavior of CI-NEB can be critical if the approximation of the local tangent becomes inaccurate. The latter is based on positions and energies of the climbing image and its neighbors (3.58 - 3.63) and therefore is limited by the image density.

3.2.3 The dimer method

The dimer method for searching transition states is inspired by the concept of following local normal-modes of the PES [113, 114]. In this method, starting from a minimum geometric configuration of the PES, one follows uphill in energy along the direction of a certain normal mode where the Hessian matrix is evaluated for each step. This is rather expensive and these methods scale poorly with the number of degrees of freedom. The dimer method [22], presented in this section, makes it possible to approximate the direction of the lowest eigenmode, hence it is applicable for systems with a large number of degrees of freedom.

The dimer shown in Figure 3.3 consists of two images, $\underline{R}^{(1)}$ and $\underline{R}^{(2)}$, that are separated by a fixed distance $2\Delta R$ and the central point of the dimer $\underline{R}^{(0)}$ that lies in the middle between $\underline{R}^{(1)}$ and $\underline{R}^{(2)}$. Analogous to the image definition for the NEB method, each image $\underline{R}^{(i)}$ represents a different geometry of the system and is defined by the coordinates of the nuclei $\underline{R}^{(i)} = \{\underline{R}_1^{(i)}, \dots, \underline{R}_{N_n}^{(i)}\}$. The dimer orientation axis \underline{N} is the normalized vector pointing from the image $\underline{R}^{(2)}$ to the image $\underline{R}^{(1)}$. (see Figure 3.3).

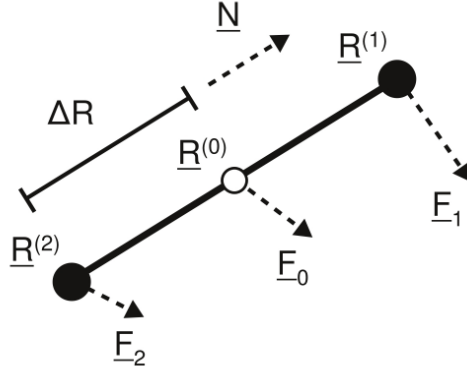


Figure 3.3: Illustration of a dimer constructed by the images $\underline{R}^{(0)}$, $\underline{R}^{(1)}$ and $\underline{R}^{(2)}$.

The energy of each image $\underline{R}^{(i)}$ is given by the potential $\underline{E}_i = V(\underline{R}^{(i)})$ and the force acting on the image $\underline{R}^{(i)}$ is the negative gradient of the potential $\underline{F}_i = -\nabla V(\underline{R}^{(i)})$. The total energy of the dimer E is the sum of E_1 and E_2 .

$$E = E_1 + E_2 \quad (3.67)$$

The dimer saddle point search algorithm moves the dimer along the PES towards the saddle point. This is realized by an alternating sequence of rotations around the midpoint $\underline{R}^{(0)}$ and translations of $\underline{R}^{(0)}$. The rotation step orients the dimer axis \underline{N} via forces into the direction of minimum curvature that refers to the direction of the lowest eigenmode. This strategy was developed by Voter in another context [115] and makes it possible to estimate the lowest curvature mode without having to evaluate the Hessian matrix. The translation step moves the dimer upwards along the PES in the direction of lowest curvature.

The curvature $C_{\underline{N}}$, along the dimer axis \underline{N} can be approximated by finite differences as follows:

$$C_{\underline{N}} = \frac{(\underline{F}_2 - \underline{F}_1) \cdot \underline{N}}{2\Delta R} = \frac{E - 2E_0}{(\Delta R)^2}. \quad (3.68)$$

Since the dimer length $2\Delta R$ is a constant, the curvature $C_{\underline{N}}$ is linearly related to the dimer energy E for rotations about the midpoint $\underline{R}^{(0)}$.

Henkelman et al. [22] use only the properties of the images $\underline{R}^{(1)}$ and $\underline{R}^{(2)}$. The force acting on $\underline{R}^{(0)}$ is approximated by the average of \underline{F}_0 with

$$\underline{F}_0 = \frac{\underline{F}_1 + \underline{F}_2}{2} \quad (3.69)$$

and E_0 can be expressed by the properties of the images $\underline{R}^{(1)}$ and $\underline{R}^{(2)}$ using equation (3.68)

$$E_0 = \frac{E}{2} + \frac{\Delta R}{4} (\underline{F}_2 - \underline{F}_1) \cdot \underline{N}. \quad (3.70)$$

The dimer method has been improved by Heyden et al. [116] and further by Kästner and Sherwood [117]. In contrast to the original version [22], the images $\underline{R}^{(0)}$ and $\underline{R}^{(1)}$ are used instead of $\underline{R}^{(1)}$ and $\underline{R}^{(2)}$. This has the advantage that only one image has to be considered during the rotation and that the gradient and the energy at $\underline{R}^{(0)}$ needed for the translation step are directly calculated. But it decreases the accuracy of the curvature calculation from $O(\Delta R^2)$ to $O(\Delta R)$ [116]. Here, the force \underline{F}_2 is approximated via finite differences,

$$\underline{F}_2 = 2\underline{F}_0 - \underline{F}_1 \quad (3.71)$$

yielding a new expression for the curvature

$$C_{\underline{N}} = \frac{(\underline{F}_0 - \underline{F}_1) \cdot \underline{N}}{\Delta R}. \quad (3.72)$$

3.2.3.1 Definition of the rotation plane

The normal force \underline{F}_i^\perp at the image $\underline{R}^{(i)}$ is the force component normal the dimer axis \underline{N} .

$$\underline{F}_i^\perp = \underline{F}_i - (\underline{F}_i \cdot \underline{N}) \cdot \underline{N} \quad (3.73)$$

The rotational force \underline{F}^\perp acting on the dimer is set to be the net normal force acting on $\underline{R}^{(1)}$.

$$\underline{F}^\perp = \underline{F}_1^\perp - \underline{F}_2^\perp \quad (3.74)$$

Assuming a quadratic behavior of the PES in the region of the dimer, as well as using equations (3.71) and (3.73), the rotational force acting on image $\underline{R}^{(1)}$ can also be written as

$$\underline{F}^\perp = 2(\underline{F}_1 - \underline{F}_0) - 2[(\underline{F}_1 - \underline{F}_0) \cdot \underline{N}] \cdot \underline{N}. \quad (3.75)$$

The rotation plane is spanned by vectors \underline{N} and $\underline{\Theta}$ where $\underline{\Theta}$ is a unit vector normal to \underline{N} that points in the direction of the rotation. The dimer axis \underline{N} is already determined by the dimer orientation and in general the direction $\underline{\Theta}$ of defined by the direction of the rotational force \underline{F}^\perp .

It has been shown by Henkelman et al. [22] that instead of rotating according to the rotational force but using a conjugate gradient method (CG) [107] to determine the search direction, i.e., the rotation plane, leads to better convergence.

The CG method [107] determines the new search direction \underline{G}_n based on the information provided by the force of the iteration n , \underline{F}_n and the force, as well as the search direction of the previous step, \underline{F}_{n-1} , and \underline{G}_{n-1} as follows,

$$\underline{G}_n = \underline{F}_n + \gamma_n \underline{G}_{n-1} \quad (3.76)$$

with

$$\gamma_n = \frac{(\underline{F}_n - \underline{F}_{n-1}) \cdot \underline{F}_n}{\underline{F}_n \cdot \underline{F}_n}. \quad (3.77)$$

The CG method had to be slightly modified to be applicable to the constraint minimization problem of rotation [22]. For the dimer rotation, the search direction \underline{G} is represented by the rotation plane spanned by the unit vectors \underline{N} and \underline{Q} where \underline{N} is already specified by the dimer orientation. Therefore, the update of the search direction \underline{G} is restricted to an update of \underline{G}^\perp , a vector that is normal with respect to \underline{N} .

Using equation (3.76) to evaluate the new search vector, \underline{G}_n^\perp would yield a vector that is not normal with respect to the new dimer orientation axis \underline{N}_n , as demanded by the constraints of the dimer rotation. The reason is that $\underline{G}_{n-1}^\perp$ is per definition parallel with respect to \underline{Q}_{n-1} , hence it is normal with respect to the old dimer axis \underline{N}_{n-1} as illustrated in Figure 3.4.

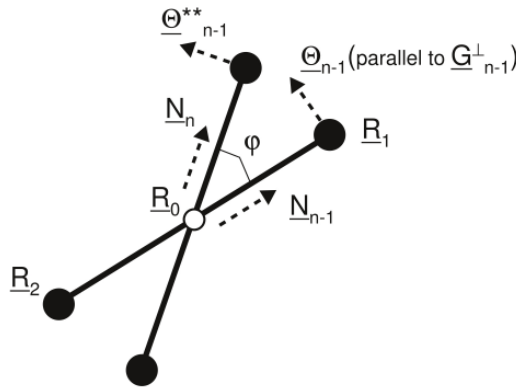


Figure 3.4: Definition of \underline{Q}_{n-1}^{**} used in the modified CG method for the dimer rotation. All vectors are in the plane of rotation spanned by the unit vectors \underline{N}_{n-1} and \underline{Q}_{n-1} .

In order ensure that \underline{G}_n^\perp and the actual dimer orientation \underline{N}_n are normal with respect to each other, Henkelman et al. [22] propose in their modified scheme to use a vector with the length of $|\underline{G}_{n-1}^\perp|$ pointing in the direction $\underline{\Theta}_{n-1}^{**}$ instead of $\underline{G}_{n-1}^\perp$ itself for their update of the search direction. Here $\underline{\Theta}_{n-1}^{**}$ is a unit vector that lies in the old rotation plane but is perpendicular to \underline{N}_n (see Figure 3.4).

$$\underline{\Theta}_{n-1}^{**} = \frac{\underline{G}_{n-1}^\perp - (\underline{G}_{n-1}^\perp \cdot \underline{N}_n) \cdot \underline{N}_n}{\left| \underline{G}_{n-1}^\perp - (\underline{G}_{n-1}^\perp \cdot \underline{N}_n) \cdot \underline{N}_n \right|} \quad (3.78)$$

This slight modification leads to the modified CG scheme [22]

$$\underline{G}_n^\perp = \underline{F}_n^\perp + \gamma_n \left| \underline{G}_{n-1}^\perp \right| \underline{\Theta}_{n-1}^{**} \quad (3.79)$$

where

$$\gamma_n = \frac{(\underline{F}_n^\perp - \underline{F}_{n-1}^\perp) \cdot \underline{F}_n^\perp}{\underline{F}_n^\perp \cdot \underline{F}_n^\perp}. \quad (3.80)$$

3.2.3.2 Rotation of the dimer

After evaluating the search direction the optimal step length in case of a rotation, the optimal rotation angle φ_{\min} that rotates the dimer into the direction of minimum curvature has to be determined. Originally, Newton's method [22] and an improved method based on a Taylor expansion [22] of the energy were proposed to determine φ_{\min} . Another strategy to evaluate φ_{\min} was presented later by Heyden et al. [116]. This is the basis of the dimer implementation in the present work discussed in this section.

It has been shown [116] that a rough estimate for the rotation angle φ_{\min} can be made by using the forces \underline{F}_0 and \underline{F}_1 . The estimated angle φ_1

$$\varphi_1 = \frac{1}{2} \arctan \frac{\partial C_{\underline{N}} / \partial \varphi}{2 |C_{\underline{N}}|} \quad (3.81)$$

with

$$\frac{\partial C_{\underline{N}}}{\partial \varphi} = \frac{2(\underline{F}_0 - \underline{F}_1) \cdot \underline{\Theta}}{\Delta R} \quad (3.82)$$

is required for two purposes. First, it helps to decide if a rotation step is necessary. If φ_1 is smaller than a given threshold $|\varphi_{tol}|$, it is assumed that the dimer is already oriented well enough and no rotation is needed. Second, if a rotation step is carried out, the

dimer gets rotated first by φ_I and the forces of the rotated image $\underline{R}^{(I)*}$ are evaluated. Then both the information at the initial point $\underline{R}^{(I)}$ and the point $\underline{R}^{(I)*}$ is used to evaluate the optimal step length φ_{\min} .

Heyden et al. [116] showed that the curvature $C_{\underline{N}}$ during a rotation in the plane spanned by \underline{N} and $\underline{\Theta}$ can be expressed by a Fourier series.

$$C_{\underline{N}}(\varphi) = \frac{a_0}{2} + a_1 \cos(2\varphi) + b_1 \sin(2\varphi) \quad (3.83)$$

The constants a_0 , a_1 , and b_1 are determined by the eigenvalues and eigenvectors of the exact Hessian and can be approximated assuming a locally quadratic PES [116] where

$$b_1 = \frac{1}{2} \frac{\partial C_{\underline{N}}(\varphi=0)}{\partial \varphi}, \quad (3.84)$$

$$a_1 = \frac{C_{\underline{N}}(\varphi=0) - C_{\underline{N}}(\varphi=\varphi_1) + b_1 \sin(2\varphi_1)}{1 - \cos(2\varphi_1)}, \quad (3.85)$$

and

$$a_0 = 2C_{\underline{N}}(\varphi=0) - 2a_1. \quad (3.86)$$

Together with eq. (3.83), the optimal rotation angle φ_{\min} is given by

$$\varphi_{\min} = \frac{1}{2} \arctan \frac{b_1}{a_1}. \quad (3.87)$$

To ensure that φ_{\min} does not rotate the dimer into the direction of maximum curvature, the curvature at φ_{\min} can be checked using equation (3.83) if the rotational force is not converged after rotation the new rotation axis $\underline{\Theta}$ is evaluated. In the present work, the modified CG method [22] as described above is used to determine the new rotation axis $\underline{\Theta}$.

3.2.3.3 Dimer translation

After rotating the dimer into the direction of minimum curvature, it is translated. To evaluate the direction of translation, the force component along the dimer axis \underline{N} is inverted.

$$\underline{F}^T = \underline{F}_0 - 2\underline{F}_0 \cdot \underline{N} \quad (3.88)$$

This modified translation force (3.88) moves the dimer uphill in the direction \underline{N} that, after successful rotation, approximates the direction of the lowest eigenmode.

Considering the fact that the tangent of the MEP coincides with the direction of the lowest eigenmode, this strategy of force modification is very similar to the definition of the modified force for the climbing image (3.65) in the CI-NEB scheme. There the force component along the direction defined by the approximation of the MEP is inverted.

The BFGS optimization algorithm is used for the dimer translation. This is motivated by the work of Kästner and Sherwood [117]. They compared four different optimization algorithms (BFGS, CG, Steepest descent and Damped dynamics) for the translation and found that the BFGS optimization leads to significantly faster convergence. Finally, rotation and translation steps are repeated until the force \underline{E}_0 acting on the central point of the dimer $\underline{R}^{(0)}$ is sufficiently small.

4 Perfect and reduced vanadium pentoxide, V_2O_5

Vanadium pentoxide, or V_2O_5 , is widely used in catalytic applications. Industrial catalysts for the SCR process to remove nitric oxides from waste gas contain V_2O_5 and it is generally accepted that V_2O_5 provides the active sites for the reaction (see Chapter 2). These catalysts are very complex multi-metal oxide compounds and the structural details of the catalysts are unknown. Therefore, in the present work a model catalyst, the $V_2O_5(010)$ surface, is studied. As a first step, before investigating adsorption, diffusion, and reaction processes at the $V_2O_5(010)$ surface, the surface model itself has to be analyzed. In this section, a brief overview of the geometric and electronic properties of the perfect V_2O_5 crystal, the cluster approach, and a detailed description of the specific cluster models that are considered will be presented.

In the second part, the properties of the reduced $V_2O_5(010)$ surface will be discussed. This is motivated by the fact that the SCR reaction is supposed to involve reduction of the catalyst surface, which very likely leads to the formation of oxygen vacancies (see Chapter 2). Therefore, the reduced surface is modeled by the presence of oxygen vacancy sites. In addition to the properties of the different oxygen vacancy sites, vacancy diffusion at the $V_2O_5(010)$ surface layer will be discussed.

4.1 The perfect $V_2O_5(010)$ surface

4.1.1 Crystal structure of V_2O_5

Vanadium pentoxide, V_2O_5 , forms a layer-type orthorhombic lattice [118-121] with lattice constants $a = 11.519 \text{ \AA}$, $b = 4.373 \text{ \AA}$, $c = 3.564 \text{ \AA}$ [121]. The elementary cell contains two elemental units ($2 \times V_2O_5$, 14 atoms), see Figure 4.1. The crystal layers are composed of 8 planar atom layers (6 oxygen layers, 2 vanadium layers) and extend parallel to the (010) direction [11]. Note that depending on the choice of the orthorhombic crystal axes, the layer netplane orientation may also be denoted by (001). The latter corresponds to an interchange of the orthorhombic lattice vectors \underline{b} and \underline{c} as proposed in Ref. [121]. The structure contains 3 differently coordinated types of

oxygen: singly coordinated vanadyl oxygen O(1), doubly coordinated bridging oxygen O(2), and triply coordinated oxygen O(3).

The crystal structure of orthorhombic V_2O_5 , with a view along the (001) direction, is shown in Figure 4.1 where the top-most (010) single layer is emphasized with shading. The elementary unit and crystal axes \underline{a} , \underline{b} , and \underline{c} are shown at the bottom. In the bulk terminated $V_2O_5(010)$ surface layer, each of the three differently coordinated oxygen types O(1), O(2), and O(3) can point either inside the crystal or stick out of the surface with respect to the closest vanadium atom. Therefore the surface layer contains six different types of oxygen. The oxygen pointing inside will be denoted O(1'), O(2'), and O(3').

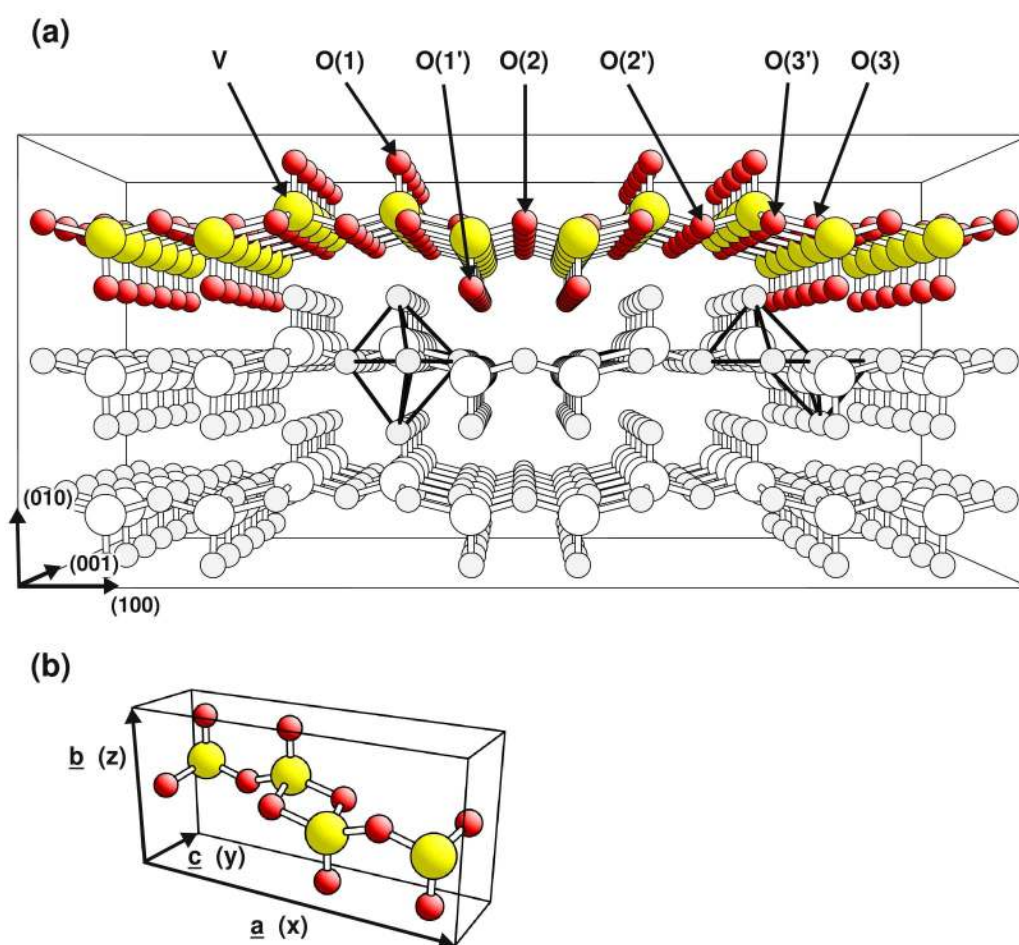


Figure 4.1: (a) Crystal structure of orthorhombic V_2O_5 , with a view along the (001) direction, where the top-most (010) single layer is emphasized with shading. Vanadium centers are shown by large yellow and oxygen centers by red balls. Neighboring atom centers are connected by lines to represent structural details. The non-equivalent oxygen centers of the (010) surface are labeled accordingly. In the second layer, the shapes of octahedral VO_6 (left) and bipyramidal V_2O_8 (right) units are emphasized. (b) The unit cell and crystal axes \underline{a} , \underline{b} and \underline{c} are shown at the bottom.

The crystal structure can be derived from packing of VO_6 octahedra as emphasized in Figure 4.1(a) on the left-hand side. A VO_6 unit and its V-O distances [118] are shown in Figure 4.2(a). The octahedron is strongly distorted along the (010) direction; short/long V-O(1) distances are 1.58/2.79 Å. A crystal layer is formed by double rows of these octahedra along the (001) direction. Adjacent double rows are mirrored along the (010) plane and connected at the octahedral edges.

This picture does not reflect the layer-type character of the V_2O_5 crystal structure. A more intuitive way to describe the crystal layers is a periodic arrangement of edges and corner sharing V_2O_8 bi-pyramids (Figure 4.1(a), right-hand side). A bipyramidal unit with the differently coordinated oxygen atoms and the V-O distances [118] labeled accordingly is presented in Figure 4.2(b).

Obviously, the strong distortion of the VO_6 octahedral units, and thus the large V-O distance between two layers, causes weak interlayer interactions [11]. Therefore, the (010) plane is the cleavage plane and atomically clean $\text{V}_2\text{O}_5(010)$ surfaces can be obtained by pushing razor blades into the crystal in high vacuum [122]. This also suggests that the $\text{V}_2\text{O}_5(010)$ surface undergoes only minor reconstructions and, therefore, the ideal bulk crystal structure provides a good model for the (010) surface. This has been confirmed by scanning tunneling microscopy (STM) [123, 124], atomic force microscopy (AFM) [124, 125], and high resolution electron energy loss spectroscopy (HREELS) [126] investigations.

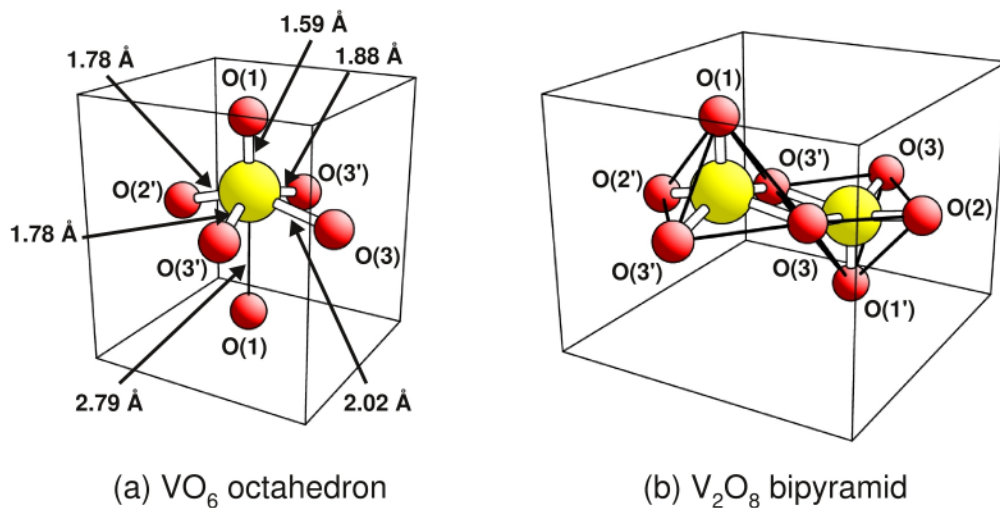


Figure 4.2: (a) octahedral VO_6 and (b) bipyramidal V_2O_8 unit of the V_2O_5 crystal structure (V-O bond distances in Ångström, [Å]). Vanadium centers are shown by large yellow and oxygen centers by red balls. The oxygen atoms are labeled according to their coordination.

The bulk structure of V_2O_5 has also been studied extensively by theory. The experimental structures could be confirmed based on total energy minimization [127-132], as well as in molecular dynamics studies [133, 134]. Further, the conclusion that the geometric structure of $V_2O_5(010)$ surface is very close to the bulk crystal structure was validated by theoretical studies [128, 129, 132, 133].

4.1.2 Cluster models for the $V_2O_5(010)$ surface

The experimental findings [123-126] that interlayer interactions are weak and that the $V_2O_5(010)$ surface only shows minor reconstructions indicate that interlayer interactions can be neglected and a bulk-structured $V_2O_5(010)$ single-layer is a reasonable surface model. Theoretical comparisons of multi- and single-layer models [128, 129, 132] showed that a $V_2O_5(010)$ single-layer indeed provides a good geometric and electronic description of the $V_2O_5(010)$ surface.

In the present work model, clusters cut out of a $V_2O_5(010)$ single layer with atoms at the positions of the ideal bulk crystal are used to describe local sections the perfect $V_2O_5(010)$ surface. To account for the missing interactions between the cluster atoms and the missing atoms of the extended system, the dangling bonds at the cluster edges are saturated by hydrogen atoms that are positioned along the O-V bond at a typical O-H distance (0.99 Å). The hydrogen saturation is chosen to ensure that the cluster keeps the formal valence charge of the surface (V^{5+} , O^{2-}) according to the formula

$$5 N_V - 2 N_O + N_H = 0, \quad (4.1)$$

where $N_{V,O,H}$ refers to the number of atoms that belong to the specific element in the cluster. For reduced surfaces, the presence of atoms from the underlying layer may become important, as will be discussed in Section 4.2.

Various model clusters are used to describe different surface sites of the perfect $V_2O_5(010)$ surface. These are the $V_{10}O_{31}H_{12}$, $V_{14}O_{42}H_{14}$, and $V_{14}O_{46}H_{22}$ clusters (see Figures 4.3 and 4.4). Because of the inversion symmetry of V_2O_5 bulk, the two sides of a (010) single-layer model clusters correspond to different $V_2O_5(010)$ surface areas. This is illustrated in Figure 4.3, where the different surface areas that are represented by the two (010) surfaces of the three different model clusters are emphasized by shading. At the left, the clusters are oriented in a way that they are centered at the vanadyl double row sticking out of the surface. At the right it can be seen that the other side of the same clusters can be used to model the valley between two vanadyl double rows.

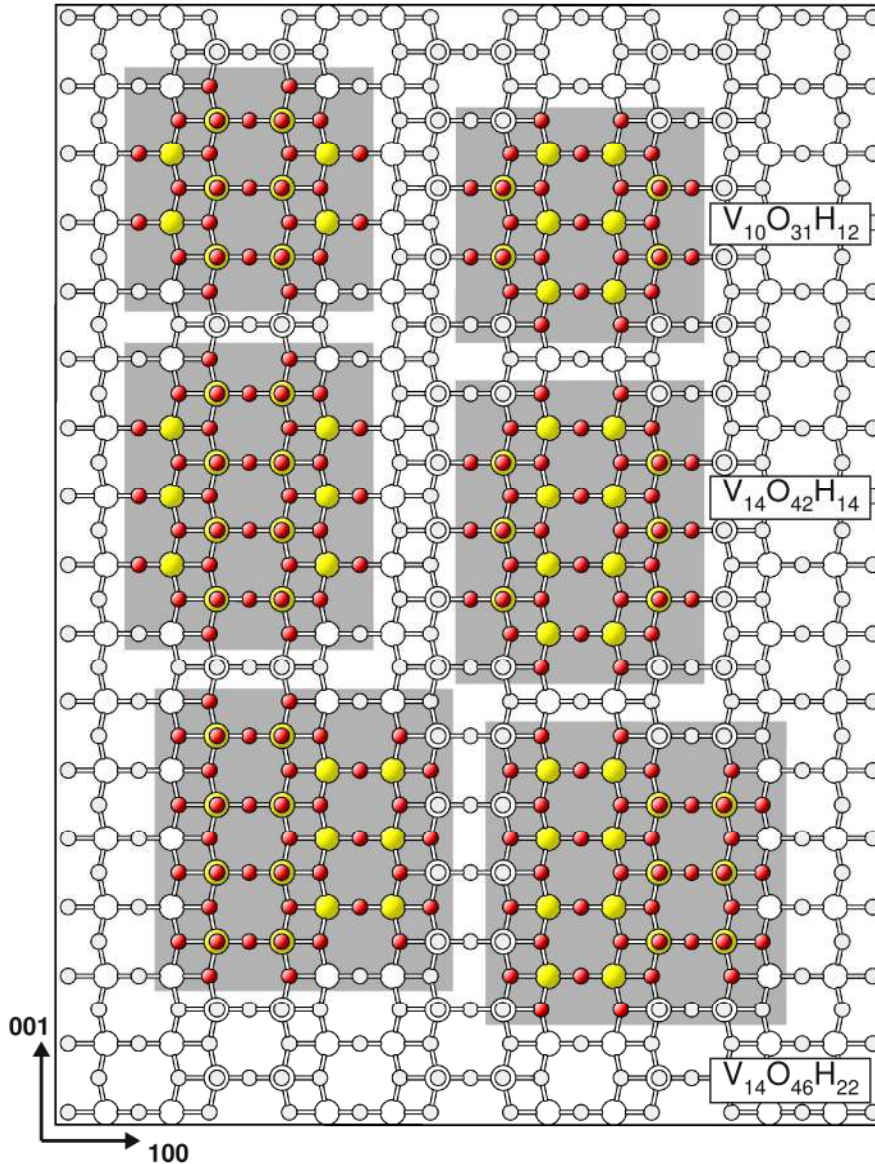


Figure 4.3: Top view of $V_2O_5(010)$ surface layer. Both sides of model clusters that are used to represent different surface areas are emphasized with shading; vanadium centers are shown by large yellow and oxygen centers by red balls.

The simulation of the cluster interaction with the missing extended environment by hydrogen termination is an approximation. As a consequence, it generates slight variations of the properties for different cluster atoms that are otherwise translationally equivalent in an infinitely extended system (as discussed in [23, 24]). Naturally, the variations are larger for atoms at the boundary zone than for central atoms. Surface processes such as adsorption, individual reaction and diffusion steps are located at specific surface sites or surface areas. Thus, it is important to choose a cluster model that is large enough to ensure that atoms belonging to the surface area of interest are not in the boundary zone.

The different clusters used in the present work are chosen in a way that the corresponding surface region of interest is located in the center of the cluster. This has the advantage that even small clusters can represent a relatively large surface area that does not contain atoms from the boundary zone. The different clusters are shown in Figure 4.4 with the specific surface sites that are modeled by the cluster and labeled accordingly.

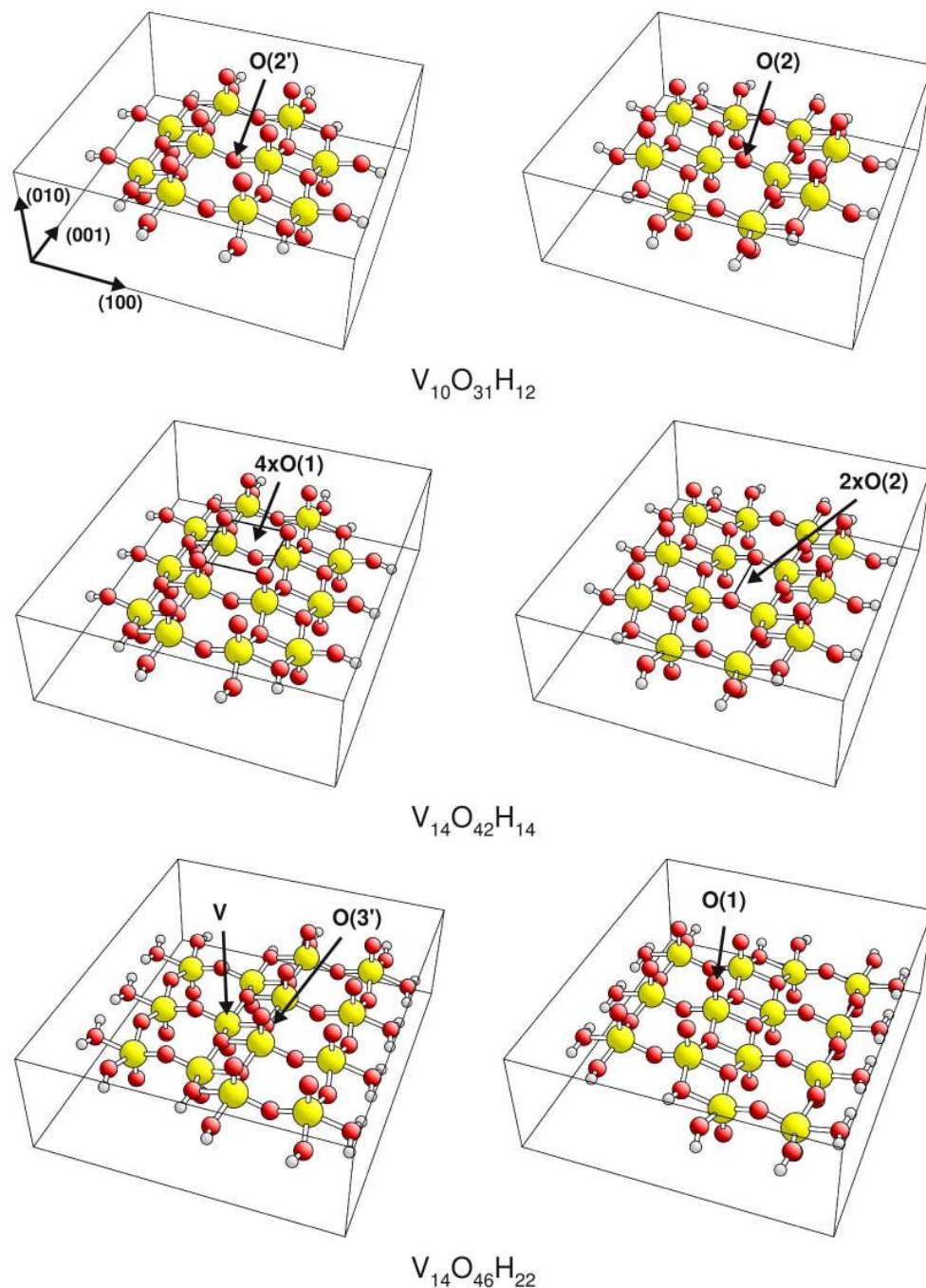


Figure 4.4: Cluster models for different surface sites of the perfect $V_2O_5(010)$ surface ($4xO(1)$ and $2xO(2)$ are connected by black lines). Vanadium centers are shown by large yellow balls, oxygen centers by red balls, and terminal hydrogen centers by small gray balls.

The center of the $V_{10}O_{31}H_{12}$ cluster is a doubly coordinated oxygen site. The two (010) surfaces of this cluster are used to describe the local surface environment of the O(2) and O(2') sites. The remaining O(1), O(3), O(3') sites, and the V site are modeled by the central region of the $V_{14}O_{46}H_{22}$ cluster.

As will be discussed in Chapter 5, the NH_4 molecule can interact with several surface atoms simultaneously, which results in adsorption sites consisting of four neighboring vanadyl oxygen sites that will be denoted as $4xO(1)$, as well as two adjacent bridging oxygen sites, $2xO(2)$. These two multi-atom adsorption sites are modeled by the $V_{14}O_{42}H_{14}$ cluster shown in Figure 4.4, where the four O(1) and two O(2) atoms are connected by black lines.

These model clusters are based on previous cluster studies of the $V_2O_5(010)$ surface [23, 24, 135-137]. The convergence behavior for different cluster sizes has been investigated extensively [23, 24], concluding that electronic and geometric properties converge rather quickly according to cluster size. As a result, the central section of a $V_{10}O_{31}H_{12}$ cluster was found to be well converged.

4.1.2.1 Geometric and energetic properties of $V_2O_5(010)$ cluster models

Due to the cluster approximation, atoms that are otherwise translationally equivalent in an infinitely extended system vary in their properties. As a result the cluster with the ideal bulk structure does not reflect the minimum geometry. Performing a geometry relaxation based on electronic structure calculations leads to a different cluster geometry. An educational example that illustrates this effect is to perform a geometry optimization where only the positions of the terminal hydrogen atoms are kept fixed. Figure 4.5 compares the geometry of the relaxed structure with that of perfect V_2O_5 bulk geometry.

It can be seen immediately that the cluster geometry changes due to the relaxation. Yet it conserves the overall topology of the perfect $V_2O_5(010)$ surface due to the peripheral hydrogen. The displacements are smaller for atoms in the center of the cluster. In order to quantify this, the cluster has been divided into a central V_2O_9 unit (atoms labeled with \mathbf{x} in Figure 4.5) and the remaining boundary zone. The corresponding largest atom displacement, Δr_{\max} and maximum change of V-O bond distance, $\Delta d(V-O)_{\max}$ for the central V_2O_9 unit as well as the boundary zone are presented in Table 4.1.

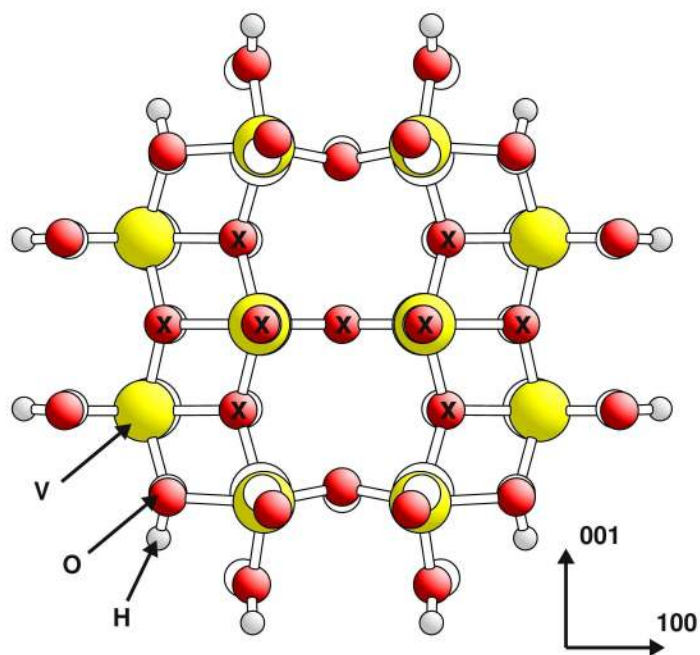


Figure 4.5: Relaxed structure of the $V_{10}O_{31}H_{12}$ cluster (only hydrogen atoms kept fixed). Vanadium centers are shown by large yellow balls, oxygen centers by red balls, and small gray balls refer to hydrogen centers. Atoms of the central V_2O_9 are labeled with x . The lateral atom positions of the ideal structure are indicated with white balls.

Table 4.1: Cluster artifacts of the $V_{10}O_{31}H_{12}$ cluster (only terminal hydrogen are kept fixed in geometry optimization). Cluster correction energy, E_{corr} (in [eV]). Maximum change in V-O bond length $\Delta d(\text{V-O})_{\text{max}}$ and atom positions Δr_{max} (in [\AA]) for the central V_2O_9 unit and the remaining the boundary zone.

Cluster	$V_{10}O_{31}H_{12}$	
E_{corr}	-1.88	
Region	Central V_2O_9	Boundary zone
$\Delta d(\text{V-O})_{\text{max}}$	0.07	0.16
Δr_{max}	0.12	0.44

The atom positions of the central V_2O_9 unit remain very close to the ideal structure ($\Delta r_{\text{max}} = 0.12 \text{ \AA}$) and the deviations are significantly smaller compared to the boundary zone ($\Delta r_{\text{max}} = 0.44 \text{ \AA}$). In general, only minor variations of bond distances ($\leq 0.16 \text{ \AA}$) have been found for all bonds.

The geometry optimization of the cluster results in a lowering of the total energy. The total energy difference between the cluster with perfect V_2O_5 bulk geometry, $E_{\text{tot}}(\text{Cluster})$, and the relaxed structure, $E_{\text{tot}}^r(\text{Cluster})$, is denoted as cluster correction energy

$$E_{\text{corr}} = E_{\text{tot}}^r(\text{Cluster}) - E_{\text{tot}}(\text{Cluster}). \quad (4.2)$$

The cluster correction energy can become very large. For example, it is -1.88 eV (Table 4.1) for the relaxed $V_{10}O_{31}H_{12}$ (hydrogen atoms fixed). For this reason, it is important to consider E_{corr} for the definition of energetic quantities that are based on total energy differences, which is the case for the vacancy formation energy (Section 4.2) and the adsorption energy (Chapter 5). This will be discussed in detail in the corresponding sections.

Surface processes such as adsorption, reaction, and diffusion are accompanied by geometric changes of the surface. It is necessary to consider the relaxation of surface atoms here, but it may induce cluster artifacts as shown above. In general, large atom displacements in the central region of the cluster compared to the perfect V_2O_5 bulk structure are indicators that the cluster model is not appropriate. To minimize the artifacts and incorporate surface rearrangements at the same time, most cluster atoms are fixed and only the atoms in a central region are free to relax. For the clusters used in the present work - if not mentioned otherwise - this central region is defined by the specific site of interest as well as nearest and next-nearest neighbor atoms.

The three different clusters considering the specific central region yield six cluster models that are used to describe sections of the perfect $V_2O_5(010)$ surface. Table 4.2 compares cluster correction energies, E_{corr} , largest atom displacement, Δr_{max} , and maximum change of V-O bond distance, $\Delta d(\text{V-O})_{\text{max}}$, due to relaxation of central regions for the six cluster models. The changes in atom positions are smaller than 0.18 Å and the bond distance variations are below 0.05 Å. The cluster correction energies are smaller than 0.31 eV. This shows that the chosen cluster models provide a reasonable description of the geometric and energetic properties of the surface.

Table 4.2: Cluster artifacts of cluster models for different sites (site, nearest and next-nearest neighbors considered in geometry optimization). Cluster correction energy, E_{corr} (in [eV]). Maximum change in V-O bond length $\Delta d(\text{V-O})_{\text{max}}$ and atom positions Δr_{max} (in [\AA]).

Cluster	$\text{V}_{10}\text{O}_{31}\text{H}_{12}$	$\text{V}_{14}\text{O}_{42}\text{H}_{14}$		$\text{V}_{14}\text{O}_{46}\text{H}_{22}$		
Site	O(2)	4xO(1)	2xO(2)	O(1)	O(3)	V
E_{corr}	-0.18	-0.17	-0.31	-0.11	-0.22	-0.18
$\Delta d(\text{V-O})_{\text{max}}$	0.03	0.03	0.03	0.03	0.05	0.04
Δr_{max}	0.13	0.09	0.18	0.13	0.14	0.14

4.1.3 Electronic structure of the $\text{V}_2\text{O}_5(010)$ surface

Vanadium pentoxide is an insulator with a visible band gap of 2.35 eV [138], as indicated by its orange color. Optical adsorption experiments show a band gap of 2.3 eV [139], while optical reflectance experiments yield 2.38 eV [140].

The valence band is mainly formed by oxygen 2sp electron states with only a minor admixture of vanadium 3d states. Angle-resolved ultra-violet photoemission spectroscopy (ARUPS) experiments and DFT-based theoretical work [130, 141] determined a valence band width of 5.5 eV in good agreement.

The formal valence charge in V_2O_5 is V^{+5} and O^{-2} . However, there are sizable covalent contributions to binding. Therefore, local charging of the different atoms should be significantly smaller. Based on data from resonant photoemission spectroscopy (RPES) experiments, the charge distribution of V_2O_5 was approximated to be V^{+3} and $\text{O}^{-1.2}$ [142].

4.1.3.1 Electronic properties of $\text{V}_2\text{O}_5(010)$ cluster models

The electronic structure of the different cluster models is analyzed by comparing the atom charges and the density of states (DOS) with the previous theoretical and experimental studies mentioned above.

All atom charges are obtained by a Bader charge analysis [143] and from now on will be denoted as atom charges q . The calculated discrete DOS spectra have been smoothed by a Gaussian level broadening of 0.4 eV (full width at half maximum [FWHM]). To compare different DOS plots, the energy of the highest occupied orbital is shifted to the energy zero that is also marked by a gray vertical line in the plots.

The central region of the clusters is used to describe the surface properties. Therefore, the electronic properties of these areas are analyzed. Based on a Mullikan population analysis [144], the DOS can be projected on the different atom centers. As discussed in Section 4.1.1, the crystal structure can be described by V_2O_8 bipyramidal building blocks. Due to the inversion symmetry of the V_2O_5 bulk, it is sufficient to consider only a central VO_5 unit that already contains the different oxygen and vanadium species, although it does not reflect the correct stoichiometry. Therefore, in order to correlate the DOS of the central VO_5 pyramid with the total DOS of the extended system, contributions of different atom types are weighted according to the stoichiometry,

$$w = n(V_2O_5 \text{ unit cell})/n(VO_5). \quad (4.3)$$

The total DOS and the atom projected DOS's for the $V_{14}O_{46}H_{22}$ cluster are presented in Figure 4.6. The valence band region lies between -6 eV and 0 eV. It has a multi-peak structure. As shown by the atom projected DOS's, the main contribution comes from the oxygen 2sp electron states and smaller V 3d contributions where O(1) electronic states concentrate in the central region and O(2,3) electronic states cover the whole valence band. Important features like overall shape, valence bandwidth (5.6 eV) and band gap (1.8 eV) could be reproduced in good agreement with former theoretical studies and experimental results [23, 24, 141].

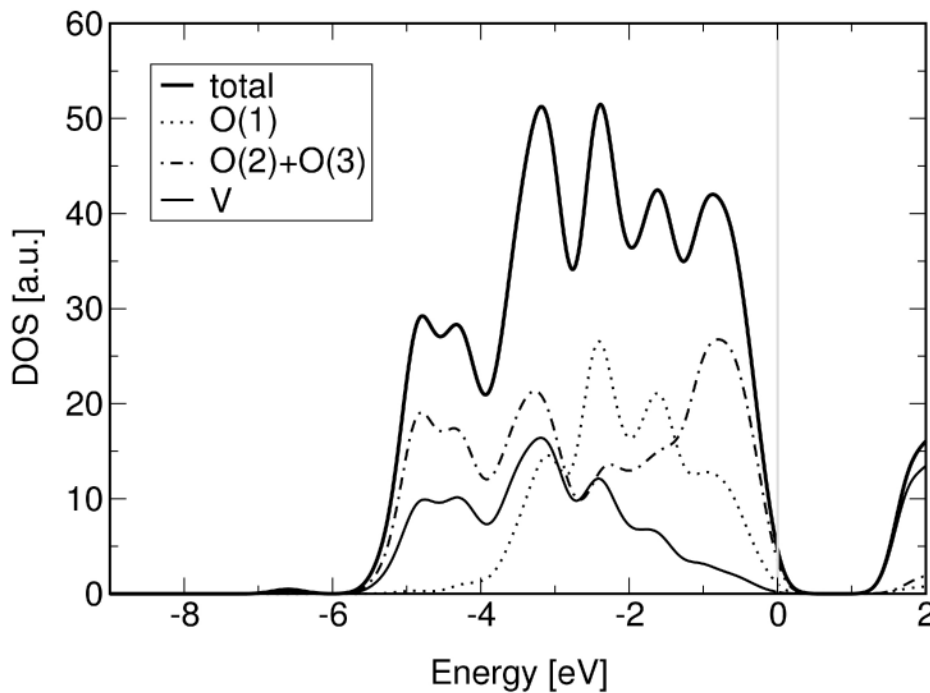


Figure 4.6: Total DOS (thick solid line) and atom-projected DOS (V solid, O(1) dotted, and O(2)+O(3) dotted-dashed line) for the central VO_5 unit of the $V_{14}O_{46}H_{22}$ cluster. The curves refer to a Gaussian level broadening of 0.4 eV (FWHM); HOMO energy levels are shifted to 0.0 eV.

The corresponding atom q charges are listed in the right column of Table 4.3. The vanadium atom is positively charged and the oxygen atoms negatively charged, which is concordant with the large O 2sp contribution in the valence band found for the atom-projected DOS (Figure 4.6). The differently coordinated oxygen O(1), O(2), and O(3) can be clearly distinguished as higher coordination results in accumulation of more negative charge. The local charging of the atoms is in agreement with chemical intuition. Nevertheless the atom charges are significantly smaller than the formal valence charges V^{+5} and O^{-2} , implying that the inter-atomic binding of V_2O_5 has sizeable covalent contributions.

Table 4.3: Atom charges q of the central VO_5 pyramid for the three different model clusters, $V_{10}O_{31}H_{12}$, $V_{14}O_{42}H_{14}$, and $V_{14}O_{46}H_{22}$, with perfect V_2O_5 bulk structure (in atomic units, [au]).

Cluster	$V_{10}O_{31}H_{12}$	$V_{14}O_{42}H_{14}$	$V_{14}O_{46}H_{22}$
$q(V)$	2.11	2.11	2.12
$q(O(1))$	-0.59	-0.59	-0.61
$q(O(2))$	-0.93	-0.93	-0.93
$q(O(3))$	-1.07	-1.07	-1.07

In the next step, the DOS plots as well as the atom charges obtained for the three different model clusters are compared. Figure 4.7 shows total DOS's obtained using the central VO_5 unit of the three clusters with perfect V_2O_5 bulk structure. The valence band multi-peak structures obtained for the three clusters differ only little. Also the valence bandwidth and the band gap are reproduced by all three clusters. In addition, the atom charges q listed in Table 4.3 confirm that the central region of all three clusters provide a good model for the electronic structure of $V_2O_5(010)$ surface.

So far only the electronic structures of clusters with the perfect V_2O_5 bulk structure have been analyzed. As discussed in Section 4.1.2, allowing for relaxation can induce geometric and energetic changes. Here the influence of local relaxation of the next and next-nearest neighbors on the electronic structure is discussed.

Figure 4.8 compares the total DOS's obtained for the central VO_5 unit of a $V_{14}O_{46}H_{22}$ cluster with perfect bulk structure and of $V_{14}O_{46}H_{22}$ clusters where the different central regions as defined for the O(1), O(3), and V site are relaxed. As can be seen, the local relaxation only causes minor changes.

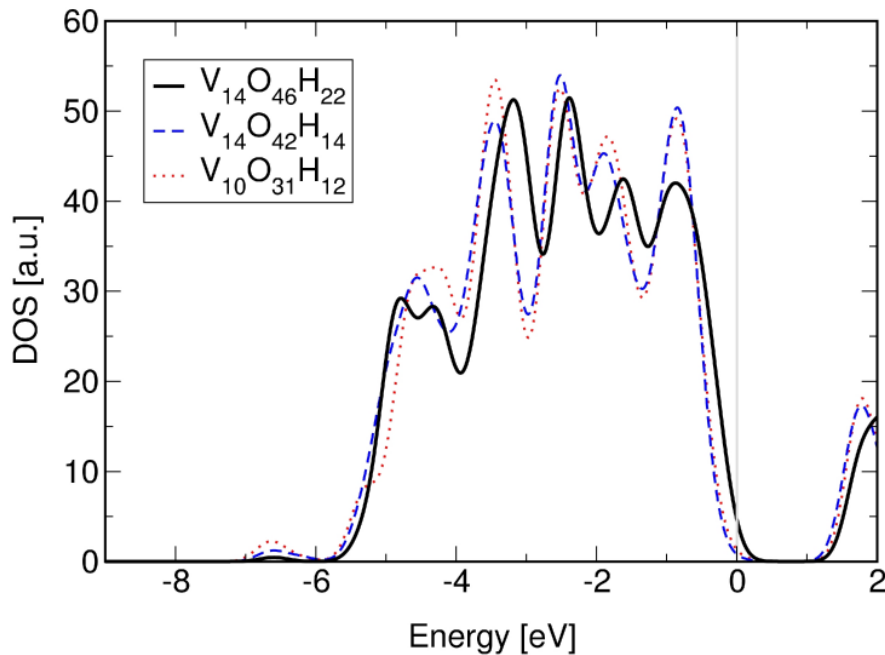


Figure 4.7: Total DOS curves for the central VO_5 unit of three different clusters, $V_{14}O_{46}H_{22}$ (black/solid line), $V_{14}O_{42}H_{14}$ (blue/dashed line), and $V_{10}O_{31}H_{12}$ (red/dotted line). The projected DOS for the atoms of the central VO_5 unit are weighted according to the stoichiometry of the V_2O_5 bulk. The curves refer to a Gaussian level broadening of 0.4 eV (FWHM); HOMO energy levels are shifted to 0.0 eV.

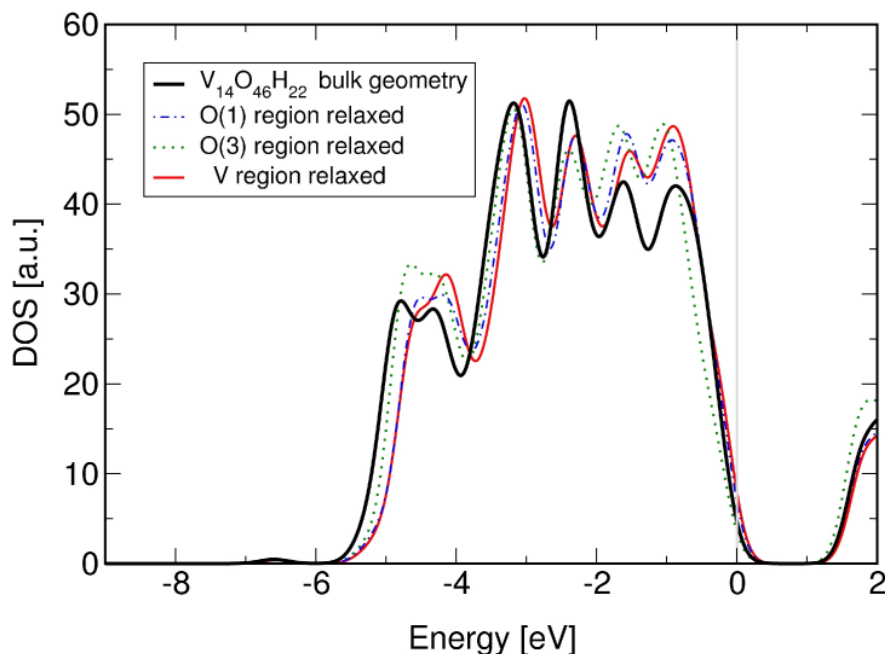


Figure 4.8: Total DOS curves for the central VO_5 unit of the $V_{14}O_{46}H_{22}$ cluster considering different relaxation areas (all atoms fixed represented by the black/thick/solid, nearest neighbors and next-nearest neighbors of O(1) by the blue/dotted-dashed, O(3) green/dotted, and V red/solid line). The projected DOS for the atoms of the central VO_5 unit are weighted according to the stoichiometry of the V_2O_5 bulk. The curves refer to a Gaussian level broadening of 0.4 eV (FWHM), HOMO energy levels are shifted to 0.0 eV.

The atom charges for all cluster models (as defined in Section 4.1.2) used to describe the perfect $V_2O_5(010)$ surface are listed in Table 4.4. The VO_5 unit contains three O(3) oxygen sites, therefore all three values are presented. The variations for the atom charges are very small; resulting in a maximum deviation of 0.05 au for corresponding atoms in different cluster models (Table 4.4).

Table 4.4: Atom charges q of the central VO_5 pyramid for the model clusters that are used to describe the different sites of the $V_2O_5(010)$ surface (in atomic units, [au]).

Cluster	$V_{10}O_{31}H_{12}$	$V_{14}O_{42}H_{14}$		$V_{14}O_{46}H_{22}$		
Site	O(2)	4xO(1)	2xO(2)	O(1)	O(3)	V
$q(V)$	2.10	2.15	2.11	2.14	2.15	2.14
$q(O(1))$	-0.61	-0.61	-0.60	-0.62	-0.62	-0.62
$q(O(2))$	-0.94	-0.96	-0.94	-0.96	-0.97	-0.95
$q(O(3))$	-1.08	-1.08	-1.07	-1.07	-1.08	-1.07
	-1.08	-1.07	-1.08	-1.07		-1.07
	-1.05	-1.07	-1.07	-1.06		-1.06

Altogether, the cluster models used in the present work provide a good description of the $V_2O_5(010)$ surface in agreement with previous theoretical studies [11, 23, 24, 129]. The different models that include local relaxation are comparable as illustrated by the geometric rearrangements, corresponding cluster correction energies, as well as the total DOS and the atom charges of the central region.

4.2 The reduced $V_2O_5(010)$ surface, oxygen vacancies

This work focuses on catalytic applications in which the fact that vanadium oxides are easy to reduce and to oxidize is important [145]. The oxidation state of unsupported and supported V_2O_5 after calcination is found to be V^{5+} [43, 145-147]. Under reaction conditions performing catalytic reactions, such as the SCR [43] or the oxidative dehydrogenation (ODH) of hydrocarbons [146], the catalyst gets partly reduced and vanadium atoms occur in an oxidation state between V^{3+} and V^{5+} [43, 146], where the exact oxidation state of the active site is uncertain [29].

For both catalytic reactions, SCR [17, 29] and ODH [145, 146, 148-151], a Mars and van Krevelen mechanism [57] was proposed. In this mechanism, lattice oxygen from the catalyst acts as a reactant that oxidizes the molecule. Thus, oxygen vacancies are formed and in a subsequent step, the catalyst gets re-oxidized by dissociative

adsorption of gas phase dioxygen. Hence, the catalytic performance depends strongly on the ability to provide lattice oxygen. In order to understand the catalytic properties, it is also necessary to investigate the geometric, energetic, and electronic properties of oxygen vacancies. As will be shown in the following, the neighborhood of a vacancy site is reduced and therefore the vacancy clusters discussed in the following section can provide models for the reduced $V_2O_5(010)$ surface.

Besides the surface reaction as discussed above, it has been shown that vacancies can be found after adsorption of atomic hydrogen [152], low energy electron bombardment of the surface [153] or heating at 400 °C [154]. Furthermore, as shown by isotopic labeling experiments [155], oxygen is quite mobile in V_2O_5 , as it can exchange its whole bulk oxygen with oxygen from the gas phase.

Matching the terminology used to address the different oxygen sites in Section 4.1, the vacancy site obtained by removing oxygen from an n-fold coordinated site will be denoted as O(n) vacancy or $O(n)_{vac}$.

The experimental characterization of oxygen vacancies of V_2O_5 is unclear. Scanning tunneling microscopy (STM) and angle-resolved X-ray photoelectron spectroscopy (ARXPS) experiments indicate the existence of O(1) vacancies [123, 156, 157], while high resolution electron energy loss spectroscopy (HREELS) suggests O(2) vacancies [152] and ARUPS spectra O(2) and/or O(3) vacancies [141].

Oxygen vacancies have also been studied theoretically [11, 23, 24, 135-137, 158-163]. This includes cluster [11, 23, 24, 135-137] and periodic [158, 160] DFT calculations with GGA functionals performed for vacancies related to all three differently coordinated oxygen sites. Additional studies on oxygen vacancies employed functionals that correct for on-site Coulomb interactions in strongly correlated systems, GGA + U [162, 163]. Furthermore, a cluster study of the O(1) vacancy compared standard GGA and GGA-hybrid functionals [161]. In general, all studies are in accordance with one another regarding geometric properties and the relative stability of oxygen vacancies, but there is some diversity in the vacancy formation energies.

The vacancy formation energy can be defined by total energies differences,

$$E_D^r(O) = E_{tot}^r(\text{Cluster-O}_{vac}) + E_{tot}(O) - E_{tot}^r(\text{Cluster}) \quad (4.4)$$

where $E_{tot}^r(\text{Cluster})$ and $E_{tot}^r(\text{Cluster-O}_{vac})$ are the total energies of the cluster that is relaxed with respect to the atom positions of the central region before and after the oxygen is removed. $E_{tot}(O)$ is the total energy of the free oxygen atom used as reference.

As discussed in Section 4.1.2.1, a cluster with its atoms at the positions of the perfect bulk structure does not represent the minimum configuration due to the cluster approximation. For cluster models that account for surface relaxation by allowing

rearrangements of cluster atoms, it is necessary to separate geometric, energetic, and electronic changes induced by the vacancy formation from the cluster artifacts caused by the local relaxation of the surface cluster. Therefore the relaxed cluster (with respect to the degrees of freedom defined by the cluster model) is used as a reference system and not the cluster with the ideal bulk structure.

In order to quantify the relaxation effects induced by the vacancy formation, the process is divided into two steps, the oxygen removal and the geometric relaxation. The ‘frozen’ vacancy formation energy E_D^f is defined as follows:

$$E_D^f(\text{O}) = E_{\text{tot}}^f(\text{Cluster-O}_{\text{vac.}}) + E_{\text{tot}}(\text{O}) - E_{\text{tot}}^r(\text{Cluster}) \quad (4.5)$$

where $E_{\text{tot}}^f(\text{Cluster-O}_{\text{vac.}})$ is the total energy of the vacancy cluster with all atoms frozen at the corresponding position, as defined by the relaxed surface cluster. Then the relaxation energy can be written as

$$E_{\text{relax}}(\text{O}) = E_D^r(\text{O}) - E_D^f(\text{O}) = E_{\text{tot}}^r(\text{Cluster-O}_{\text{vac.}}) - E_{\text{tot}}^f(\text{Cluster-O}_{\text{vac.}}). \quad (4.6)$$

The definition of the vacancy formation energy given in equations (4.4) and (4.5) refers to the removal of atomic oxygen, which is unlikely to happen. It is common to define the vacancy formation energies with respect to O_2 in gas phase instead,

$$E_D^{f,r}(\frac{1}{2} \text{O}_2) = E_{\text{tot}}^{f,r}(\text{Cluster-O}_{\text{vac.}}) + \frac{1}{2} E_{\text{tot}}(\text{O}_2) - E_{\text{tot}}^r(\text{Cluster}). \quad (4.7)$$

This alternative definition shifts the vacancy formation energy down by half the dissociation energy of O_2 (in the present work the calculated value of 2.79 eV is used) and does not affect the relative energetic order.

Different theoretical methods lead to variations in the vacancy formation energies. As expected, functionals that partly correct the DFT self-interaction error, such as GGA-hybrid and GGA + U, tend to localize electrons more strongly at the vacancy sites [161, 162]. This is accompanied by a significant drop of the vacancy formation energy. Scanlon et al. [162] found that their vacancy formation energies for the different vacancy sites calculated with a GGA + U functional are between 0.31 eV and 0.46 eV lower compared to their GGA energies. A similar result has been found comparing GGA and GGA-hybrid functionals for the O(1) vacancy sites, where the hybrid functional yielded a vacancy formation energy that was 0.66 eV smaller [161].

4.2.1 Results for surface O(1), O(2), O(3) and sub-surface O(1') vacancies

The $V_2O_5(010)$ surface layer contains six different types of oxygen (Figure 4.1) and therefore six different types of oxygen vacancies can be created. In contrast to the other oxygen sites, the O(1') site that is covered by the surface layer is not directly accessible from the surface. Therefore, although the O(1') oxygen is part of the surface layer, it will be denoted as sub-surface vacancy site.

It has been shown that interlayer interactions are important [23, 24, 137, 158-163] for the description of the O(1) vacancy in the V_2O_5 bulk and the $V_2O_5(010)$ surface. Due to the O(1)_{vac} formation, a bond is formed with an atom of the lower layer (as will be discussed in more detail later in this section). Hence, the single-layer cluster that represents the O(1) site at the perfect surface cannot be used as a model cluster for the O(1) vacancy site.

Previous cluster calculations have been performed with a $V_{20}H_{62}H_{12}$ two-layer cluster [23], where each of the two layers is represented by a $V_{10}O_{31}H_{12}$ cluster. Later, Friedrich [24] showed that also the smaller $V_{12}O_{40}H_{20}$ cluster – composed of a $V_{10}O_{31}H_{12}$ cluster describing the surface layer and a $V_2O_9H_6$ cluster that accounts for the contribution of the second layer (see Figure 4.9) – can be used to describe the properties of the O(1) vacancy. This cluster is used also in the present work. Analogously to the surface models defined in Section 4.1.2, the nearest and next-nearest neighbor atoms of the vacancy site were considered flexible to account for surface relaxation. This includes the O(1) site from the lower layer under the vacancy.

In contrast to the O(1)_{vac}, no bonds are formed with the lower layer due to O(2)_{vac} or O(3)_{vac} formation [23, 158, 160]. Cluster results comparing a two-layer $V_{20}O_{62}H_{24}$ cluster with a single-layer $V_{10}O_{31}H_{12}$ cluster found similar O(2) and O(3) vacancy formation energies ($\Delta E_D^f \leq 0.31$ eV) [23]. In the present study, the model clusters, $V_{10}O_{31}H_{12}$ used for the O(2) site and $V_{14}O_{46}H_{22}$ used for the O(3) site are used to describe the corresponding vacancy sites as well.

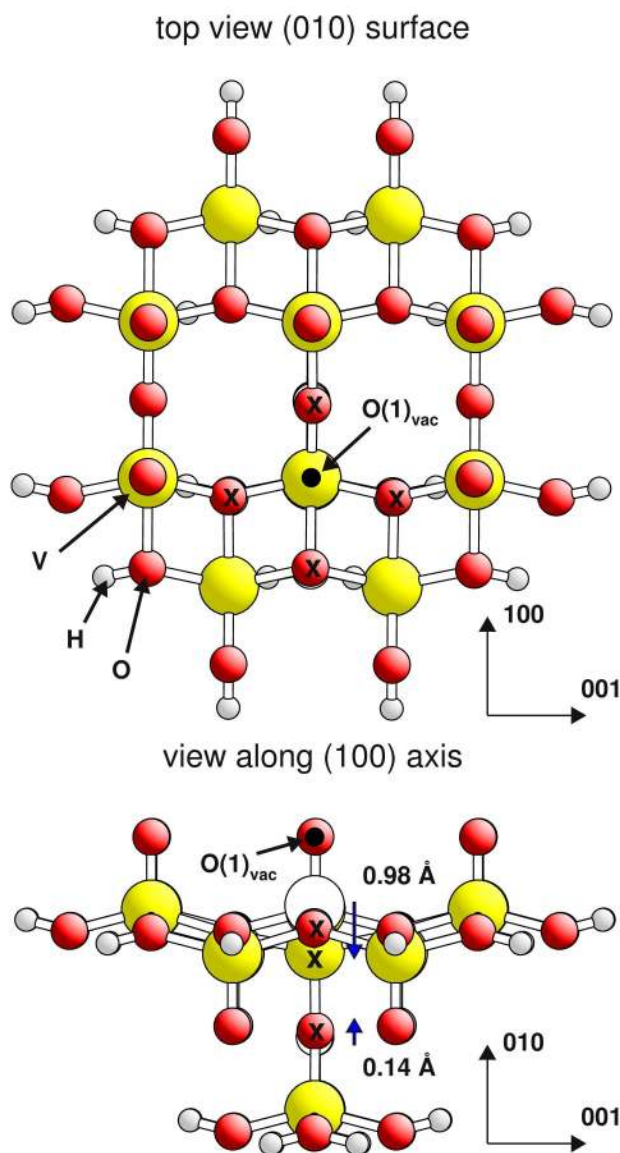


Figure 4.9: *O(1) vacancy cluster $V_{12}O_{39}H_{20}$, top view and view along (001) axis. Vanadium centers are shown by large yellow balls, oxygen centers by red balls, and small gray balls refer to hydrogen centers. The position of the missing oxygen atom is indicated by a small black dot. Atoms considered in the geometry optimization are labeled with **x**. The lateral positions of the surface cluster atoms before oxygen removal are indicated with white balls.*

The sub-surface $O(1')_{\text{vac}}$ site has not been considered so far, as $O(1')$ oxygen is hidden under vanadium atoms and therefore not directly accessible from the surface. But driven by oxygen diffusion processes, it could be possible to transform an oxygen vacancy created on the surface into an $O(1')_{\text{vac}}$. This kind of defect should not be excluded.

An additional model for the sub-surface $O(1')$ vacancy is necessary. A two-layer model similar to the one used for the $O(1)$ vacancy is used. The $V_2O_9H_8$ cluster that mimics the second layer is positioned on the other side of a $V_{10}O_{31}H_{12}$ cluster, generating the $V_{12}O_{40}H_{20}^*$ model cluster and $V_{12}O_{39}H_{20}^*$ cluster for the vacancy (Figure 4.10).

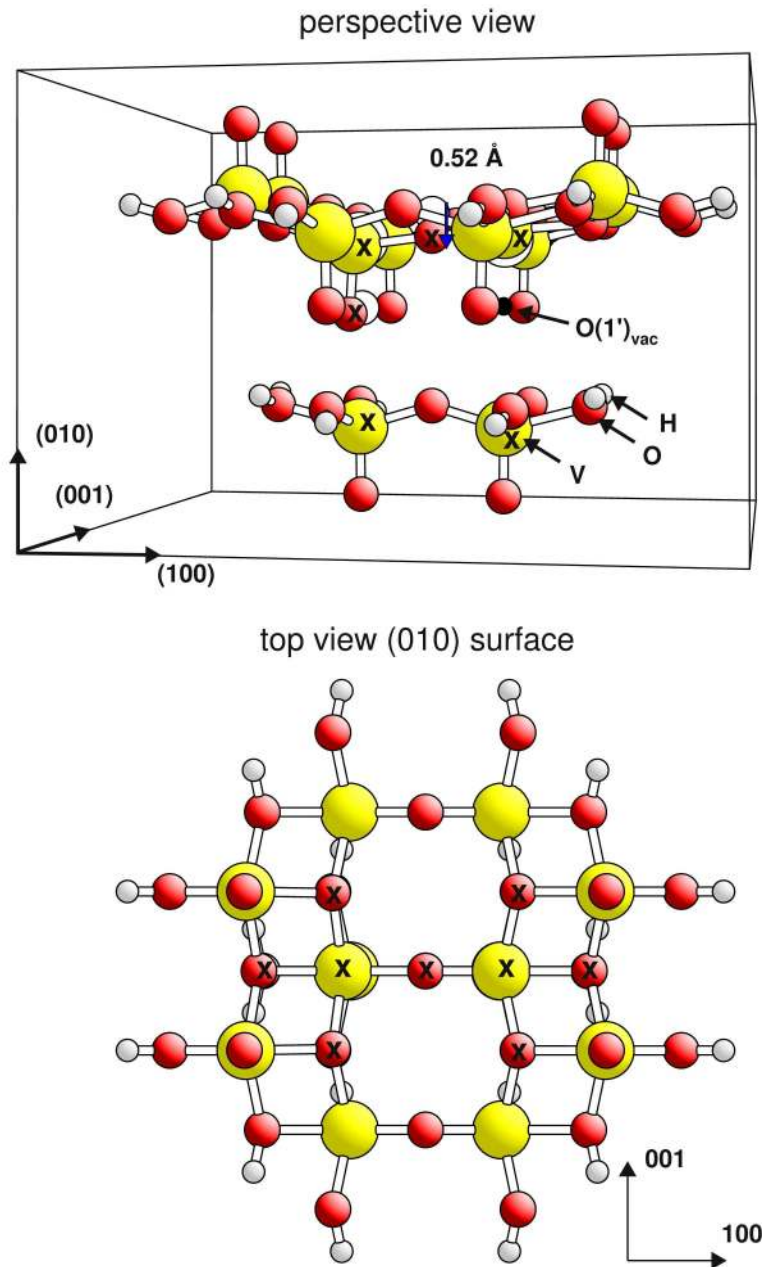


Figure 4.10: $O(1')$ vacancy cluster $V_{12}O_{39}H_{20}^*$, perspective and top view. Vanadium centers are shown by large yellow balls, oxygen centers by red balls, and small gray balls refer to hydrogen centers. The position of the missing oxygen atom is indicated by a small black dot. Atoms considered in the geometry optimization are labeled with x ($O(3)$ oxygen atoms of top layer are only indicated in top view). The lateral positions of the surface cluster atoms before oxygen removal are indicated with white balls.

By comparing the results for a calculation considering the nearest and next-nearest neighbors with a calculation considering the whole central unit of the top $V_{10}O_{30}H_{12}$ cluster, showed that in contrast to the cluster model used for the $O(1)_{vac}$, including more atoms causes a significant geometric change for the cluster model used for the $O(1')_{vac}$ ($\Delta r_{max} = 0.55 \text{ \AA}$). Therefore all atoms of the central V_2O_8 unit of the $V_{10}O_{30}H_{12}$ cluster (analog to the $O(2)$ vacancy) and the two vanadium atoms of the second layer have been considered in the geometry optimization (see Figure 4.10).

The results obtained for the different vacancy sites are summarized in Table 4.5. Analyzing the influence of the geometric relaxation the process is divided into two steps: the oxygen removal and the subsequent geometric relaxation. Three different settings are described in Table 4.5: (i) the surface cluster as reference system (relaxed with respect to the degrees of freedom defined by the cluster model), (ii) the cluster after removal of the oxygen atom ‘frozen’ in the geometry of the corresponding surface cluster and (iii) the relaxed vacancy cluster. The corresponding results will be discussed in the following section.

Table 4.5: Oxygen vacancy formation energies, $E_D(\text{O})$ and $E_D(\frac{1}{2}\text{O}_2)$, cluster correction energies, E_{corr} , relaxation energy, E_{relax} , and the difference between the triplet and singlet total energies, $E^{\text{trip}} - E^{\text{sing}}$ (in [eV]), atom charges q (in atomic units, [au]), of vanadium neighbors of vacancy sites (as the $\text{O}(1)_{\text{vac}}$ formation is accompanied by a strong reconstruction of the vanadium atom towards the $\text{O}(1)$ site of the lower layer the atom charge of this site is listed in addition to the vanadium atom charges), and largest change in atom positions induced by the vacancy formation Δr_{max} (in [\AA]). See text for further details.

	$\text{O}(1)_{\text{vac}}$	$\text{O}(2^{(s)})_{\text{vac}}$	$\text{O}(3^{(s)})_{\text{vac}}$	$\text{O}(1')_{\text{vac}}$
(i) Surface cluster				
E_{corr}	-0.07	-0.18	-0.22	-0.23
$q(\text{V})$	2.17	2.10 2.10	2.13 2.13 2.15	2.14
$q(\text{O}(1))$	-0.63	--	--	--
(ii) Surface cluster oxygen removed				
$E_D^f(\text{O})$	6.26	7.25	6.47	5.99
$q^f(\text{V})$	1.80	1.76 1.76	1.81 1.81 1.92	1.82
$q^f(\text{O}(1))$	-0.63	--	--	--
(iii) Surface cluster oxygen removed and relaxed				
$E_D^r(\text{O})$	4.98	6.44	6.18	5.69
$E_D^r(\frac{1}{2}\text{O}_2)$	2.19	3.65	3.39	2.90
E_{relax}	-1.28	-0.82	-0.29	-0.30
$q^r(\text{V})$	2.07	1.94 1.94	1.86 1.86 1.94	1.82
$q^r(\text{O}(1))$	-0.87	--	--	--
Δr_{max}	0.98	0.43	0.16	0.52
$E^{\text{trip}} - E^{\text{sing}}$	-0.29	-0.15	0.13	-0.42

4.2.1.1 Geometric and energetic properties for surface and sub-surface oxygen vacancies

The most significant geometric change can be found for the $\text{O}(1)$ vacancy formation. As mentioned above, interlayer interactions play an important role. The relaxed geometry of the $\text{O}(1)_{\text{vac}}$ cluster (Figure 4.9) shows that the vanadium atom next to the vacancy moves 0.97 \AA towards the $\text{O}(1)$ site of the second layer below surface. Due to the interaction with the vanadium atom, the V-O bond of the sub-surface vanadyl becomes weakened and a V-O-V bridge between vanadium atoms of the different

layers is formed instead. The bridging character of the transformed vanadyl oxygen is also reflected in the V-O-V bond distances. In the newly formed interlayer bridge they are 1.73 / 1.77 Å (vanadium atom from surface / sub-surface layer) and very close to the V-O(2)-V distance in the surface layer, 1.78 Å. This strong geometric change that includes a bond formation is also represented in the relaxation energy that is as large as -1.28 eV (Table 4.5). That both the geometric changes and the relaxation energy are dominated by the interlayer interactions can be demonstrated by comparing this result with a model that considers only the $V_{10}O_{31}H_{12}$ cluster of the first layer. For the latter, the vertical displacement of the vanadium atom next to the vacancy ($\Delta z = 0.33$ Å), as well as the relaxation energy ($E^{\text{relax}} = -0.18$ eV) are significantly smaller compared to the two-layer model.

The O(2) vacancy is depicted in Figure 4.11. To compensate for the missing oxygen the two vanadium atoms next to the vacancy interact more strongly with the remaining oxygen neighbors. As a result they are pulled apart by the relaxation. Thus the vacancy ‘hole’ opens around the O(2) vacancy. The V-V distance increases by 0.77 Å. Although no new additional bond is formed, as it is the case for the O(1)_{vac} formation, the large opening of the surface and thus stronger interaction with the surrounding atoms has a significant energetic impact, which is reflected by an $E_{\text{relax}}(\text{O}(2))$ of -0.82 eV.

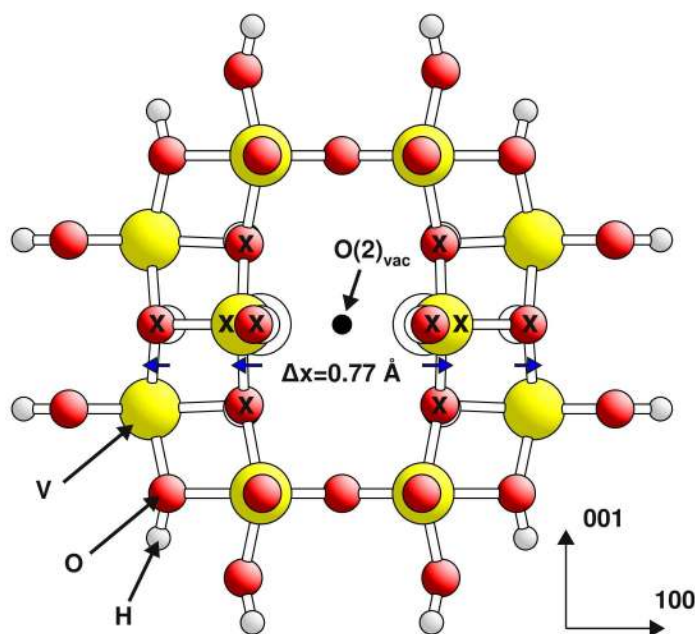


Figure 4.11: O(2) vacancy cluster $V_{12}O_{30}H_{12}$, top view. Vanadium centers are shown by large yellow balls, oxygen centers by red balls, and small gray balls refer to hydrogen centers. The position of the missing oxygen atom is indicated by a small black dot. Atoms considered in the geometry optimization are labeled with x. The lateral positions of the surface cluster atoms before oxygen removal are indicated with white balls.

In contrast to the previous two cases only minor rearrangements have been found, after relaxation of the surrounding of the $O(3)_{\text{vac}}$ site, $\Delta r_{\text{max}} > 0.13 \text{ \AA}$ (see Figure 4.12). This is also reflected by the small relaxation energy of -0.29 eV (Table 4.5).

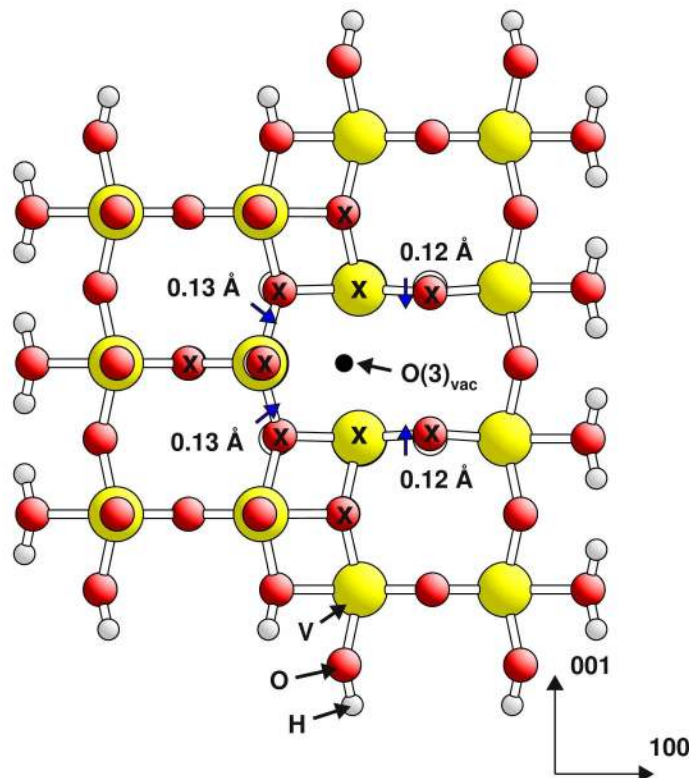


Figure 4.12: $O(3)$ vacancy cluster $V_{14}O_{45}H_{22}$, top view. Vanadium centers are shown by large yellow balls, oxygen centers by red balls, and small gray balls refer to hydrogen centers. The position of the missing oxygen atom is indicated by a small black dot. Atoms considered in the geometry optimization are labeled with x . The lateral positions of the surface cluster atoms before oxygen removal are indicated with white balls.

The relaxation induced by the $O(1')$ vacancy formation is not as pronounced or well defined as has been found for the $O(1)_{\text{vac}}$ site. The vanadium next to the vacancy site is shifted upwards and the vanadium atom on the other site of the $V-O(2)-V$ bridge is shifted downwards (see Figure 4.10) resulting in the largest change in atom position for the $O(2)$ site bridging between the two vanadium atoms ($\Delta r_{\text{max}} = 0.52 \text{ \AA}$). Despite the large atom displacements, the changes in the bond distances between the vanadium sites and the neighboring oxygen atoms are smaller than 0.10 \AA . This could be a possible explanation for the relatively moderate relaxation energy of -0.3 eV (Table 4.5).

All vacancy formation energies are quite large. The smallest is the formation energy of the $O(1)_{\text{vac}}$, 4.98 eV. The $O(2)_{\text{vac}}$ and $O(3)_{\text{vac}}$ have similar formation energies that are more than 1 eV larger compared to the $O(1)_{\text{vac}}$. The corresponding energy of the $O(1')_{\text{vac}}$ is intermediate. These vacancy formation energies indicate that it is difficult to remove oxygen atoms by themselves from the surface. Concurrent processes are necessary to facilitate the vacancy formation, e.g., oxygen recombining to O_2 (see equation (4.7)) or the formation of surface OH, H_2O , [137] or CO_2 [24].

4.2.1.2 Electronic properties for surface and sub-surface oxygen vacancies

In the present section the electronic properties of the vacancy sites will be discussed based on the atom charges as well as the atom-projected DOS curves for the vanadium neighbors of the vacancy sites. As described above, the vacancy formation process is divided into two steps (see Table 4.5) where (i) represents the surface cluster, (ii) the cluster after removal of the oxygen atom without relaxation and (iii) the relaxed vacancy cluster.

The oxygen atoms in the cluster are negatively charged (see Table 4.5). On the other hand, the vacancy is formed by removing a neutral oxygen atom. Therefore, the remaining negative excess charge has to be distributed over the atoms close to the vacancy site, i.e., mainly the neighboring vanadium atoms. This is the microscopic picture of chemical reduction of the metal site by vacancy formation. In general the same pattern could be identified for all four different surface vacancy sites: the neighboring vanadium atoms get reduced and this reduction gets partly reversed by the relaxation.

The bond formation of the vanadium atom next to the $O(1)_{\text{vac}}$ with the oxygen atom of the lower layer is nicely represented in the changes of the atom charges. After removing the $O(1)$ atom the vanadium atom gets strongly reduced as shown by the corresponding atom charge for the surface cluster $q(V) = 2.17$ au and the frozen $O(1)$ vacancy cluster, $q(V) = 1.80$ au. The atom charge of the $O(1)$ oxygen from the lower layer is basically not affected by the vacancy formation, as can be seen in (ii) of Table 4.5. The geometric relaxation leads to a bond formation between the vanadium atom next to the vacancy site and the $O(1)$ from the lower layer. The reduction of the vanadium atom gets partly reversed and the atom charge of the $O(1)$ site from the lower layer changes from -0.63 au to -0.87 au. The latter is very close the value that has been found for $O(2)$ oxygen in the ideal V_2O_5 crystal, which is in good agreement with the observation that the interlayer bridge bond lengths are very similar to the $V-O(2)-V$ bridge in the perfect bulk.

Although no new bond can be formed to compensate for the missing oxygen at the $O(2)_{\text{vac}}$ site, the relaxation clearly shows that the vanadium atoms interact more strongly with the neighboring atoms. In agreement with these geometric changes accompanied by a significant relaxation energy, the vanadium neighbors of the $O(2)_{\text{vac}}$ site accumulate positive charge due to the relaxation. Only minor reconstructions were found in the neighborhood of a $O(3)_{\text{vac}}$ site and, as can be seen in Table 4.5, these are accompanied by only minor changes of atom charges.

After removing the $O(1')$ atom without relaxation (ii), the charge of the reduced vanadium atom is similar to that found for the $O(1)_{\text{vac}}$ formation. Although there are significant atom displacements due to relaxation, the changes in bond distances are very small and the reduction of the vanadium atom is not affected.

Figures 4.13a-4.13d show the atom-projected DOS's of the vanadium neighbors for the four different vacancy sites. Analogous to the previous discussion, the surface cluster (i), the frozen vacancy cluster (ii) and the relaxed vacancy cluster (iii) are compared. The results coincide with previous theoretical studies based on cluster [23] as well as periodic [158] calculations, the latter considering only $O(1)_{\text{vac}}$.

In general the DOS's can confirm the picture derived from the atom charges. Due to the reduction induced by the oxygen removal, the unoccupied V 3d electron states get occupied (i) \rightarrow (ii), as indicated by the shift of the of the DOS to lower energies. The relaxation allows the reduced vanadium atom to react stronger with the oxygen environment (iii). Therefore the density of states close to the Fermi edge is lowered after relaxation (ii) \rightarrow (iii). In general, the amount of change correlates very well with the corresponding atom charges.

An exception is the $O(1')$ cluster where relaxation does not induce changes for the atom charges but for the atom projected DOS. This deviation can be explained by the uncertainty to define atomic charges unambiguously in molecules and solids. The atom-projected DOS is based on a Mulliken charge analysis where the Bader charge analysis is used to evaluate the atom charges. In contrast to the $O(1)$ and $O(2)$ vacancies, the relaxation due to $O(1')_{\text{vac}}$ formation is accompanied by large changes in the geometry, but only by small variations of the V-O distances. This could explain why Bader atom charges based on a topological analysis are not affected. On the other hand, the significant geometric rearrangement could imply a change in the hybridization, which then is reflected in the Mulliken charge analysis based atom-projected DOS plot.

As shown by the DOS plots, the oxygen vacancy formation transfers electrons from the valence to the conduction band. The electronic states in the conduction band can be energetically very close. Therefore, it is possible that the energy gain in exchange-correlation going from a singlet to a triplet state is larger than the energy that is necessary for the change in occupation. Thus, principally the spin multiplicity of the

vacancy cluster is not known. The total energy difference between singlet and triplet ($E^{\text{trip}} - E^{\text{sing}}$) are shown in Table 4.5, where a negative value indicates that the triplet state is energetically more favorable. This is the case for all oxygen vacancies except the O(3) vacancy, but in general the differences are small compared to the vacancy formation energies.

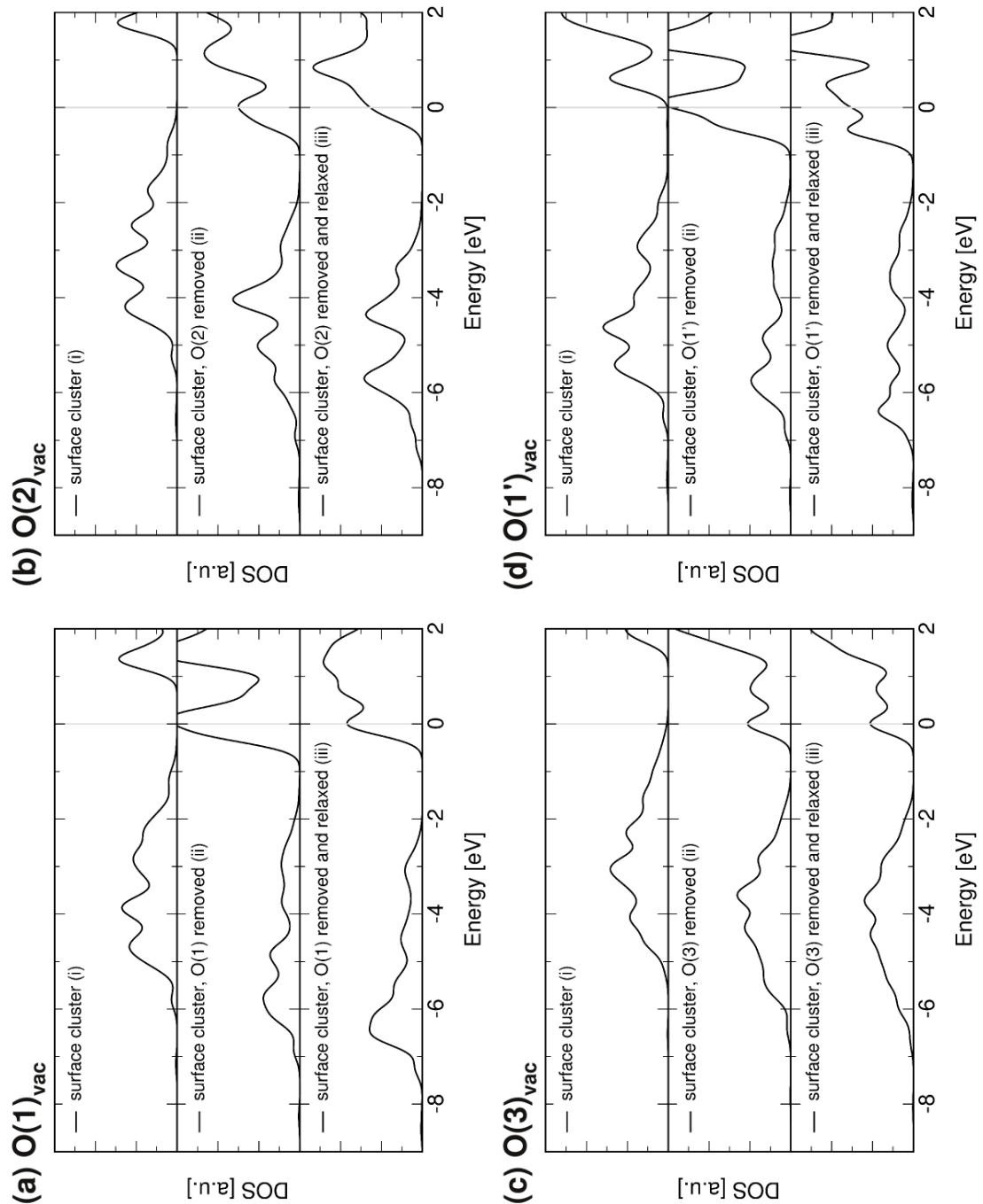


Figure 4.13: Atom-projected DOS curves for the vanadium atoms next to the (a) $O(1)_{\text{vac}}$, (b) $O(2)_{\text{vac}}$, (c) $O(3)_{\text{vac}}$, and (d) $O(1')_{\text{vac}}$ site for the surface cluster (i), the surface cluster after removing the O(1) atom (ii), and the relaxed vacancy cluster (iii). The curves refer to a Gaussian level broadening of 0.4 eV (FWHM); HOMO energy levels are shifted to 0.0 eV.

The model clusters used to describe the O(1) and O(2) vacancies are similar to those presented in the study of C. Friedrich [24]. His results could be reproduced. The $V_{14}O_{46}H_{22}$ cluster that is used to describe the O(3)_{vac} site in the present work is larger than the $V_{10}O_{31}H_{12}$ cluster used in previous studies [24]. For the small cluster, the region that can be considered flexible to account for surface relaxation is restricted, since as the O(3) sites are close to the cluster edge. Therefore, a formation energy that accounts for the full surface relaxation was approximated to be a value between 6.07 eV and 6.24 eV [24]. This estimate could be nicely confirmed by the present work, where the $E_D^r(O(3))$ is found to be 6.18 eV.

4.3 Oxygen vacancy diffusion at the $V_2O_5(010)$ surface

When examining the catalytic performance, not only static properties of oxygen vacancies are important, but vacancy diffusion processes are as well. As discussed above for the Mars and van Krevelen-type catalytic processes, lattice oxygen of the catalyst is consumed by the oxidation reaction (and the catalyst gets re-oxidized subsequently by gas phase O_2) [57]. Thus, oxygen vacancy diffusion processes can be important for the catalytic performance. The formation of sub-surface vacancy, such as O(1')_{vac}, which is not directly accessible from the surface, relies on vacancy diffusion events. Furthermore, it could be the first step for the exchange of bulk oxygen with the surface layer. This is of interest as it has been shown experimentally that V_2O_5 can exchange its bulk oxygen with oxygen from the gas phase [155].

The experimental investigation of the details of oxygen and oxygen vacancy diffusion is difficult. Nonetheless, in one study [164] experimental data of oxygen chemisorption on V_2O_5 were examined according to classic kinetic models yielding an activation energy of 0.65 eV for vacancy diffusion. However, no diffusion paths have been considered.

Oxygen vacancy diffusion in the surface layer has been also studied theoretically by means of model diffusion paths providing an upper boundary for the diffusion barriers [137]. Most of the approximated barriers are in the range of 1 eV to 1.6 eV. The two exceptions are the small barrier for the diffusion step O(2')_{vac} to O(1)_{vac} ($E_{\text{barr}} = 0.46$ eV) and the largest barrier that was found for the diffusion step O(2)_{vac} to O(3)_{vac} ($E_{\text{barr}} = 2.47$ eV). The latter suggests that an alternative two-step indirect diffusion path via the O(1)_{vac} site for vacancy diffusion in the V-O plain could be energetically favorable.

Vacancy diffusion describes a neighboring oxygen atom that diffuses into the vacancy site, which is equivalent to a vacancy diffusing into neighboring oxygen sites. The vacancy diffusion processes that have been considered in this work can be divided into three groups: (I) vacancies at the vanadyl sites pointing outside the surface O(1) can diffuse to oxygen sites from the vanadium oxygen plane, O(2), O(2'), O(3), and O(3'); (II) alternatively, sub-surface vanadyl oxygen vacancies $O(1')_{vac}$ can also diffuse to oxygen sites from the vanadium-oxygen plane; and (III) vacancies in the vanadium-oxygen plane can interchange.

In addition, diffusion processes between the same types of vacancies are also possible. This could be diffusion from $O(2)_{vac}$ to $O(2)_{vac}$ / $O(2')_{vac}$ to $O(2')_{vac}$ and $O(1)_{vac}$ to $O(1)_{vac}$ / $O(1')_{vac}$ to $O(1')_{vac}$. Direct diffusion between $O(3)_{vac}$ and $O(3)_{vac}$ or $O(3')_{vac}$ and $O(3')_{vac}$ can be excluded since there is no direct connection between these sites. The focus of this work is the relative stability of the different vacancy sites. Therefore, diffusion processes between the same types of vacancies are not included in the following discussion.

The energetics for the diffusion is analyzed by the energy difference between the total energy of initial and final state E_{diff} (Figure 4.14) of all diffusion steps of (I),(II), and (III) (positive energies always refer to endothermic processes) and additionally the barriers that have been calculated for selected diffusion steps $O(n)_{vac} \leftrightarrow O(i)_{vac}$. Each calculated path yields two energy barriers $E_{barr}^{1,2}$, where the index 1,2 refers to $O(n)_{vac}$ or $O(i)_{vac}$ as the initial state, hence the direction of the diffusion step (see Figure 4.14).

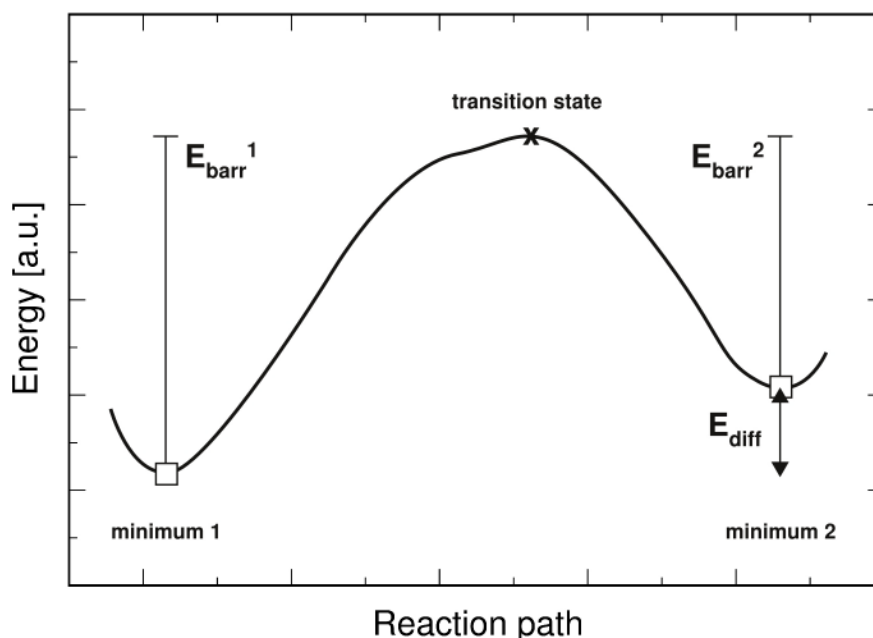


Figure 4.14: Definition of the total energy difference between the initial and final state, E_{diff} , and the energy barriers for oxygen vacancy diffusion, $E_{barr}^{1,2}$.

The results for the oxygen vacancy diffusion in $V_2O_5(010)$ surface are listed in Table 4.6 (note that E_{diff} is given with respect to the energetically more favorable vacancy site, which is always the first listed in the left column).

Based on the energy differences, some preliminary conclusions for the oxygen vacancy diffusion processes can be already drawn. The $O(1)_{\text{vac}}$ is the most stable and the energy differences with respect to the $O(2')$, $O(3)$, and $O(3')_{\text{vac}}$ are larger than 1 eV. This implies for all diffusion steps in the group (I) that the diffusion of a $O(1)_{\text{vac}}$ to the surface layer is highly endothermic. On the other hand, it is possible that oxygen vacancies in the V-O plane could be annihilated by $O(1)$ oxygen diffusing into these vacancy sites. The same can be found for the group (II) diffusion steps between the $O(1')_{\text{vac}}$ sites and the V-O plane, but the E_{diff} are smaller than found for the $O(1)_{\text{vac}}$ sites. The formation energies of the vacancy sites in the V-O plane are similar, thus the E_{diff} for diffusion steps that belong to the group (III) may be small. This indicates that small barriers for diffusion in both directions are possible.

Table 4.6: The energy difference between the initial and final states E_{diff} , as well as the energy barriers $E_{\text{barr}}^{1,2}$ for oxygen vacancy diffusion at the $V_2O_5(010)$ surface layer (in [eV]).

Diffusion step		E_{diff}	$E_{\text{barr}}^1 \rightarrow$	$E_{\text{barr}}^2 \leftarrow$
(I)	$O(1)_{\text{vac}} \leftrightarrow O(2')_{\text{vac}}$	1.46	~ 1.40	~ 0.00
	$O(1)_{\text{vac}} \leftrightarrow O(3)_{\text{vac}}$	1.20	--	--
	$O(1)_{\text{vac}} \leftrightarrow O(3')_{\text{vac}}$	1.20	--	--
(II)	$O(1')_{\text{vac}} \leftrightarrow O(2)_{\text{vac}}$	0.75	0.93	0.08
	$O(1')_{\text{vac}} \leftrightarrow O(3)_{\text{vac}}$	0.49	--	--
	$O(1')_{\text{vac}} \leftrightarrow O(3')_{\text{vac}}$	0.49	1.38	0.94
(III)	$O(3)_{\text{vac}} \leftrightarrow O(2)_{\text{vac}}$	0.26	0.61	0.57
	$O(3)_{\text{vac}} \leftrightarrow O(3')_{\text{vac}}$	0.00	0.44	0.44

In a next step, the barriers for specific diffusion steps are calculated. It is important to mention that the cluster models for diffusion can differ from those used for modeling the oxygen vacancies as described in Section 4.2. All diffusion clusters and their properties are discussed in Appendix C, and show that the description of the vacancy sites can vary slightly between the different cluster models. For the vacancy $O(3)_{\text{vac}}$, the singlet state is more stable than the triplet state. Spin crossing cannot be treated in the present model. As the energy difference between triplet and singlet for the $O(3)_{\text{vac}}$ is small (≤ 0.13 eV), and the triplet state is the energetically favorable for all other vacancies, diffusion calculations for the transformation of an $O(3)_{\text{vac}}$ into another

vacancy site were performed for the triplet state only. The individual steps are presented in the order according to Table 4.6 in the following.

A diffusion path between the $O(1)_{vac}$ and the $O(2')_{vac}$ site was determined by NEB calculations (see Section 3.2.2). As shown in Figure 4.15, no barrier could be located along the minimum energy path (MEP) approximated by the 15 images. The path between the images 12 and 15 in Figure 4.15 was linearly interpolated by 97 images. The energy barrier found for the approximated MEP is $5 \cdot 10^{-4}$ eV, which is in the energy region of the numerical noise. Based on this results, the assumptions that can be made, are that the potential energy surface (PES) near the $O(2')_{vac}$ equilibrium geometry is very flat and since the path is interpolated with a high density, the real barrier of the transition must be very small. Yet no real transition state could be located. The flat PES near the $O(2')_{vac}$ equilibrium geometry was confirmed by a vibrational analysis of this configuration, which showed a very low energy vibrational mode at 31 cm^{-1} .

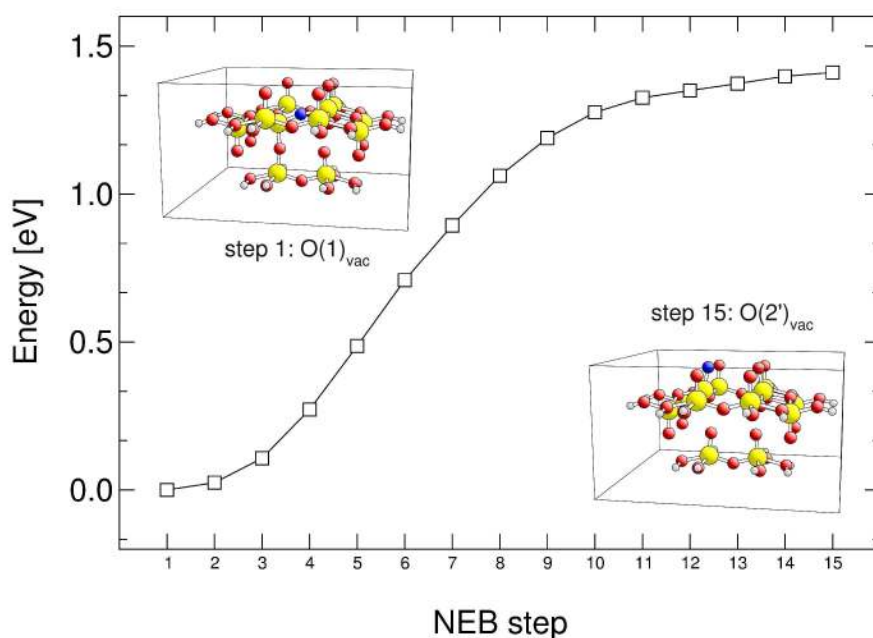


Figure 4.15: Vacancy diffusion path for $O(1)_{vac} \leftrightarrow O(2')_{vac}$. as well as initial and final state geometries. Vanadium centers are shown by large yellow balls, oxygen centers by red balls, small bright gray balls refer to hydrogen centers, and diffusing oxygen atom is labeled as a blue ball.

The energy of the NEB path obtained for the diffusion step between the $O(1')_{vac}$ and the $O(2)_{vac}$ site as well as the structures of initial, transition, and final states can be seen in Figure 4.16. Starting with the $O(2)_{vac}$ configuration, no bond has to be broken, but a new V-O bond is formed accompanied by a slight weakening of the V-O(1') bond. The identified barriers ($E_{barr}^{1,2} = 0.93/0.08$ eV) are very close to the barrier-less diffusion process indicating that $O(2)_{vac}$ sites can be easily transformed into $O(1')_{vac}$ sites.

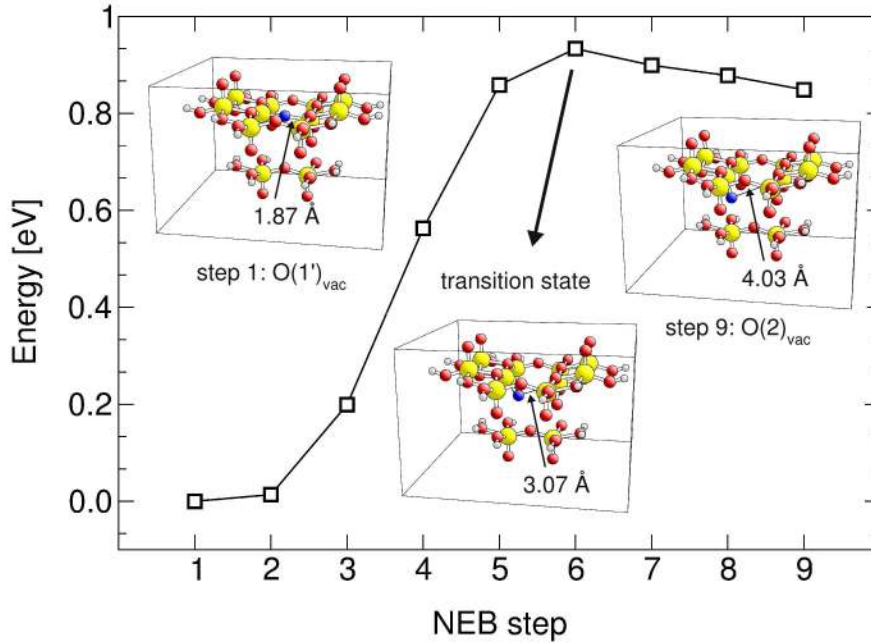


Figure 4.16: Vacancy diffusion path for $O(1')_{vac} \leftrightarrow O(2)_{vac}$, as well as initial, transition, and final state geometries. Vanadium centers are shown by large yellow balls, oxygen centers by red balls, small bright gray balls refer to hydrogen centers, and diffusing oxygen atom is labeled as a blue ball.

The results for the diffusion step between the $O(1')_{vac}$ and the $O(3')_{vac}$ sites (see Figure 4.17) were obtained by a combination of the NEB and the dimer method. The energetically highest image of a converged NEB path was used as starting point for a subsequent dimer calculation (it was not possible to reach convergence employing CI-NEB). The energies of the converged NEB path including the transition state located with the dimer method and structures of initial, transition, and final states are shown in Figure 4.17. Both barriers, $E_{barr}^1 = 1.38$ eV and $E_{barr}^2 = 0.94$ eV, are large. Thus the transfer of $O(1')$ oxygen into the $O(3')_{vac}$ site is significantly more difficult compared to similar processes of diffusion into the $O(2)_{vac}$ site.

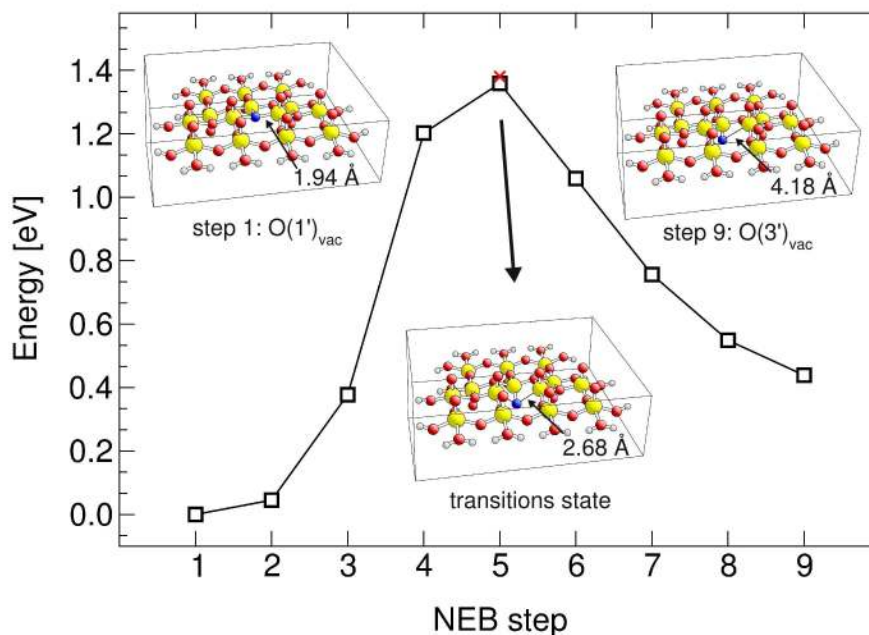


Figure 4.17: Vacancy diffusion path for $O(1')_{vac} \leftrightarrow O(3')_{vac}$. (dimer transition state indicated by red cross) as well as initial, transition, and final state geometries. Vanadium centers are shown by large yellow balls, oxygen centers by red balls, small bright gray balls refer to hydrogen centers, and diffusing oxygen atom is labeled as a blue ball.

Oxygen vacancy diffusion in V-O plane implies V-O bond-breaking processes for both diffusion directions. Nevertheless, as will be shown in the following the resulting barriers are moderate.

Figure 4.18 shows initial, transition and final states of the diffusion between the $O(3)_{vac}$ and $O(2)_{vac}$ site and the corresponding NEB path. Because of the inversion symmetry of a single $V_2O_5(010)$ layer, this also represents the diffusion between the $O(3')_{vac}$ and $O(2')_{vac}$ sites. In the transition state, the diffusing oxygen atom is only bonded to one vanadium center. The remaining V-O bond is stronger in the transition state, as indicated by the V-O distances at initial, transition, and final state that are 1.77 Å, 1.68 Å, and 1.84 Å, respectively, and partly compensate for the bond breaking. Besides the moving oxygen atom, no large displacements of other surface atoms were found. The result are moderate diffusion barriers, $E_{barr}^1 = 0.61$ eV and $E_{barr}^2 = 0.57$ eV.

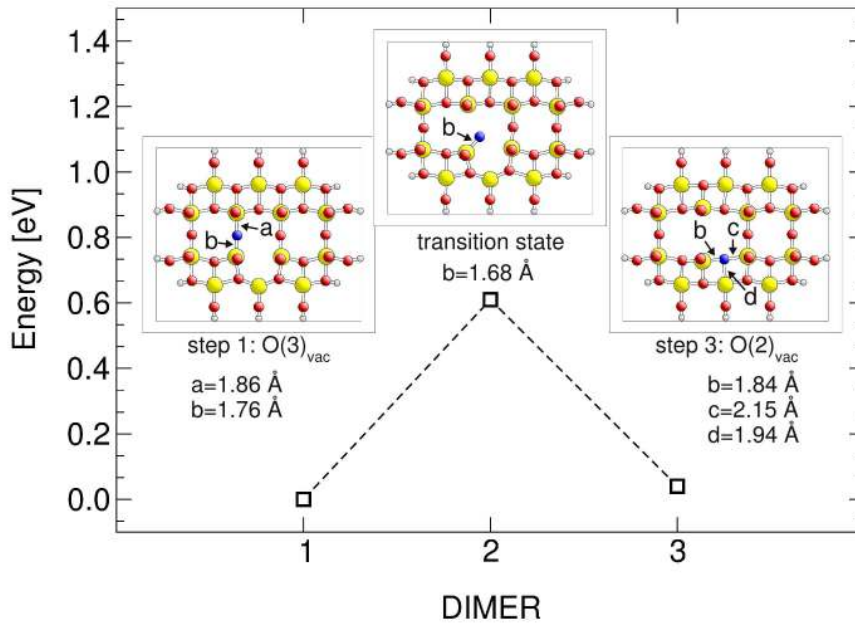


Figure 4.18: Vacancy diffusion path for $O(3)_{vac} \leftrightarrow O(2)_{vac}$, as well as initial, transition, and final state geometries. Vanadium centers are shown by large yellow balls, oxygen centers by red balls, while small bright gray balls refer to hydrogen centers, and diffusing oxygen atom is labeled as a blue ball.

Finally, the diffusion between the $O(3)_{vac}$ and the $O(3')_{vac}$ site is investigated (Table 4.6). As found for the previous diffusion step ($O(3)_{vac} \leftrightarrow O(2)_{vac}$), the breaking of the V-O bonds is partly compensated by a strengthening of the remaining V-O bonds at the transition state (see Figure 4.19). This yields in a diffusion barrier of 0.44 eV.

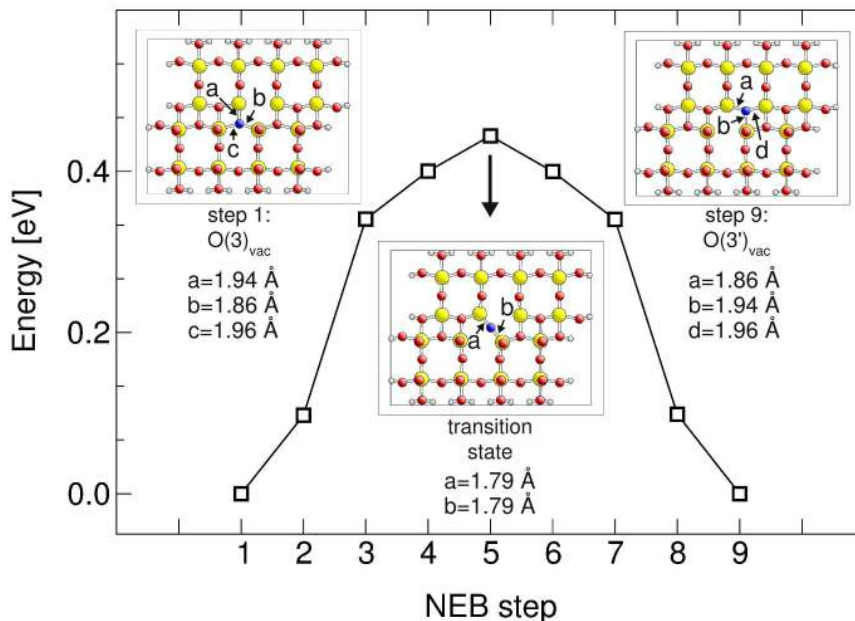


Figure 4.19: Vacancy diffusion path for $O(3)_{vac} \leftrightarrow O(3')_{vac}$, as well as initial, transition, and final state geometries. Vanadium centers are shown by large yellow balls, oxygen centers by red balls, small bright gray balls refer to hydrogen centers, and diffusing oxygen atom is labeled as a blue ball.

In a previous study [137] approximated diffusion paths yielding large upper boundaries for the energy barriers of vacancy diffusion steps in the V-O plane (III) were discussed. This suggests that an indirect two-step path via the $O(1)_{\text{vac}}$ site may be energetically more favorable [137]. The present calculations of the MEP's that also account for local geometric relaxations yield significantly smaller barriers for vacancy diffusion in the V-O plane, $E_{\text{barr}} \leq 0.61$ eV. As the energy differences between the $O(1)$ vacancy and the vacancies in the V-O plane, $O(2)_{\text{vac}}$, $O(2')_{\text{vac}}$, $O(3)_{\text{vac}}$, and $O(3')_{\text{vac}}$ are larger than 1.2 eV (see Table 4.6) these results provide evidence that direct diffusion is energetically favorable.

As discussed earlier, the experimental characterizations of oxygen vacancies of V_2O_5 are contradictory. Different experiments conclude that preferentially $O(1)$ vacancies [123, 156, 157], $O(2)$ [152] and/or $O(3)$ vacancies [141] exist. Based on the present results, the stability of $O(2)$ as well as of $O(2')$ vacancies is questionable since these vacancies can easily be annihilated by diffusing into the $O(1')_{\text{vac}}$ or $O(1)_{\text{vac}}$ sites respectively (Table 4.6). For diffusion of vanadyl oxygen into $O(3)$ or $O(3')$ vacancy sites, only one of the four possible reaction paths has been evaluated. Therefore, no decisive conclusions about the stability of $O(3)$ and $O(3')$ vacancies can be made based on these data.

5 H, NH_x, (x = 0,...,4), and NO adsorption at the V₂O₅(010) surface

In this chapter, the adsorption of H, NH_x, (x = 0,...,4), and NO at the V₂O₅(010) surface is discussed. Adsorption processes are essential for understanding reactions on surfaces. Especially for catalytic applications, adsorption processes are important, because one or more reactants form an intermediate with the catalyst, which then reacts further to become the desired product. Therefore, the equilibrium geometries of different surface species, and their stability, are the starting points for further investigations of processes on surfaces, such as diffusion, defect formation, and reactions.

The considered molecules play an important role for the selective catalytic reduction (SCR) reaction. NH₃ and NO are in the feed stock and react at the catalyst surface. After initial adsorption, (de)hydrogenation processes are necessary during the reaction, and can lead to different NH_x surface species and surface hydrogen [17]. Further, surface hydrogen is of special interest. As for many oxidation reactions on V₂O₅ containing catalysts, a Mars van Krevelen type of mechanism [57] is proposed which includes oxygen vacancy formation. As discussed in the previous section, the oxygen vacancy formation energies are large and therefore, supporting processes, e.g., formation and desorption of surface OH and H₂O, become important.

In the first part, the results for H, NH_x, (x = 0,...,4), and NO adsorption at the perfect V₂O₅(010) surface are presented, followed by adsorption properties of the reduced surface. Finally, NH₃ adsorption, that is generally accepted to be the initial step of the SCR reaction [17], is discussed in detail for different scenarios comparing theoretical and experimental findings.

Analogous to the vacancy formation energy, as well as for the definition of the adsorption energy, E_{ads} , the total energy of the relaxed surface cluster, $E_{\text{tot}}^{\text{r}}(\text{Cluster})$, is used as a reference in order to account for the cluster artifacts. Thus, the adsorption energies are defined by total energy differences as follows:

$$E_{\text{ads}}(\text{X}) = E_{\text{tot}}^{\text{r}}(\text{Cluster-X}) - E_{\text{tot}}(\text{X}) - E_{\text{tot}}^{\text{r}}(\text{Cluster}). \quad (5.1)$$

The cluster models that are used to describe the different surface sites of the perfect surface, as well as the reduced V₂O₅(010) surface, are discussed in Chapter 4.

5.1 Adsorption of H, NH_x, (x = 0,...,4), and NO at the perfect V₂O₅(010) surface

The V₂O₅(010) surface layer contains six different oxygen and the vanadium sites. The O(1') site is located sub-surface and is covered by the vanadium oxygen plane, hence it is not directly accessible. Therefore, only the five oxygen sites O(1), O(2), O(2'), O(3), and O(3'), as well as the vanadium site, have been considered as possible adsorption sites at the perfect V₂O₅(010) surface (Figure 4.1). The results obtained for the different adsorbates are discussed in detail in the following section.

5.1.1 Hydrogen adsorption at the perfect V₂O₅(010) surface

Hydrogen can bind at all five oxygen sites forming surface OH groups, denoted O(n)H. On the other hand, no adsorption at the vanadium site was observed. Figure 5.1 visualizes the resulting equilibrium geometries for different surface sites. The geometric, energetic, and electronic results of the calculations are listed in Table 5.1. All O(n)H groups have a similar O-H bond length of 0.97 - 0.98 Å. As a result of the O(n)H bond formation, the corresponding V-O(n) bonds get weakened and elongated. For the different sites and bonds, this elongation can vary between 0.15 Å and 0.26 Å (Table 5.1). The O(1)H group is tilted towards the opposite O(1), by an angle of 72° with respect to the surface normal, the (010) axis (V-O(1)-H angle 113°). Also, the O(2)H and the O(3)H groups are tilted, but in the (001) and the (001) direction respectively. The bending angles of 45° and 41° are smaller compared to what has been found for the O(1)H group (Figure 5.1).

Table 5.1: Hydrogen adsorption at the perfect $V_2O_5(010)$ surface. Distances between the participating oxygen atom and the neighboring vanadium sites, $d(V-O)$, and distances between the oxygen and the hydrogen atom, $d(O-H)$ (in \AA), atom charges, q of corresponding atoms (in atomic units, [au]), for the substrate clusters, with and without hydrogen adsorbed, and adsorption energies of atomic hydrogen, E_{ads} (in [eV]).

	O(1)	O(2)	O(2')	O(3)	O(3')	V	
substrate cluster	$d(V-O)$	1.59	1.81	1.90	1.90	--	
			1.81	2.02	2.02		
	$q(O)$	-0.62	-0.94	-1.08	-1.08	--	
	$q(V)$	2.14	2.10	2.13	2.13	--	
			2.10	2.15	2.15		
H adsorbed	$d(O-H)$	0.98	0.98	0.98	0.98	0.97	--
	$d(V-O)$	1.77	1.97	2.00	2.05	2.05	--
			1.97	2.00	2.05	2.05	
				2.17	2.28	2.28	
	$q(H)$	0.60	0.60	0.59	0.60	0.59	--
	$q(O)$	-0.93	-1.15	-1.12	-1.20	-1.14	--
	$q(OH)$	-0.33	-0.55	-0.53	-0.60	-0.55	--
	$q(V)$	2.10	2.03	2.04	2.05	2.05	--
		2.03	2.04	2.05	2.05		
			2.08	2.06	2.06		
E_{ads}	-2.64	-2.76	-2.62	-2.52	-2.36	--	

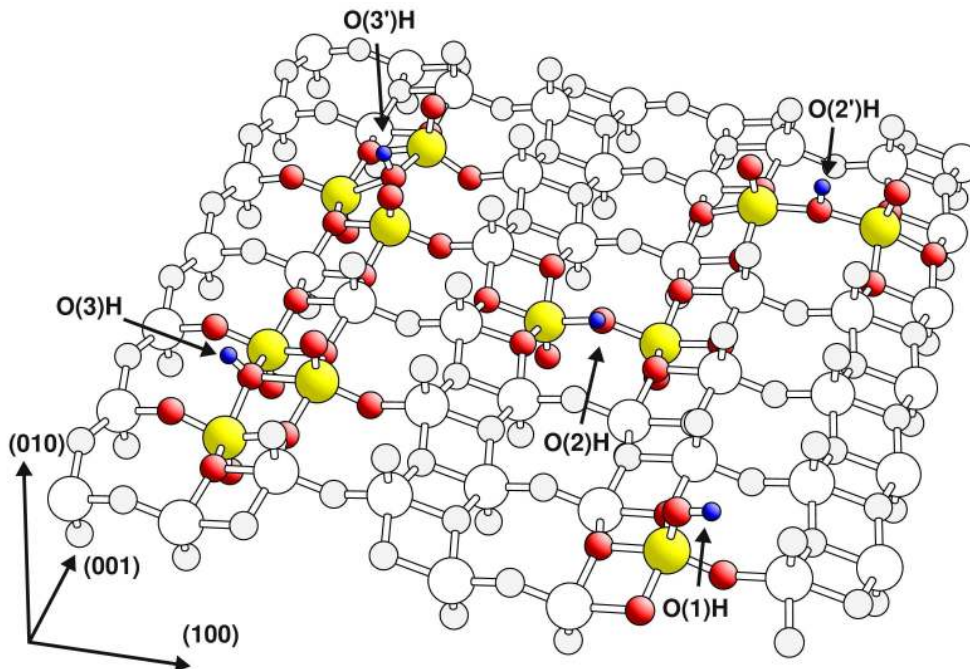


Figure 5.1: Equilibrium geometries of hydrogen adsorbed at the perfect $V_2O_5(010)$ surface, resulting $O(n)H$ groups are labeled accordingly. Vanadium centers are shown by large yellow balls, oxygen centers by red balls and hydrogen centers by small blue balls. Surface atoms that are included in the optimization are emphasized with shading.

The O(2') and O(3') sites are located between two vanadyl groups that are sticking out of the surface. Adsorption at these sites induces large displacements of neighboring atoms (see Figures 5.2 and 5.3). The O(2') atom itself gets pulled out by 1.12 Å. The neighboring vanadyl groups VO(1) also move upwards, this is accompanied by an opening of the surface around the O(2') site. The V-V distance after adsorption, $d(\text{V-V}) = 3.95$ Å, is 0.50 Å larger in comparison to the surface cluster. The opening is more dramatic for the vanadyl oxygen. The O(1)-O(1) distance increases by 1.24 Å. This structure is quite different from the configurations of hydrogen adsorbed at the O(2) sites, but the V-O bond lengths of both structures – which connect the neighboring vanadium atoms with their five surrounding oxygen neighbors – differ by less than 0.03 Å.

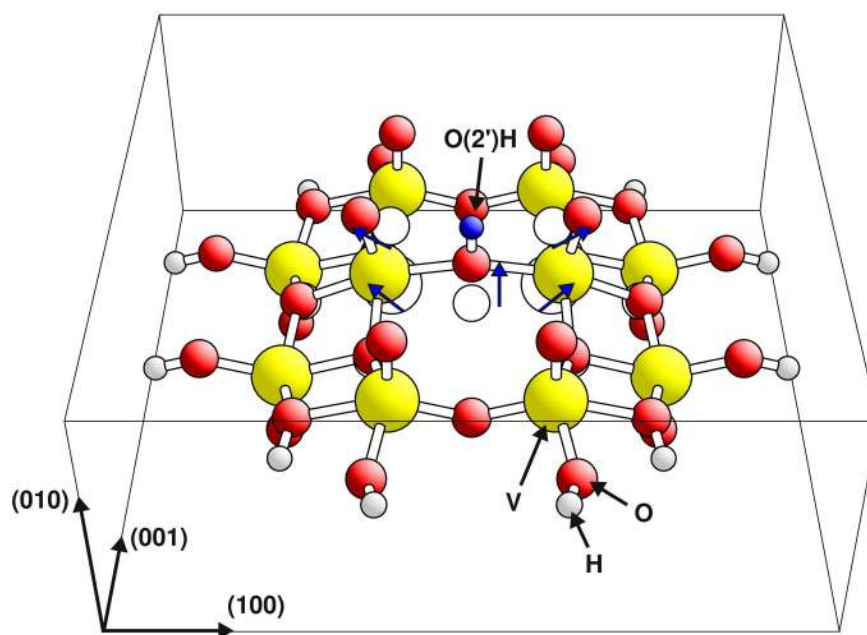


Figure 5.2: *Equilibrium geometry of hydrogen adsorbed at the O(2') site of the perfect V₂O₅(010) surface. Vanadium centers are shown by large yellow balls, oxygen centers by red balls, adsorbed hydrogen by small blue balls and saturating hydrogen by small bright gray balls. Surface atom positions before adsorption are indicated by white balls.*

The relaxation induced by hydrogen adsorption at the O(3') site follows the same pattern, but the atom displacements are smaller. Due to the hydrogen adsorption, the O(3) oxygen moves upwards by 0.89 Å and the V-V and O(1)-O(1) distances of the neighboring vanadyl groups increase by 0.37 Å and 0.93 Å, respectively. Also, the V-O bond lengths of the three neighboring vanadium atoms are very similar for an O(3')H and an O(3)H group. Except for the long V-O(3') distance that differs by 0.11 Å (Table 5.1), the differences between the other corresponding V-O bond lengths for the O(3)H and the O(3')H structures are smaller than 0.03 Å. The resulting more open structures make the O(2') and the O(3') sites well accessible for a hydrogen atom, and the OH groups that are formed have similar bond lengths, as found in the previous cases (Table 5.1).

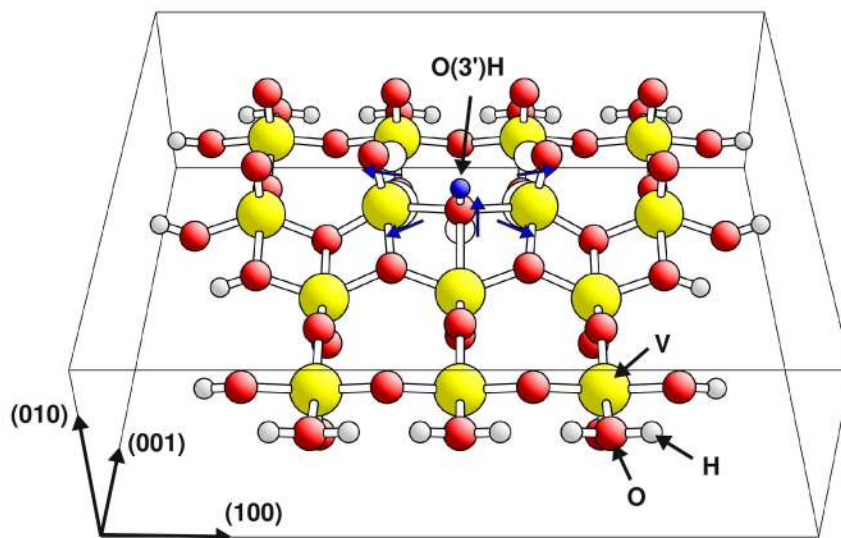


Figure 5.3: *Equilibrium geometries of hydrogen adsorbed at the O(3') site of the perfect V₂O₅(010) surface. Vanadium centers are shown by large yellow balls, oxygen centers by red balls, adsorbed hydrogen by small blue balls and saturating hydrogen by small bright gray balls. Surface atom positions before adsorption are indicated by white balls.*

The adsorption energies of atomic hydrogen with respect to atomic hydrogen in gas phase as reference are large at all five adsorption sites. The strongest binding was found at the O(2) site, $E_{\text{ads}} = -2.76$ eV, and the weakest binding at the O(3') site, $E_{\text{ads}} = -2.36$ eV (Table 5.1). Although hydrogen adsorption at the O(2') and the O(3') sites is accompanied by large displacements, the equilibrium geometries have similar local geometric properties, as found for hydrogen adsorbed at the corresponding O(2) and O(3) sites (indicated by the V-O bond lengths of the neighboring vanadium atoms), yielding comparable adsorption energies.

In all cases, the hydrogen atom transfers a charge to the oxygen atom, which then becomes more negatively charged (Table 5.1). The charge of the resulting O(n)H group is negative, but it is less negatively charged compared to the oxygen site before adsorption. The excess negative charge is distributed among the neighboring atoms, resulting in a slight reduction of the surface.

Previous theoretical studies have investigated hydrogen adsorption at the perfect V₂O₅(010) surface. These studies considered cluster [23, 24, 68, 137] as well as periodic surface models [160, 165]. All studies found that hydrogen can form bonds with the O(1), O(2), and O(3) sites, but not with a vanadium site which is confirmed by the present calculations. The geometries of adsorbed hydrogen that are proposed in these studies are also consistent with the present results. OH groups that are formed by adsorption at the different oxygen sites have a bond length between 0.97 Å and 1.05 Å, where as a result of the O-H bond, the V-O bonds to the adjacent vanadium atoms

become weaker, with V-O distances elongated. A comparison of the adsorption energies found in five different studies, including the present, is shown in Table 5.2. The different hydrogen adsorption energies, considering the O(1), O(2), and O(3) sites, vary between -1.86 eV and -3.04 eV. Obviously, the variation of adsorption energies between different oxygen sites decreases if more atoms are considered in the geometry optimization (Table 5.2). For periodic calculations that include all atoms of the unit cell in the optimization, the variation of the binding energy for hydrogen adsorption at the O(1), O(2), and O(3) sites is only 0.2 eV [160, 165] (Table 5.2). The adsorption energies obtained in this study using cluster models agree very well with the results of Yin et al.'s study using periodic models ($\Delta E_{\text{ads}} < 0.18$ eV) [165].

Table 5.2: Comparison of theoretical results for the adsorption energy, E_{ads} , of atomic hydrogen at different surface oxygen sites of the perfect $\text{V}_2\text{O}_5(010)$ surface (in [eV]).

Method	O(1)	O(2)	O(2')	O(3)	O(3')
DFT (BLYP, periodic) ^[165]	-2.70	-2.61	--	-2.57	--
MSINDO (large cluster) ^[68]	-2.65	-2.05	--	-1.86	--
DFT (RPBE, cluster) ^[23, 137]	-2.34	-2.21	-0.54	-1.88	-0.76
DFT (RPBE, cluster) ^[24]	-2.64	-2.37	--	-1.91	--
DFT (PW91, periodic) ^[160]	-3.04	-2.96	--	-2.88	--
DFT (RPBE, cluster) ^[this work]	-2.64	-2.76	-2.63	-2.52	-2.36

Most of the studies did not include adsorption at the O(2') and the O(3') sites [24, 68, 160, 165]. This is motivated by the fact that both sites are located between two neighboring vanadyl O(1) sites, that are exposed at the surface and, therefore, more likely react with the hydrogen atom before it can approach the O(2') or O(3') sites. Cluster studies considering these sites found significantly smaller adsorption energies compared to the other oxygen sites [23, 137]. In these studies, a $\text{V}_{10}\text{O}_{31}\text{H}_{12}$ cluster was used to model the surface, and all atoms except for the OH group were kept fixed in the geometry optimization (one study also considered relaxation of the opposite O(1) atom for the special case of adsorption at the O(1) site [24]).

In contrast to previous investigations of cluster models [23, 24, 137], in the present work various clusters for the different adsorption sites are used, and larger flexible areas around the adsorption site are taken into account (see Section 4.1.2). As shown for adsorption at the O(1), O(2), and the O(3) sites, the primary relaxation causes an elongation of the V-O bonds. The geometries are very similar the studies [23, 24, 137] that considered less atoms in accounting for surface relaxation effects. Nevertheless, a larger degree of freedom in the surface geometry leads to larger adsorption energies, as well as smaller differences between the adsorption energies at different oxygen sites. The present results for hydrogen adsorption at O(2') and O(3') oxygen sites that are located between two adjacent vanadyl oxygens, differ significantly from the findings in [23, 137]. This can be explained by the fact that adsorption at these sites is accompanied by large atom displacements. Therefore a model system that includes surface relaxation is necessary. The present extension of the model clusters revealed much larger adsorption energies. From an energetic point of view, adsorption at the O(2') and at the O(3') sites is comparable to adsorption at the remaining surface oxygen sites. However, both oxygen sites are located between two vanadyl oxygen sites which most likely react with the hydrogen atom, and furthermore, adsorption is accompanied by large surface atom displacements. This indicates that the adsorption process at these sites may be accompanied by energy barriers. Possible adsorption paths that start with an O(1)H group to form O(2')H or O(3')H groups have been calculated and yield large energy barriers ($E_{\text{barr}} \geq 1.1$ eV), as will be discussed in detail in Chapter 6.

5.1.2 NH_x , ($x = 0,1,2$), adsorption at the perfect $\text{V}_2\text{O}_5(010)$ surface

Experimental and theoretical studies that focus on NH_3 adsorption on vanadia surfaces provide no structural or energetic details of NH_x , ($x = 0,1,2$) adsorption. However, infrared (IR) spectroscopy studies performed on V_2O_5 , titania supported V_2O_5 , and titania supported $\text{WO}_3\text{-V}_2\text{O}_5$ [26] show indications for the existence of surface NH_2 species after ammonia adsorption, that have been confirmed by nuclear magnetic resonance (NMR) studies performed on titania supported vanadia catalysts [64]. It is claimed that the ability to dehydrogenate NH_3 and form NH_2 may be important for the catalytic performance in the SCR reaction [26]. Hence, deeper insight in the surface dehydrogenation properties of ammonia, and therefore the knowledge of the relative stability of the different NH_x surface species on the catalyst surface, is necessary.

The adsorbates N, NH and NH_2 are grouped together because they have similar adsorption properties, as will be discussed in the following section. The results obtained for adsorption at the perfect $\text{V}_2\text{O}_5(010)$ surface are summarized in Table 5.3 and the equilibrium structures are presented in Figures 5.4 - 5.6.

Table 5.3: NH_x , ($x = 0,1,2$) adsorption at the perfect $\text{V}_2\text{O}_5(010)$ surface. Distances between the participating oxygen atom and the neighboring vanadium sites, $d(\text{V-O})$, and distances between the surface and the adsorbate, $d(\text{O-NH}_x)$ or $d(\text{V-NH}_x)$ (in [\AA]), atom charges, q of corresponding atoms (in atomic units, [au]), for the substrate clusters, with and without NH_x adsorbed, and adsorption energies, E_{ads} (in [eV]).

		O(1)	O(2)	O(2')	O(3)	O(3')	V
substrate cluster	$d(\text{V-O})$	1.59	1.81		1.90		--
			1.81		1.90		
					2.02		
	$q(\text{O})$	-0.62	-0.94		-1.08		--
	$q(\text{V})$	2.14	2.10		2.13		2.14
			2.10		2.13		
					2.15		
N adsorbed	$d(\text{O-N})$	1.21	1.30	1.28	1.32	--	--
	$d(\text{V-O})$	1.84	2.04	2.03	2.14	--	--
			2.05	2.35	2.14		
					2.34		
	$q(\text{N})$	0.36	0.16	0.25	0.19	--	--
	$q(\text{O})$	-0.64	-0.69	-0.67	-0.79	--	--
	$q(\text{V})$	2.08	2.00	2.00	2.05	--	--
			2.00	1.94	2.05		
				2.07			
	$q(\text{ON})$	-0.28	-0.53	-0.42	-0.60	--	--
	E_{ads}	-1.54	-1.09	-0.53	-0.51	--	--
NH adsorbed	$d(\text{O-NH})$	1.30	1.36	--	1.44	--	--
	$d(\text{V-O})$	1.73	1.97	--	2.02	--	--
			1.98		2.02		
					2.19		
	$q(\text{NH})$	0.27	0.12	--	0.03	--	--
	$q(\text{O})$	-0.60	-0.78	--	-0.83	--	--
	$q(\text{V})$	2.08	2.01	--	2.05	--	--
			2.08		2.05		
				2.07			
	$q(\text{ONH})$	-0.33	-0.66	--	-0.80	--	--
	E_{ads}	-0.95	-0.76	--	-0.06	--	--
NH₂ adsorbed	$d(\text{O-NH}_2)/d(\text{V-NH}_2)$	1.40	1.45	--	1.47	--	2.75
	$d_{\text{V-O}}$	1.75	1.94	--	2.06	--	--
			1.96		2.07		
					2.21		
	$q(\text{NH}_2)$	0.41	0.29	-	0.30	--	0.06
	$q(\text{O})$	-0.61	-0.78	--	-0.80	--	--
	$q(\text{V})$	2.09	2.07	--	2.08	--	2.16
			2.03		2.06		
				2.07			
	$q(\text{ONH}_2)$	-0.20	-0.48	--	-0.51	--	--
	E_{ads}	-0.46	-0.74	--	-0.16	--	-0.12

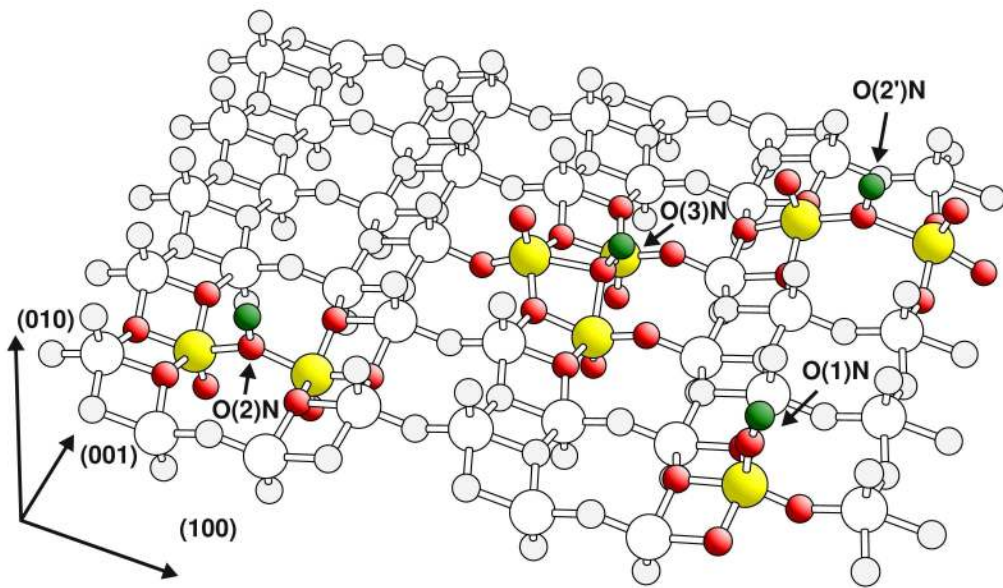


Figure 5.4: Equilibrium geometries of nitrogen adsorbed at the perfect $V_2O_5(010)$ surface, resulting $O(n)N$ groups are labeled accordingly. Vanadium centers are shown by large yellow balls, oxygen centers by red balls, and nitrogen centers by green balls. Surface atoms that are included in the optimization are emphasized with shading.

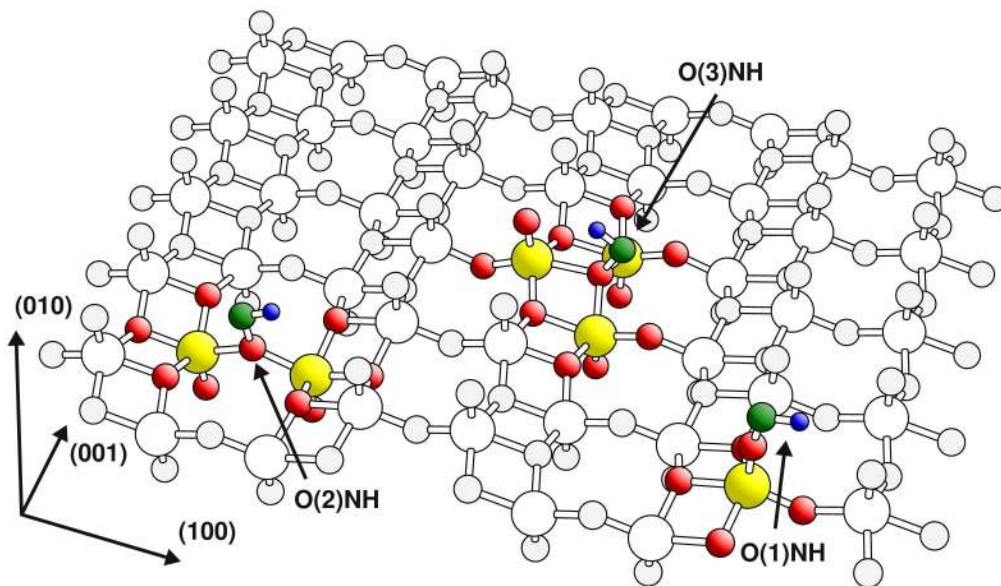


Figure 5.5: Equilibrium geometries of NH adsorbed at the perfect $V_2O_5(010)$ surface. Vanadium centers are shown by large yellow balls, oxygen centers by red balls, nitrogen centers by green balls, and hydrogen centers by small blue balls. Surface atoms that are included in the optimization are emphasized with shading.

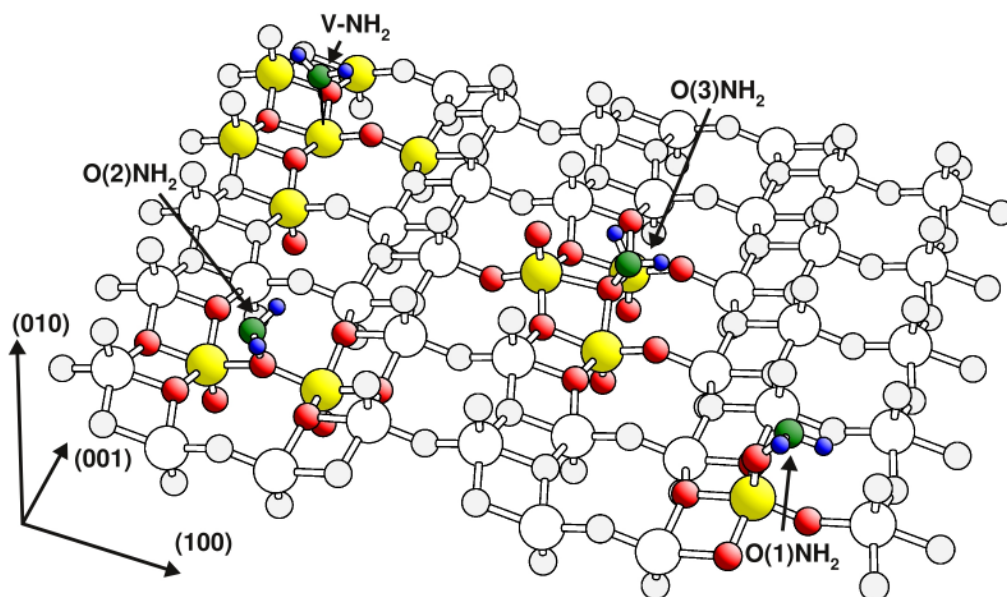


Figure 5.6: Equilibrium geometries of NH_2 adsorbed at the perfect $\text{V}_2\text{O}_5(010)$ surface. Vanadium centers are shown by large yellow balls, oxygen centers by red balls, nitrogen centers by green balls, and hydrogen centers by small blue balls. Surface atoms that are included in the optimization are emphasized with shading.

All three adsorbates N, NH, and NH_2 adsorb at the O(1), O(2), and the O(3) sites, where the nitrogen atom forms the bond with the oxygen atom. The O(1)N group generated by nitrogen adsorption stands almost upright, as evidenced by the small tilt angle of 10° with respect to the surface normal. The O(1)-N bond length of 1.21 \AA is close to the bond length of gaseous NO, 1.15 \AA [166] (Figure 5.4). The geometry found for NH adsorbed at the O(1) site is very similar to what has been found for nitrogen adsorption. The corresponding atom positions of the surface cluster atoms, as well as the nitrogen atom of the two equilibrium structures, differ by less than 0.10 \AA . The additional hydrogen atom points towards the opposite O(1) site with the NH bond bent by an angle of 83° with respect to the surface normal (Figure 5.5). NH_2 also adsorbs on top of the O(1) site, but the resulting O(1)-N bond is tilted more strongly (36° with respect to the (010) direction). One hydrogen points towards the opposite O(1) site, as found for NH adsorption, and the other one points mainly towards the (001) direction (Figure 5.6).

Nitrogen adsorbed at the O(2) site binds upright on top of the O(2) site at a distance of 1.30 \AA (Figure 5.4). The adsorbed NH on top of the O(2) site does not stand upright, instead it is bent along the (100) direction where the O(2)-N bond forms an angle of 8° and the N-H bond an angle of 66° on the opposite side along the (010) direction with respect to the surface normal (Figure 5.5). The geometry of NH_2 adsorbed at the O(2) site resembles the geometry of NH binding at the bridging oxygen site (Figure 5.6). NH_2 sits on top of the O(2) site, with the O(2)-N bond bent by 8° , and the two N-H

bonds bent by 71° with respect to the surface normal. In contrast to NH, the hydrogen is not pointing directly into the (100) direction, instead the NH_2 scissor formed by the two hydrogen atoms is opened to yield an angle of 109° .

Due to O(3) bond formation with the nitrogen atom, the corresponding O(3) site is shifted out of the surface by 0.80 \AA ($\Delta z = 0.75 \text{ \AA}$). This large displacement is also reflected in the enlarged distances between the O(3) site and its vanadium neighbors (Table 5.4). The O(3)N unit that is formed is bent away from the O(1) double row with respect to the surface normal by 25° (Figure 5.4). NH adsorbs at the O(3) site in a geometry with the O(3)-N bond (1.44 \AA) twisted by 28° with respect to the surface normal, the (010) direction, pointing away from the neighboring vanadyl oxygen. The hydrogen atom points towards the O(1) site. The O(3) oxygen gets drawn out of the surface by 0.59 \AA ($\Delta z = 0.58 \text{ \AA}$) (Figure 5.5). After adsorption of NH_2 , as found for the previous cases, the O(3) oxygen gets drawn out of the surface by 0.55 \AA ($\Delta z = 0.52 \text{ \AA}$). The O(3)-N bond is tilted away from the surface normal by 24° . One hydrogen is oriented towards the O(1) site and the other ones towards the neighboring O(2) sites (Figure 5.6).

Nitrogen can adsorb also at the O(2') site. The equilibrium geometry is reminiscent to what was found for hydrogen adsorption at the O(2') site. Due to the adsorption, the O(2') oxygen gets pulled outward by 1.52 \AA ; this is accompanied by upward movement of the two neighboring vanadyl, VO(1) units. In addition, the V-V distance opens by 0.73 \AA and the O(1)-O(1) distance by 1.78 \AA (Figure 5.4). In contrast, with hydrogen adsorption the O(2')N does not sit symmetrically between the two neighboring vanadium atoms. The short and long V-O(2') distances are 2.03 \AA and 2.35 \AA respectively. No adsorption at the O(2') site was observed for NH and NH_2 and none of the three adsorbates, nitrogen, NH, or NH_2 , can stabilize near the O(3') site.

As can be seen in Table 5.3, the O-N bond lengths are the smallest for adsorption at the O(1) site, and largest at the O(2) site. The O-N distances increase somewhat going from nitrogen to NH to NH_2 . For all cases, the NH bond lengths are between 1.02 \AA and 1.05 \AA .

The NH_2 molecule is the first (following the order of this chapter) that can stabilize in the neighborhood of the vanadium atom. NH_2 adsorbs at a distance of 2.75 \AA with its nitrogen atom pointing towards the vanadium site. The molecule is oriented along the (100) direction with both hydrogen atoms pointing out of the surface, see Figure 5.6.

The adsorption energies for NH_x , ($x = 0,1,2$), are smaller compared to hydrogen (Table 5.3). Comparing the adsorption energies for the different adsorbates at the most favorable adsorption site, $E_{\text{ads}}(\text{N}) = -1.54 \text{ eV}$, $E_{\text{ads}}(\text{NH}) = -0.95 \text{ eV}$, and $E_{\text{ads}}(\text{NH}_2) = -0.74 \text{ eV}$, shows that adding hydrogen atoms to nitrogen weakens the binding to the surface.

The atom charges show that the adsorbate always loses negative charge, but the resulting O-NH_x group is positively charged compared to the corresponding oxygen site before adsorption, inducing a slight reduction of the neighboring surface atoms (Table 5.3). NH₂ that adsorbs on top of the vanadium site, stabilizes at a distance of 2.75 Å with small adsorption energies. The weak interaction with the surface is also represented by the small changes in the atom charges of the adsorbed molecule and the vanadium atom.

5.1.3 Ammonia adsorption at the perfect V₂O₅(010) surface

NH₃ adsorption has been studied extensively, both theoretically and experimentally. A detailed comparison of experimental findings and theoretical results can be found in Section 5.3. The theoretical work includes periodic DFT calculations using a GGA functional (BLYP) [70] and cluster models [68, 69, 71], employing a GGA-hybrid functional (B3LYP) [69, 71], as well as semi-empirical methods (MSINDO) [68]. The results show no [69, 71] or only weak [68, 70] ammonia adsorption on top of vanadium site of the perfect V₂O₅(010) surface.

The present calculations confirm the earlier results [68, 70]. The only adsorption site for ammonia on the perfect V₂O₅(010) surface that has been found is on top of bare vanadium atoms, as shown in Figure 5.7. However, for this configuration the binding distance to the surface, $d(\text{V-N}) = 2.70 \text{ \AA}$, is rather large, yielding a small adsorption energy, $E_{\text{ads}} = -0.25 \text{ eV}$, and very small changes in the atom charges induced by adsorption ($\Delta q(\text{NH}_3) = 0.08 \text{ au}$).

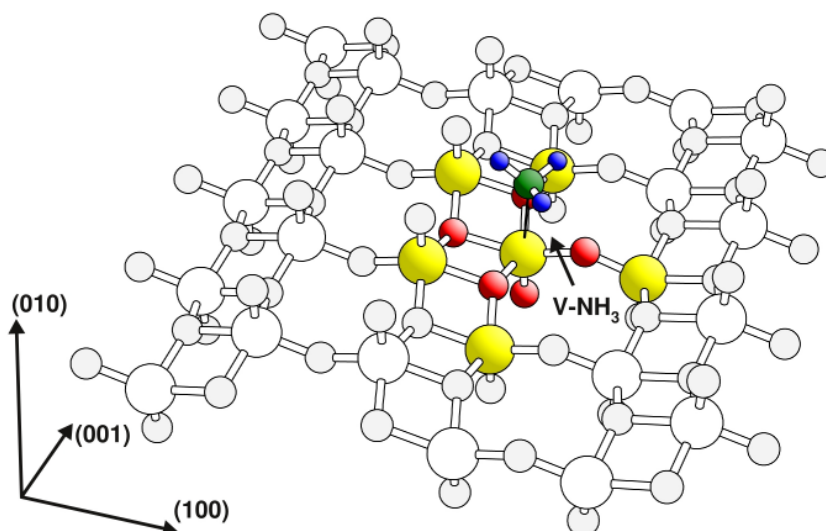


Figure 5.7: Equilibrium geometries of NH₃ adsorbed at the perfect V₂O₅(010) surface. Vanadium centers are shown by large yellow balls, oxygen centers by red balls, nitrogen centers by green balls and hydrogen centers by small blue balls. Surface atoms that are included in the optimization are emphasized with shading.

5.1.4 NH₄ adsorption at the perfect V₂O₅(010) surface

Surface NH₄ has also been studied theoretically [67-72] and experimentally [25, 62]. How this relates to the present work is discussed in detail in Section 5.3. The adsorption of NH₄ at the perfect V₂O₅(010) surface is different from the previous cases. Due to its geometry, the molecule binds with its hydrogen atoms to the surface. Further, the adsorption energies are significantly larger compared to findings for the previous adsorbates, as will be discussed in the following text.

Table 5.4: NH₄ adsorption at the perfect V₂O₅(010) surface. Distances between the participating oxygen atom and the neighboring vanadium sites, $d(\text{V-O})$, and distances between the closest surface oxygen atoms and the hydrogen from the NH₄ molecule, $d(\text{O-NH}_4)$ (in [Å]), atom charges, q of corresponding atoms (in atomic units, [au]), for the substrate clusters, with and without NH₄ adsorbed, and adsorption energies, E_{ads} (in [eV]).

		4xO(1)	2xO(2)	O(3)	O(3')	V
substrate cluster	$d(\text{V-O})$	1.59	1.81 1.81	1.90 1.90 2.02		--
	$q(\text{O})$	-0.62	-0.94	-1.08		--
	$q(\text{V})$	2.14	2.11 2.11	2.13 2.13 2.15		2.14
NH ₄ adsorbed	$d(\text{O-NH}_4)$	1.81 2.28	1.79	1.56 2.08	1.64 2.15	1.81 1.82
	$d(\text{V-O})$	1.63 1.61	1.85	1.95 1.95 2.05	1.96 1.96 2.07	--
	$q(\text{NH}_4)$	0.88	0.89	0.84	0.87	0.86
	$q(\text{O})$	-0.74 -0.71	-1.03	-1.13	-1.13	--
	$q(\text{V})$	2.10 2.10	2.06 2.06	2.05 2.06 2.09	2.08 2.08 2.05	2.06
	E_{ads}	-3.90	-3.57	-3.27	-3.23	-3.38

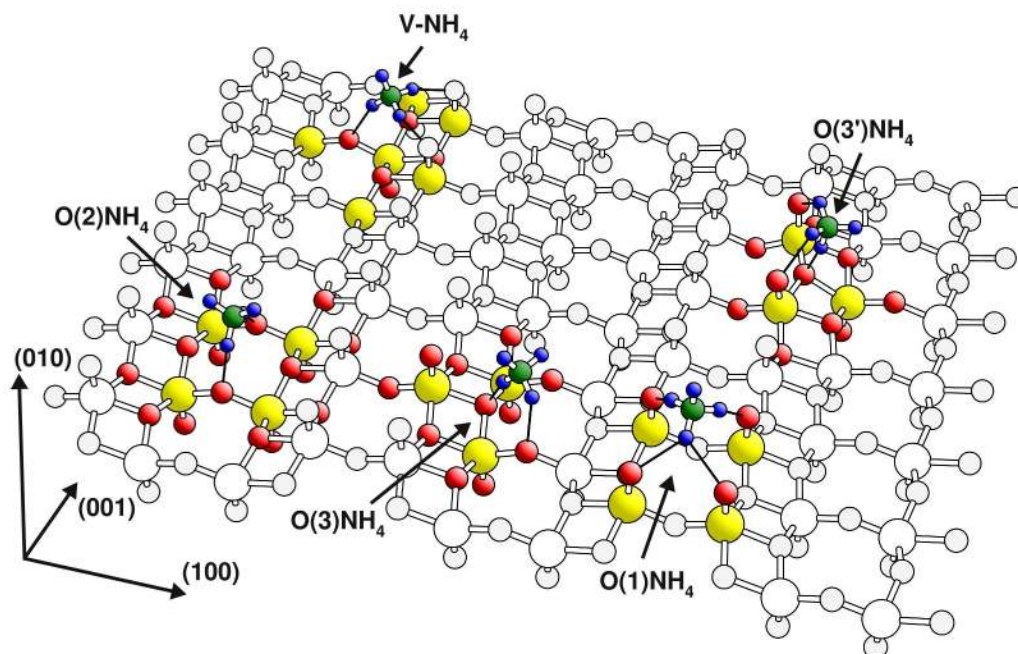


Figure 5.8: Equilibrium geometries of NH_4 adsorbed at the perfect $\text{V}_2\text{O}_5(010)$ surface. Vanadium centers are shown by large yellow balls, oxygen centers by red balls, nitrogen centers by green balls and hydrogen centers by small blue balls. Surface atoms that are included in the optimization are emphasized with shading.

Near the O(1) sites, NH_4 adsorbs over a square formed by four O(1) sites of the vanadyl double rows, which contrasts with forming a bond with one vanadyl oxygen (see Figure 5.8). Thus, a different cluster model than for a single O(1) site is used, the $\text{V}_{14}\text{O}_{42}\text{H}_{14}$ cluster, as discussed in Section 4.1.2. Figure 5.8 shows that the two hydrogen atoms of adsorbed NH_4 are pointing towards oxygen atoms of neighboring vanadyl rows, $d(\text{O}(1)\text{-H}) = 1.81 \text{ \AA}$, one into the (001) direction, $d(\text{O}(1)\text{-H}) = 2.28 \text{ \AA}$, and the fourth sticks out of the surface in the (010) direction. The rearrangements of the surface atoms due to adsorption are small, as indicated by the atom position shifts, $\Delta r < 0.06 \text{ \AA}$.

NH_4 can interact simultaneously with two adjacent bridging oxygen sites, in a symmetric arrangement. In order to provide an equivalent description for both O(2) sites, the $\text{V}_{14}\text{O}_{42}\text{H}_{14}$ cluster is also used (Section 4.1.2). NH_4 sits between the two O(2) sites, with one of its hydrogen pointing towards each of these sites, $d(\text{O}(2)\text{-H}) = 1.79 \text{ \AA}$ (see Figure 5.8). Analogous to adsorption on top of the O(1) sites, the adsorption at the O(2) sites induces only minor atom position shifts at the surface ($\Delta r < 0.09 \text{ \AA}$).

For NH_4 adsorption at the O(3) site, the definition of one atom as an adsorption site is meaningful. In contrast to previous cases, there is one oxygen-hydrogen distance that is significantly shorter than the others: the O(3)-H distance, $d(\text{O}(3)\text{-H}) = 1.56 \text{ \AA}$. It is also shorter than the O-H distances found in previous cases of adsorption at the O(1) and O(2) sites. The stronger interaction of one hydrogen with the surface is also reflected in

the slight elongation of the H-N bond of the hydrogen that interacts with the O(3) site (1.09 Å vs. 1.03 Å, 1.02 Å). The adsorbed molecule leans towards the O(2) valley forming one relatively short O(2)-H distance, $d(\text{O}(2)\text{-H}) = 2.08 \text{ \AA}$. The surface atom displacements induced by NH_4 adsorption at the O(3) site are smaller than 0.14 Å.

No binding of NH_4 has been found at the O(2') site. A geometry optimization resulted in the same configuration as NH_4 adsorbed on top of the O(1) double row. But, NH_4 can stabilize near the O(3') site. The same reconstruction pattern is similar to the one found for hydrogen adsorption at the O(3') site, where due to the adsorption, the O(3') oxygen moves out of the surface and the neighboring vanadyl groups open. This is reasonable because only the hydrogen atom, and not the whole molecule, has to be squeezed between the two adjacent vanadyl oxygen atoms of the surface. However, the V-V opening by 0.19 Å due to adsorption, and the O(1)-O(1) opening by 0.67 Å, are smaller than for hydrogen adsorption. The remainder of the adsorbed NH_4 leans towards the open valley between the vanadyl rows. There it is oriented in a way that establishes three relatively short O-H bonds to the O(3') site, $d(\text{O}(3')\text{-H}) = 1.64 \text{ \AA}$, and the two neighboring O(1) sites, $d(\text{O}(1)\text{-H}) = 2.15 \text{ \AA}$.

NH_4 stabilizes near the vanadium site in a geometry where its hydrogen atoms point towards oxygen sites yielding three relatively short O-H distances to the neighboring O(1) sites, $d(\text{O}(1)\text{-H}) = 1.81 \text{ \AA}$ and 1.82 \AA , and the O(2) site, $d(\text{O}(2)\text{-H}) = 2.36 \text{ \AA}$. These distances are comparable to what has been found for adsorption near the oxygen sites. Consistent with the previous cases, only minor displacements of the surface atoms are found ($\Delta r < 0.07 \text{ \AA}$).

All adsorption energies are very large (see Table 5.4) if the free NH_4 radical is taken as reference. The strongest binding was found on top of the O(1) ridge, and the weakest binding at the O(3) and O(3') sites. These adsorption energies have to be interpreted with caution, because the adsorption of an NH_4 species from a gas phase is a process that is very unlikely to happen on the real catalyst surface, since NH_4 does not appear in a gas phase. However other processes, such as the adsorption of ammonia at already existing surface OH groups, can create NH_4 surface species yielding significantly smaller adsorption energies, as will be discussed at the end of this section.

After adsorption, the NH_4 molecule is highly positively charged. As evidenced from Table 5.4, the amounts of charges vary only slightly with the different adsorption sites between 0.84 au at the O(3) and 0.89 au at the O(2) site. The strong positive charge, the large O-H bond distances, and the small displacements of the surface atoms, in combination with the large binding energies, indicate large ionic contributions to the binding.

Surface NH_4 species can also be created by ammonia adsorption at already existing surface OH groups. In catalytic chemistry, surface OH groups are usually called Brønsted acid sites. They are defined as acid sites that can act as both electron

acceptors and proton donors. Total energies obtained for the clusters presenting surface NH_4 , as identified above, can be used to calculate the binding energy $E_{\text{ads}}(\text{NH}_3/\text{OH})$ of NH_3 at surface OH sites. Here the new reference at infinite adsorbate-substrate separation must be the sum of total energy of the surface cluster, with the attached hydrogen atom, and the total energy of the NH_3 molecule. Thus, the adsorption energy $E_{\text{ads}}(\text{NH}_3/\text{OH})$ is given by:

$$E_{\text{ads}}(\text{NH}_3/\text{OH}) = E_{\text{tot}}^{\text{r}}(\text{Cluster-NH}_4) - E_{\text{tot}}(\text{NH}_3) - E_{\text{tot}}^{\text{r}}(\text{Cluster-H}). \quad (5.2)$$

The numerical results are presented in Table 5.5. As already suggested by the strong binding found for NH_4 on the surface, the adsorption energies $E_{\text{ads}}(\text{NH}_3/\text{OH})$ of NH_3 at OH groups are significantly larger than for NH_3 adsorption at the perfect $\text{V}_2\text{O}_5(010)$ surface ($E_{\text{ads}}(\text{NH}_3) = -0.25$). The adsorption energies vary between -0.88 eV at the O(2)H site, and up to -1.40 eV at the O(1)H site. This strongly indicates that surface OH groups can favor ammonia adsorption.

Table 5.5: Adsorption energies $E_{\text{ads}}(\text{NH}_3/\text{OH})$ of ammonia at surface OH groups of the $\text{V}_2\text{O}_5(010)$ surface, forming surface NH_4 (in [eV]).

E_{ads} [eV]	O(1)	O(1')	O(2)	O(2')	O(3)	O(3')	V
NH_3 at Brønsted site	-1.40	--	-0.88	--	-0.89	-1.01	--

5.1.5 NO adsorption at the perfect $\text{V}_2\text{O}_5(010)$ surface

In agreement with previous theoretical [68, 71] and experimental [17] studies, nitric oxide, NO, is found to interact weakly with the surface. The present results find NO to stabilize either near the vanadyl ridge, or on top of the valley, at approximately 3 \AA distance from the nearest surface atoms, see Figure 5.9. The adsorption energy near the O(1) ridge is -0.28 eV and the NO molecule is positively charged (0.27 au). Both the adsorption energy, $E_{\text{ads}} = -0.20$ eV, and the amount of positive charge accumulated by the NO molecule (0.14 au) are slightly smaller if NO stabilizes on top of the valley.

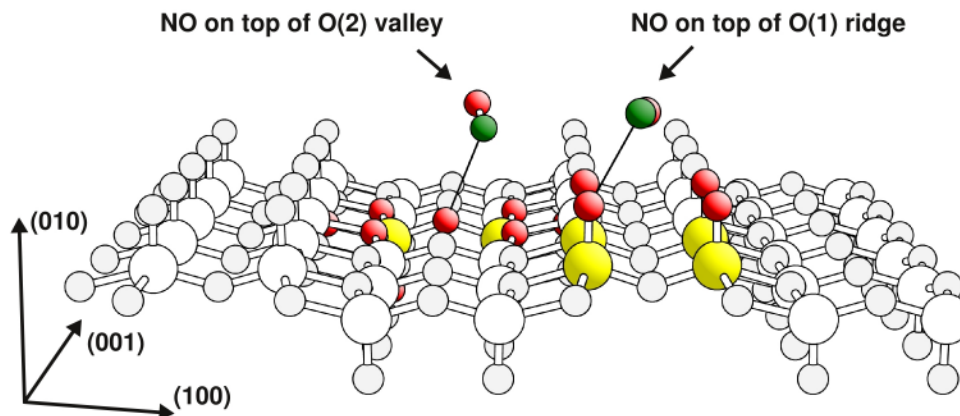


Figure 5.9: *Equilibrium geometries of nitric oxide adsorbed at the perfect $V_2O_5(010)$ surface. Vanadium centers are shown by large yellow balls, oxygen centers by red balls, and nitrogen centers by green balls. Surface atoms that are included in the optimization are emphasized using shading.*

5.2 Adsorption of H, NH_x , ($x = 0, \dots, 4$), and NO at the reduced $V_2O_5(010)$ surface

As discussed in Section 4.2, the oxygen vacancy clusters serve as models for a reduced surface. In addition to surface vacancy sites O(1), O(2), O(2'), O(3), and O(3'), adsorption at the vanadium atom above the sub-surface oxygen vacancy O(1')_{vac} can also be considered. This will become important in combination with vacancy diffusion processes. The different adsorbates, atomic hydrogen, NH_x , ($x = 0, \dots, 4$), and NO, can be divided into three classes, based on their adsorption properties near oxygen vacancy sites of the $V_2O_5(010)$ surface. The first class, consisting of atomic hydrogen, atomic nitrogen, NH, NH_2 , and NO, adsorbs by substituting the missing oxygen at all surface vacancy sites (substitutional adsorption). The second, the NH_3 molecule, results in substitutional adsorption only at the O(1) vacancy site, and can induce vacancy diffusion at other sites. The third, the NH_4 molecule, always adsorbs near vacancy sites, avoiding substitution due to its size. The results for adsorption at the reduced surface are summarized in Table 5.6a and Table 5.6b.

Table 5.6a: H, N, NH and NH₂ adsorption at the reduced V₂O₅(010) surface near oxygen vacancy sites. Atom charges q of the vanadium atoms next to the vacancy site (for O(1)_{vac} site also q of sub-surface O(1) atom from lower layer) and the adsorbates (in atomic units, [au]), largest atom position shifts with respect to the relaxed surface cluster, Δr_{\max} , (for O(1)_{vac} and O(1')_{vac} sites additional the vertical shift of vanadium atom $\Delta z(V)$) (in [\AA]), and adsorption energies E_{ads} (in [eV]).

	O(1) _{vac}	O(2) _{vac}	O(2') _{vac}	O(3) _{vac}	O(3') _{vac}	O(1') _{vac}
cluster	$q(V)$	2.17	2.10 2.10	2.13 2.13 2.15	2.14	
	$q(O)$	-0.63	--	--	--	--
vac. cluster	$q(V)$	2.07	1.94 1.94	1.86 1.86 1.94	1.82	
	$q(O)$	-0.87	--	--	--	--
	Δr_{\max}	0.98	0.43	0.16	0.52	
	$\Delta z(V)$	-0.98	--	--	0.20	
H adsorbed	$q(H)$	-0.25	-0.44	-0.46	-0.21	
	$q(V)$	1.97	1.99 1.99	1.97 1.97 2.04	1.95	
	$q(O)$	-0.69	--	--	--	--
	Δr_{\max}	0.28	0.12	0.13	0.61	
	$\Delta z(V)$	-0.28	--	--	0.61	
	E_{ads}	-1.41	-2.59	-2.60	-2.08	
N adsorbed	$q(N)$	-0.46	-0.74	-0.95	-0.51	
	$q(V)$	1.95	2.03 2.03	2.06 2.06 2.10	1.95	
	$q(O)$	-0.64	--	--	--	--
	Δr_{\max}	0.10	0.24	0.10	0.83	
	$\Delta z(V)$	-0.05	--	--	0.82	
	E_{ads}	-2.17	-4.10	-3.81	-2.72	
NH adsorbed	$q(NH)$	-0.45	-0.70 -0.70	-0.83 -0.80	-0.46	
	$q(V)$	2.06	2.05 2.06 2.05	2.08 2.08 2.06 2.06	2.06	
	$q(O)$	-0.63	--	--	--	--
	Δr_{\max}	0.02	0.07	0.67	0.93	
	$\Delta z(V)$	0.01	--	--	0.92	
	E_{ads}	-3.16	-4.92	-4.48	-3.58	
NH₂ adsorbed	$q(NH_2)$	-0.25	-0.42 -0.44	-0.42 -0.40	-0.23	
	$q(V)$	2.09	2.04 2.04 2.01 2.01	2.06 2.07 2.00 2.00 2.06 2.07	2.06	
	$q(O)$	-0.65	--	--	--	--
	Δr_{\max}	0.07	0.14	0.81	0.97	
	$\Delta z(V)$	-0.07	--	--	0.97	
	E_{ads}	-2.25	-3.90	-3.35	-2.84	

Table 5.6b: NH_3 , NH_4 , and NO adsorption at the reduced $\text{V}_2\text{O}_5(010)$ surface near oxygen vacancy sites. Atom charges q of the vanadium atoms next to the vacancy site (for $\text{O}(1)_{\text{vac}}$ site also q of sub-surface $\text{O}(1)$ atom from lower layer) and the adsorbates (in atomic units, [au]), largest atom position shifts with respect to the relaxed surface cluster, Δr_{max} , (for $\text{O}(1)_{\text{vac}}$ and $\text{O}(1')_{\text{vac}}$ sites additional the vertical shift of vanadium atom $\Delta z(\text{V})$) (in [\AA]), and adsorption energies E_{ads} (in [eV]).

	$\text{O}(1)_{\text{vac}}$	$\text{O}(2)_{\text{vac}}$	$\text{O}(2')_{\text{vac}}$	$\text{O}(3)_{\text{vac}}$	$\text{O}(3')_{\text{vac}}$	$\text{O}(1')_{\text{vac}}$	
cluster	$q(\text{V})$	2.17	2.10 2.10	2.13 2.13 2.15	2.14		
	$q(\text{O})$	-0.63	--	--	--	--	
vac. cluster	$q(\text{V})$	2.07	1.94 1.94	1.86 1.86 1.94	1.82		
	$q(\text{O})$	-0.87	--	--	--	--	
	Δr_{max}	0.98	0.43	0.16	0.52		
	$\Delta z(\text{V})$	-0.97	--	--	0.20		
NH_3 adsorbed	$q(\text{NH}_3)$	0.19	--	--	0.08	0.22	
	$q(\text{V})$	2.03	--	--	1.86 1.86 1.99	1.92	
	$q(\text{O})$	-0.85	--	--	--	--	
	Δr_{max}	0.79	--	--	0.29	0.63	
	$\Delta z(\text{V})$	-0.79	--	--	--	0.62	
	E_{ads}	-0.87	$\rightarrow\text{O}(1')_{\text{vac}}$	--	$\rightarrow\text{O}(1')_{\text{vac}}$	-0.31	-1.24
NH_4 adsorbed	$q(\text{NH}_4)$	0.85	0.85	0.87	0.83	0.88	
	$q(\text{V})$	2.05	1.92 1.96	1.95 1.95	1.84 1.84 1.85	1.84 1.84 1.96	
	$q(\text{O})$	-0.86	--	--	--	--	
	Δr_{max}	0.99	0.45	0.45	0.44	0.29	
	$\Delta z(\text{V})$	-0.99	--	--	--	--	
	E_{ads}	-3.25	-2.83	-3.47	-3.20	-3.67	-2.84
NO adsorbed	$q(\text{NO})$	-0.32	-0.66	-0.65	-0.72	-0.67	
	$q(\text{V})$	2.01	2.04 2.04	1.98 2.06	2.04 2.04 2.06	1.98 1.98 2.06	
	$q(\text{O})$	-0.67	--	--	--	--	
	Δr_{max}	0.15	0.15	0.97	0.43	0.65	
	$\Delta z(\text{V})$	-0.14	--	--	--	--	
	E_{ads}	-1.00	-1.96	-1.59	-1.11	-0.87	-1.38

5.2.1 Substitutional adsorption near oxygen vacancy sites of the $V_2O_5(010)$ surface

The five different adsorbates, H, N, NH, NH_2 , and NO, are quite similar in their adsorption properties. These atoms or molecules substitute the missing oxygen atom at all surface vacancy sites. Here ‘substitute’ means that adsorption occurs at that the position of the missing oxygen atom. As a result, depending on the adsorbate, geometric and electronic properties of the perfect surface are partly recovered. For the sub-surface oxygen vacancy $O(1')_{vac}$, adsorption at the vanadium atom above the vacancy site is considered.

As discussed in Section 4.2, after removing an oxygen atom from the O(1) site of the $V_2O_5(010)$ surface, creating a vacancy $O(1)_{vac}$, the vanadium atom next to the vacancy forms a new bond with the vanadyl of the underlying V_2O_5 layer. This bond formation is accompanied by a downward movement of the vanadium atom by $\Delta z(V) = 0.98 \text{ \AA}$, with respect to the surface cluster. Both the relaxation due to the $O(1)_{vac}$ formation, as well as the relaxation after adsorption at the $O(1)_{vac}$ site, are dominated by the vertical shift of the vanadium atom. Here all five adsorbates can form strong bonds with the vanadium atom at the vacancy site. As a result, the V-O(1) bond that was formed with the vanadyl oxygen of the second layer during the vacancy formation is weakened, and the vanadium atom moves back in the direction of its original position at the perfect surface (see Figure 5.10). Table 5.6a and Table 5.6b lists the largest atom position shifts Δr_{max} , and the vertical shifts of the vanadium atom $\Delta z(V)$ with respect to the surface cluster. The vertical shift is the largest for hydrogen adsorption ($\Delta z(V) = -0.28 \text{ \AA}$), and the smallest for NH adsorption that pulls the vanadium atom back in its original vertical position.

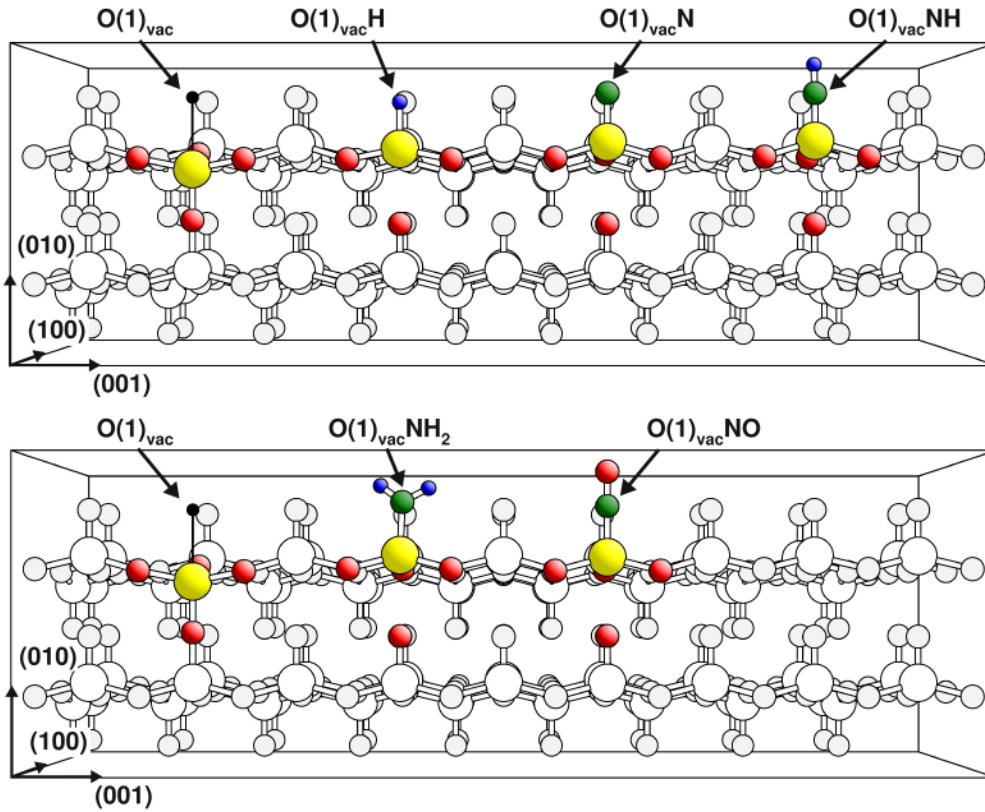


Figure 5.10: *Equilibrium geometries of the $O(1)_{vac}$ and H , NH_x , ($x = 0,1,2$), and NO adsorbed at this vacancy site. The surface is cut at the $V-O(3)$ bond pointing towards the viewer to make the vanadium position more visible ($O(3)$ pointing towards the viewer is missing). Vanadium centers are shown by large yellow balls, oxygen centers by red balls, nitrogen centers by green balls, hydrogen centers by small blue balls and missing oxygen at vacancy site is indicated by a small black dot. Surface atoms that are included in the optimization are emphasized with shading.*

The removal of the bridging oxygen at the $O(2)$ site of the $V_2O_5(010)$ surface creates a vacancy $O(2)_{vac}$, and the surface opens around the vacancy site. The distance between the two neighboring vanadium atoms increases by 0.77 \AA (Section 4.2). When either H , NH_x , ($x = 0,1,2$), or NO adsorbs at this vacancy site, the neighboring vanadium atoms shift back close to their original position at the perfect surface, hence, towards the $O(2)_{vac}$ site, see Figure 5.11. This also applies for the other surface atoms, which after adsorption, arrange in positions closer to those of the perfect surface, $\Delta r_{max} \leq 0.24 \text{ \AA}$, compared to the vacancy cluster ($\Delta r_{max} = 0.43 \text{ \AA}$).

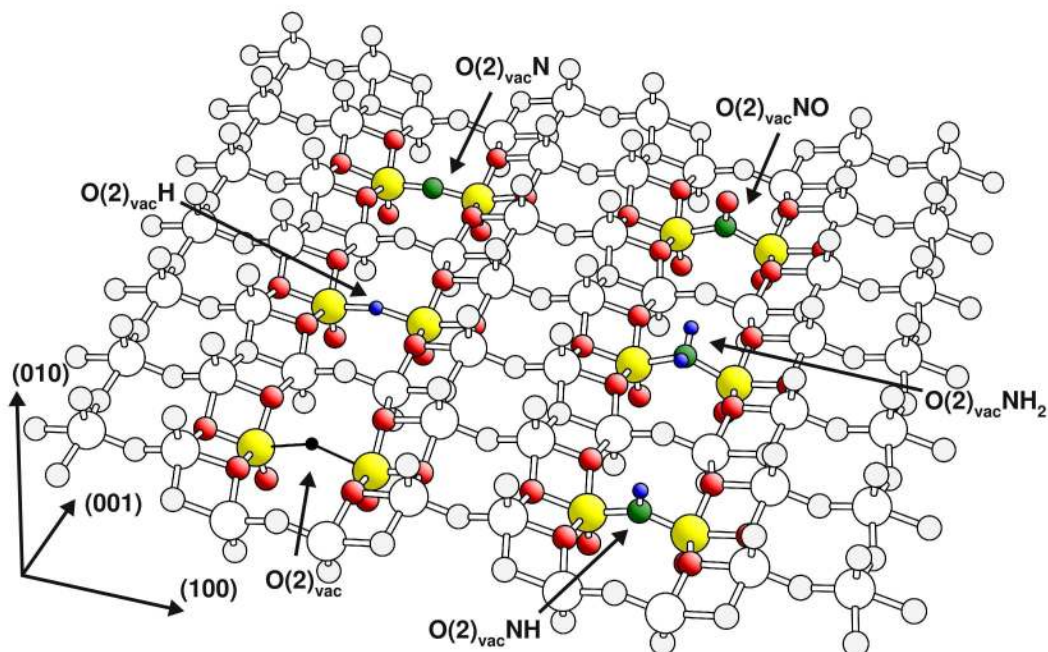


Figure 5.11: Equilibrium geometries of the $O(2)_{vac}$ and H , NH_x ($x = 0,1,2$), and NO adsorbed at this vacancy site. Vanadium centers are shown by large yellow balls, oxygen centers by red balls, nitrogen centers by green balls, hydrogen centers by small blue balls and missing oxygen at vacancy site is indicated by a small black dot. Surface atoms that are included in the optimization are emphasized with shading.

Formation of an $O(3)_{vac}$ causes only minor rearrangements of the neighboring atoms (see Section 4.2), and atom positions of the $O(3)_{vac}$ cluster and the surface cluster differ by less than 0.16 \AA . After substitutional adsorption, large changes in surface atom positions have been found only for NH_2 and NO adsorption, with $\Delta r_{max} = 0.33 \text{ \AA}$ and 0.43 \AA , caused by a tilt of the two neighboring vanadyl groups pointing inside the surface towards each other (Figure 5.12). However, for all five adsorbates, the V-O bond lengths of the vanadium atoms next to the $O(3)_{vac}$ site with its oxygen neighbors differ by less than 0.07 \AA to those of the perfect surface.

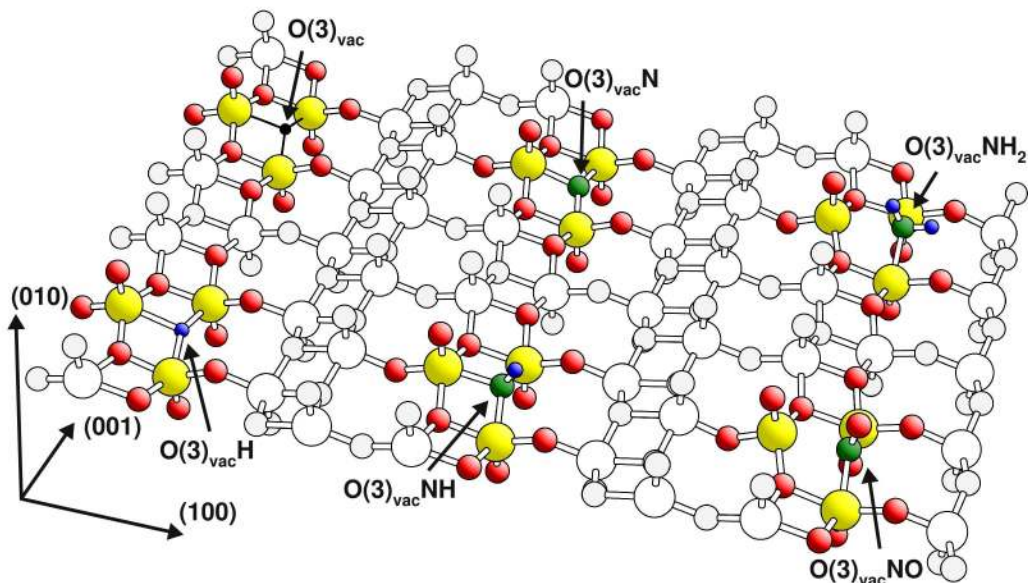


Figure 5.12: Equilibrium geometries of the $O(3)_{vac}$ and H , NH_x , ($x = 0, 1, 2$), and NO adsorbed near the $O(3)_{vac}$ site. Vanadium centers are shown by large yellow balls, oxygen centers by red balls, nitrogen centers by green balls, hydrogen centers by small blue balls and missing oxygen at vacancy site is indicated by a small black dot. Surface atoms that are included in the optimization are emphasized with shading.

Considering adsorption at the $O(2')$ vacancies, $O(2')_{vac}$, hydrogen and nitrogen stabilize in the same equilibrium geometry as found for adsorption at the $O(2)_{vac}$ site. This can be understood by the inversion symmetry of the single-layer model cluster. The calculated equilibrium geometries of NH , NH_2 and NO adsorbed at the $O(2')_{vac}$ site show similarities to the geometry of hydrogen adsorbed at the $O(2')$ site of the perfect surface (see Section 5.1.1). The two vanadyl groups adjacent to the $O(2)_{vac}$ site open up. The corresponding $O(1)-O(1)$ distances increase by 1.02 \AA , 1.26 \AA , and 1.13 \AA , after adsorption of NH , NH_2 , and NO , respectively. The three molecules can use this open space to adsorb at the vacancy site, where they substitute for the missing oxygen atom. The resulting distances between the vanadium atoms next to the $O(2')_{vac}$ site, and the neighboring oxygen atoms, differ by less than 0.09 \AA from the corresponding $V-O$ distances in the surface cluster. The hydrogen atoms of NH and NH_2 (oxygen for NO) point outwards at the surface. In contrast to NH and NH_2 , which are positioned symmetrically, the geometry of adsorbed NO is slightly distorted (Figure 5.13).

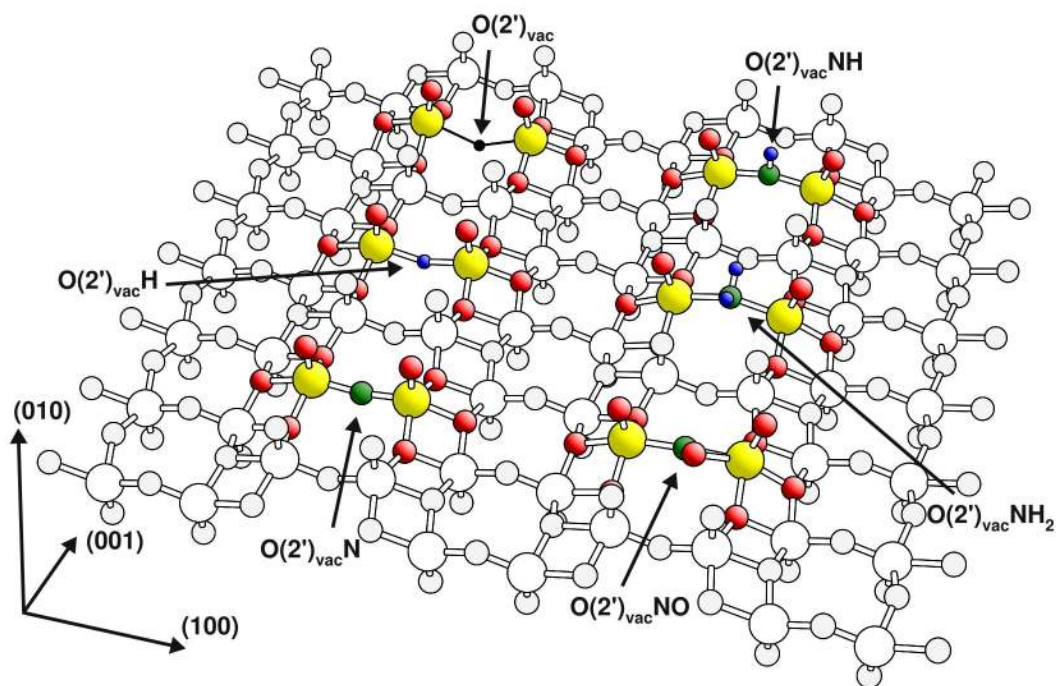


Figure 5.13: Equilibrium geometries of the $O(2')_{vac}$ and H , NH_x ($x = 0,1,2$), and NO adsorbed near the $O(2')_{vac}$ site. Vanadium centers are shown by large yellow balls, oxygen centers by red balls, nitrogen centers by green balls, hydrogen centers by small blue balls and missing oxygen at vacancy site is indicated by a small black dot. Surface atoms that are included in the optimization are emphasized with shading.

Adsorption at $O(3')_{vac}$ sites is similar to adsorption at the $O(2')_{vac}$ site. As described above, hydrogen and nitrogen stabilize in the same equilibrium geometry as found for adsorption at the $O(3)_{vac}$ site. The two $VO(1)$ groups next to the $O(3')_{vac}$ site open up, after adsorption of NH , NH_2 , and NO , with $O(1)-O(1)$ distances increasing by 1.04 Å, 1.61 Å, and 1.40 Å, respectively (Figure 5.14). The local geometries are comparable to the corresponding surface cluster, since V-O bond lengths of the neighboring vanadium atoms differ by less than 0.05 Å.

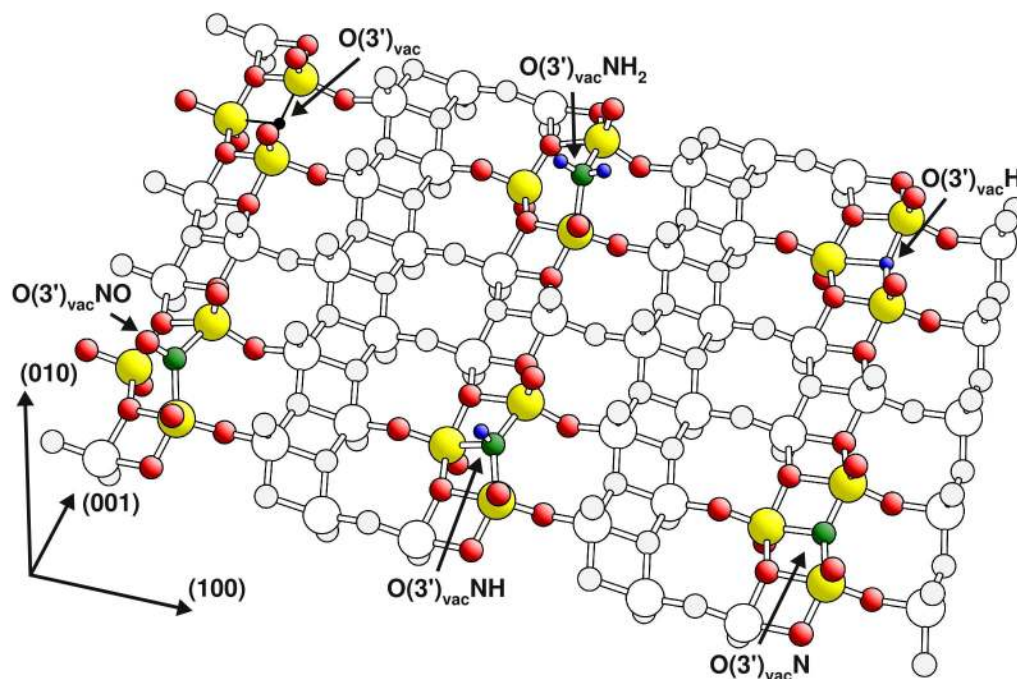


Figure 5.14: *Equilibrium geometries of the $O(3')_{\text{vac}}$ and H , NH_x , ($x = 0,1,2$), and NO adsorbed near the $O(3')_{\text{vac}}$ site. Vanadium centers are shown by large yellow balls, oxygen centers by red balls, nitrogen centers by green balls, hydrogen centers by small blue balls and missing oxygen at vacancy site is indicated by a small black dot. Surface atoms that are included in the optimization are emphasized with shading.*

Both oxygen vacancies, the $O(2')_{\text{vac}}$ and the $O(3')_{\text{vac}}$, are located between two $O(1)$ oxygen that stick out of the surface. It has been found that hydrogen, nitrogen, and NH can alternatively stabilize at these vanadyl oxygens $O(1)$ next to the vacancy site. Both the geometry and adsorption energy ($\Delta E_{\text{ads}} < 0.16$ eV) are close to what has been found for adsorption at the $O(1)$ site of the perfect $V_2O_5(010)$ surface.

While the (sub-surface) vanadyl position $O(1')$ is covered by the surface, and therefore not directly accessible, the opposite site of the vanadium atom (with respect to the missing oxygen) next to the $O(1')$ vacancy, $O(1')_{\text{vac}}$, is directly accessible at the surface. Atomic hydrogen, NH_x , ($x = 0,1,2$), and NO can adsorb at this opposite side. Due to the adsorption, the vanadium atom near the $O(1')$ vacancy, which already sticks out from the surface, moves even more outwards (see Figure 5.15). Therefore, the atom position shifts (with respect to the surface cluster), getting even larger after adsorption at the $O(1')_{\text{vac}}$. This effect is weakest for hydrogen and strongest for the adsorbed NH_2 molecule (Tables 5.6a and 5.6b). However, the V-O distances between the vanadium atoms that are considered in the geometry optimization (see Section 4.2), and their oxygen neighbors are close to the corresponding distances in the surface cluster. The largest deviations from the V-O bond lengths of the surface cluster have been found for adsorbed hydrogen, $\Delta d(\text{V-O}) \leq 0.14$ Å, and the smallest for NH adsorption at $\Delta d(\text{V-O}) \leq 0.06$ Å.

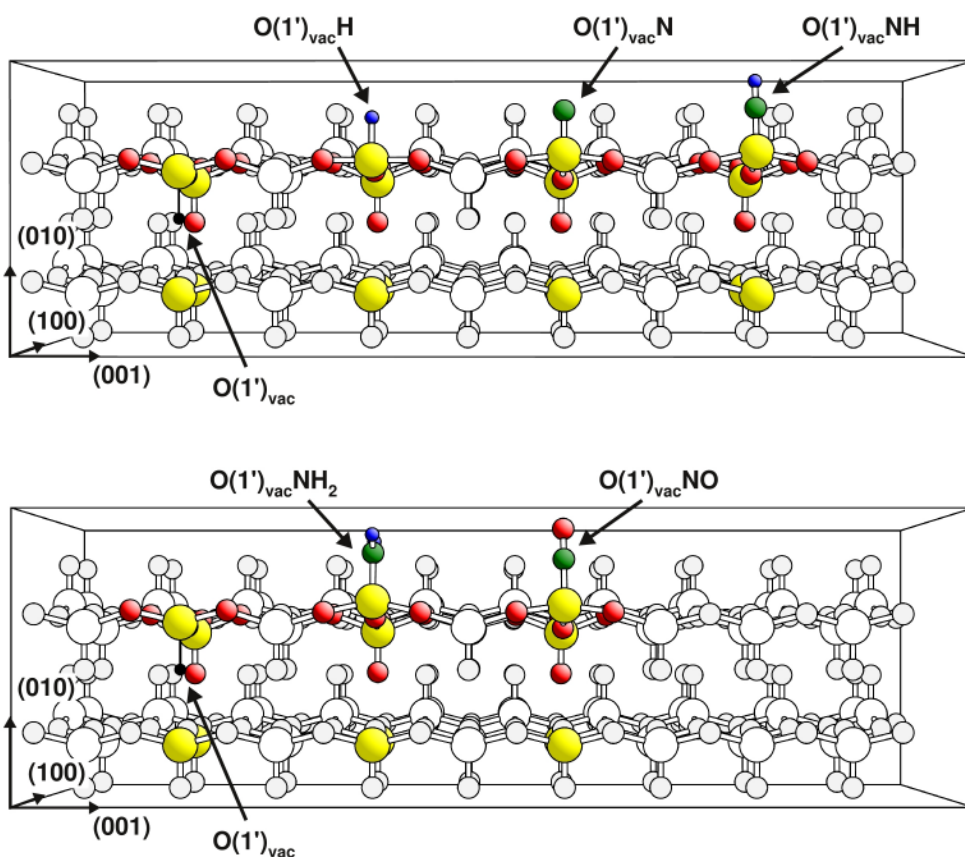


Figure 5.15: Equilibrium geometries of the $O(1')_{\text{vac}}$ and H , NH_x , ($x = 0,1,2$), and NO adsorbed at this vacancy site. The surface is cut at the $V-O(3)$ bond pointing towards the viewer to make the vanadium position more visible. ($O(3)$ pointing towards the viewer missing). Vanadium centers are shown by large yellow balls, oxygen centers by red balls, nitrogen centers by green balls, hydrogen centers by small blue balls and missing oxygen at vacancy sites by a very small black ball. Surface atoms that are included in the optimization are emphasized with shading.

The adsorption energies of H , NH_x , ($x = 0,1,2$), and NO show that for all considered oxygen vacancy sites, NH adsorbs the strongest and NO the weakest. The binding energies evaluated for atomic nitrogen and the NH_2 molecule are between those of atomic hydrogen and NH (Tables 5.6a and 5.6b). Further, it can be seen that hydrogen adsorption at the oxygen sites of the perfect $V_2O_5(010)$ is preferable (Table 5.1). However, the adsorption energies found for NH_x , ($x = 0,1,2$), and NO at the reduced $V_2O_5(010)$ surface, are significantly larger than at the perfect surface. The binding to the surface at different sites also correlates with the vacancy formation energies. It is larger for $O(2)_{\text{vac}}$ and $O(3)_{\text{vac}}$ (large vacancy formation energy) compared to the $O(1)_{\text{vac}}$ (smallest formation energy). The adsorption energies at the vacancy sites close to the vanadyl oxygen $O(2')_{\text{vac}}$ and $O(3')_{\text{vac}}$, as well as on top of the $O(1')_{\text{vac}}$ site, are intermediate. The only exception is nitric oxide that adsorbs the weakest at the $O(3')_{\text{vac}}$ site, instead of the $O(1)_{\text{vac}}$ site.

The electronic rearrangement due to substitutional adsorption near the $O(1)_{\text{vac}}$ is unique. In contrast to the other vacancies, a bond is formed with the vanadyl oxygen from the lower layer after removal of the $O(1)$ oxygen. The reduction of the vanadium atom induced by the vacancy formation is, to a large extent, compensated for by the bond formed with the lower layer where the sub-surface oxygen accumulates negative charge (-0.87 au), and thus becomes reduced, (see Section 4.2.1). Adsorption of H, NH_x , ($x = 0,1,2$), or NO at the vacancy site weakens the vanadium bond formed with the vanadyl oxygen from the lower layer. This $O(1)$ site becomes re-oxidized, resulting in an atom charge after adsorption between -0.63 au (NH adsorption) and -0.69 au (H adsorption). This is very close to what has been found for the atom charge of this $O(1)$ site in the surface cluster before vacancy formation (-0.63 au). On the other hand, the vanadium atom now interacts with the adsorbing atom or molecule that itself accumulates negative charge. The adsorption induced change of the vanadium's atom charge is a combination of the reduction caused by the breaking of the bond with the $O(1)$ atom from the lower layer, and the oxidation caused by the bond formation with the adsorbate. As a result, the adsorption of NH and NH_2 which interact the strongest with the vanadium atom does not affect its atom charge. The bonds formed with H, N, and NO cannot compensate for the missing bond with the oxygen, and the vanadium atom is more strongly reduced after adsorption (Tables 5.6a and 5.6b).

The electronic rearrangements caused by adsorption near the $O(2)_{\text{vac}}$, $O(2')_{\text{vac}}$, $O(3)_{\text{vac}}$, $O(3')_{\text{vac}}$ and $O(1')_{\text{vac}}$ sites are consistent. The recovery of the surface clusters geometry, or at least the local binding situation, as it is the case for the $O(2')$, $O(3')$ and $O(1')$, is accompanied by a partial recovery of the initial reduction state of the vanadium atoms near the vacancy site. This is illustrated in Table 5.6a and Table 5.6b by the atom charges of the adsorbate, that can accumulate negative charges, causing an oxidation of the surface atoms.

5.2.2 Ammonia adsorption near oxygen vacancy sites of the $V_2O_5(010)$ surface

Ammonia is found to adsorb substitutionally only at the $O(1)_{\text{vac}}$ site without further reconstructing. It has been found that the presence of NH_3 near other vacancy sites can induce vacancy diffusion processes, resulting in three different stable configurations for the reduced $V_2O_5(010)$ surface, as shown in Figure 5.16.

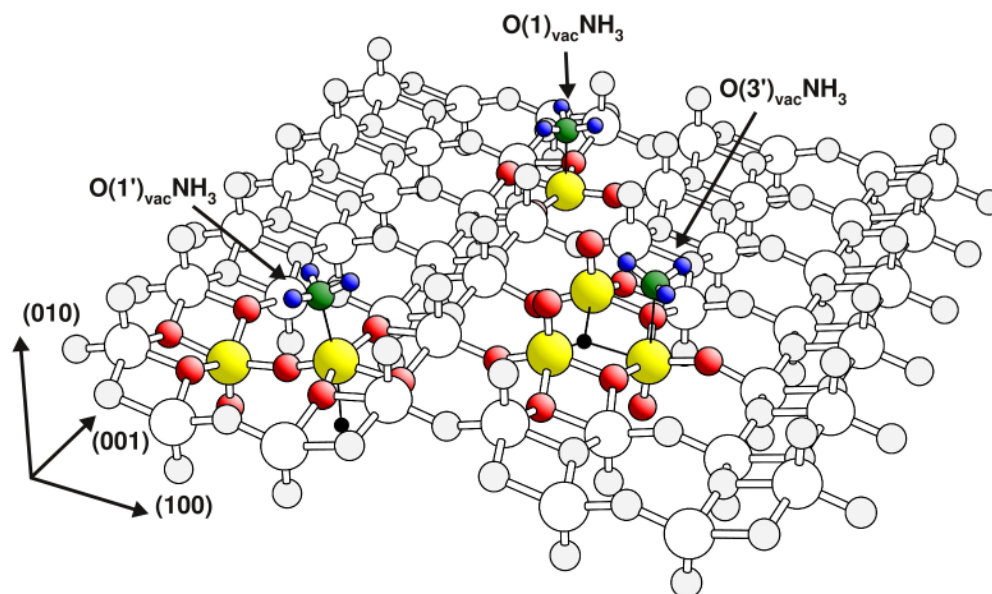


Figure 5.16: Equilibrium geometries of NH_3 adsorbed at the reduced $\text{V}_2\text{O}_5(010)$ surface. Vanadium centers are shown by large yellow balls, oxygen centers by red balls, nitrogen centers by green balls, and hydrogen centers by small blue balls. Surface atoms that are included in the optimization are emphasized with shading.

The $\text{O}(1)_{\text{vac}}$ sites provide enough space for NH_3 to adsorb in a similar way, as discussed above for substitutional adsorption. Ammonia binds directly at the vanadium site at a distance of 2.21 Å where it substitutes for the missing oxygen atom. In contrast to hydrogen, NH_x ($x = 0,1,2$) and NO , its ability to relax the V-O-V bridge between adjacent V_2O_5 layers formed by the $\text{O}(1)$ vacancy is much weaker. This is reflected in a vertical shift of the vanadium atom, $\Delta z(\text{V}) = -0.79$ Å, that is larger in comparison with the effects of adsorbates discussed above.

The vacancy sites created by the removal of $\text{O}(2)$ or $\text{O}(3)$ oxygen do not allow NH_3 to adsorb substitutionally. Instead, the ammonia stabilizes on top of a neighboring vanadium atom. This is accompanied by oxygen (vacancy) diffusion near the adsorption site. The NH_3 molecule close to the $\text{O}(2)_{\text{vac}}$ or $\text{O}(3)_{\text{vac}}$ disturbs the surface in a way that the sub-surface $\text{O}(1')$ oxygen diffuses into the corresponding $\text{O}(2)$ or $\text{O}(3)$ vacancy site. This has also been tested for the $\text{O}(2)_{\text{vac}}$ using a two-layer cluster model. Since this is the result of geometry optimizations starting with NH_3 positioned in the vicinity of $\text{O}(2)$ or $\text{O}(3)$ vacancy sites, these process are accompanied by no or very small energy barriers. In fact, Section 4.3 discusses vacancy diffusion of the $\text{O}(2)_{\text{vac}}$ into the $\text{O}(1')_{\text{vac}}$ whose barrier is very small. Thus, NH_3 approaching towards $\text{O}(2)_{\text{vac}}$ or $\text{O}(3)_{\text{vac}}$ leads to ammonia being adsorbed at a vanadium atom, with an $\text{O}(1')_{\text{vac}}$ underneath, see Figure 5.16.

NH₃ adsorbs at the vanadium site above the sub-surface vacancy O(1')_{vac} at a distance of 2.10 Å. As found for substitutional adsorption, the vanadium atom at the adsorption site moves outward from the surface ($\Delta z(\text{V}) = 0.62$ Å). Analogous to what has been found for substitutional adsorption, the V-O distances between the vanadium atoms considered in the geometry optimization (see Section 4.2.1) and their oxygen neighbors, are very close to the corresponding V-O distances in the perfect surface cluster (differences smaller than 0.13 Å). A stable configuration of NH₃ sitting on top of the vanadium atom next to the O(3') vacancy has been identified. The resulting geometry is similar to ammonia adsorbed at the V site of the perfect V₂O₅(010) surface. No stable configuration of NH₃ at the O(2')_{vac} site has been found.

The adsorption energies for NH₃ are smaller compared to NH_x adsorption at the vacancy sites. In addition, the energies for adsorption near the O(1)_{vac} site, $E_{\text{ads}} = -0.87$ eV, and near the O(1')_{vac} site, $E_{\text{ads}} = -1.24$ eV, are larger compared to ammonia adsorption at the perfect surface. The third stable configuration near the O(3') vacancy is both geometrically, but also energetically close to adsorption at the vanadium site of the perfect surface, $E_{\text{ads}} = -0.31$ eV.

In contrast to the previous cases, NH₃ accumulates positive charge. The adsorption induced changes in the adsorbate and surface atom charges are smaller compared to findings for adsorption of atomic hydrogen, NH_x, ($x = 0, 1, 2$), and NO (see Tables 5.6a and 5.6b).

5.2.3 NH₄ adsorption near oxygen vacancy sites of the V₂O₅(010) surface

Ammonium, NH₄, differs from the other adsorbates, not only with respect to its adsorption properties at the perfect, but also at the reduced surface. NH₄ can interact with the surface only via its hydrogen atoms and is, at all sites, too large to fit into the vacancies. This is illustrated in Figure 5.17, which sketches out the different configurations of NH₄ adsorbed at the reduced V₂O₅(010) surface. It shows that the NH₄ adsorbate does not interact directly with the vanadium atoms next to the vacancy site.

Most of the configurations can be related to configurations at the perfect V₂O₅(010) surface. Close to the O(1)_{vac}, O(2')_{vac} and O(3')_{vac} sites, NH₄ adsorbs at the O(1) ridge. At the O(1')_{vac} and the O(3)_{vac} sites, the molecule stabilizes in the valley, as is also found for the O(2) site of the perfect surface. The adsorbate geometry found close to the O(2)_{vac} site has no counterpart at the perfect surface. As can be seen in Figure 5.17, the molecule binds towards two opposite O(3) sites. This is possible since the distortion of the surface near the O(2)_{vac} site reduces the distance between the O(3) oxygen neighbors.

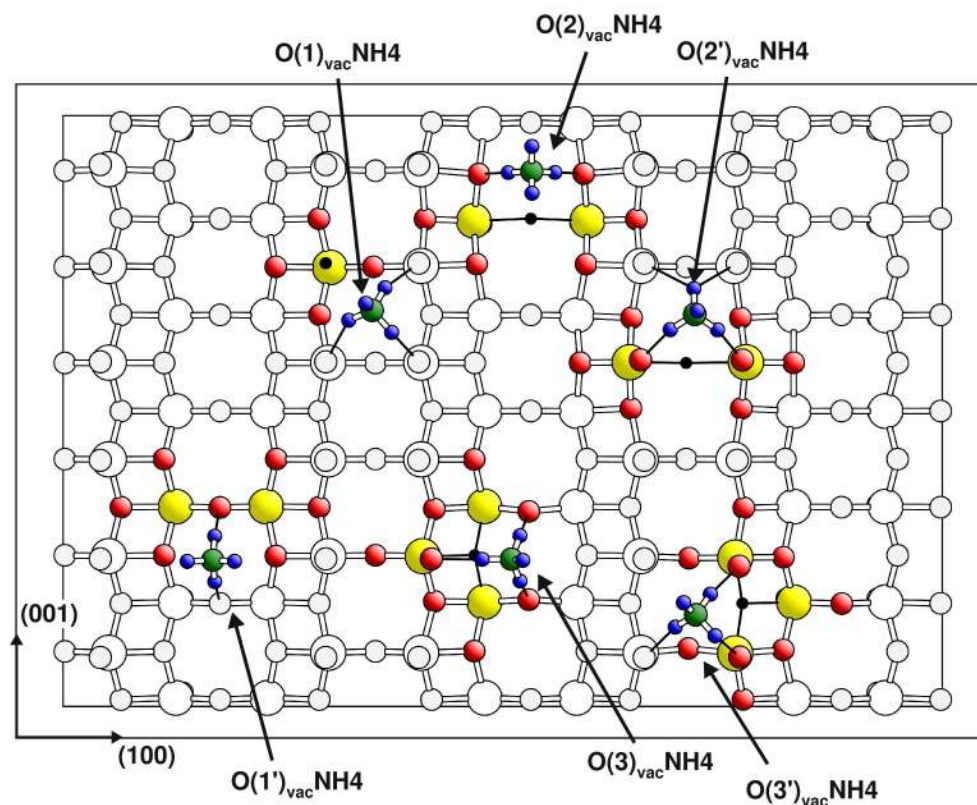


Figure 5.17: Equilibrium geometries of NH_4 adsorbed at the reduced $\text{V}_2\text{O}_5(010)$ surface. Vanadium centers are shown by large yellow balls, oxygen centers by red balls, nitrogen centers by green balls, and hydrogen centers by small blue balls. Surface atoms that are included in the optimization are emphasized with shading.

The NH_4 surface species near vacancy sites are highly positively charged. Hence they reduce the surface atoms as already found for adsorption at the perfect $\text{V}_2\text{O}_5(010)$ surface. NH_4 does not interact with the vanadium atoms, and as can be seen in Table 5.6b, there are only small changes for the atom charges of the vanadium atoms next to the vacancy sites after NH_4 adsorption.

For all stable configurations close to the vacancy sites, the adsorption energy is found to be smaller compared with those for the corresponding sites at the perfect surface. The NH_4 adsorption depends on the ability of the surface to accept negative charge and thus the formation of surface NH_4^+ . Obviously, this is not favored by surface pre-reduction, as it is the case for the oxygen vacancy formation.

5.3 Ammonia adsorption at $V_2O_5(010)$ surface, theory and experiment

This section compares the present results for ammonia adsorption at the $V_2O_5(010)$ surface with previous theoretical studies. After this, the experimental results of NH_3 adsorption will be discussed. Further, it will be shown how the results of this work, and especially the consideration of reduced adsorption sites, can help to interpret the experimental findings.

The adsorption of NH_3 at the perfect $V_2O_5(010)$ surface, and surface OH groups (Brønsted acid sites), has already been studied by theoretically [67-72]. The corresponding adsorption energies are presented in Table 5.7.

Table 5.7: Comparison of different theoretical results for ammonia adsorption at the perfect $V_2O_5(010)$ surface and at O(1)H groups forming surface NH_4 , adsorption energy E_{ads} (in [eV]). If no energy is quoted, no adsorption was observed.

Method	$E_{ads}(NH_3)$	$E_{ads}(NH_3/O(1)H)$
DFT (BP, V_2 cluster) ^[72]	--	-1.08
DFT (BLYP, periodic) ^[70]	-0.10	-1.19
MSINDO (large cluster) ^[68]	-0.33	-0.87
DFT (B3LYP, V_4/V_6 cluster) ^[67]	--	-1.14 / -1.37
DFT (B3LYP, V_2 cluster) ^[69]	--	-1.24
DFT (B3LYP, $V_2/V_6/V_{10}$ cluster) ^[71]	--	-0.60 / -1.11 / -1.23
DFT (RPBE, V_{14} cluster) ^[this work]	-0.26	-1.40

Ammonia was found to interact only weakly with the perfect $V_2O_5(010)$ surface. Only two studies find a stable configuration of NH_3 adsorbed at the vanadium site [68, 70]. They report that, in agreement with the present study, NH_3 adsorbs at a relatively large distance to the surface (2.28 Å [70] and 2.54 Å [68]), with very small adsorption energies.

All theoretical studies agree that ammonia binds strongly with surface OH groups, Brønsted sites, yielding surface NH_4^+ , where adsorption at a O(1)H group being energetically the most favorable [67-72]. The variation of the different adsorption energies presented in Table 5.7 is quite large (0.8 eV). Considering only the adsorption energies that have been calculated with DFT employing GGA or GGA-hybrid functionals and used reasonably large clusters or periodic models, yield a much smaller

variation for adsorption energies of 0.2 eV. Most of the researchers [67-70, 72] proposed a geometry with NH_4 on top of the O(1) ridge with two hydrogen atoms pointing toward two O(1) oxygen atoms identified in the present calculations as a saddle point (see Section 6.2). The structure found in the present work is in agreement with the work of Yuan et al. [71], where NH_4 sits on top of a square of four O(1) sites, with three hydrogen atoms pointing at the surface, and one pointing to the top (Section 5.1.4). The incorrect prediction of NH_4 adsorption can be explained by the fact that the underlying PES is very flat, thus the energy differences are very small. This will be discussed in detail in Section 6.2. On the other hand, two studies [69, 72], used only very small clusters $\text{V}_2\text{O}_x\text{H}_y$, that do not present a square of four neighboring vanadyl oxygen sites.

In contrast to previous theoretical studies, the present surface model is extended by including the reduced surface sites. The vanadium atom next to an oxygen vacancy representing a Lewis acid site becomes more reactive (see Section 5.2.2) compared to the perfect surface. The resulting adsorption energies of NH_3 at the $\text{O}(1)_{\text{vac}}$ and the $\text{O}(1')_{\text{vac}}$ sites are -0.87 eV and -1.24 eV, respectively, hence comparable to those at surface OH groups (Brønsted acid sites).

The experimental identification of surface species after ammonia adsorption on oxide surfaces is mainly based on interpretation of infrared (IR) spectroscopy data. An extensive experimental study of ammonia adsorption at different stages of dehydroxylation on various oxide surfaces suggested three different kinds of adsorbed ammonia species [167]:

- (i) Ammonia can bind via one of its hydrogen atoms towards a surface oxygen atom (or oxygen of a surface hydroxyl group).
- (ii) The nitrogen atom of ammonia can form a bond with the hydrogen atom of a surface hydroxyl group (Brønsted acid site). It is possible that during the adsorption, the proton is transferred, forming surface NH_4^+ species.
- (iii) Adsorbed NH_3 , the so called '*coordinated ammonia*', binds with the nitrogen atom to the electron-deficient metal atom center (Lewis acid site).

Further, Tsyganenko et al. [167] claim that, in addition, dehydrogenation of adsorbed NH_3 can take place resulting in surface NH_2 or NH and OH species.

The assignment of the different surface species is based on fundamental IR bands of ammonia, amine groups and ammonium ions as listed in Reference [167]. Most important for the analysis of NH_3 adsorption at the $\text{V}_2\text{O}_5(010)$ surface are the symmetric and asymmetric N-H bending modes δ_s and δ_{as} of NH_3 and NH_4^+ . The symmetric bending mode δ_s of NH_3 at 950 cm^{-1} [167] is the famous 'umbrella mode', in which the nitrogen atom oscillates through the plane of the three hydrogen atoms. If NH_3 adsorbs at a Lewis acid site (iii), the interaction with the nitrogen atom causes a

shift in the umbrella mode towards higher energies. Therefore, this mode can be used not only to identify adsorbed NH_3 , but the amount of the shift is also an indicator of the strength of the Lewis acid-base interaction. The asymmetric bending mode of NH_3 δ_{as} has an energy of 1628 cm^{-1} [167]. Surface NH_4^+ can be detected by the symmetric bending mode, δ_{s} at 1680 cm^{-1} , and the asymmetric mode, δ_{as} at 1400 cm^{-1} . The N-H stretching modes are not as useful for distinguishing between different surface species, because NH_3 , NH_4^+ , as well as NH_2 species, contain various modes in the energy region between 3040 cm^{-1} and 3400 cm^{-1} [167].

Infrared studies of the interaction of adsorbed ammonia with the $\text{V}_2\text{O}_5(010)$ surface [25, 26] found two different surface species, NH_3 adsorbed at Brønsted acid sites (i) and NH_3 adsorbed at Lewis acid sites (iii). The first part of Table 5.8 lists the measured values that have been interpreted as the δ_{s} and δ_{as} modes of surface NH_3 and NH_4^+ . The umbrella mode of adsorbed NH_3 is shifted by 300 cm^{-1} to higher energies, indicating strong interactions with the surface. Further, the study by Belokopytov et al. [25], as well as that of Ramis et al. [26], consider the adsorbed NH_3 species to be more stable since after heating up the sample to 393°K [25] or 423°K [26], the modes assigned to NH_4^+ disappeared, while those assigned to ammonia remained visible. Most of the experimental work, [17] (and references therein), was performed on supported V_2O_5 and V_2O_5 containing mixed-metal oxide catalysts, rather than on pure V_2O_5 material. However, the general findings, as discussed above, are rather similar. In addition to IR studies, NMR experiments [64] that have been performed for NH_3 adsorption at titania supported vanadia catalysts could confirm the existence of NH_3 and NH_4^+ surface species.

To compare the experimental and theoretical findings, vibration spectra for the different adsorbed NH_3 species were calculated. Table 5.8 shows a comparison of experimental results [25, 26], as well as the previous [69, 168] and present theoretical results. Beside the most stable configuration at the perfect surface, the two vacancy sites that are also found to interact strongly with NH_3 , the $\text{O}(1)_{\text{vac}}$ and the $\text{O}(1')_{\text{vac}}$, are considered. As seen for the NH_4 bending modes, the calculated frequencies for the NH_4 species at the perfect, and at the reduced $\text{V}_2\text{O}_5(010)$ surface, are very similar and in close agreement with the experiments. Thus, the theoretical IR spectra support the assignment of these bands to NH_4 species, but no conclusions as to a preference for a certain adsorption site can be drawn.

Table 5.8: Measured and calculated wave numbers for vibrations of NH_3 and NH_4^+ species in gas phase and at the $\text{V}_2\text{O}_5(010)$ surface (in $[\text{cm}^{-1}]$).

Modes	$\delta_s \text{NH}_3$	$\delta_{as} \text{NH}_3$	$\delta_s \text{NH}_4^+$	$\delta_{as} \text{NH}_4^+$
Experiment				
gas phase ^[167]	950	1628	1680	1400
$\text{V}_2\text{O}_5(010)$ ^[25]	1260	1620	--	1425
$\text{V}_2\text{O}_5(010)$ ^[26]	1249	1605	1680	1425
Calculated				
$\text{V}_2\text{O}_5(010)$ ^[168]	--	--	1663	1483
$\text{V}_2\text{O}_5(010)$ ^[69]	--	--	1528	1392
Present work				
gas phase	1066	1639 1640	1703 1704	1450 1451 1452
clean $\text{V}_2\text{O}_5(010)$	1111	1628 1635	1669 1694	1350 1439 1510
reduced $\text{V}_2\text{O}_5(010)$ near $\text{O}(1)_{\text{vac}}$	1232	1616 1649	1659 1692	1336 1446 1505
reduced $\text{V}_2\text{O}_5(010)$ above $\text{O}(1')_{\text{vac}}$	1226	1614 1619	1679 1698	1345 1461 1530

The asymmetric bending mode of NH_3 also undergoes only minor changes due to adsorption. It can be assigned to the weakly adsorbed species at the perfect surface, as well as to NH_3 adsorbed at the reduced vanadium sites near $\text{O}(1)_{\text{vac}}$ and $\text{O}(1')_{\text{vac}}$ sites. The symmetric umbrella mode shifts towards higher energies, because of the interaction with the Lewis site. The calculations also predict a shift in the umbrella mode for adsorbed NH_3 . Most importantly, NH_3 adsorbed at the perfect $\text{V}_2\text{O}_5(010)$ surface interacts weakly with the vanadium atom, and the shift in the resulting band at 1066 cm^{-1} is too low in energy. In contrast, for the two species adsorbed at the reduced sites, the shifts are larger and the IR bands, at 1232 cm^{-1} and 1226 cm^{-1} for NH_3 adsorbed at $\text{O}(1)_{\text{vac}}$ and $\text{O}(1')_{\text{vac}}$ respectively, are in extremely close agreement with the experiments.

Comparing theoretical and experimental results shows that the existence of a strongly adsorbed NH_4^+ species can be confirmed. However, no surface species consistent with adsorbed ammonia and clearly identified by experiment, has been found in theoretical studies at the perfect $\text{V}_2\text{O}_5(010)$ surface. Theoretical results can not explain the fact that adsorbed ammonia is more stable than surface NH_4^+ , nor can they explain the large shift of the NH_3 umbrella mode that has been found in experiment [25, 26]. Considering reduced surface sites, as modeled by the vanadium center close to an

$O(1)_{\text{vac}}$ or an $O(1')_{\text{vac}}$ site, could offer a possible explanation. Ammonia adsorbed at these reduced vanadium sites yields larger adsorption energies compared to the perfect surface. These energies are comparable to what has been found for ammonia adsorption at Brønsted acid sites. In addition NH_3 surface species near the reduced vanadium atoms show a strong shift of the umbrella mode, as suggested by experiments [25, 26].

6 Diffusion of adsorbates at the $V_2O_5(010)$ surface

In this chapter, the results for diffusion properties at the perfect $V_2O_5(010)$ surface are presented. Diffusion processes are important since they are implicitly involved in many surface reactions. For example, reactions that follow a Langmuir-Hinshelwood type mechanism [169] involve adsorbate diffusion processes. A surface that provides different adsorption sites may allow a molecule to initially bind not at the reactive site, but to diffuse to this site instead. In some cases, reaction sites may not be immediately accessible, but can be created through a combination of adsorption and diffusion processes.

Considering the SCR reaction, the diffusion properties of hydrogen are relevant for the water formation at the catalyst surface [17]. Further, hydrogen with its small mass can diffuse more easily compared to other adsorbates. In addition, the diffusion of NH_4 will be discussed. This is an interesting example since it adsorbs at the $V_2O_5(010)$ surface with strong electrostatic binding contributions. Moreover, hydrogen and NH_4 show large binding energies on the surface, implying that desorption and re-adsorption is hindered. However, since for both adsorbates, the binding energies at different adsorption sites are comparable, small diffusion barriers are possible. Therefore, explicit knowledge of diffusion paths and barriers is needed to describe reaction details.

The cluster models that have been used to describe the surface diffusion processes may need to be different from the ones that have been used in the previous chapter to investigate the adsorption properties (similar as discussed for vacancy diffusion in Section 4.3). This is necessary because the clusters, as well as the atoms that are considered in order to take surface relaxation into account, have to provide a good description for initial and final states and, at the same time, for the diffusion path itself. Depending on the specific diffusion process, it may be necessary consider more atoms to describe the surface relaxation, or even to use larger clusters. Different models can result in slightly different adsorption energies compared to the results of Chapter 5. These deviations and the details of the model clusters used to model surface diffusion are discussed in Appendix C.

6.1 Hydrogen diffusion and H₂O formation at the perfect V₂O₅(010) surface

The surface behavior of hydrogen is of special interest since hydrogen is involved in many catalytic reactions. The present results show that hydrogen can adsorb at all five surface oxygen sites with similar binding energies. In order to better understand (de)hydrogenation reactions of NH_x, which are important steps of the SCR reaction [17], it is interesting to examine whether hydrogen is anchored to the adsorption sites or whether it can also be mobile. In catalytic processes like the oxidation of hydrocarbons [150] or the reduction of NO with NH₃ [17], water is one of the reaction products. It has been shown experimentally that water can be formed with participation of surface oxygen from the catalyst [49, 50]. In a Langmuir-Hinshelwood type reaction this will also require diffusion of adsorbed hydrogen.

6.1.1 Hydrogen diffusion at the V₂O₅(010) surface

It has been shown in Section 5.1.1 that hydrogen cannot stabilize at vanadium sites. Hence, possible diffusion steps connect different oxygen sites. Figure 6.1 shows the perfect V₂O₅(010) surface and all hydrogen diffusion steps considered in this study. Based on its geometric properties, the V₂O₅(010) surface can be divided into three different regions which characterize corresponding to the diffusion energy barriers. These regions are the vanadyl double rows describing the O(1) ridge, the O(2) valley between the double rows, and the transition region between ridge and valley. Numerical results for the diffusion barriers obtained in this work are listed in Table 6.1. In the following, the corresponding diffusion paths will be discussed in detail.

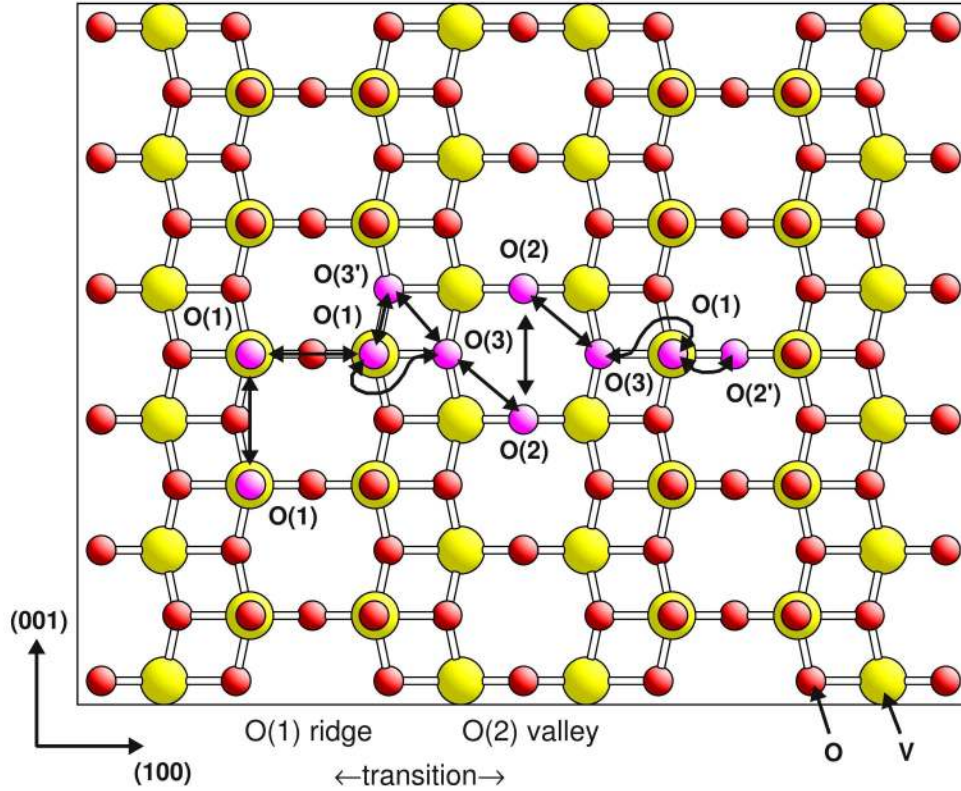


Figure 6.1: Hydrogen diffusion steps at the perfect $V_2O_5(010)$ surface. Vanadium centers are shown by large yellow balls, oxygen centers by red balls, and oxygen centers connected by diffusion steps by magenta balls.

Table 6.1: The energy difference between initial and final state E_{diff} and the energy barriers $E_{\text{barr}}^{1,2}$, for hydrogen diffusion between different oxygen sites at the $V_2O_5(010)$ surface layer (in [eV]).

Diffusion step		E_{diff}	$E_{\text{barr}}^1 \rightarrow$	$E_{\text{barr}}^2 \leftarrow$
(i) ridge region	O(1) \leftrightarrow O(1) in (001) direction	0.00	0.43	0.43
	O(1) \leftrightarrow O(1) in (100) direction	0.00	0.16	0.16
	O(1) \leftrightarrow O(2')	0.07	1.14	1.08
(ii) transition region	O(1) \leftrightarrow O(3')	0.25	1.25	1.00
	O(3') \leftrightarrow O(3)	-0.19	1.34	1.52
	O(1) \leftrightarrow O(3)	0.11	1.20	1.09
(iii) valley region	O(3) \leftrightarrow O(2)	-0.20	0.64	0.83
	O(2) \leftrightarrow O(2)	0.00	0.80	0.80

6.1.1.1 Hydrogen diffusion on the vanadyl ridge

Two diffusion processes between neighboring O(1) sites at the vanadyl ridge are possible: diffusion between O(1) neighbors along ((001) direction) or perpendicular to the ridge ((100) direction). Both processes are qualitatively similar. The VO(1) group with the vanadyl oxygen can tilt easily in all directions. This is exactly what happens during the hydrogen transfer. In the transition state configuration, the two oxygen atoms tilt towards each other and a planar O-H-O bridge is formed (Figure 6.2). In both cases, the O-O distance is shortened from 3.63 Å to 2.44 Å (for (001) diffusion), and from 3.07 Å to 2.43 Å (for (100) diffusion), with the hydrogen atom sitting in the middle. For diffusion parallel to the vanadyl rows, the hydrogen also rotates about the (010) axis by about 90° which consumes very little energy and does not affect the overall diffusion energetics. This means that instead of breaking a separate OH bond, the hydrogen transfer can be established via the O-H-O bridge formation at the transition state. Because the vanadyl oxygen atoms are easy to tilt, the resulting diffusion barriers, $E_{\text{barr}} \leq 0.43$ eV, are very small compared to the adsorption energies at the O(1) site, $E_{\text{ads}}(\text{O}(1)) = -2.64$ eV, (Table 6.1 and Table 5.1). As will be shown for the remaining diffusion steps, the formation of an O-H-O bridge configuration at the transition state is a general characteristic of hydrogen diffusion. Hence, the mobility of the participating oxygen determines the diffusion energy barriers to a large extent.

Alternatively to diffusion between O(1) sites, hydrogen can also transfer to the O(2') site. In contrast to the two previous symmetric diffusion paths, here the O-H-O bridge that is formed at the transition state is asymmetric with corresponding O(1)-H and O(2')-H distances, $d(\text{O}(1)\text{-H}) = 1.22$ Å and $d(\text{O}(2')\text{-H}) = 1.33$ Å (Figure 6.2). Moreover, the bridge is not planar but bent by an angle of 43°. The O(2') site is less mobile compared to O(1) oxygen yielding larger energy barriers, $E_{\text{barr}}^1 = 1.14$ eV (O(1) → O(2')) and $E_{\text{barr}}^2 = 1.08$ eV (O(2') → O(1)). This indicates that hydrogen will more likely diffuse along the O(1) sites. Further, these results are interesting in regards to hydrogen adsorption at the O(2') site itself. If the hydrogen is adsorbing at the O(1) site beforehand, it has to overcome quite a large barrier to reach the O(2') site. However, the barrier for the reverse process E_{barr}^2 is also large, hindering the immediate transformation back into an O(1)H group if hydrogen reaches the O(2') site.

Under the vanadyl oxygen rows, hydrogen can diffuse between the O(2') and the O(3') sites. It was not possible to evaluate a converged diffusion path that directly connects these two sites.

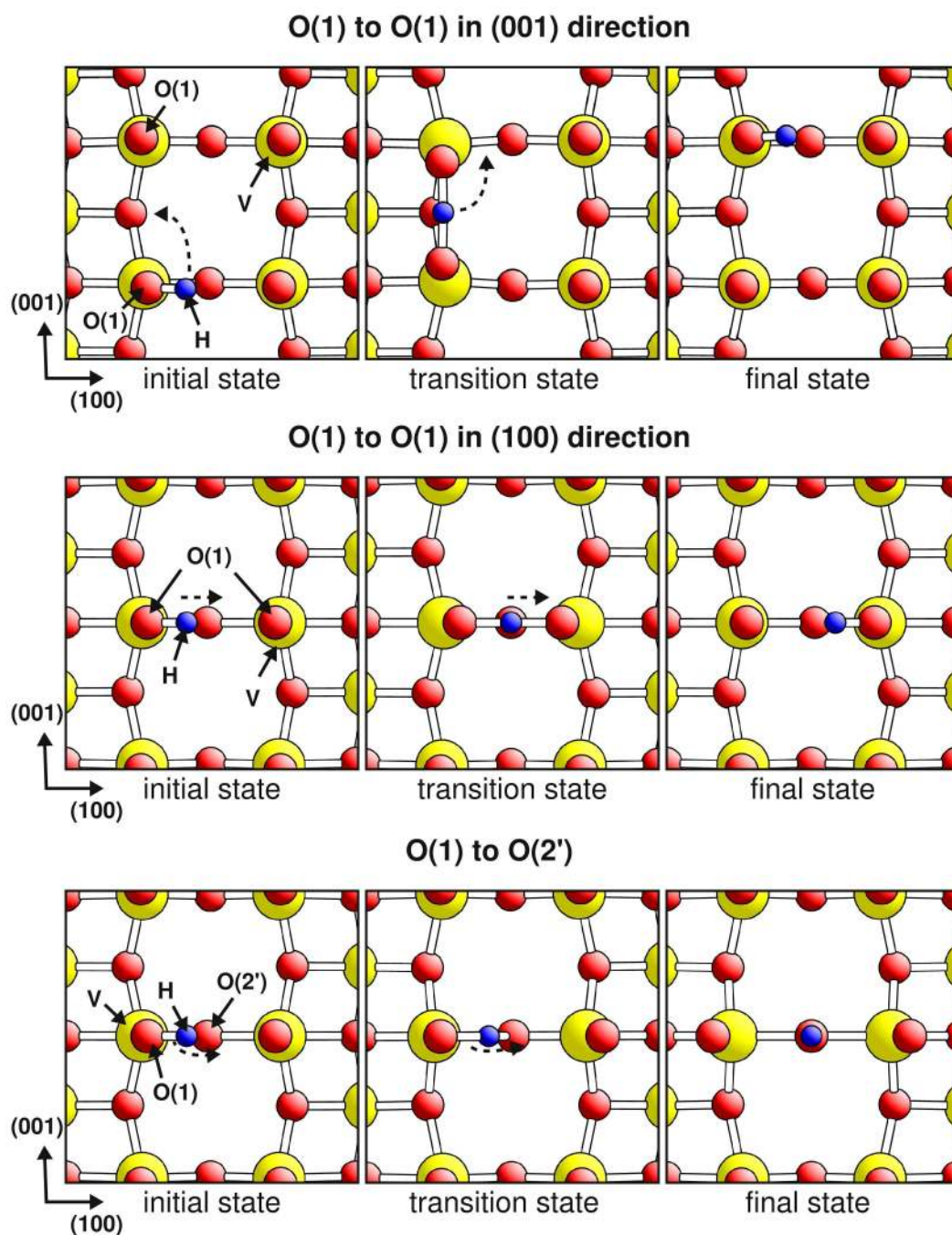


Figure 6.2: Initial, transition and final states for hydrogen diffusion at the O(1) ridge region. Vanadium centers are shown by large yellow balls, oxygen centers by red balls, and hydrogen centers by small blue balls.

6.1.1.2 Hydrogen diffusion between ridge and valley

Two different diffusion paths for hydrogen transfer from the O(1) ridge into the O(2) valley between adjacent O(1) double rows have been considered. First, diffusion from the O(1) to the O(3') site, and in a subsequent step, to the O(3) site in the valley. Alternatively, hydrogen can rotate and diffuse directly to the O(3) site (Figure 6.1).

In the two-step path at the beginning, hydrogen diffuses from the O(1) to the O(3') site. The O(3') oxygen is coordinated to three vanadium atoms and thus is less flexible than O(1). Further, the geometry of hydrogen adsorbed at the O(3') site includes strong relaxation of atom neighbors. The O(3') oxygen gets drawn out of the surface and the neighboring vanadyl groups open with respect to each other (see Section 5.1.1). As before, hydrogen diffusion results in the two participating oxygen atoms forming an O-H-O bridge at the transition state, with similar O-H distances like those found for hydrogen diffusion between O(1) sites, $d(\text{O}(1)\text{-H}) = 1.24 \text{ \AA}$ and $d(\text{O}(3')\text{-H}) = 1.28 \text{ \AA}$. The bridge formed by the two OH bonds is bent by 41° (Figure 6.3). The energy barriers $E_{\text{barr}}^1 = 1.25 \text{ eV}$ and $E_{\text{barr}}^2 = 1.00 \text{ eV}$, are comparable to what has been found for diffusion between the O(1) and the O(2') site (Table 6.1). To complete the transition between ridge and valley, a second diffusion step is necessary where the hydrogen diffuses from the O(3') to the O(3) site (Figure 6.1). The process follows the same pattern found for the previous steps, i.e., the formation of an O-H-O bridge configuration at the transition state (Figure 6.3), with corresponding O(3')-H and O(3)-H distances, $d(\text{O}(3')\text{-H}) = 1.24 \text{ \AA}$ and $d(\text{O}(3)\text{-H}) = 1.23 \text{ \AA}$, and a bend angle of 51° . The evaluated energy barriers, $E_{\text{barr}}^1 = 1.34 \text{ eV}$ and $E_{\text{barr}}^2 = 1.52 \text{ eV}$, are the largest that have been found for the different diffusion steps (Table 6.1). This can be understood as a combination of three effects. First, both participating oxygen atoms are coordinated to three vanadium atoms, second, the configuration of hydrogen adsorbed at O(3') is accompanied by large atom displacements, and third, the hydrogen atom has to be transferred along the densest part of the crystal.

Considering adsorption at the O(3') site, this result shows that if the hydrogen reacts beforehand with the more exposed neighboring O(1) or O(3) sites, it has to overcome large barriers to reach the O(3') site. This indicates that the O(3') sites may not be easily accessible to hydrogen adsorption. However, due to the stability of O(3')H groups, it has been found that the energy barriers for diffusion from the O(3') atom to the neighboring oxygen sites are large as well.

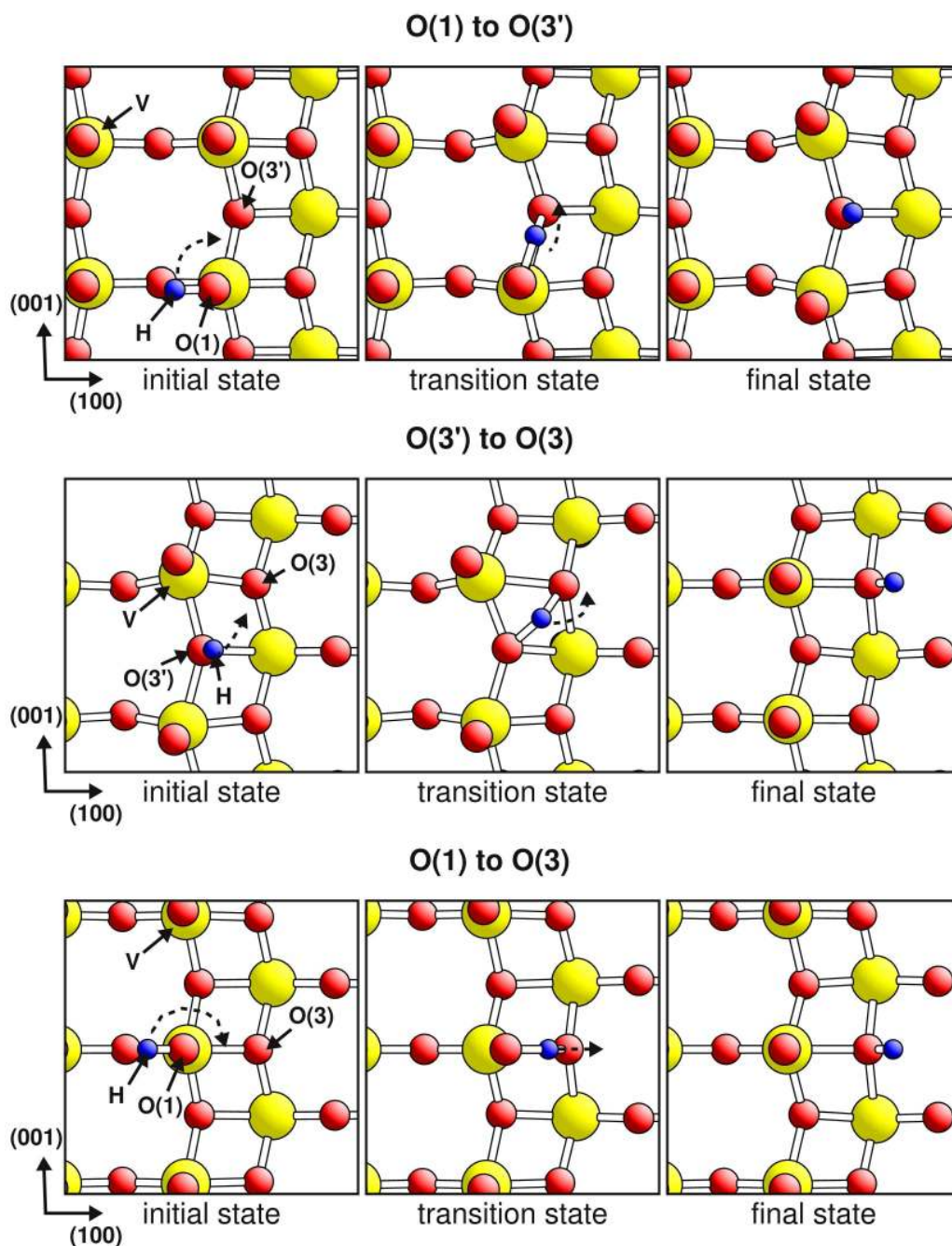


Figure 6.3: Initial, transition and final states for hydrogen diffusion steps connecting the O(1) ridge with the O(2) valley. Vanadium centers are shown by large yellow balls, oxygen centers by red balls, and hydrogen centers by small blue balls.

The diffusion process from O(1) to O(3) can be divided into two parts, although it contains only one transition state, see Figure 6.3. First, the hydrogen atom rotates about the (010) axis until it points in the direction of the O(3) site. This motion requires only minimal energy. The second part of this diffusion step is similar to the previous diffusion steps, with an O-H-O bridge formed at the transition state. There the O-H distances are $d(\text{O}(1)\text{-H}) = 1.25 \text{ \AA}$ and $d(\text{O}(3)\text{-H}) = 1.28 \text{ \AA}$. The two OH bonds form an angle 37° . The diffusion barriers, $E_{\text{barr}}^1 = 1.20 \text{ eV}$ and $E_{\text{barr}}^2 = 1.09 \text{ eV}$ are slightly smaller than for the diffusion path via the O(3') site.

6.1.1.3 Hydrogen diffusion in the valley

The O(2) valley contains bridging oxygen in its center and O(3) oxygen at the border (Figure 6.1). There, two diffusion steps have been considered. First, hydrogen transfer from the O(3) site to the O(2) site, and second, hydrogen transfer between two neighboring O(2) sites.

The diffusion from the O(3) to the O(2) site proceeds over an O(3)-H-O(2) bridge (see Figure 6.4). with distances $d(\text{O}(3)\text{-H}) = 1.24 \text{ \AA}$ and $d(\text{O}(2)\text{-H}) = 1.25 \text{ \AA}$. The energy barriers, $E_{\text{barr}}^1 = 0.64 \text{ eV}$ and $E_{\text{barr}}^2 = 0.83 \text{ eV}$ are significantly smaller compared to the other diffusion steps that involve triply coordinated oxygen.

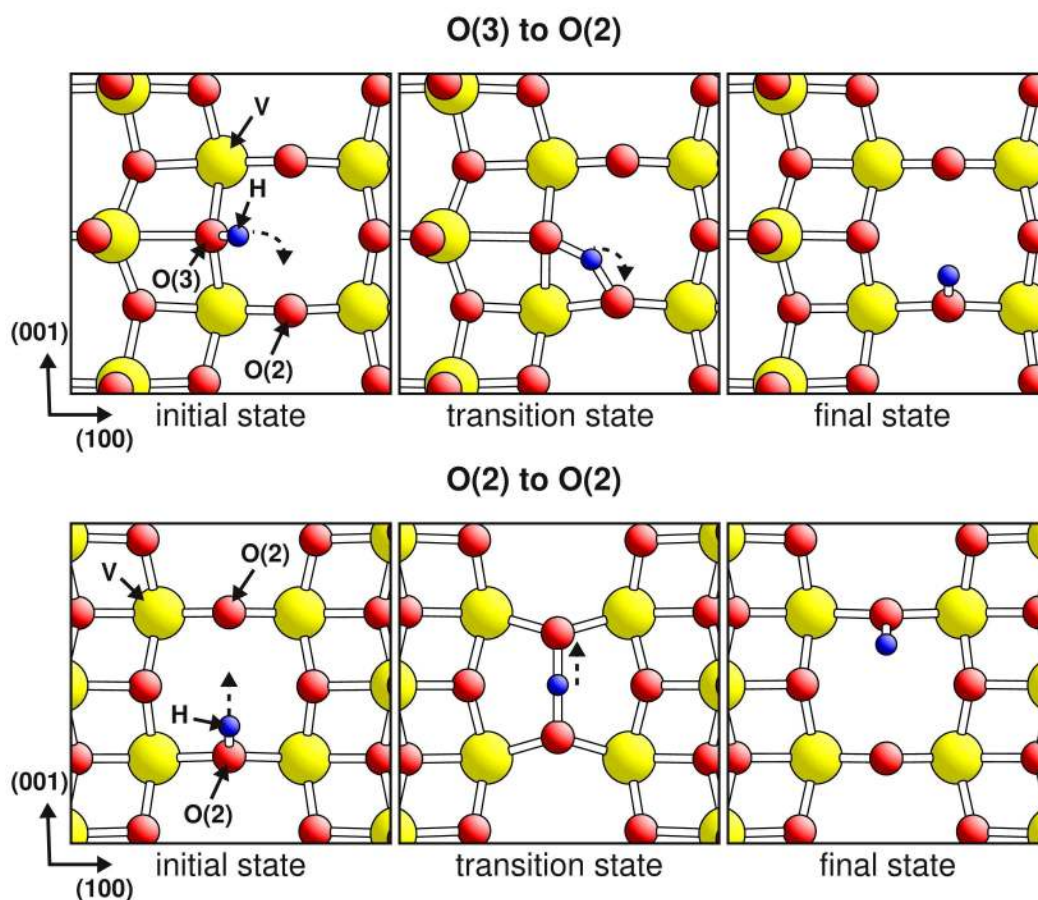


Figure 6.4: Initial, transition and final states for hydrogen diffusion steps in the O(2) valley. Vanadium centers are shown by large yellow balls, oxygen centers by red balls, and hydrogen centers by small blue balls.

The transition state for the hydrogen transfer between two bridging oxygen atoms is a straight symmetric O(2)-H-O(2) bridge configuration with the hydrogen atom sitting in the middle (Figure 6.4). The O-O distance gets shortened from 3.49 \AA to 2.53 \AA . The energy barriers, $E_{\text{barr}}^{1,2} = 0.80 \text{ eV}$ are larger than for O(1) to O(1) diffusion, which indicates that the distortion of the participating O(2) atoms during the diffusion consumes more energy than the tilt of the VO(1) groups.

In conclusion, all diffusion steps for hydrogen at the $V_2O_5(010)$ surface follow the same pattern. The hydrogen transfer occurs via formation of an O-H-O bridge at the transition state. In all cases, the O-H distances of this bridge are between 1.2 Å and 1.3 Å. All barriers are significantly smaller in comparison to the hydrogen adsorption energies, see Table 6.1 and Table 5.1. The size of the diffusion barriers depends on the flexibility of the oxygen atoms that are involved. This flexibility directly correlates with the density of the crystal structure. Thus, the diffusion can be grouped into three regions: the O(1) ridges, the O(2) valleys, and the transition region connecting the two. At the ridges, the O(1) oxygen is very flexible and thus easy to tilt. Therefore, the diffusion barriers are very small, with values between 0.16 eV and 0.43 eV. For diffusion through the transition region between ridge and valley, the surface has to distort much more, due to the denser packing of oxygen and vanadium atoms. As a result, the diffusion barriers in the transition region are higher than on the ridge. In the valley region between the ridges, the formation of an O-H-O bridge results in more costly distortions during the diffusion process compared with ridge diffusion. Therefore, the diffusion barriers are larger compared with barriers for ridge diffusion. However, they are smaller than for diffusion in the transition region.

6.1.2 H_2O formation at the $V_2O_5(010)$ surface

For many oxidation reactions on VO_x containing catalysts, a Mars van Krevelen type mechanism [57] is proposed which includes oxygen vacancy formation and re-oxidation by molecular oxygen. This is also the case for the selective catalytic reduction (SCR) of NO by ammonia. Here water can be formed also with oxygen from the catalyst surface as shown by isotopic labeling studies [49, 50]. Since hydrogen is rather mobile at the surface the question arises whether two neighboring hydrogen atoms can form a surface water species that further desorbs from the surface.

The simulations of surface H_2O formation start with two hydrogen atoms adsorbed at neighboring O(1) oxygen sites (Figure 6.5). Since the water desorption results in an oxygen vacancy, it is necessary for the simulations to use a vanadium oxide substrate cluster, which includes two physical layers. For a detailed description for the cluster model used to describe the surface H_2O formation, see Appendix C.

The energy barriers for the reaction $HO(1) + HO(1) \leftrightarrow H_2O(1) + O(1)$ are shown in Table 6.2. Surface water is 0.07 eV more stable than two neighboring OH groups at the surface. The water formation by hydrogen diffusion from an OH group to the neighboring OH group is similar to diffusion between two O(1) sites discussed in the previous section. Analogously, in the transition state configuration, an O-H-O bridge is formed. The corresponding O(1)-O(1) distance is 2.47 Å, and the O(1)-H distances amount to 1.15 Å and 1.33 Å, respectively, where the smaller distance refers to the

oxygen atom that loses the hydrogen atom. The barrier for surface water formation E_{barr}^1 amounts to 0.34 eV, which is close to what has been found for the diffusion energy barriers along the O(1) ridge.

Table 6.2: The energy difference between initial and final state E_{diff} and the energy barriers $E_{\text{barr}}^{1,2}$, for H₂O formation from two adjacent O(1)H groups and H₂O desorption energy ($=E_{\text{diff}}$) at the V₂O₅(010) surface layer (in [eV]).

H ₂ O formation / desorption	E_{diff}	$E_{\text{barr}}^1 \rightarrow$	$E_{\text{barr}}^2 \leftarrow$
$2 \times \text{O}(1)\text{H} \leftrightarrow \text{H}_2\text{O}(1) + \text{O}(1)$	-0.07	0.34	0.41
$\text{H}_2\text{O}(1) \leftrightarrow \text{H}_2\text{O}_{\text{gas phase}} + \text{O}(1)_{\text{vac}}$	0.44	--	--

Another interesting aspect of the surface water formation is the relaxation of the neighboring atoms. As discussed in Section 5.1.1, hydrogen adsorption is accompanied by an elongation of the V-O(1) bond, but this affects the position of the vanadium atom itself only slightly. By adding another hydrogen atom to the O(1)H group, the connected V-O(1) bond is weakened further as indicated by the bond length, $d(\text{V-O}(1)) = 1.81 \text{ \AA}$ in the initial state (two neighboring O(1)H groups), and $d(\text{V-O}(1)) = 2.29 \text{ \AA}$ in the final state (surface H₂O(1) group). As a result of this bond weakening, the vanadium atom couples with the lower-lying O(1) oxygen atom, and moves towards the second layer. The distance to the O(1) of the lower layer reduces from $d(\text{V-O}(1)_{\text{second layer}}) = 2.88 \text{ \AA}$ (initial state) to $d(\text{V-O}(1)_{\text{second layer}}) = 1.93 \text{ \AA}$ (final state). This is similar to what has been found for the O(1) vacancy formation, where as a result of the missing O(1) oxygen, the connected vanadium atom forms a bond with the O(1) site of the lower layer, see Section 4.2.1.

The coupling is also apparent in the atom charge of the vanadyl oxygen from the lower layer. For the configuration with two separate O(1)H groups, it is -0.64 au, thus, almost the same as found for vanadyl oxygen in the perfect crystal, -0.62 au, (see Table 4.4). Transferring the hydrogen causes an increase of the negative charge of the vanadyl oxygen from the lower layer under the surface H₂O to -0.84 au, which is close to the findings for the corresponding oxygen atom in the vacancy cluster, -0.87 au (see Table 4.5).

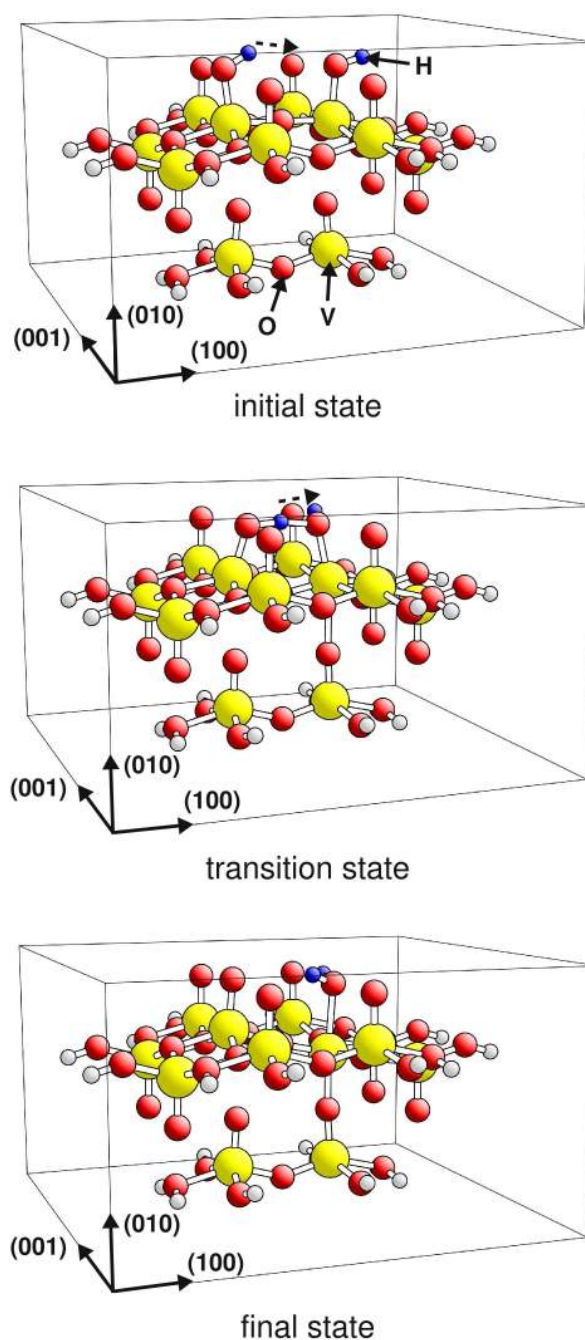


Figure 6.5: Initial, transition and final state for H_2O formation. Vanadium centers are shown by large yellow balls, oxygen centers by red balls, hydrogen centers by small blue balls, and saturation hydrogen by small light gray balls.

When surface water is formed, it can either dissociate into two OH groups or desorb from the surface, leading to an O(1) vacancy. The barrier for dissociation, 0.41 eV, is close to the calculated desorption energy of surface water, 0.44 eV, (see Table 6.2). Thus, from an energetic perspective, both processes are likely to occur. Further, the surface water desorption energy is found to be significantly smaller compared with the vacancy formation energy obtained for the O(1) site ($E_D^f(O(1)) = 4.98$ eV (see

Table 4.5). Obviously, pre-adsorbed hydrogen forming surface OH and H₂O groups can facilitate vacancy formation successively.

Surface water formation has also been investigated by Fu and colleagues as part of a theoretical study of propane oxidative dehydrogenation [170]. They found that surface water formation is a barrier-free process and that the desorption energy of surface water is 0.56 eV. The energy barriers found for hydrogen diffusion, water formation and desorption at the O(1) ridges in this work are weaker than 0.44 eV. Despite these differences, both results lead to the same conclusion: The weak energy barriers support water formation. This could explain that water formed with surface oxygen of the catalyst is observed during the SCR reaction [49, 50].

6.2 NH₄ diffusion at the perfect V₂O₅(010) surface

NH₄ can bind at many different surface sites, with fairly large adsorption energies as discussed earlier in Section 5.1.4. Therefore, diffusion via desorption and re-adsorption seems unfavorable. Similar to adsorbed hydrogen, the adsorption energies at different sites of the V₂O₅(010) surface are in the same range such that from an energetic point of view, diffusion may be easy. Again, the surface can be divided into three different regions: (i) the O(1) ridge, (ii) the O(2) valley, and (iii) the transition region connecting ridge and valley. The different diffusion steps considered in this work are shown in Figure 6.6. The corresponding diffusion energy barriers are listed in Table 6.3. The cluster models used for NH₄ diffusion are discussed in Appendix C.

Table 6.3: The energy difference between initial and final state E_{diff} and the energy barriers $E_{\text{barr}}^{1,2}$, for NH₄ diffusion between different adsorption sites at the V₂O₅(010) surface layer (in [eV]).

Diffusion step		E_{diff}	$E_{\text{barr}}^1 \rightarrow$	$E_{\text{barr}}^2 \leftarrow$
(i) ridge region	O(1) ↔ O(1) tumble	0.00	0.17	0.17
	O(1) ↔ O(1) twist	0.001	0.002	0.001
(ii) transition region	O(1) ↔ V	0.26	0.30	0.04
(iii) valley region	V ↔ O(2)	0.07	0.14	0.07
	O(2) ↔ O(2')	0.00	0.10	0.10

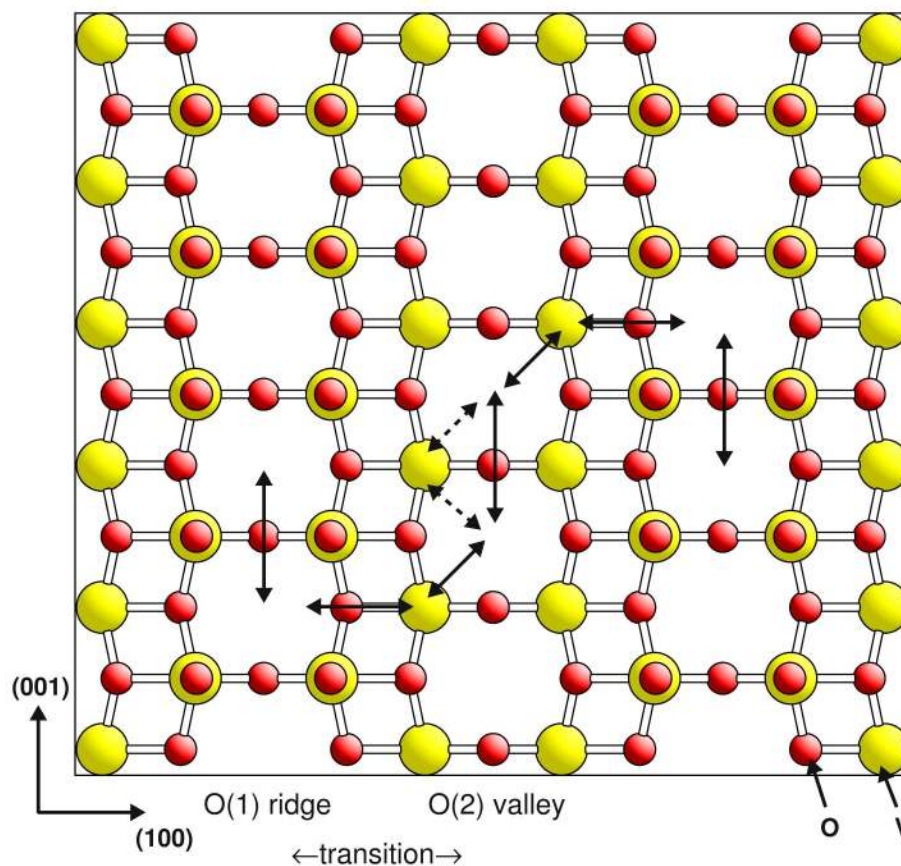


Figure 6.6: NH_4 diffusion steps at the perfect $\text{V}_2\text{O}_5(010)$ surface. Vanadium centers are shown by large yellow and oxygen centers by red balls.

6.2.1 NH_4 diffusion on the vanadyl ridge

The optimized diffusion paths for NH_4 indicate a fairly simple mechanism. Here, two diffusion steps are necessary to describe diffusion along the vanadyl double rows. In the first step, NH_4 tumbles – with its two hydrogen atoms pointing towards two vanadyl oxygen – from one square of vanadyl oxygen to the other, see Figure 6.7. The energy barrier for tumbling to the next O(1) square is very small, $E_{\text{barr}} = 0.17$ eV. Interestingly, the geometry of the transition state, with the NH_4 on top of two vanadyl oxygen sites, is exactly the configuration declared the minimum for NH_4 adsorption on top of the O(1) site by various theoretical studies (see Section 5.3). To enable tumbling into the next O(1) square, the NH_4 molecule has to be rotated (twisted) by 60° . This is achieved by two 30° rotations (see Figure 6.8). As seen in Table 6.3, the corresponding rotation barrier is almost zero. Thus, the combined tumble-twist propagation results in a overall energy barrier of only 0.17 eV for diffusion along the O(1) ridge, which has to be compared with the strong adsorption energy of NH_4 at the surface amounting to -3.90 eV.

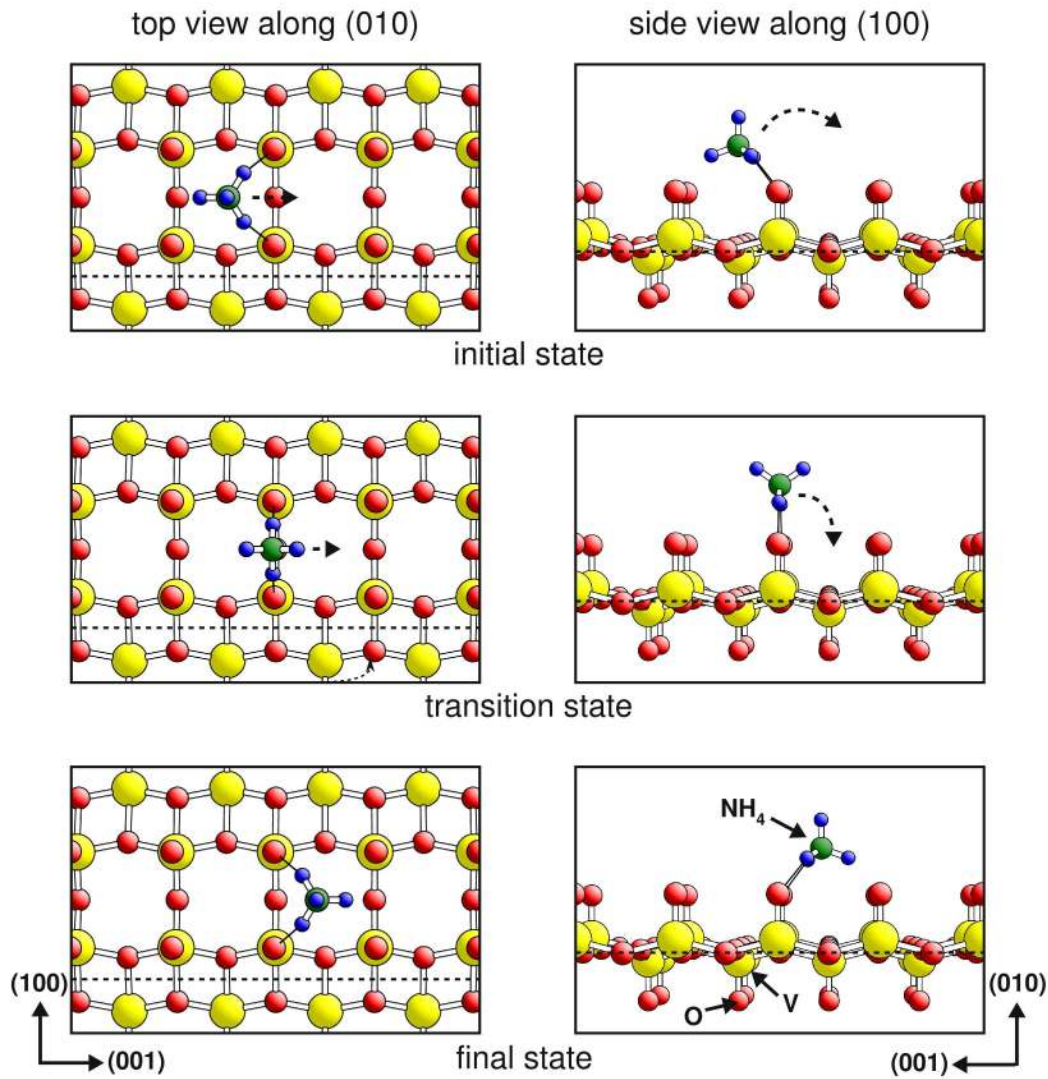


Figure 6.7: Initial, transition and final state for NH_4 'tumble' diffusion step along the $O(1)$ ridge. Vanadium centers are shown by large yellow balls, oxygen centers by red balls, nitrogen centers by green balls, and hydrogen centers by small blue balls.

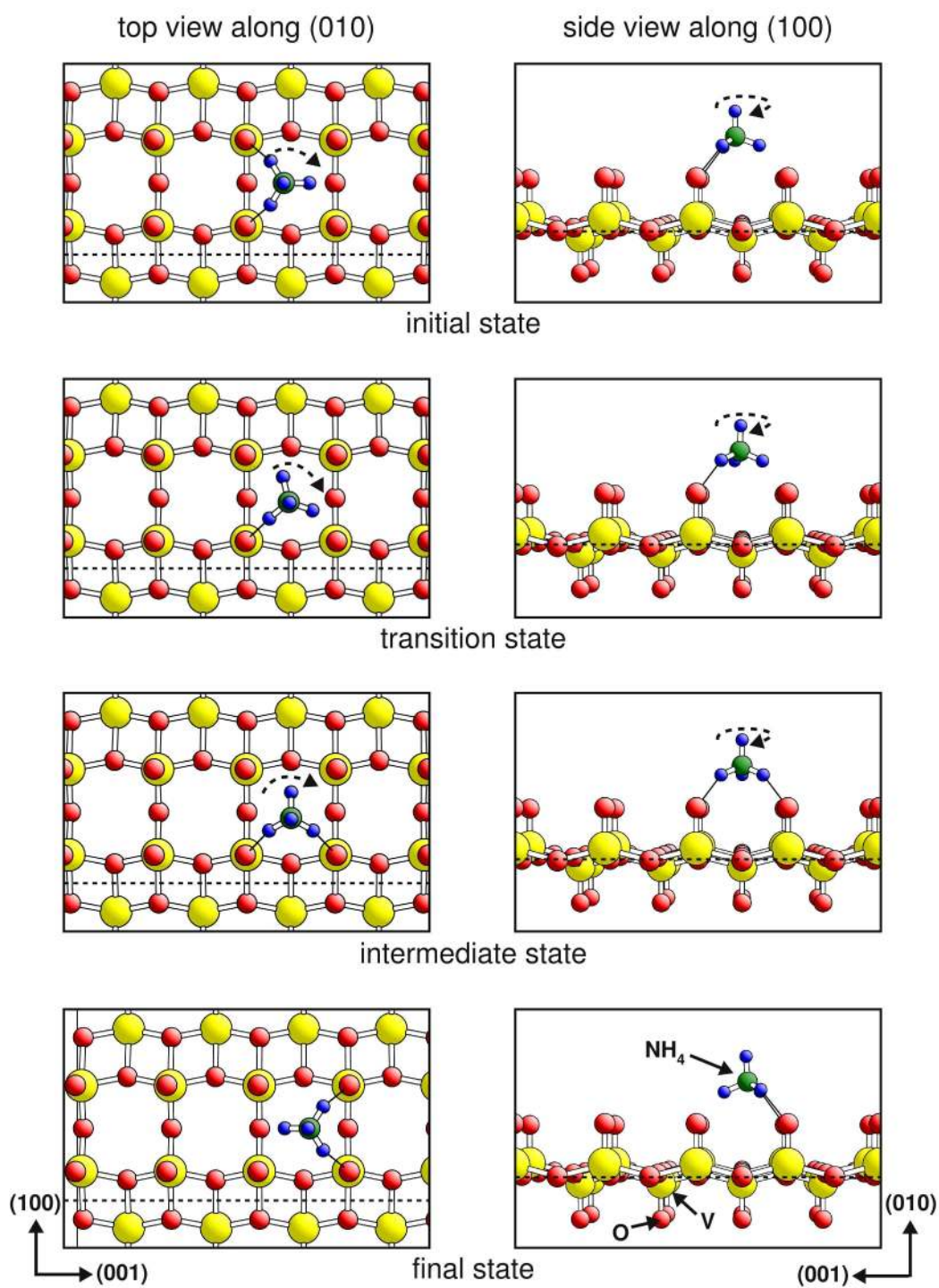


Figure 6.8: Initial, transition and final state for NH_4 'twist' diffusion step along the $O(1)$ ridge. Vanadium centers are shown by large yellow balls, oxygen centers by red balls, nitrogen centers by green balls, and hydrogen centers by small blue balls.

6.2.2 NH_4 diffusion between ridge and valley

Instead of tumbling towards the neighboring square along the O(1) ridge, it is also possible to tumble into the valley (Figure 6.9). Tumbling between the O(1) square to the V site yields barriers of $E_{\text{barr}}^1 = 0.30$ eV and $E_{\text{barr}}^2 = 0.04$ eV.

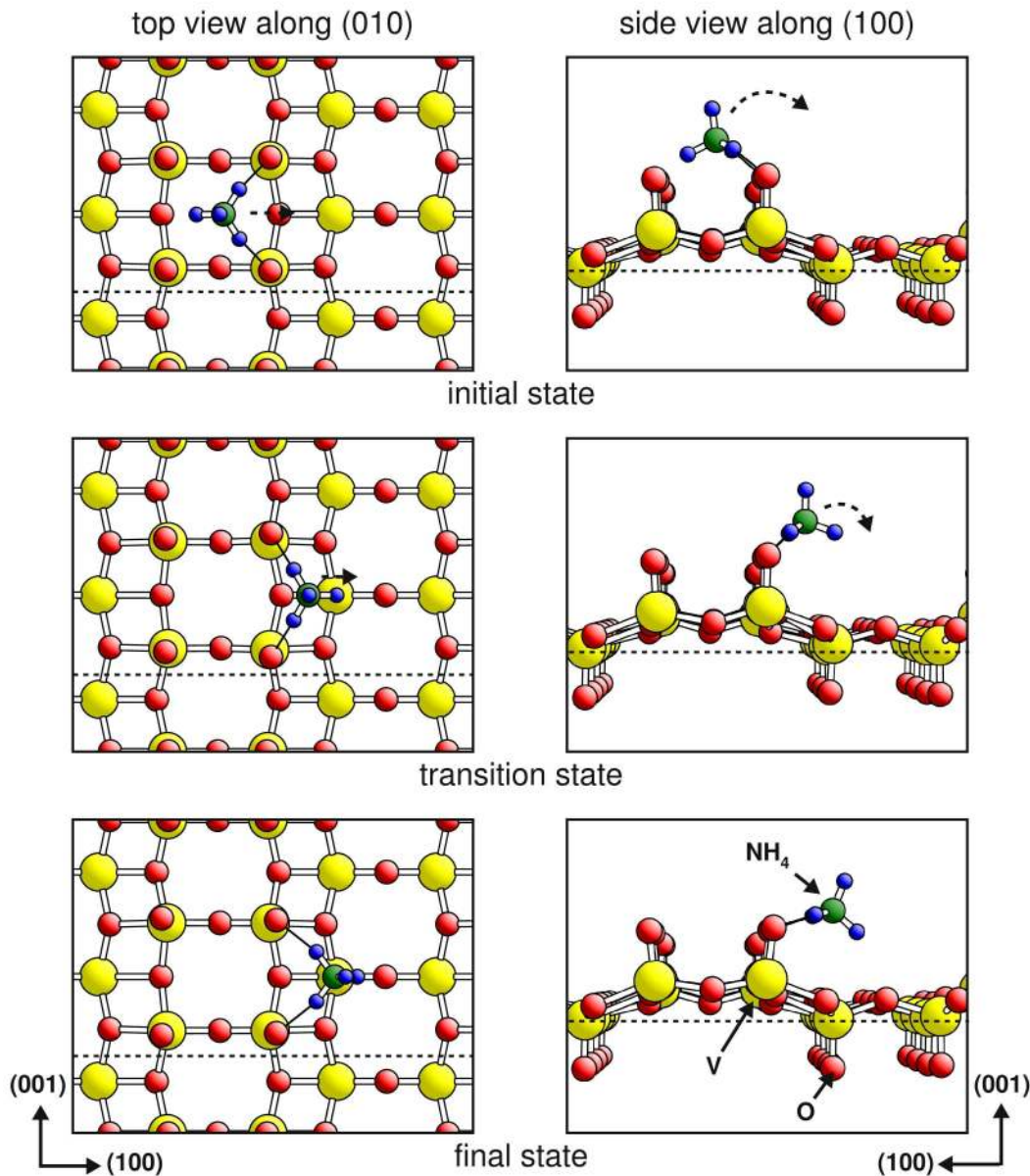


Figure 6.9: Initial, transition and final state for NH_4 diffusion step from the O(1) to the V site. Vanadium centers are shown by large yellow balls, oxygen centers by red balls, nitrogen centers by green balls, and hydrogen centers by small blue balls.

6.2.3 NH_4 diffusion in the valley

Here, two possible diffusion paths have been identified. The NH_4 molecule can diffuse directly along the bridging $\text{O}(2)$ rows, and it can diffuse from the V site to $\text{O}(2)$ site.

The optimized path for direct diffusion between bridging $\text{O}(2)$ species is shown in Figure 6.10. It can be described by a tumble-twist motion analogous to that found for ridge diffusion. NH_4 tumbles from two $\text{O}(2)$ on top of one $\text{O}(2)$ combined with a simultaneous twist of 30° . This is followed by NH_4 tumbling down to the other side of the $\text{O}(2)$, combined with another 30° twist to connect with the next two $\text{O}(2)$ atoms. The calculated energy barrier for this diffusion step is very weak, $E_{\text{barr}} = 0.1 \text{ eV}$.

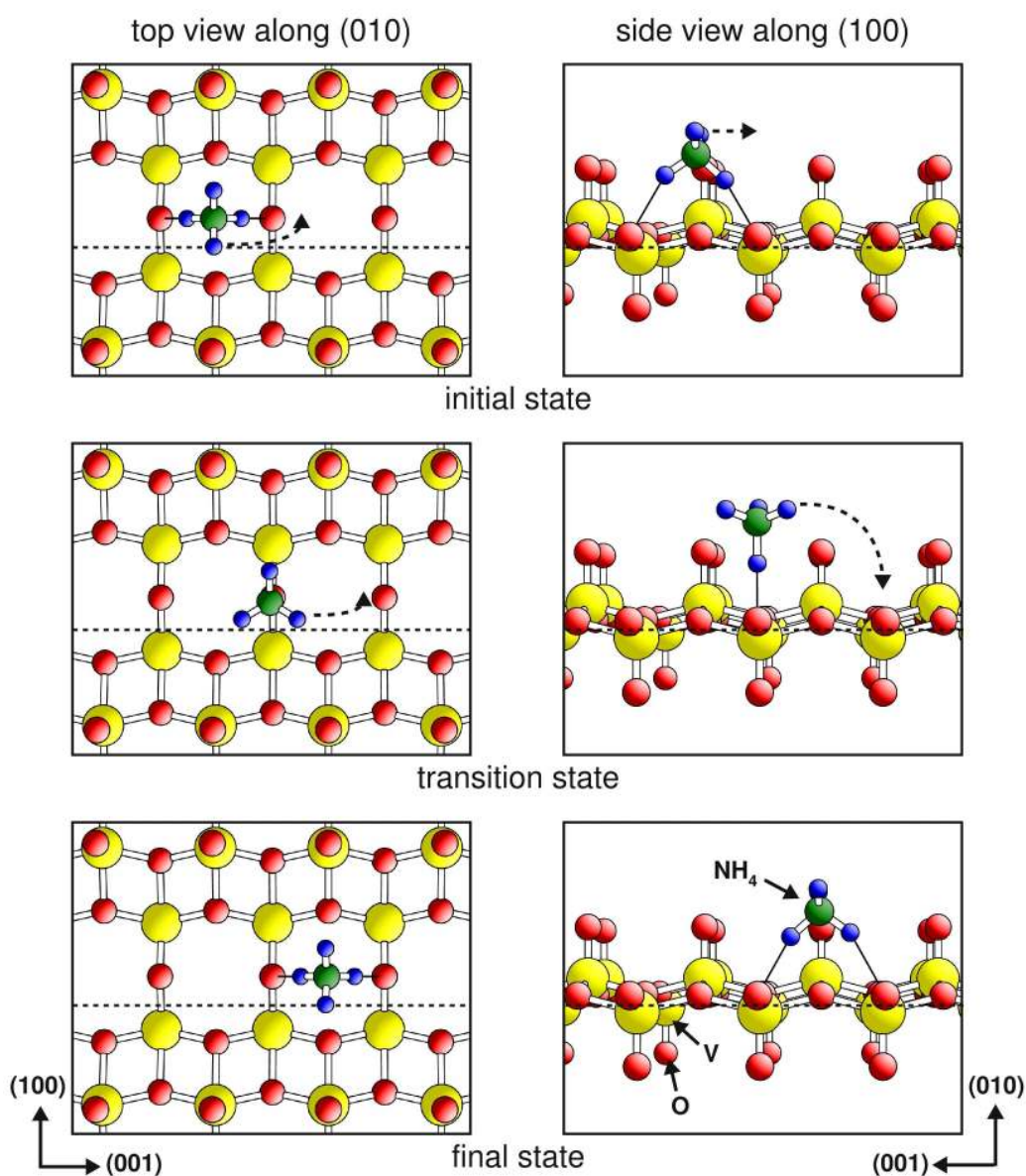


Figure 6.10: Initial, transition and final state for NH_4 diffusion step from $2 \times \text{O}(2)$ to the next $2 \times \text{O}(2)$ site. Vanadium centers are shown by large yellow balls, oxygen centers by red balls, nitrogen centers by green balls, and hydrogen centers by small blue balls.

Diffusion of NH_4 from vanadium near the ridge to O(2) in the valley is shown in Figure 6.11. Here, the molecule twists and moves towards the O(2) oxygen in a combined step. In agreement with previous diffusion steps, the energy barriers that must be overcome are rather weak, $E_{\text{barr}}^1 = 0.14 \text{ eV}$ and $E_{\text{barr}}^2 = 0.07 \text{ eV}$ (Table 6.3). Thus, combining diffusion steps V site \rightarrow O(2) site and O(2) site \rightarrow V site, it is possible to move the NH_4 molecule through, as well as along the valley.

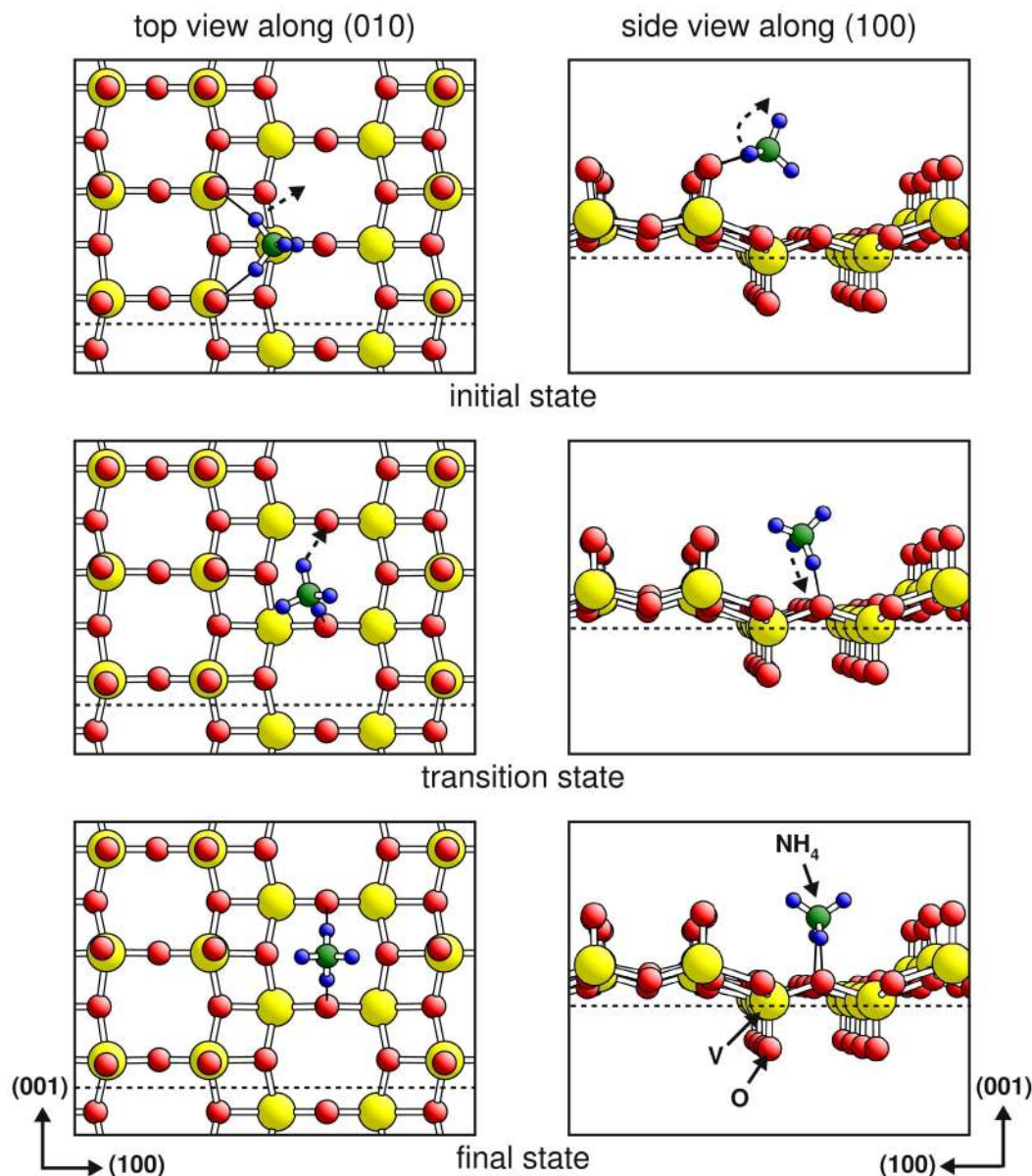


Figure 6.11: Initial, transition and final state for NH_4 diffusion step from the V to the $2x\text{O}(2)$ site. Vanadium centers are shown using large yellow balls, oxygen centers by red balls, nitrogen centers by green balls and hydrogen centers by small blue balls.

In conclusion, NH_4 interacts via its hydrogen atoms with the oxygen atoms of the $\text{V}_2\text{O}_5(010)$ surface, where it can move in a way that preserves bonding to several oxygen sites, see Figures 6.7 - 6.11. Therefore, the resulting barriers calculated for NH_4 diffusion are always found to be low. The adsorbed NH_4 species acts like a magnet on a refrigerator, being highly mobile on the surface, but at the same time binding strongly.

7 (De)hydrogenation of NH_x , ($x = 0, \dots, 4$) at the $\text{V}_2\text{O}_5(010)$ surface

Experiments on the SCR reaction clearly detect NH_3 and NH_4 surface species [17, 25, 26] and find indications of the presence of NH_2 species [26, 64]. The resulting different reaction mechanisms that are proposed by experimentalists include (de)hydrogenation steps [17]. Further, it is important to consider how (de)hydrogenation affects the relative stability of the different NH_x surface species. Therefore, in this chapter the (de)hydrogenation of NH_x in the gas phase and at the $\text{V}_2\text{O}_5(010)$ surface will be discussed, where in addition to the perfect surface the presence of reduced surface sites is considered. Here we base our discussion on Born-Haber cycles.

7.1 The Born-Haber cycle

The Born-Haber cycle was introduced 1919 by Max Born and Fritz Haber [27] as a gedanken experiment to analyze reaction energies. It is based on Hess's law which states that the enthalpy of a chemical process is independent of the path connecting initial and final states. The idea is to construct a closed process by connecting adequate thermodynamic quantities. If all quantities but one are known for this process, the unknown quantity can be expressed using the remaining ones. Thus the Born-Haber cycle enables the evaluation of quantities that may be difficult to access by experimental techniques. This approach has been widely used, for example to describe electron affinities in crystals [27], which cannot be measured directly.

7.2 Energetics for (de)hydrogenation of NH_x , at the $\text{V}_2\text{O}_5(010)$ surface

In the present work, a Born-Haber cycle process is used to describe reaction energies, E_R , of NH_x , (de)hydrogenation at the $\text{V}_2\text{O}_5(010)$ surface. These quantities are important for understanding catalytic reactions, such as the SCR of NO_x by ammonia [17] (see Chapter 2) or the Sohio process to produce acrylonitrile [171], since in both reactions, NH_3 (de)hydrogenation steps may appear. Further, the relative stability of different

NH_x surface species can help to explain experimental results [17, 26, 172], indicating that NH_4 , NH_3 , or NH_2 are reactive surface species participating in the catalytic process. Moreover, surface nitrogen could be formed by the dehydrogenation of NH_3 . This could open an alternative reaction channel for the direct conversion of NH_3 into surface H_2O and N_2 thereby reducing the selectivity of the desired reaction.

The Born-Haber cycle defined for the dehydrogenation reaction on the surface is illustrated in Figure 7.1. The alternative reaction path proceeds via desorption of the NH_x molecule, dehydrogenation of NH_x in the gas phase, and re-adsorption of NH_{x-1} and the hydrogen atom at the surface. For hydrogenation, the same cycle has to be executed in the reverse direction. As a result, E_R at the surface can be expressed by the adsorption energies of NH_x , NH_{x-1} and hydrogen at the $\text{V}_2\text{O}_5(010)$ surface, and the binding energies of NH_{x-1} with hydrogen in gas phase. Note that in contrast to adsorption energies, binding energies are positive by convention. Thus,

$$E_R(\text{NH}_x \rightarrow \text{NH}_{x-1} + \text{H})_{\text{surface}} = -E_{\text{ads}}(\text{NH}_x) + E_{\text{bind}}(\text{NH}_{x-1}|\text{H}) + E_{\text{ads}}(\text{NH}_{x-1}) + E_{\text{ads}}(\text{H}). \quad (7.1)$$

All adsorption energies necessary have been evaluated and presented in Chapter 5. It is assumed that adsorption takes place at the energetically most favorable site, and the corresponding adsorption energy is used to evaluate the reaction energy. The required hydrogen binding energies in the gas phase are obtained from corresponding gas phase dehydrogenation energies, with - in a first approach - atomic hydrogen as a reference after dissociation. Calculated and experimental values are listed in Table 7.1.

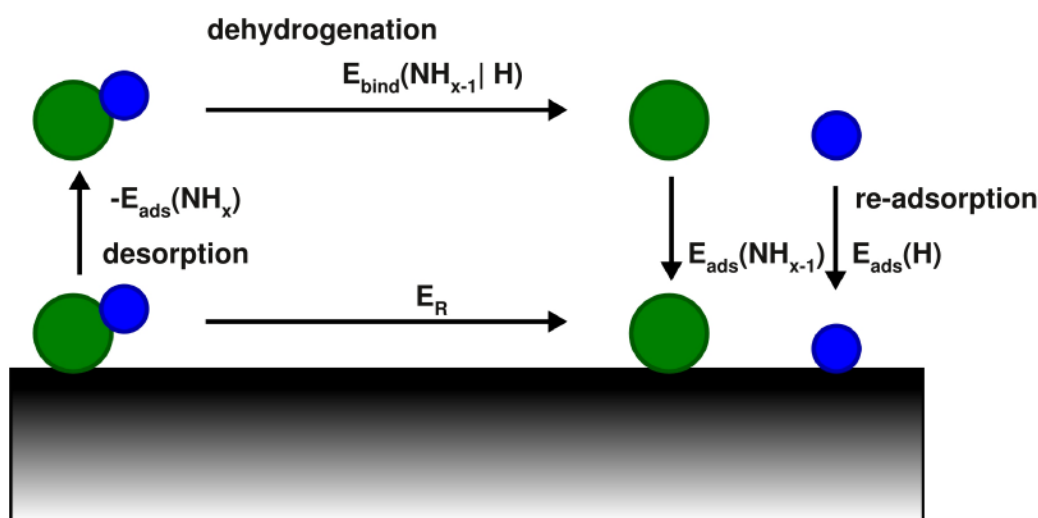


Figure 7.1: Born-Haber cycle for dehydrogenation reaction of NH_x at the surface. The dehydrogenation reaction energy on the surface, E_R , can be expressed by summing up the adsorption and binding energies of the alternative path. (Note that in contrast to adsorption energies, binding energies of a bound state are positive by convention)

Table 7.1: Calculated and experimental dehydrogenation energies E_R , for H_2 and NH_x , ($x = 1, \dots, 4$) (in [eV]) with atomic hydrogen (gas phase H) and molecular hydrogen (gas phase H_2) used as reference.

Dehydrogenation energy E_R in gas phase	atomic H as reference		$\frac{1}{2} H_2$ as reference
	Calculated	Measured [173, 174]	Calculated
$H_2 \rightarrow H + H$	4.57	4.52 ^[174]	2.29
$NH_4 \rightarrow NH_3 + H$	0.14	--	-2.15
$NH_3 \rightarrow NH_2 + H$	4.77	4.77 ^[173]	2.49
$NH_2 \rightarrow NH + H$	4.20	4.03 ^[173]	1.92
$NH \rightarrow N + H$	3.71	3.25 ^[173]	1.43

While reaction energies E_R can be easily calculated by applying the Born-Haber cycle, the reactions include many processes that are not obvious from values of E_R . NH_x species as well as hydrogen adsorb at different surface sites. Therefore, the (de)hydrogenation reaction includes diffusion processes and hence diffusion barriers. In addition, a barrier must be overcome to break or form the H- NH_{x-1} bond. Thus, the reaction energy E_R defined by equation (7.1) represents the limiting case of a barrier-free reaction. Reactions with a corresponding reaction energy E_R that is either negative (exothermic reaction) or only slightly positive (mild endothermic reaction) are much more likely than processes with an E_R that is highly positive. However, it should be noted that all reactions with promising E_R values may still be hindered by large diffusion and reaction barriers.

7.2.1 Gas phase reactions

The measured and calculated binding energies of NH_x , ($x = 0, \dots, 3$) with atomic hydrogen are listed in Table 7.1. The binding energy of ammonia and atomic hydrogen, $E_{\text{bind}}(NH_3|H) = 0.14$ eV, is very small, implying that NH_4 is only slightly energetically favored over separated $NH_3 + H$. In contrast to this, the binding energies of N, NH, and NH_2 with atomic hydrogen are very large, $3.71 \text{ eV} \leq E_{\text{bind}}(NH_{x=0,1,2}|H) \leq 4.77$ eV. Here atomic hydrogen is considered as a reference after dissociation. However, this does not account for the gas phase experiment. Atomic hydrogen is very reactive, and if no other intermediate is considered, it forms molecular hydrogen, H_2 . Thus, a more realistic model can be established by defining the reaction energy E_R with respect to a reservoir of molecular hydrogen H_2 .

This gas phase reaction energy E_R is defined in equation (7.2),

$$E_R(\text{NH}_x \rightarrow \text{NH}_{x-1} + \frac{1}{2}\text{H}_2)_{\text{gas-phase}} = E_{\text{bind}}(\text{NH}_{x-1}\text{H}) - \frac{1}{2}E_D(\text{H}_2), \quad (7.2)$$

where $E_D(\text{H}_2) = 4.57$ eV is the calculated dissociation energy of molecular hydrogen. The resulting dehydrogenation energies for the gas phase reaction are listed in Table 7.1. Considering H_2 as hydrogen reservoir, ammonia becomes the most stable species. Both processes, the NH_3 hydrogenation to form NH_4 , as well as the NH_3 dehydrogenation forming $\text{NH}_2 + \frac{1}{2}\text{H}_2$ (and subsequent dehydrogenation steps), are highly endothermic.

7.2.2 Reactions at the $\text{V}_2\text{O}_5(010)$ surface

Two different scenarios for the (de)hydrogenation reaction were studied, reaction at the perfect and at the reduced $\text{V}_2\text{O}_5(010)$ surface. As discussed in Section 4.2, the reduced surface is modeled by the presence of oxygen vacancies, where four different vacancy sites have been considered for the (de)hydrogenation in the present study. These are vacancy sites $\text{O}(1)_{\text{vac}}$, $\text{O}(2)_{\text{vac}}$, $\text{O}(3)_{\text{vac}}$, and the sub-surface vanadyl vacancy site, $\text{O}(1')_{\text{vac}}$, representing the reduced vanadium site above the vacancy. For employing the Born-Haber cycle, it is assumed that the adsorbate always stabilizes at the most favorable binding site that is available. Further, it is assumed that the adsorption sites of the perfect surface are also present on the reduced surface.

Table 7.2: Reaction energies, E_R of dehydrogenation steps for $\text{NH}_4 \rightarrow \text{N} + 4\text{H}$ reaction at the perfect and the reduced $\text{V}_2\text{O}_5(010)$ surface, the latter being represented by different oxygen vacancy sites (in [eV]). Energies are evaluated by employing the Born-Haber cycle using adsorption and hydrogen binding energies. Adsorption sites of the perfect surface are assumed to be available at reduced surfaces as well.

Dehydrogenation energy E_R	at perfect $\text{V}_2\text{O}_5(010)$	near $\text{O}(1)_{\text{vac}}$ at $\text{V}_2\text{O}_5(010)$	near $\text{O}(1')_{\text{vac}}$ at $\text{V}_2\text{O}_5(010)$	near $\text{O}(2)_{\text{vac}}$ at $\text{V}_2\text{O}_5(010)$	near $\text{O}(3)_{\text{vac}}$ at $\text{V}_2\text{O}_5(010)$
$\text{NH}_4 \rightarrow \text{NH}_3 + \text{H}$	1.03	0.41	0.04	1.03	1.03
$\text{NH}_3 \rightarrow \text{NH}_2 + \text{H}$	1.52	0.63	0.41	-1.63	-0.66
$\text{NH}_2 \rightarrow \text{NH} + \text{H}$	1.23	0.53	0.70	0.42	-0.21
$\text{NH} \rightarrow \text{N} + \text{H}$	0.36	1.94	1.81	1.77	1.72

The reaction energies, E_R , for the perfect $V_2O_5(010)$ surface are shown in Table 7.2. Obviously, E_R for all (de)hydrogenation steps is significantly lower compared to the gas phase reaction, see also Figure 7.2. However, all dehydrogenation steps are endothermic, and a significant amount of energy is still necessary for these reactions. One important difference from the gas phase reaction is that, as a result of the very strong surface binding of the NH_4 adsorbate, on the surface NH_4 becomes the energetically most favorable species. This is in agreement with experimental findings of surface NH_4 after ammonia adsorption at the $V_2O_5(010)$ surface [17] (see Section 5.3).

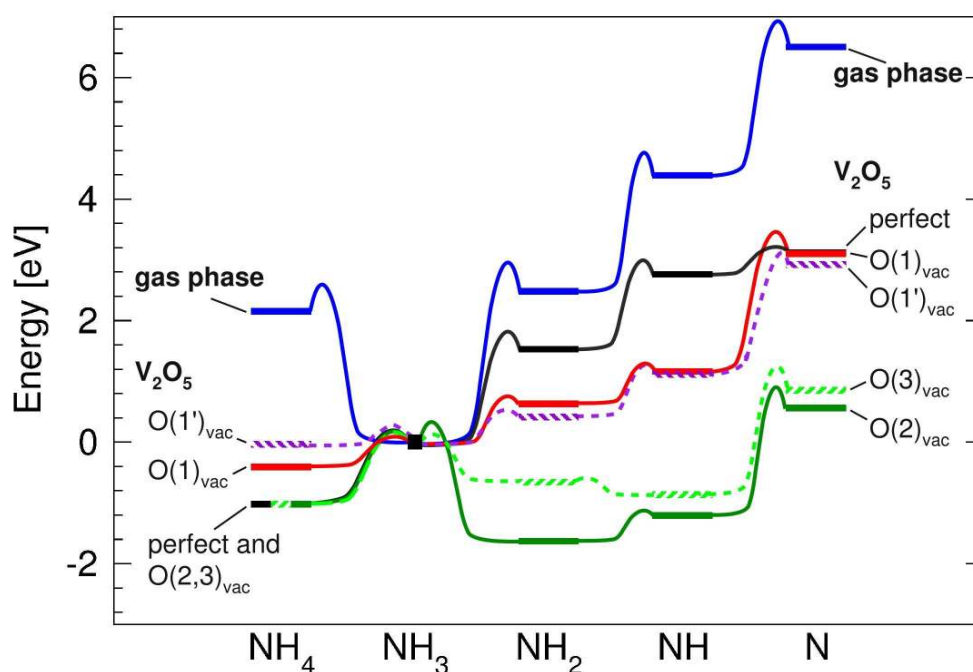


Figure 7.2: Energies of NH_x ($x = 0, \dots, 4$) (de)hydrogenation reaction in gas phase (blue), at the perfect $V_2O_5(010)$ surface (black), and at the reduced $V_2O_5(010)$ surface near $O(1)_{vac}$ (red) / $O(1')_{vac}$ (dashed purple) / $O(2)_{vac}$ (green) / $O(3)_{vac}$ (dashed light green) sites (in [eV]). Energies are evaluated by employing the Born-Haber cycle using adsorption and gas phase binding energies. Adsorption sites of the perfect surface are assumed to be present at reduced surfaces. The energy value of NH_3 is shifted to the zero of the energy axis (black square).

Furthermore, the (de)hydrogenation reaction energies E_R for the reaction at the reduced $V_2O_5(010)$ surface near $O(1)_{vac}$, $O(1')_{vac}$, $O(2)_{vac}$, and $O(3)_{vac}$ sites are presented in Table 7.2 and Figure 7.2. As hydrogen adsorption is energetically most favorable at the $O(2)$ site of the perfect surface (see Chapter 5) and, as mentioned above, the adsorption sites of the perfect surface are also assumed to be available at the reduced surface, the hydrogen adsorption energy at the $O(2)$ site enters in the (de)hydrogenation Born-Haber cycle process near vacancy sites as well.

As a consequence, the change of the (de)hydrogenation energies, E_R , when comparing the perfect and the reduced $V_2O_5(010)$ surface, is determined only by the change of the NH_x and NH_{x-1} adsorption energies, thus the difference $E_{ads}(NH_{x-1}) - E_{ads}(NH_x)$, see equation (7.1). Therefore, if the presence of the vacancy site results in an energy difference that is weaker or more negative with respect to the perfect surface, then dehydrogenation is supported and vice versa.

Close to vacancy sites $O(1)_{vac}$, or $O(1')_{vac}$, NH_3 has a larger adsorption energy compared to adsorption at the perfect surface. However, NH_4 preferably binds to adsorption sites of the perfect surface. This relative shift in adsorption energies stabilizes separated NH_3 plus hydrogen with respect to surface NH_4 , resulting in the lowering of the dehydrogenation energy of NH_4 . The reaction energies for the dehydrogenation steps $NH_3 \rightarrow NH_2 + H$ and $NH_2 \rightarrow NH + H$ are decreased in the presence of $O(1)_{vac}$ and $O(1')_{vac}$ oxygen vacancies as well. In contrast, the E_R for the reaction $NH \rightarrow N + H$ is significantly larger than at the perfect $V_2O_5(010)$ surface (Table 7.2), thus, avoiding direct nitrogen formation.

Both NH_4 and NH_3 adsorbates prefer binding to the perfect surface sites over adsorption near $O(2)_{vac}$ or $O(3)_{vac}$ sites. Thus, the dehydrogenation reaction energy of NH_4 at a surface considering additional $O(2)_{vac}$ or $O(3)_{vac}$ sites is the same as at the perfect surface (Table 7.2). Similar to findings for the reaction near $O(1)_{vac}$ or $O(1')_{vac}$ sites, E_R for the dehydrogenation processes $NH_3 \rightarrow NH_2 + H$ and $NH_2 \rightarrow NH + H$ are lowered. The effect of lowering the dehydrogenation energy is larger in comparison to the vanadyl oxygen vacancies, thus certain dehydrogenation reaction steps even become exothermic, see Table 7.2 and Figure 7.2. Similar to what has been found for the dehydrogenation reaction near $O(1)_{vac}$ or $O(1')_{vac}$ sites, the last dehydrogenation step, $NH \rightarrow N + H$, is highly endothermic.

In conclusion, NH_4 formation and dehydrogenation of NH_3 – both highly endothermic in the gas phase – are significantly facilitated by the presence of the $V_2O_5(010)$ surface. This effect becomes stronger if reduced surface sites are included. Close to $O(2)_{vac}$ and $O(3)_{vac}$ sites, NH_3 dehydrogenation to NH_2 even becomes exothermic. The impact of the presence of $O(2)_{vac}$ and $O(3)_{vac}$ sites on the formation of surface NH_2 and NH , as depicted by the Born-Haber cycle, has to be interpreted carefully. These vacancies can easily be transformed into the more stable sub-surface $O(1')$ vacancy, see Section 4.3. The barriers for these processes can be very small, as shown explicitly for the $O(2)_{vac}$ site (Section 4.3), and the interaction with adsorbates such as ammonia can induce vacancy diffusion, as findings in Section 5.2.2 indicate. The relative instability of these sites brings into question the importance of the $O(2)_{vac}$ and $O(3)_{vac}$ sites under reaction conditions. At the perfect as well as at the reduced $V_2O_5(010)$ surface, the complete NH_3 dehydrogenation to form surface nitrogen includes at least one large endothermic step that hinders the undesired conversion of NH_3 into surface OH groups and nitrogen.

8 Selective catalytic reduction of nitric oxide by ammonia at vanadium oxide surfaces

In this chapter the selective catalytic reduction (SCR) of NO in the presence of NH₃ on vanadium oxide surfaces will be discussed. A general introduction of the SCR reaction and an overview of experimental and theoretical findings can be found also in Chapter 2. Here, ammonia adsorption, (de)hydrogenation, surface water formation, surface reduction, and diffusion processes at the VO_x catalyst are found to contribute elementary steps that have been discussed in the Chapters 4 - 7. Based on these results, two possible reaction mechanisms at different surface sites can be suggested in which the reaction paths will be examined in detail.

Various reaction mechanisms considering different intermediates have been proposed in the literature [17] (and references therein). Based on mass spectroscopic data of NH₃ reacting with NO on vanadium oxide catalysts, nitrosamide (NH₂NO) was identified [175], which suggests that nitrosamide is a key intermediate in the reaction. Ramis et al., presented a 'amide-nitrosamide' type mechanism [62] that involves the formation of NH₂NO. Theoretical investigations showed that the reaction of NO and NH₂ in the gas phase produces N₂ and H₂O via the intermediate NH₂NO [176, 177]. Moreover, most of the theoretical studies investigating the SCR reaction at V₂O₅ surfaces, as well as TiO₂ supported V₂O₅ surfaces, find NH₂NO to be the intermediate [67, 69, 71, 76, 168]. Therefore, here we focus on possible SCR reaction mechanisms with nitrosamide as the key intermediate.

The SCR reaction via NH₂NO formation can be divided into four parts: (i) the initial adsorption of NH₃ and NO, (ii) the NH₂NO formation, (iii) the diffusion to an active site for the NH₂NO decomposition, and (iv) the NH₂NO decomposition into N₂ and H₂O. As shown in previous studies, the decomposition of NH₂NO, step (iv), can be performed at Brønsted acid sites (OH groups) of the V₂O₅(010) surface [67, 69] with relatively low barriers of about 0.6 eV (see Section 8.4). This indicates that barriers connected with the NH₂NO formation and diffusion represent crucial catalytic steps. Steps (i)-(iii) have been investigated in this study and will be discussed in detail in the following pages. The NH₂NO decomposition itself, step (iv), was not considered in the present work since it has been investigated by two independent studies [67, 69], yielding results that are in very good agreement. However, in order to provide a comprehensive picture, their results for the decomposition will be summarized in Section 8.4.

8.1 Preliminary considerations for modeling the SCR reaction based on the initial ammonia adsorption.

There is common agreement that during the SCR reaction, adsorbed ammonia reacts with gaseous or weakly adsorbed NO [17]. Thus, the adsorption of ammonia may be considered the initial reaction step, and the adsorption site defines the active catalytic site for the reaction with nitric oxide [17]. As discussed in Section 5.3, experimental work [25, 26] suggests two types of strongly binding ammonia species on the $V_2O_5(010)$ surface: NH_3 adsorbed at OH groups (Brønsted acid sites) forming a surface NH_4^+ species, and NH_3 adsorbed at vanadium atom centers (Lewis acid sites). Therefore, two possible active sites for the SCR reaction are proposed [17], either Brønsted or Lewis acid sites. It is still an ongoing debate, whether in experiment one - or possibly both sites - are involved in the SCR reaction.

So far, theoretical studies on the NH_3 adsorption and SCR reaction at the $V_2O_5(010)$ surface find only that ammonia binds strongly to Brønsted acid sites, but not to Lewis acid sites of the perfect surface [67-72]. Therefore, most studies focus on Brønsted acid site based reaction mechanism [67, 69, 71, 168]. One study considered the reaction near Lewis acid sites, but found it to be unfavorable [71]. The adsorption of ammonia at various surface sites is also investigated in the present study, as discussed in Chapter 5. Here, in contrast to previous theoretical studies [67-72], not only the adsorption at various sites of the perfect surface and surface OH groups, but also reduced vanadium sites, as represented by the vanadium atoms next to oxygen vacancies, are investigated. The results show that reduced vanadium atom centers provide more reactive Lewis acid sites compared to the vanadium atom at the perfect surface, yielding NH_3 binding energies that are comparable to adsorption at the Brønsted acid site. This could give a possible explanation for the experimental findings of two strongly adsorbed surface species mentioned above [25, 26]. As discussed in Section 5.3, this interpretation is substantiated by the fact that the experimental infrared (IR) bands [25, 26] used to identify ammonia near Lewis acid sites could be reproduced by ammonia adsorbed at vanadium sites of the reduced surface, but not by ammonia adsorbed at the vanadium sites of the perfect surface. Therefore in the following, the more reactive Lewis acid sites of the reduced surface are considered for a Lewis acid based reaction mechanism. In summary, two SCR reaction mechanisms will be presented. One with initial NH_3 adsorption and NH_4^+ formation at Brønsted acid sites [67, 69, 71, 168], and an 'amide-nitrosamide' type mechanism, as proposed by Ramis et al. [62], with initial NH_3 adsorption and dehydrogenation at Lewis acid sites. These two reaction mechanisms are investigated at the $V_2O_5(010)$ surface, and for two additional catalyst surface models, that are introduced in the following section. This is followed by a discussion of the individual reaction steps for the two reaction mechanisms, also

emphasizing the differences obtained for the three catalyst models, and how the results relate to previous theoretical studies.

8.2 Surface and particle models

Two model systems differing in the type of catalyst substrate, are investigated: the $V_2O_5(010)$ surface and silica supported vanadium particles. The surface is modeled by a $V_{10}O_{31}H_{12}$ cluster, as introduced in Section 4.1.2. Here the two central vanadyl units, and the connecting bridging oxygen, are considered flexible in order to account for surface relaxation. The silica supported vanadium oxide particles are models for vanadium oxide catalysts supported on SBA-15. SBA-15 is a well-ordered hexagonal mesoporous silica structure [178, 179], that has gained interest as support material for catalysts. Vanadia supported on SBA-15 is active in the SCR reaction [180] and it is well characterized [181], hence it can serve as a model catalyst simulating high performance catalysts. Sauer et al. [161] introduced clusters that are similar to 1-octahydrosilasesquioxane, in which silicon atoms are replaced by vanadyl groups to describe SBA-15 supported vanadia catalyst surfaces. These clusters have been used very successfully as model structures for theoretical simulations to interpret NEXAFS data [182] of such catalysts. There, a combination of various substitutions of silicon atoms by one or more vanadyl groups was used [182]. In the present study, we focus on a supported vanadyl dimer obtained by replacing two neighboring silicon atoms by vanadyls, which results in a $V_2Si_6O_{14}H_6$ cluster, where all atoms are considered flexible, see Figure 8.1

In addition to the surface model and the silica supported particle, a small $V_2O_9H_8$ cluster, referring to a vanadium oxide dimer cut out of the perfect surface, is considered. Analogous to the surface model, the two central vanadyl units and the connecting bridging oxygen are flexible in order to account for surface relaxation. The small V_2 cluster also used in previous studies [69, 71, 168], represents only the near proximity to the reaction site, and can give indications about if and how the catalytic properties change in the presence of an extended surface or the silica support.

All model clusters are shown in Figure 8.1. The Brønsted acid site is modeled by an OH group at the vanadyl oxygen O(1) due to the fact that the O(1) hydroxyl group has been found to be the most reactive for NH_3 adsorption. The Lewis acid site is modeled by a reduced vanadium site represented by the clusters, after removal of the O(1) oxygen atom, yielding an O(1) vacancy.

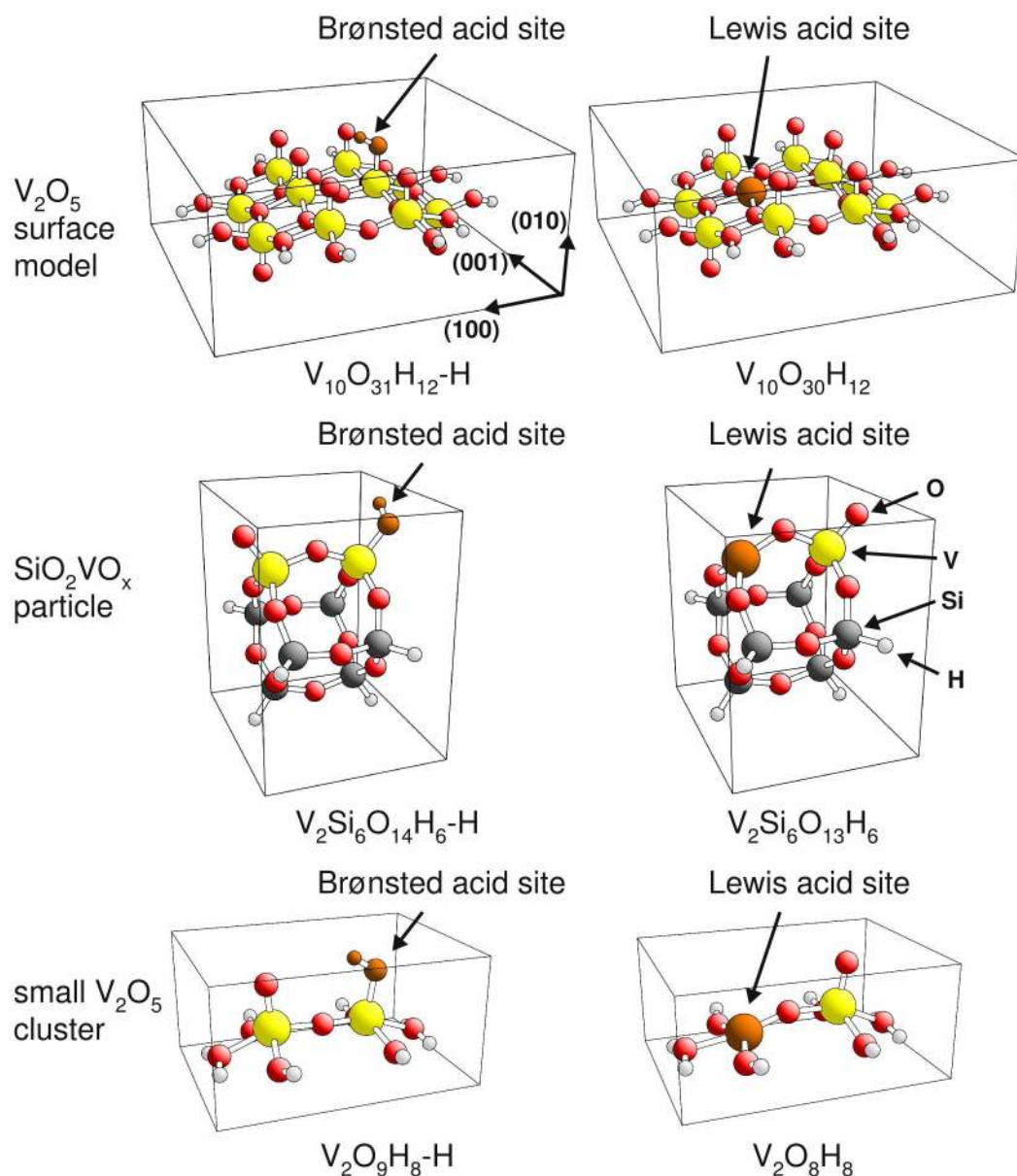


Figure 8.1: The three different catalyst models, $V_{10}O_{31}H_{12}$ cluster (surface model), $V_2Si_6O_{14}H_6$ particle, and small $V_2O_9H_8$ cluster. Vanadium centers are shown by large yellow balls, oxygen centers by red balls, silica centers by dark gray balls, and hydrogen centers by small light gray balls. The active, Brønsted (left), and Lewis (right) acid sites are indicated with dark orange shading.

8.3 Initial adsorption, nitrosamide (NH₂NO) formation, and diffusion near Brønsted and Lewis acid sites

8.3.1 Reaction near Brønsted acid sites

In this section, all relevant reaction steps and intermediates for the reaction near Brønsted acid sites, as represented by a surface O(1)H group, are discussed on the basis of a detailed description of specific reaction paths for the V₁₀O₃₁H₁₂ surface model cluster. This is followed by a comparison with the reaction paths obtained for the V₂Si₆O₁₄H₆ particle and the V₂O₉H₈ cluster. At the end of the section, the results are compared with previous theoretical studies investigating the SCR reaction. Intermediates and transition states of nitrosamide formation and desorption are labeled **(B1)** to **(B6)**, and illustrated in Figure 8.3. The corresponding reaction energies are presented in Table 8.1 and Figure 8.2.

Table 8.1: Energies for intermediates and transition states for the calculated SCR reaction path near Brønsted acid sites as represented by an O(1)H group at the surface model (V₁₀O₃₁H₁₂ cluster), the silica supported VO_x particle (V₂Si₆O₁₄H₆), and the small V₂O₅ cluster (V₂O₉H₈) (in [eV]). The energy zero is set to be the sum of the total energies of the cluster with an hydrogen atom attached at the O(1) site, and the molecules NH₃ and NO in gas phase.

Reaction Step		V ₂ O ₅ (010) surface model	V ₂ Si ₆ O ₁₄ H ₆ particle	V ₂ O ₉ H ₈ cluster
(i) NH ₃ and NO adsorption	B1 + (NH ₃) _{gas} + (NO) _{gas}	0.00	0.00	0.00
	B2 + (NO) _{gas}	-1.36	-0.86	-0.81
(ii) NH ₂ NO formation	B3	-1.51	-1.01	-1.05
	B4 ^{TS}	0.01	0.26	0.35
	B5	-0.66	-0.52	-0.41
(iii) NH ₂ NO desorption and re-adsorption	B6 + (NH ₂ NO) _{gas}	-0.08	-0.11	-0.15
	B7	-0.57	-0.57	-0.61
(iv) NH ₂ NO decomposition	B8 + (N ₂) _{gas} + (H ₂ O) _{gas}	-2.57	-2.60	-2.64

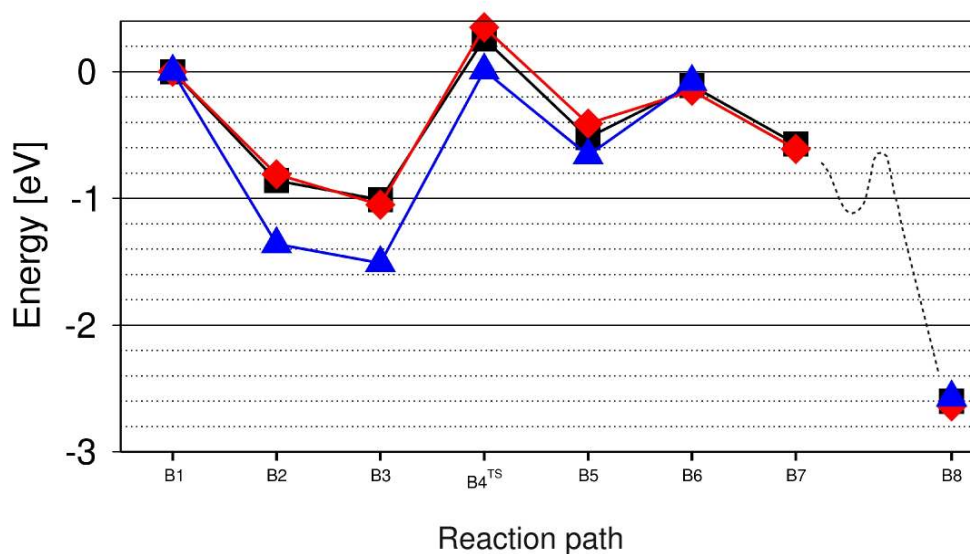


Figure 8.2: Energies for intermediates and transition states for the calculated SCR reaction path near Brønsted acid sites of the different catalyst models: surface model blue triangles, $V_2Si_6O_{14}H_6$ particle black squares, and $V_2O_9H_8$ cluster red diamonds (in [eV]). The energy zero is set to be the sum of the total energies of the cluster with an hydrogen atom attached at the O(1) site, and the molecules NH_3 and NO in gas phase.

The starting point is the catalyst surface with a hydrogen atom attached at the O(1) site, forming a surface O(1)H group (Brønsted acid site), as represented by the cluster models shown to the left of Figure 8.1. NH_3 and NO are assumed to be in gas phase. The sum of the total energies of the cluster with hydrogen adsorbed at the vanadyl oxygen, and the isolated molecules, is set as the reference (**B1**) for the energy zero in Table 8.1.

The first reaction step is the adsorption of NH_3 at the catalyst surface. When adsorption occurs at an OH group, surface NH_4^+ is formed which sits on top of four O(1) oxygen atoms (**B2**) (see also Section 5.1.4). The adsorption energy of NH_3 binding to surface OH is as large as -1.36 eV, while the NO molecule is assumed to be still in gas phase.

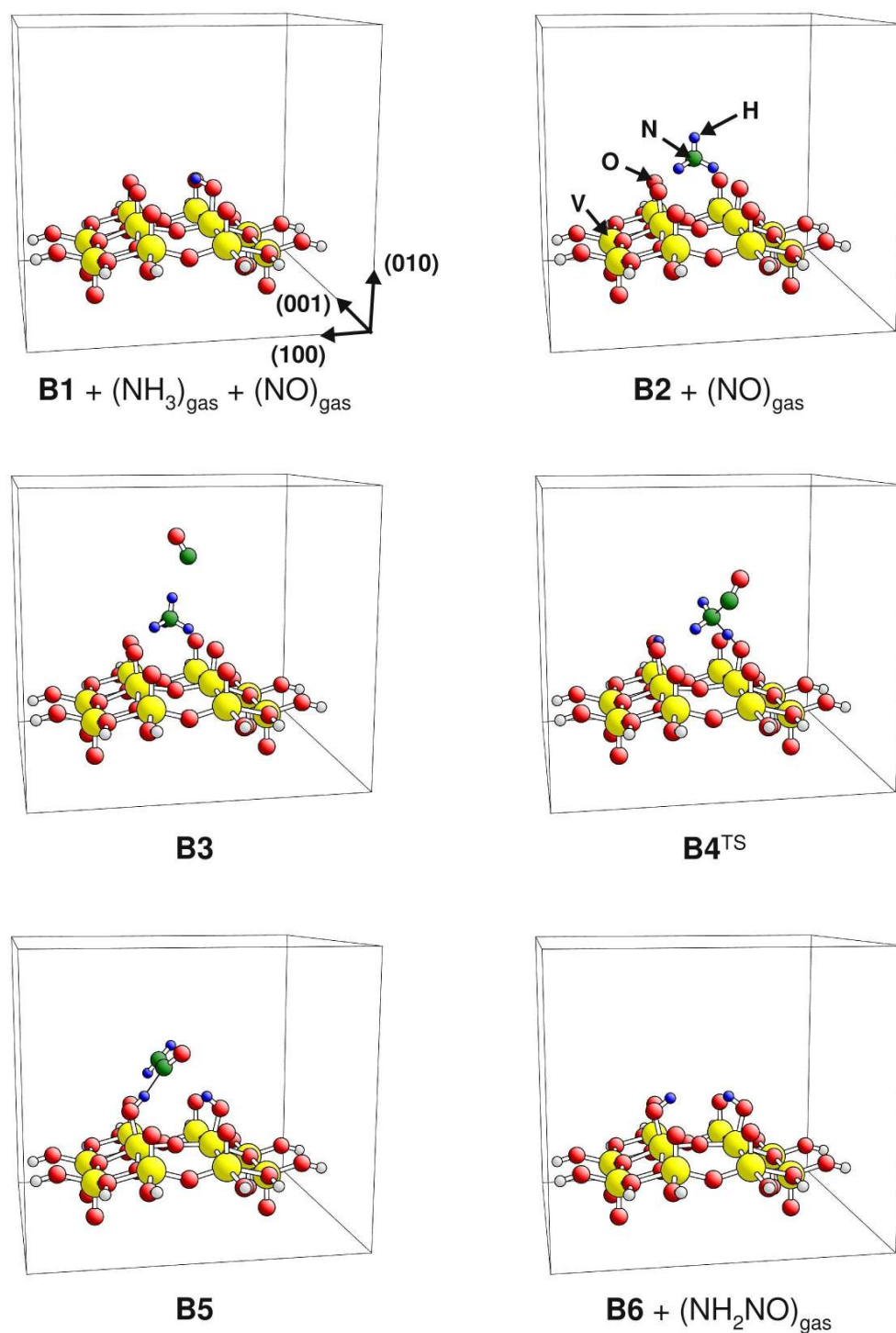


Figure 8.3: Intermediates and transition states for a path of the SCR reaction near Brønsted acid sites of the surface model. Vanadium centers are shown by large yellow balls, oxygen centers by red balls, nitrogen centers by green balls, hydrogen centers by small blue balls, and saturation hydrogen by small light gray balls.

Nitric oxide that approaches the surface NH_4 forms a weakly bound, $\text{NH}_4\text{-NO}$ precursor state (**B3**), with a slightly tilted NO adsorbate that binds on top of the NH_4 molecule with a distance of 2.16 Å between the nitrogen atom of NO and the hydrogen atom of NH_4 . The adsorption energy of NO binding to NH_4 is very small, $E_{\text{ads}}(\text{NO}/\text{NH}_4) = -0.15$ eV. Due to the weak interaction of NO and NH_4 , different energetically similar geometric configurations exist. Nevertheless, (**B3**) provides an intermediate that includes all reactants. It can be used as a starting point to locate the reaction path and transition states of the interaction between adsorbed ammonia and nitric oxide coming from gas phase. Including NO influences the multiplicity of the system. The surface cluster with the attached hydrogen has an unpaired electron, and the electronic ground state of the cluster is a doublet. By adding the closed shell molecule NH_3 , the multiplicity of the ground state is not affected. Adsorption of NO, with its unpaired electron, results in an even number of electrons for the system. Similar to what has been found for oxygen vacancies (Section 4.2.1.2), the multiplicity is not known. For all further intermediates, the corresponding local minima on the potential energy surface (PES) for multiplicity 1 and 3 have been calculated. In all cases, the triplet state was found to be favorable in energy. Therefore, the reaction will be discussed for the potential energy surface related to multiplicity 3.

The reaction of the weakly adsorbed NO with the surface NH_4 is the crucial step for the NH_2NO formation at the Brønsted acid site (**B3** \rightarrow **B4**^{TS} \rightarrow **B5**). When NO and NH_4 react, the surface NH_4 dehydrogenates to NH_2 that can form a nitrogen-nitrogen bond with NO. The two hydrogen atoms that get separated from the adsorbed NH_4 molecule get transferred to adjacent O(1) sites provided by the catalyst surface. At the end of this process, NH_2NO is formed.

Interestingly, no stable intermediate configuration could be found after the first dehydrogenation of NH_4 . Instead, the reaction path goes further uphill in energy along the PES towards the second dehydrogenation step, see Figure 8.2. As shown in Figure 8.3, for the geometry of the transition state (**B4**^{TS}), one hydrogen is already fully separated and has formed a distinct O(1)H group with the surface oxygen. This is reflected in the O(1)-H bond distance of 0.98 Å, which is the same O-H distance as found for isolated surface OH groups (see hydrogen adsorption in Section 5.1.1).

Subsequently, another hydrogen atom gets transferred from the remaining NH_3 to a nearby surface O(1) site. Simultaneously, the nitrogen atom of the NH_3 becomes more reactive while losing the hydrogen atom, and the emerging NH_2 species can react with the NO molecule. At the transition state, the transferring hydrogen atom is located between the nitrogen of the NH_2 and the O(1) site of the surface. As shown by the two distances, the bridge formed between the surface O(1) atom, the transferring hydrogen atom and the nitrogen atom of the NH_2 species, O(1)-H- NH_2 (Figure 8.3), the hydrogen is not fully transferred, ($d(\text{O}(1)\text{-H}) = 1.19$ Å, $d(\text{H-}\text{NH}_2) = 1.32$ Å). Further, the bond that is formed between the nitrogen atoms of emerging NH_2 and the NO molecule,

$d(\text{NH}_2\text{-NO}) = 1.57 \text{ \AA}$, is not fully developed, as it is 0.22 \AA larger than the corresponding distance in the isolated NH_2NO molecule. The barrier for this process is very large, $E_{\text{barr}}(\mathbf{B3} \rightarrow \mathbf{B5}) = 1.52 \text{ eV}$. Once the hydrogen atom is transferred, the NH_2NO intermediate can form along the reaction path going downhill in energy. The nitrosamide swings around until the local minimum ($\mathbf{B5}$) is reached. At this stable geometry, the NO part of the NH_2NO molecule points towards the two OH groups of the catalyst surface and the NH_2 part points towards the neighboring O(1) site that is not covered by a hydrogen atom (Figure 8.3). This configuration ($\mathbf{B5}$) is stabilized, with respect to the transition state, by -0.67 eV . Although no stable intermediate has been found along the double-dehydrogenation step, the PES between the first and the second hydrogen abstraction is very flat. Thus instead of an intermediate state, one could refer to an intermediate plateau.

In order to get decomposed into N_2 and H_2O , the nitrosamide has to reach an active site for the decomposition. It has been shown that near an O(1)H group with an adjacent O(1) site, as represented by the surface O(1)H group in the intermediate ($\mathbf{B1}$), the decomposition reaction occurs with fairly small energy barriers [67, 69]. This will be discussed detailed in Section 8.4.

After the double-dehydrogenation both O(1) sites are covered with hydrogen. However, the surface model (Figure 8.1) provides not only two, but six neighboring vanadyl oxygen sites. Interestingly, as shown in Figure 8.3, after the NH_2NO formation ($\mathbf{B4}$), NH_2NO rotates towards one of the neighboring O(1) sites, and stabilizes on top of one O(1)H group and the neighboring O(1) site ($\mathbf{B5}$). Therefore, it can be decomposed directly. Alternatively, NH_2NO can diffuse to another Brønsted acid site. An upper boundary for the corresponding diffusion energy barrier can be determined by the process of desorption and re-adsorption. Desorption results in the catalyst surface with two neighboring O(1)H groups and nitrosamide in the gas phase ($\mathbf{B6}$). In the subsequent re-adsorption step, the NH_2NO can adsorb at an isolated Brønsted acid site ($\mathbf{B7}$).

The decomposition NH_2NO into N_2 and H_2O was not considered in the present work. However, the energy of the resulting product of the reaction, i.e., the catalyst surface with two OH groups and the N_2 and H_2O molecules in gas phase ($\mathbf{B8}$), is included in Table 8.1, showing that the decomposition of nitrosamide is highly exothermic.

8.3.1.1 Comparison of the different catalyst models

A comparison between the surface model, the $\text{V}_2\text{Si}_6\text{O}_{14}\text{H}_6$ particle, and the $\text{V}_2\text{O}_9\text{H}_8$ cluster, shows that the reaction path for the NH_2NO formation is similar for all three systems. The corresponding intermediates and transition states are shown in Table 8.1 and Figure 8.2, and the illustrations of the corresponding reaction paths can be found in

Appendix D. Similar to what has been found for the reaction at the surface model, no stable intermediate could be identified after the abstraction of the first hydrogen atom. The nitrosamide is formed in a double dehydrogenation step (**B3** \rightarrow **B4**^{TS} \rightarrow **B5**), where the transition state (**B4**^{TS}) occurs during the transfer of the second hydrogen atom. The adsorption energy of NH₃ at the O(1)H site, resulting in NH₄ on the top of a square formed by four O(1) sites at the surface model, is 0.5 eV larger compared to the particle and the small cluster, which provide only two vanadyl sites. The availability of only two vanadyl oxygen sites at the particle and the small cluster also affects the decomposition of NH₂NO into N₂ and H₂O. After the double-dehydrogenation, both vanadyl sites are covered with hydrogen. Therefore, a direct decomposition is not possible. Alternatively, either one hydrogen atom diffuses to another oxygen site, or the decomposition takes place at a different site, where in the present study, the latter is considered by the corresponding energies for desorption (**B6**) and re-adsorption (**B8**). Nevertheless, for all three catalyst models, the largest energy barrier was found for the double-dehydrogenation step yielding comparable barrier energies, $1.27 \text{ eV} \leq E_{\text{barr}}(\mathbf{B3} \rightarrow \mathbf{B5}) \leq 1.52 \text{ eV}$.

8.3.1.2 Comparison with previous theoretical studies

Previous DFT cluster studies using GGA-hybrid functionals have already investigated the reaction near Brønsted acid sites [67, 69, 71, 168]. These studies include hydrogen saturated, vanadyl dimer clusters [69, 168] and larger clusters (V₆O₂₀H₁₀) [67, 71]. Although the details of the reaction paths vary, the overall statements agree with those in the present study.

The reaction path proposed by Yuan et al. [71] begins like the Brønsted acid site based reaction mechanism presented in this work. The starting point is a surface cluster that provides an O(1)H group (Brønsted acid site), plus NH₃ and NO in the gas phase (**B1**). Ammonia adsorbs at this OH group and forms surface NH₄⁺ (**B2**). At (**B2**), the two reaction paths split. A precursor state corresponding to (**B3**) has not been considered. Instead, the nitric oxide interacts directly with the surface NH₄⁺. Yuan proposes NH₃NOH as an intermediate, where the NO molecule squeezes its nitrogen atom between one N-H bond of the surface NH₄. From this intermediate, NH₂NO is formed by a double-dehydrogenation step. First, hydrogen from the NH₃ part of the molecule gets transferred to the surface, followed by the hydrogen on the NOH side of the NH₃NOH intermediate. After the double-dehydrogenation, the resulting NH₂NO stabilizes at the surface in a similar configuration, as represented by (**B5**) in this study where the two different reaction paths converge. The corresponding energies are presented in Table 8.2. Two other studies that investigated the SCR reaction at the Brønsted acid site of the V₂O₅(010) surface [67, 69] present similar reaction paths to those found in [71]. In contrast to the latter [71], these two studies [67, 69], could not

evaluate transition states. Instead, the missing transition states were described approximately, where the energy barriers seem to be overestimated (Table 8.2).

Table 8.2: Energies for intermediates and transition states for the calculated SCR reaction path near Brønsted acid sites for different SCR reaction paths, as presented in literature and the present work (in [eV]). The energy zero is set to be the sum of the total energies of the cluster with an hydrogen atom attached at the O(1) site and the molecules NH_3 and NO in gas phase.

Reaction Step	Soyer ^[69]	Anstrom ^[67]	Yuan ^[71]	This work	
	$\text{V}_2\text{O}_9\text{H}_7\text{-H}$	$\text{V}_4\text{O}_{16}\text{H}_{11}\text{-H}$	$\text{V}_6\text{O}_{20}\text{H}_{11}\text{-H}$	$\text{V}_2\text{O}_9\text{H}_8\text{-H}$	$\text{V}_{10}\text{O}_{31}\text{H}_{12}\text{-H}$
start	0.00	0.00	0.00	(B1) 0.00	0.00
$(\text{NH}_4)_{\text{ads}}$	-1.24	-1.14	-1.11	(B2) -0.81	-1.36
TS'	~ 0.67	~ 0.04	0.00	--	--
intermediate	-0.10	-0.26	-0.02	--	--
TS	~ 0.70	~ 0.50	0.38	(B4 ^{TS}) 0.35	0.01
$(\text{NH}_2\text{NO})_{\text{ads}}$	-0.61	-0.90	-0.45	(B5) -0.41	-0.66

The reaction path via the formation of an NH_3NOH intermediate differs from the path found in the present study, but the two reaction paths share some important details. Both mechanisms include a double-dehydrogenation step. However, in contrast to the path presented in the previous section, NH_2NO forms in a two-step process with an additional reaction intermediate, NH_3NOH on the surface [71]. Dividing the process into two steps yields smaller individual energy barriers, as can be seen in Table 8.2. However, the NH_3NOH intermediate is stabilized by only -0.02 eV, and the question arises whether this represents a truly stable intermediate configuration. Combining the two energy barriers into a single NH_2NO formation step results in an energy barrier of 1.48 eV, thus comparable to the findings in the present work.

In addition to theoretical studies of the SCR reaction near Brønsted acid sites of the perfect $\text{V}_2\text{O}_5(010)$ surface [67, 69, 71, 168], one study investigates the NH_2NO formation near the Brønsted acid site of TiO_2 supported V_2O_5 catalyst surface [76] (using periodic surface models and a GGA functional). This study focused on the individual energy barrier of the reaction step forming NH_2NO directly from a surface NO-NH_3 species after the first dehydrogenation step, and obtained a barrier of 0.8 eV [76]. This relatively small barrier may be misleading, as it does not include the energy necessary to form the NO-NH_3 complex starting from adsorbed NH_4 and NO in gas phase.

8.3.2 Reaction near Lewis acid sites

In this section, all relevant reaction steps and intermediates for the reaction near Lewis acid sites as represented by the (reduced) vanadium atom near an O(1) vacancy are discussed on the basis of a detailed description of specific reaction paths for the $V_{10}O_{31}H_{12}$ surface model cluster. This is followed by a comparison with the reaction paths obtained for the $V_2Si_6O_{14}H_6$ particle and the $V_2O_9H_8$ cluster. At the end of the section, the results are compared with previous theoretical studies. All intermediates and transition states of the reaction path are labeled (**L1**) to (**L12**), and illustrated in Figures 8.5 - 8.7. The corresponding reaction energies are presented in Table 8.3 and Figure 8.4.

Table 8.3: Energies for intermediates and transition states for the calculated SCR reaction path near Lewis acid sites, represented by the vanadium site next to an O(1) vacancy at the surface model ($V_{10}O_{31}H_{12}$ cluster), the silica supported VO_x particle ($V_2Si_6O_{14}H_6$), and the small V_2O_5 cluster ($V_2O_9H_8$) (in [eV]). The energy zero is set to be the sum of the total energies of the cluster with an hydrogen atom attached at the O(1) site and the molecules NH_3 and NO in gas phase.

Reaction Step		$V_2O_5(010)$ surface model	$V_2Si_6O_{14}H_6$ particle	$V_2O_9H_8$ cluster
(i) NH_3 adsorption	L1 + $(NH_3)_{gas} + (NO)_{gas}$	0.00	0.00	0.00
	L2 + $(NO)_{gas}$	-1.52	-1.15	-0.83
(ii) NH_2NO formation	L3 ^{TS} + $(NO)_{gas}$	-0.84	-0.36	app. -0.01
	L4 + $(NO)_{gas}$	-0.92	-0.87	-0.53
	L5	-1.04	-0.94	-0.61
	L5.1 ^{TS}	--	-0.91	--
	L5.2	--	-1.94	--
	L6 ^{TS}	-0.52	-1.01	-0.15
	L7	-0.92	-1.12	-0.65
	L8 ^{TS}	-0.79	-1.03	-0.49
(iii) NH_2NO diffusion	L9	-1.23	-1.13	-0.67
	L10 ^{TS}	-0.37	--	--
(iiib) NH_2NO desorption and re-adsorption	L11	-0.42	--	--
	L12 + $(NH_2NO)_{gas}$	0.08	-0.08	0.29
(iv) NH_2NO decomposition	L13	-0.41	-0.54	-0.16
	L14 + $(N_2)_{gas} + (H_2O)_{gas}$	-2.41	-2.57	-2.20

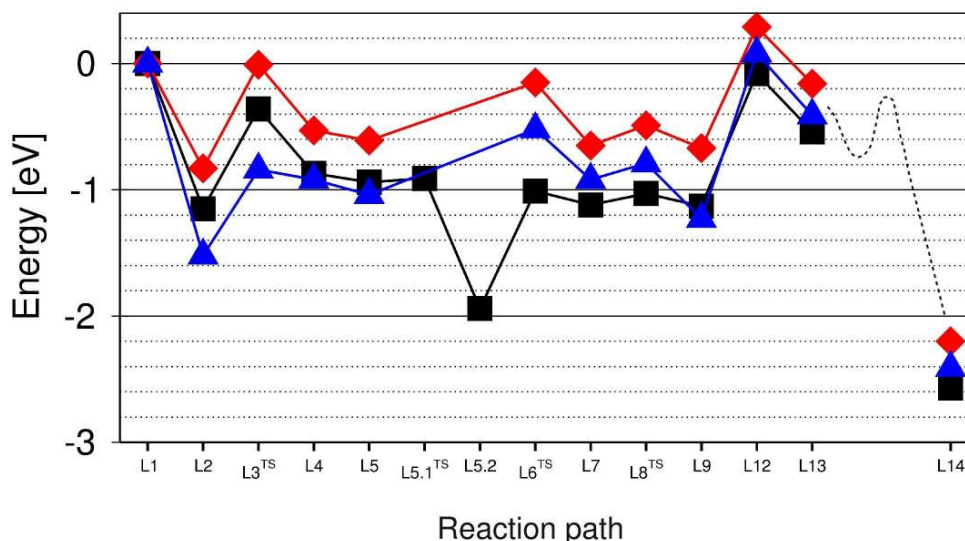


Figure 8.4: Energies for intermediates and transition states for the calculated SCR reaction path near Lewis acid sites of the different catalyst models: surface model blue triangles, $V_2Si_6O_{13}H_6$ particle black squares, and $V_2O_8H_8$ cluster red diamonds (in [eV]). The energy zero is set to be the sum of the total energies of the cluster with an hydrogen atom attached at the O(1) site and the molecules NH_3 and NO in gas phase.

The starting point is a catalyst that provides the active reaction site, represented by the (reduced) vanadium atom at an O(1) vacancy site, as shown in the cluster model at the upper right of Figure 8.1. The molecules NH_3 and NO are assumed to be in gas phase. The sum of the total energies of the vacancy cluster and the isolated molecules is set to be the reference (**L1**) for the energy zero. For the vacancy cluster (as discussed in Section 4.2), the electronic triplet state is energetically favorable over the singlet state. This holds also for the intermediates (**L2**) and (**L4**), where the corresponding local minima on the PES for multiplicity 1 and 3 have been calculated.

Adsorption of NH_3 at the catalyst surface is the first step. At the Lewis acid site, NH_3 stabilizes on top of the reduced vanadium atom, substituting the missing O(1) oxygen atom (see Section 5.2.2) and NO is assumed to be still in gas phase (**L2**). The distance between the nitrogen center of the ammonia and the vanadium center is 2.09 Å. One hydrogen atom of the adsorbed NH_3 points towards the adjacent O(1) site (Figure 8.5). The adsorption energy of NH_3 at the reduced vanadium site is -1.52 eV.

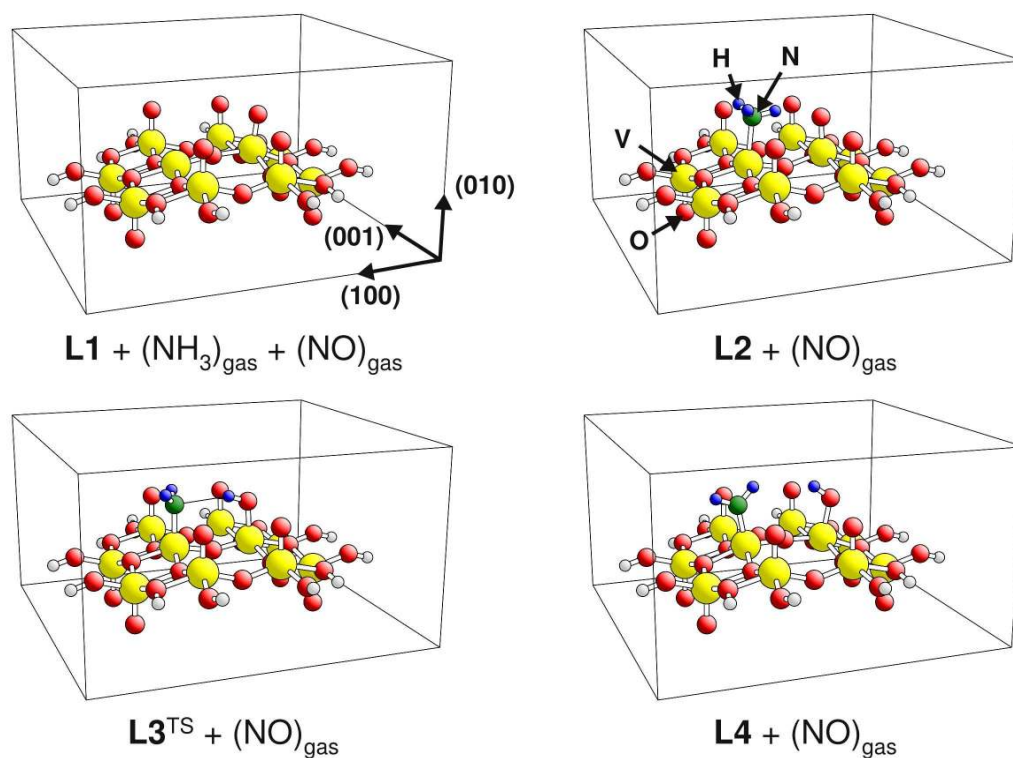


Figure 8.5: Intermediates and transition states for SCR reaction steps (**L1**) → (**L4**) (initial NH₃ adsorption and dehydrogenation) near Lewis acid sites of the surface model. Vanadium centers are shown by large yellow balls, oxygen centers by red balls, nitrogen centers by green balls, hydrogen centers by small blue balls, and saturation hydrogen by small light gray balls.

The next reaction step (**L2** → **L3^{TS}** → **L4**) is the dehydrogenation of adsorbed NH₃ in agreement with the ‘amide-nitrosamide’ SCR reaction mechanism, as proposed in [62]. This reaction leads to an O(1)H group and NH₂ adsorbed at the vacancy site. The hydrogen atom pointing towards the opposite O(1) site is transferred to this oxygen. In contrast to what has been found for the hydrogen transfer between two surface oxygen sites, here the transition state (**L3^{TS}**) found for dehydrogenation is located at the end of this hydrogen transfer. The distance between the O(1) site, and the transferring hydrogen atom in the transition state, $d(\text{O}(1)\text{-H}) = 0.98 \text{ \AA}$, is exactly what has been found for isolated surface OH groups, hence illustrating that the O(1)H bond is already formed. On the other side, the distance between the nitrogen atom of the remaining NH₂ species, and the transferring hydrogen $d(\text{NH}_2\text{-H}) = 2.42 \text{ \AA}$, is already rather large, indicating that this bond is substantially weakened. As discussed in Section 5.2.1, NH₂ can interact more strongly with the vanadium atom than ammonia. Already in the transition state (**L3^{TS}**), the distance between the vanadium center and the nitrogen atom of the emerging NH₂, $d(\text{V-NH}_2) = 1.86 \text{ \AA}$ is reduced by 0.23 \AA , with respect to adsorbed ammonia (**L2**). The energy barrier for dehydrogenation is 0.68 eV. Next, the adsorbed NH₂ species rotates about the V-N axis (close to the (010) direction of the V₂O₅ surface), forming the intermediate (**L4**) that is energetically very close to the

transition state, since it is stabilized by only -0.08 eV. This is also reflected in the bond lengths of the O(1)-H bond, $d(\text{O}(1)\text{-H}) = 0.98 \text{ \AA}$, as well as the vanadium-NH₂ bond, $d(\text{V-NH}_2) = 1.84 \text{ \AA}$, in the intermediate state (**L4**). Both are very close to what has been found for the transition state (**L3**^{TS}).

The energy barrier for the dehydrogenation of NH₃ adsorbed near the vacancy site is significantly smaller compared to the dehydrogenation reaction energy evaluated for the perfect surface $E_{\text{R}}(\text{NH}_3 \rightarrow \text{NH}_2 + \text{H}) = 1.52 \text{ eV}$ and discussed in Chapter 7. There, an analysis of the dehydrogenation energetics shows that dehydrogenation is less endothermic on the reduced surface when compared with the perfect surface. Thus, the calculated energy barrier confirms that the dehydrogenation of NH₃ is supported by a reduction of the surface and reduction not only supports the initial adsorption but it also the dehydrogenation of ammonia.

Nitric oxide adsorbs near the NH₂ surface species and binds rather weakly in a precursor state (**L5**) (Figure 8.6), analogous to what was found for the reaction at the Brønsted acid site (**B3**). The nitric oxide molecule stabilizes with the nitrogen center of the NO pointing towards the hydrogen center of the NH₂ adsorbate which points away from the O(1) double row, with a distance of $d(\text{NO-NH}_2) = 2.39 \text{ \AA}$. The adsorption energy of NO close to the surface NH₂ is rather small, $E_{\text{ads}}(\text{NO/NH}_2) = -0.12 \text{ eV}$. In contrast to the reaction at the Brønsted acid site, the added NO, with its unpaired electron, leads to an odd number of electrons and a doublet electronic ground state.

Instead of direct reaction of NO with the nitrogen atom of the adsorbed NH₂, NH₂NO is formed in two steps. First, the nitric oxide molecule interacts with the NH₂ adsorbate and the adjacent vanadium atom simultaneously (**L5** → **L6**^{TS} → **L7**). Second, the intermediate NH₂NO is formed (**L7** → **L8**^{TS} → **L9**). The nitrosamide formation via two steps is illustrated by the three distances between the NO and the NH₂ adsorbates and the vanadium atom, $d(\text{NO-NH}_2)$, $d(\text{V-NO})$ and $d(\text{V-NH}_2)$. Going from (**L5**) to (**L9**), the nitric oxide forms a bond with the vanadium, as well as with the NH₂ adsorbate. This is accompanied by a constant weakening of the vanadium-NH₂ bond.

In the transition state (**L6**^{TS}) both distances, $d(\text{NO-NH}_2) = 1.88 \text{ \AA}$ and $d(\text{V-NO}) = 2.37 \text{ \AA}$, indicate an interaction with the NO molecule. As a result, the bond between NH₂ and the vanadium is weakened, and $d(\text{V-NH}_2) = 2.00 \text{ \AA}$ is elongated by 0.16 Å compared to (**L5**). Going beyond the transition state produces the intermediate configuration (**L7**) with NH₂ and NO co-adsorbed at the reduced vanadium atom. The newly formed bonds between the two adsorbates, $d(\text{NO-NH}_2) = 1.47 \text{ \AA}$, and between NO and the surface vanadium, $d(\text{V-NO}) = 1.85 \text{ \AA}$, are strengthened, where NH₂ moves further away from the vanadium atom, $d(\text{V-NH}_2) = 2.14 \text{ \AA}$. The energy barrier from (**L5**) to (**L7**) is 0.52 eV, and the intermediate configuration (**L7**) is stabilized by -0.40 eV with respect to the transition state (**L6**).

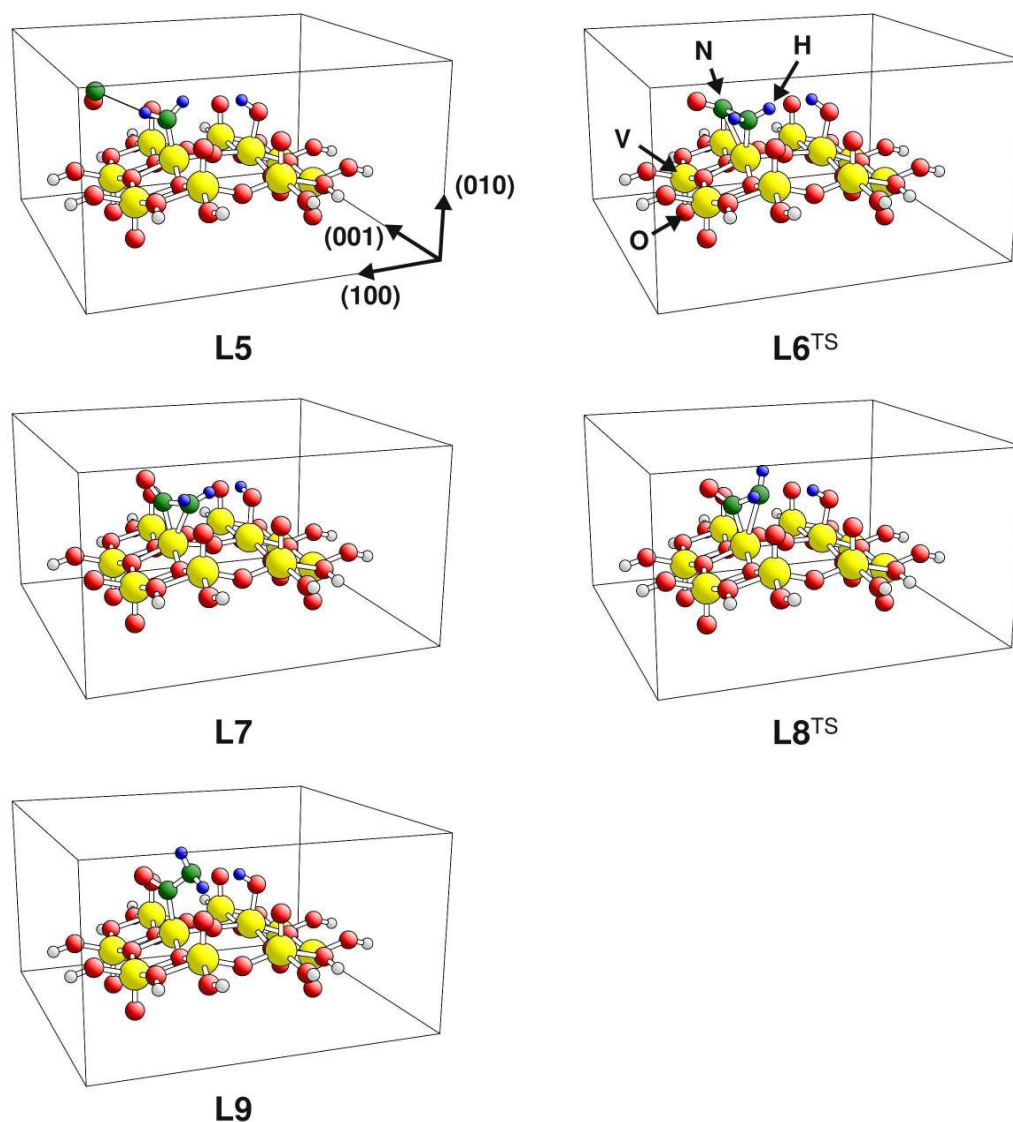


Figure 8.6: Intermediates and transition states for SCR reaction steps (**L5**) \rightarrow (**L9**) (reaction with NO and NH_2NO formation) near Lewis acid sites of the surface model. Vanadium centers are shown by large yellow balls, oxygen centers by red balls, nitrogen centers by green balls, hydrogen centers by small blue balls, and saturation hydrogen by small light gray balls.

After co-adsorption of NO next to NH_2 at the vanadium site, NH_2NO can be formed easily in the second step, (**L7**) \rightarrow (**L8**^{TS}) \rightarrow (**L9**). The NO molecule pushes its nitrogen atom between the vanadium and the NH_2 adsorbate. In the transition state (**L8**^{TS}), only minor changes have been found for the bonds involving NO, $d(\text{NO}-\text{NH}_2) = 1.47 \text{ \AA}$ and $d(\text{V}-\text{NO}) = 1.87 \text{ \AA}$, but a noticeable increase in the distance between the surface and NH_2 , $d(\text{V}-\text{NH}_2) = 2.57 \text{ \AA}$. The barrier for this process is very small, 0.13 eV. In the resulting intermediate configuration (**L9**), NH_2NO binds with the nitrogen atom next to the oxygen atom pointing towards the vanadium atom. The NO- NH_2 bond length, $d(\text{NO}-\text{NH}_2) = 1.40 \text{ \AA}$, is very close to the corresponding distance in the gas phase

molecule, $d(\text{NO-NH}_2)_{\text{gas phase}} = 1.35 \text{ \AA}$. Due to the strong interaction between NO and NH_2 , the nitrogen bond towards the surface is also a little bit weakened, $d(\text{V-NO}) = 1.96 \text{ \AA}$, and following the trend of the recent steps, the NH_2 molecule gets further pushed away from the surface, $d(\text{V-NH}_2) = 2.95 \text{ \AA}$. The intermediate is stabilized by -0.44 eV with respect to step (**L8**^{TS}).

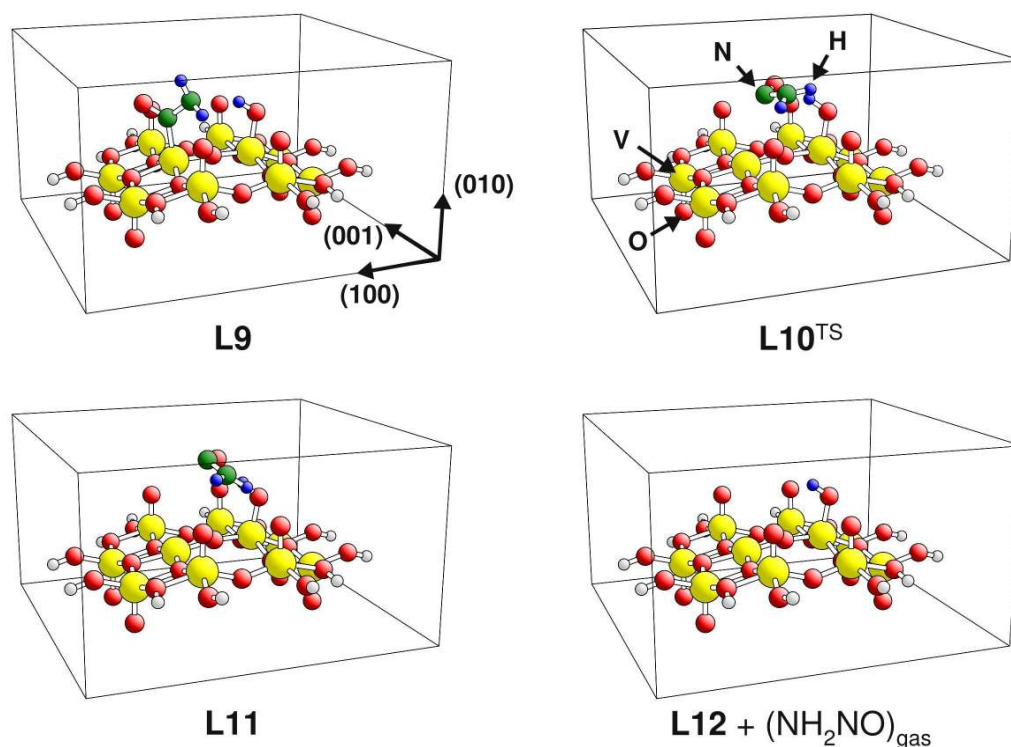


Figure 8.7: Intermediates and transition states for SCR reaction steps (**L9**) \rightarrow (**L11**) (NH_2NO diffusion and desorption) near Lewis acid sites of the surface model. Vanadium centers are shown by large yellow balls, oxygen centers by red balls, nitrogen centers by green balls, hydrogen centers by small blue balls, and saturation hydrogen by small light gray balls.

NH_2NO does not directly equilibrate on top of an active site for the decomposition after formation at the Lewis acid site (**L9**), as is found for the reaction at the Brønsted site (**B5**). Therefore, an additional diffusion step towards the active site for the NH_2NO decomposition (**L9** \rightarrow **L10**^{TS} \rightarrow **L11**) is necessary. There the bonds between the nitrogen atom and the vanadium center break, the molecule moves upwards and orients its oxygen atom towards the OH group, with one hydrogen of the molecules pointing towards the neighboring O(1) site (see Figure 8.7). The diffusion energy barrier for this process is 0.86 eV . The resulting intermediate (**L11**) is stabilized by -0.05 eV with respect to the transition state (**L10**^{TS}). Alternatively, nitrosamide can reach an active site for decomposition by desorption and re-adsorption (**L9** \rightarrow **L12** \rightarrow **L13**). The corresponding desorption energy leading to (**L12**), $E_{\text{D}}(\text{NH}_2\text{NO}) = 1.31 \text{ eV}$, is

significantly larger compared to findings at the Brønsted acid sites. After desorption, NH_2NO can be re-adsorbed at an O(1)H group (**L13**).

The decomposition of NH_2NO into N_2 and H_2O is a highly exothermic process, as shown by the corresponding energy of (**L14**), listed in Table 8.3.

8.3.2.1 Comparison of the different catalyst models

The energies of the reaction paths near Lewis acid sites for the different catalyst models are shown in Figure 8.4. The reaction path found for the reaction at the Lewis acid site of the $\text{V}_2\text{Si}_6\text{O}_{14}\text{H}_6$ particle shows an additional intermediate that is energetically very stable, resulting in two co-adsorbed intermediates along the reaction path for the particle. The additional intermediates and transition states are shown in Figure 8.8. A complete illustration of the reaction paths at the particle and the small cluster model is presented in Appendix D.

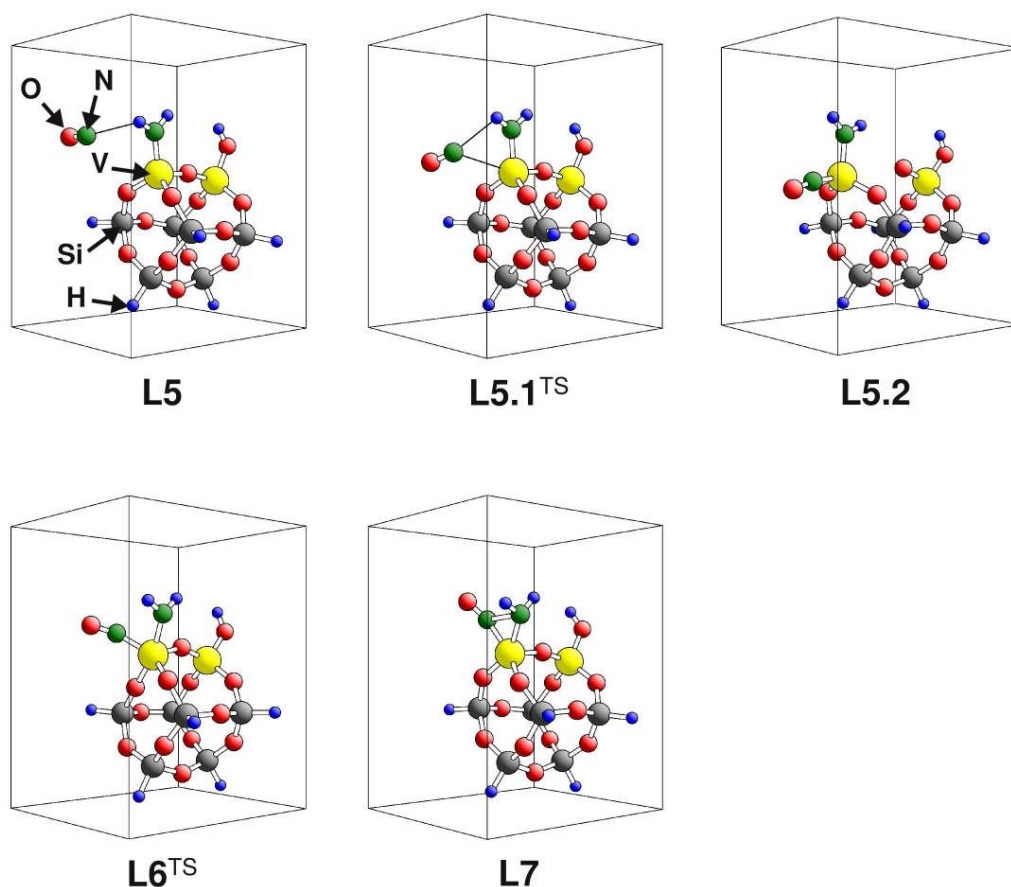


Figure 8.8: Additional intermediates and transition states for the reaction path near Lewis acid sites of the $\text{V}_2\text{Si}_6\text{O}_{14}\text{H}_6$ particle. Vanadium centers are shown by large yellow balls, oxygen centers by red balls, nitrogen centers by green balls, silicon centers by dark gray, hydrogen centers by small blue balls, and saturation hydrogen by small light gray balls.

At the particle the reaction paths found for the initial ammonia adsorption, dehydrogenation, and precursor formation with nitric oxide (**L1** \rightarrow **L5**) are similar to those found for the surface model. Ammonia adsorbs at the reduced vanadium site (**L2**) and gets dehydrogenated (**L2** \rightarrow **L3**^{TS} \rightarrow **L4**). In a next step, NO can stabilize in a weakly bound pre-cursor state pointing with its nitrogen towards the hydrogen of the adsorbed NH₂ (**L5**). The vanadium atom, as incorporated in the V₂Si₆O₁₄H₆ cluster, is more exposed compared with that of the V₂O₅(010) surface structure. Therefore, from the pre-cursor state (**L5**), the NO molecule can react with the vanadium site, avoiding a direct interaction with the adsorbed NH₂ molecule. Both adsorbates can form a strong bond with the vanadium atom, resulting in a weakening of the V-O(2) bond of vanadium atom with the adjacent bridging oxygen. This leads to the additional intermediate (**L5.2**), where the V-O(2) bond is broken, $d(\text{V-O}(2)) = 3.49 \text{ \AA}$. The vanadium bonds with both molecules are strong, as indicated by the bond distances $d(\text{V-NO}) = 1.75 \text{ \AA}$ and $d(\text{V-NH}_2) = 1.85 \text{ \AA}$. In contrast to the co-adsorbed intermediate, as found for the surface model, the separation between NO and NH₂ is rather large, $d(\text{NO-NH}_2) = 2.77 \text{ \AA}$. The transition state (**L5.1**^{TS}) is located at an early stage of the NO interaction with the vanadium atom. This can be seen by the large distance between NO and the vanadium site, $d(\text{V-NO}) = 2.87 \text{ \AA}$, and the V-O(2) distance that is only slightly elongated, $d(\text{VO}(2)) = 1.79 \text{ \AA}$. Further, the energy barrier to interaction with the vanadium site is very small, $E_{\text{barr}}(\text{L5} \rightarrow \text{L5.2}) = 0.03 \text{ eV}$. The additional intermediate (**L5.2**) is stabilized by -1.03 eV with respect to (**L5.1**^{TS}).

In order to form NH₂NO, the two adsorbates have to approach each other (**L5.2** \rightarrow **L6**^{TS} \rightarrow **L7**), where the intermediate (**L7**) is similar to the corresponding intermediate found for the surface model. The V-O(2) bond is reestablished ($d(\text{V-O}(2)) = 1.86 \text{ \AA}$), and a triangle is formed between NO, NH₂ and the vanadium atom with the distances, $d(\text{NO-NH}_2) = 2.17 \text{ \AA}$, $d(\text{V-NO}) = 1.90 \text{ \AA}$, and $d(\text{V-NH}_2) = 1.99 \text{ \AA}$. The barrier for this process, $E_{\text{barr}}(\text{L5.2} \rightarrow \text{L6}^{\text{TS}} \rightarrow \text{L7}) = 0.93 \text{ eV}$, is large and (**L7**) is stabilized by -0.11 eV with respect to (**L6**^{TS}). From (**L7**), the reaction path for the NH₂NO formation at the silica supported particle is analogous to what has been found for the surface model. The nitric oxide pushes with its nitrogen in between the NH₂ and the vanadium, resulting in NH₂NO binding with the nitrogen of the NO towards the vanadium atom. From the present results, it cannot be concluded that the additional intermediate that has been located, is a specific property of the V₂Si₆O₁₄H₆ particle, nor can be found for other SiO₂ supported VO_x particles. Therefore, further studies are needed to clarify this issue.

In contrast to the silica supported particle, the NH₂NO formation reaction at the V₂O₉H₈ cluster follows the same path as described for the surface model. It should be mentioned that no convergence for the transition state (**L3**^{TS}), for the dehydrogenation step of ammonia, was obtained. The highest energy point of the calculated MEP is given as an approximation of the transition state instead.

Both models, the particle and the small cluster provide only one O(1) site, therefore, it is necessary to diffuse to an active site for NH_2NO decomposition into N_2 and H_2O . This process is described by the corresponding energies of desorption and re-adsorption at an active site for the decomposition on a different particle (**L9** \rightarrow **L12** \rightarrow **L13**) (see Table 8.3).

8.3.2.2 Comparison with previous theoretical studies

One theoretical study addressed a reaction scenario near Lewis acid sites of the $\text{V}_2\text{O}_5(010)$ surface [71] (performing cluster DFT calculations using GGA-hybrid functional). There, in contrast to the present study, the Lewis acid site of the perfect surface is considered. Therefore, the NH_3 dehydrogenation is found to be highly endothermic, and the resulting reaction path is energetically unfavorable.

Two studies investigated the reaction near Lewis acid sites of TiO_2 supported VO_x [75, 76] (periodic DFT [76] and cluster MSINDO [75]). There it was found that ammonia can bind strongly to the vanadium site, with corresponding adsorption energies, $E_{\text{ads}}(\text{NH}_3) = -0.6$ eV [76] and $E_{\text{ads}}(\text{NH}_3) = -1.3$ eV [75]). However, the largest individual energy barriers obtained for the reaction are as large as 1.3 eV [76] and 1.5 eV [75].

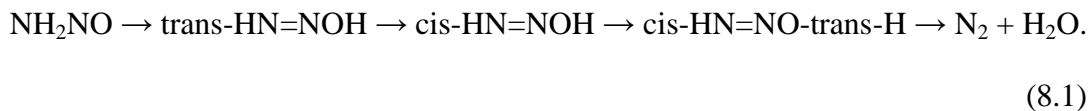
8.4 Nitrosamide (NH_2NO) decomposition

The final step of the SCR reaction is the NH_2NO decomposition to yield N_2 and H_2O . This step is not treated explicitly in this work since it has been studied extensively in earlier research [67, 69]. There it was found that the decomposition of NH_2NO can be achieved at Brønsted acid sites of the $\text{V}_2\text{O}_5(010)$ surface by a so called ‘push-pull’ mechanism [67, 69].

The active center for this ‘push-pull’ mechanism is not the Brønsted acid site itself, but it is the combination of a Brønsted acid site (OH group) with a neighboring oxygen site, O(1)H + O(1) in the case of V_2O_5 .

The ‘push-pull’ mechanism helps to transfer a hydrogen atom along the NH_2NO molecule as follows. The NH_2NO molecule approaches the active site such that one hydrogen points towards the vanadyl oxygen. The location at the NH_2NO molecule where the hydrogen should be transferred to, points towards the surface OH group. Simultaneously, the bare surface oxygen reacts with the hydrogen atom from the molecule, forming a new Brønsted acid site, and the Brønsted acid site transfers its

hydrogen to the molecule. Thus, the OH group on the surface transfers from one oxygen site to the other, and simultaneously hydrogen get transferred along the molecule. By combining several of these steps, H₂O and N₂ can be formed by the reaction,



The ‘push-pull’ steps and the intermediates, equation (8.1), are sketched in Figure 8.9, where the molecule has to rotate between the different steps (Note that Figure 8.9 presents an illustration of the principle as described in [67, 69] and shows no results of calculated reaction paths). For this mechanism, it is important that both participating oxygen sites have a similar capability to accept and release hydrogen, which is obviously the case for the two O(1) sites.

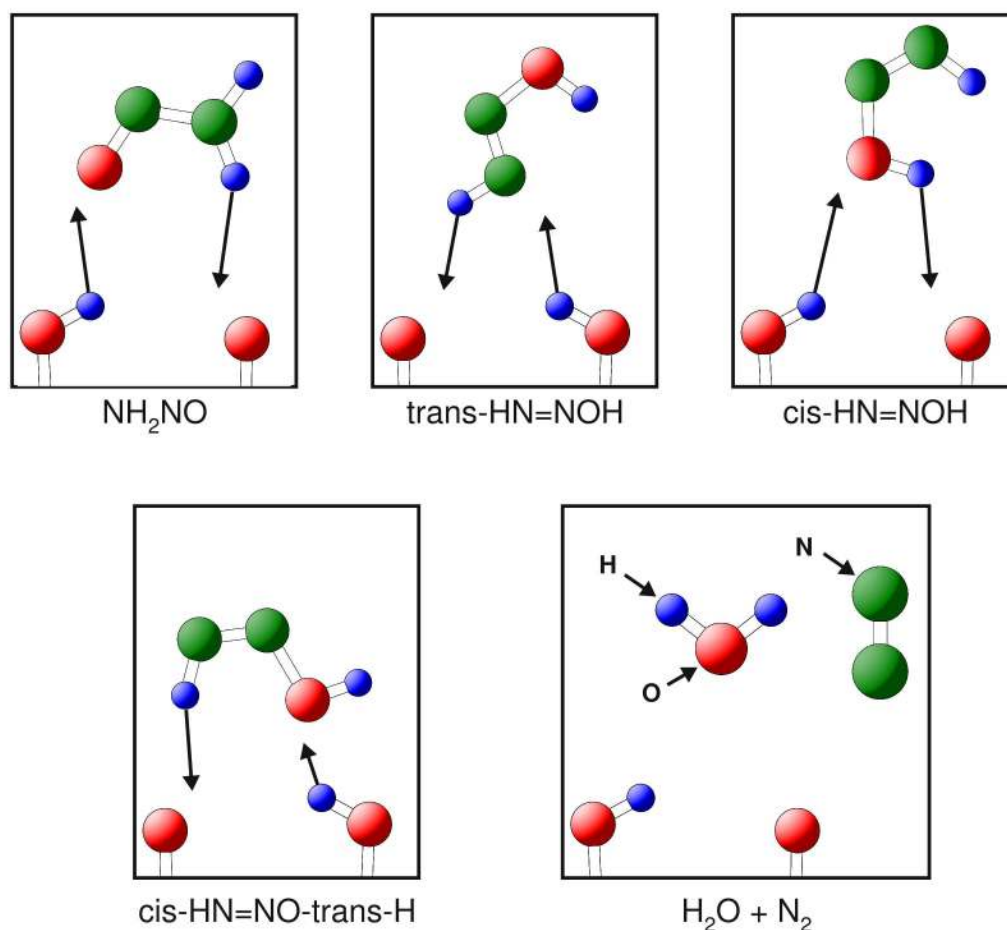


Figure 8.9: Sketch of the ‘push-pull’ mechanism of the decomposition of NH₂NO into N₂ and H₂O, where the molecule has to rotate between the different ‘push-pull’ steps. (Note that this illustration does not represent calculated structures. Oxygen centers are shown by red balls, nitrogen centers by green balls, hydrogen centers by small blue balls, and saturation hydrogen by small light gray balls.)

The energy barriers obtained for the NH_2NO decomposition at the $\text{V}_2\text{O}_5(010)$ surface, 0.62 eV [69] and 0.66 eV [67] are much smaller compared to the energy barriers calculated for the gas phase decomposition [69, 168, 176, 177], $E_{\text{barr}} \geq 1.30$ eV and $E_{\text{barr}} \leq 1.85$ eV. Moreover, these energy barriers are smaller than the energy barriers found for NH_2NO formation, see Section 8.3.

The ‘push-pull’ mechanism is not a unique property of vanadium oxide surfaces. It has been also found for H-form zeolites [183]. The active site at this H-form zeolite are two neighboring oxygen sites; one is covered by a hydrogen atom, which resembles the two O(1) sites at the $\text{V}_2\text{O}_5(010)$ surface. The active site and the mechanism are not only very similar, the energy barrier of 0.63 eV is close to the findings for V_2O_5 surface [183] as well.

8.5 Comparison of Brønsted and Lewis acid site based mechanisms

In the previous sections, two alternative mechanisms for the nitrosamide formation, a Brønsted acid site based and a Lewis acid site based mechanism are discussed. Near Brønsted acid sites, NH_3 adsorbs at the surface OH group, yielding NH_4^+ . In a next step, NH_4^+ reacts with NO forming NH_2NO and two surface OH groups by a double-dehydrogenation step, where in the transition state one hydrogen atom is already fully transferred to the surface (see Section 8.3.1). The nitrosamide can easily diffuse to an active site for the decomposition into N_2 and H_2O . Alternatively on the extended surface, direct decomposition is possible. This reaction path includes a double-dehydrogenation step, where NH_2NO is directly formed in one step uphill along the PES, resulting in large energy barriers found for all three catalyst models ($1.27 \text{ eV} \leq E_{\text{barr}} \leq 1.52 \text{ eV}$). This raises the question of whether alternative reaction paths and mechanisms are important.

The Brønsted acid site based mechanism is favored by previous theoretical studies [67, 69, 71, 168]. This is due to the fact that at the perfect $\text{V}_2\text{O}_5(010)$ surface, theoretical studies only predict the very stable NH_4^+ species, but no strongly bound ammonia species [67-72] (see Section 5.3). One possible alternative is presented by the present study. As discussed in Section 5.3, ammonia adsorbed at Lewis acid sites of the reduced $\text{V}_2\text{O}_5(010)$ surface can give a possible explanation for strongly adsorbed NH_3 surface species found in experiment [25, 26]. Therefore, in contrast to a previous theoretical study [71], the Lewis acid site based mechanism can occur near a reduced vanadium atom. There, the adsorbed NH_3 forms a bond with the reduced vanadium where it gets dehydrogenated. The remaining NH_2 species reacts with NO, forming NH_2NO in two steps; first, NO co-adsorbs next to NH_2 at the vanadium site, and then pushes itself between the NH_2 adsorbate and the vanadium atom (for reaction at the

$V_2Si_6O_{14}H_6$ particle, the NH_2NO formation is a three-step process, see Section 8.3.2.1). The resulting NH_2NO is bound with one nitrogen atom towards the Lewis acid site, and therefore in a final step has to diffuse towards the active site for decomposition (see Section 8.3.2).

It has been found that for this reaction mechanism the energy barriers, $0.86 \text{ eV} \leq E_{\text{barr}} \leq 1.05 \text{ eV}$, are smaller compared to the reaction near Brønsted acid sites. Further, the largest barriers are at the beginning (NH_3 dehydrogenation), and at the end of the NH_2NO formation (desorption or diffusion). In particular, the energy barrier which has to be overcome by gas phase or weakly adsorbed NO to form a stable intermediate in the middle of the reaction path, $0.03 \text{ eV} \leq E_{\text{barr}} \leq 0.52 \text{ eV}$, is significantly smaller compared the Brønsted acid site based mechanism.

In conclusion, none of the two reaction scenarios presented here can be excluded based on the present data. However, considering the reaction at the more reactive Lewis acid sites of the reduced $V_2O_5(010)$ surface suggests a competitive reaction mechanism that supports an ‘amide-nitrosamide’ type of mechanism as proposed by Ramis et al. [62]

9 Conclusions

The focus of the present work is the selective catalytic reduction (SCR) process. It was invented in the United States in the late 1950s to remove nitric oxides from waste gas, which is also called DeNOxing [28]. In the SCR reaction NO, molecular oxygen, and ammonia react to form molecular nitrogen and water. This reaction is of great importance as the majority of DeNOxing applications for stationary sources in industry employ the SCR process. The standard catalysts for industrial applications are TiO₂-supported V₂O₅-WO₃ and TiO₂-supported V₂O₅-MO₃ [31-36]. It is assumed that vanadium oxide species provide the active sites as removing V₂O₅ from the catalysts reduces the activity and selectivity significantly [34]. Various reaction mechanisms considering different intermediates have been proposed in literature, see [17] and references therein. However, the detailed reaction mechanism has not yet been clarified and further experimental and theoretical efforts are needed to understand the reaction details and how the catalyst operates.

In the present study the catalyst surface is analyzed, followed by an investigation of basic surface processes such as adsorption, diffusion, and dehydrogenation. Then two reaction scenarios involving different active sites are discussed in detail. The detailed structural properties of the catalysts are unknown, therefore, a model catalyst, the well characterized V₂O₅(010) surface [11] is studied instead. We model the surface by clusters that are cut out of the V₂O₅(010) layer with the dangling bonds saturated by hydrogen atoms. In order to validate these model clusters we show that the geometric, energetic, and electronic properties are in good agreement with previous theoretical [11, 23, 24, 129] and experimental studies [121, 130, 138-141].

For catalytic reactions, such as, the SCR reaction [17, 29], in analogy with the oxidative dehydrogenation (ODH) of hydrocarbons [145, 146, 148-151], a Mars and van Krevelen mechanism [57] was suggested where the catalyst surface gets reduced and oxygen vacancies are formed. Therefore, in addition to the perfect surface, here the reduced V₂O₅(010) surface, modeled by the presence of oxygen vacancies, is investigated. Besides the oxygen vacancies on the surface O(1)_{vac}, O(2)_{vac}, O(2')_{vac}, O(3)_{vac} and O(3')_{vac}, the vacancy created by the removal of the vanadyl oxygen that points sub-surface, O(1')_{vac} are considered; the latter has not been mentioned in previous theoretical studies. Although O(1') oxygen is not directly accessible from the surface O(1') vacancies could be created by accompanying processes, such as oxygen vacancy diffusion. We find that the vanadium neighbors next to the vacancy are reduced after the oxygen removal. Including surface relaxation allows the vanadium neighbors of the vacancies to interact more strongly with the remaining oxygen sites of the surrounding. This results in a lowering of the reduction of these vanadium atoms

and a lowering of the vacancy formation energies. This effect is most pronounced for the O(1) vacancy, where the neighboring vanadium atom can form a bond with the O(1) atom from the $V_2O_5(010)$ layer underneath the vacancy, yielding a sizeable relaxation energy of -1.28 eV. In general the vacancy formation energies are rather large for all vacancy sites, $4.98 \text{ eV} < E_D^f(\text{O}) < 6.44 \text{ eV}$. Hence, it is difficult to remove oxygen atoms by themselves from the surface and concurrent processes are necessary to facilitate the vacancy formation, e.g., oxygen recombining to O_2 or the formation of surface OH, H_2O [137], or CO_2 [24].

Not only the vacancy formation but also the mobility of vacancies may become important as it affects the catalyst ability to provide lattice oxygen. Moreover, sub-surface vacancies as the $O(1')_{\text{vac}}$ could be generated by the diffusion of surface vacancies. In the present work transition states and corresponding energy barriers for selected vacancy diffusion steps are evaluated. In general including surface relaxation in the transition state calculations yields much smaller diffusion energy barriers compared to previous investigation that used model paths to estimated the diffusion energy barriers [137]. We show that $O(2)_{\text{vac}}$ can be easily annihilated by $O(1')_{\text{vac}}$ as the corresponding diffusion energy barrier of 0.08 eV is very small. Thus, $O(1')$ vacancies can be created by such a diffusion processes and sub-surface oxygen gets transferred to the surface. The experimental characterization of oxygen vacancies of V_2O_5 is difficult. Besides the existence of O(1) vacancies [123, 156, 157], that were identified by theory to be the energetically most favorable ones, also O(2) vacancies [141, 152], or O(3) vacancies [141] were proposed. The present results question the importance of O(2) vacancies because they show that on the $V_2O_5(010)$ surface O(2) vacancies are not only energetically unfavorable compared to vanadyl oxygen vacancies but also easy to annihilate.

Based on the surface models established before, we investigate adsorption of H, NH_x , ($x = 0, \dots, 4$), and NO at perfect and reduced $V_2O_5(010)$ surfaces. On the perfect surface, atomic hydrogen stabilizes on top of the oxygen sites yielding large adsorption energies ($-2.36 \leq E_{\text{ads}}(\text{H}) \leq -2.76$). In previous studies, hydrogen adsorption at the $O(2')$ and the $O(3')$ sites that are located between two neighboring vanadyl oxygen was either not considered [24, 68, 160, 165] or significantly smaller adsorption energies compared to the other oxygen sites [23, 137] were found. In contrast, the present calculations yield adsorption energies that are comparable to the other oxygen sites. This is due to the fact that the present cluster models include surface relaxation to a larger extend. N, NH, and NH_2 are found to bind favorably at oxygen sites of the surface, with largest adsorption energies for nitrogen -1.54 eV and smallest for NH_2 , -0.74 eV. Ammonia and NO show only weak interaction with the perfect surface. In contrast, adsorption of NH_4 yields the largest adsorption energies ($-3.23 \leq E_{\text{ads}}(NH_4) \leq -3.90$) and highly positively charged NH_4^+ surface species.

Our results for adsorption at the reduced surface show that except for hydrogen and NH_4 , adsorption at reduced surface sites is energetically favorable compared to adsorption at the perfect surface. In most of the cases the adsorbate substitutes for the missing oxygen atom and as a result the geometric and electronic properties of the perfect surface are partly recovered.

The adsorption of NH_3 at the surface is assumed to be the initial reaction step of the SCR reaction [17]. Experiments could identify two surface species after ammonia adsorption, by infrared (IR) spectroscopy experiments [25, 26]. These are ammonia that binds with vanadium (Lewis acid site) and surface NH_4 that results from NH_3 adsorption at surface OH groups (Brønsted acid sites). So far only the presence of stable NH_4 species at the $\text{V}_2\text{O}_5(010)$ surface could be validated by theory [67-72]. In the present work we demonstrate that, in contrast to the perfect surface, NH_3 can bind strongly at reduced vanadium sites. Furthermore, our simulation of the vibrational properties show that ammonia adsorbed at reduced vanadium sites yields better agreement with IR experiments [25, 26] than ammonia species at the perfect surface.

After identification of the different adsorption sites, surface diffusion processes of two adsorbates, atomic hydrogen and NH_4 , are examined. Hydrogen with its small mass can diffuse more easily compared with other adsorbates. Moreover, the mobility of OH groups and further the formation of surface water from two surface OH groups may participate in the SCR reaction. NH_4 is an interesting example as it adsorbs at the $\text{V}_2\text{O}_5(010)$ surface with strong electrostatic binding contributions. We find that hydrogen diffusing between two oxygen sites, results always in an O-H-O bridge in the transition state. The bridge formation supports the OH bond breaking and making, yielding diffusion energy barriers that are smaller compared with a combined desorption and adsorption process. The individual height of the energy barriers depends on the mobility of the oxygen atoms that are involved. Diffusion between the fairly mobile O(1) sites results in small diffusion energy barriers, where the energy barriers for diffusion steps including the more highly coordinated O(2) and O(3) sites are larger. Further we show that the energy necessary to form and desorb surface water, starting from two neighboring O(1)H groups, are smaller than 0.44 eV. Thus, the formation and desorption of surface water facilitates the formation of surface oxygen vacancies substantially. This could also provide an explanation for the results of isotopic labeling studies [49, 50], showing that a fraction of the water formed during the SCR reaction includes oxygen from the catalyst surface.

Ammonia (de)hydrogenation steps appear in most of the reaction mechanisms that were suggested for the SCR reaction [17] (see Section 2.1.4). The (de)hydrogenation reaction energies of NH_x at the perfect as well as the reduced $\text{V}_2\text{O}_5(010)$ surface are calculated employing a Born-Haber cycle [27] that is based on H and NH_x adsorption energies and gas phase binding energies. The results demonstrate that on the surface NH_4 is very stable, in agreement with experiments [25, 26]. The dehydrogenation of NH_3 is also

avored by the presence of the surface and it is found that surface reduction further supports the dehydrogenation of ammonia.

After the discussion of the basic surface processes in Chapters 3 - 7, two reaction schemes for the NH_2NO formation involving different active sites, Brønsted and Lewis acid sites, of the catalyst surface are examined and compared. As mentioned above, ammonia binding near Lewis acid sites of the reduced surface results in adsorption energies and vibrational properties that are in better agreement with experiments than for the perfect surface. Therefore, the reduced surface model is used for the Lewis acid based reaction scheme. Both mechanism are investigated for three surface models, in addition to the $\text{V}_2\text{O}_5(010)$ surface model, we consider a small $\text{V}_2\text{O}_9\text{H}_8$ cluster and a silica supported $\text{V}_2\text{Si}_6\text{O}_{14}\text{H}_6$ particle as alternative catalyst models illustrating how the presence of an extended surface or an oxide support influences the reaction.

For the reaction near Brønsted acid sites, we find for all three catalyst models that NH_2NO is formed by a double-dehydrogenation step. In this step weakly bound NO has to overcome a large energy barrier ($1.27 \text{ eV} \leq E_{\text{barr}} \leq 1.52 \text{ eV}$) before a stable intermediate can be formed, thus, raising the question of whether alternative reaction paths and mechanisms are important. In contrast to a previous theoretical study [71], the Lewis acid site based mechanism is simulated at the reduced vanadium oxide surface. Here the energy barriers for the reaction near Lewis acid sites ($0.86 \text{ eV} \leq E_{\text{barr}} \leq 1.05 \text{ eV}$) are found to be smaller compared with the reaction near Brønsted acid sites. The largest barriers of the reaction path as found near Lewis acid sites occur at the beginning (NH_3 dehydrogenation), and at the end of the NH_2NO formation (desorption or diffusion). Further the energy barriers that involved intermediate formation with NO from the gas phase are found to amount to only $0.03 \text{ eV} \leq E_{\text{barr}} \leq 0.52 \text{ eV}$ and are, thus, much smaller compared with the reaction path near the Brønsted acid site.

In summary, reaction near Lewis acid sites of the reduced surface can provide an alternative reaction mechanism that is comparable to the Brønsted acid site based mechanism. So far the latter was clearly favored by theoretical studies [67, 69, 71, 168] of the NH_2NO formation at the $\text{V}_2\text{O}_5(010)$ surface. However, it is still unclear which mechanism is favorable and whether Brønsted-, Lewis acid sites, or combinations of both are active in the SCR reaction.

Appendices

A. Correlation energy of the Perdew-Burke-Ernzerhof functional

As discussed in Section 3.1.4, the widely-used Perdew-Burke-Ernzerhof (PBE) generalized gradient approximation (GGA) functional [94, 97, 98] is the outcome of efforts to reproduce the properties of the Perdew-Wang-91 (PW91) functional [95, 96] while minimizing the number of parameters used in the functional. This is achieved by constructing the PBE functional considering only those seven conditions that were identified to be energetically significant. The exchange part has been presented in Section 3.1.4. In the following, the definition of the PBE correlation energy will be shown. A detailed derivation and discussion which would exceed the scope of this work can be found in the original work by Perdew et al. [94, 97, 98].

The correlation energy is divided into the LDA and the gradient part H^{PBE}

$$E_c^{GGA}(\rho_\uparrow(\underline{r}), \rho_\downarrow(\underline{r})) = \int d^3r \left(\rho(\underline{r}) \left\{ \varepsilon_c^{\text{hom}}(r_s, \zeta) + H^{PBE}(r_s, \zeta, t) \right\} \right) \quad (\text{A.1})$$

where r_s is the Wigner-Seitz radius and ζ the relative spin polarization.

$$r_s = \left(\frac{3}{4} \pi \rho(\underline{r}) \right)^{\frac{1}{3}} \quad (\text{A.2})$$

$$\zeta = \frac{(\rho_\uparrow(\underline{r}) - \rho_\downarrow(\underline{r}))}{\rho(\underline{r})} \quad (\text{A.3})$$

As for the enhancement factor (see Section 3.1.4), a reduced gradient is also used here,

$$t = \frac{|\nabla \rho(\underline{r})|}{2k_s \phi \rho(\underline{r})} \quad (\text{A.4})$$

which measures the change of the density $\rho(\underline{r})$ in the scale of the local Thomas-Fermi

screening length $1/k_s$, where $k_s = \left(\frac{4k_F}{\pi} \right)^{\frac{1}{2}}$ with $\frac{2\pi}{k_F}$ being the local Fermi wavelength.

Based on specific conditions explained in [94, 97, 98] Perdew et al. determined their PBE gradient contribution H^{PBE} to the correlation energy, yielding

$$H^{PBE} = \gamma\phi^3 \ln \left\{ 1 + \frac{\beta}{\gamma} t^2 \left[\frac{1 + At^2}{1 + At^2 + A^2 t^4} \right] \right\} \quad (\text{A.5})$$

with

$$A = \frac{\beta}{\gamma} \left[\exp \left\{ \frac{-\epsilon_c^{\text{hom}}}{\gamma\phi^3} \right\} - 1 \right]^{-1} \quad (\text{A.6})$$

and the spin scaling factor

$$\phi = \frac{1}{2} \left[(1 + \zeta)^{\frac{2}{3}} + (1 - \zeta)^{\frac{2}{3}} \right] \quad (\text{A.7})$$

The parameters are set to $\gamma = 0.031$ and $\beta = 0.066725$ such that the conditions from [94, 97, 98] are fulfilled.

B. Computational details and basis set definitions

As discussed in Chapter 3, the Born-Oppenheimer approximation [81] that decouples the electronic and nuclear motions of the system is applied. Here, nuclei are treated classically and density functional theory (DFT) is employed to solve the electronic problem (see Section 3.1). The resulting total energies define the Born-Oppenheimer potential energy surface (PES). The results presented here are obtained using the StoBe DFT package [18] to calculate the total energies and investigate the corresponding PES. The important computational details will be presented below.

The Kohn-Sham DFT scheme [83] that is presented in Section 3.1 is implemented in StoBe [18]. It can be summarized by equations (3.22), (3.22a) and (3.22b) repeated here:

$$\left(-\frac{1}{2}\Delta + v_{s,0}(\underline{r})\right)\varphi_{i,0}(\underline{r}) = \varepsilon_i \varphi_{i,0}(\underline{r}), \quad \varepsilon_1 \leq \varepsilon_2 \leq \dots \quad (3.22)$$

$$v_{s,0}(\underline{r}) = v_0(\underline{r}) + \int d^3r' \frac{\rho_0(\underline{r}')}{|\underline{r} - \underline{r}'|} + v_{xc}(\rho_0; \underline{r}) \quad (3.22a)$$

$$\rho_0(\underline{r}) = \sum_{i=1}^{N_e} |\varphi_{i,0}(\underline{r})|^2 \quad (3.22b)$$

Since in the Kohn-Sham equations the local external potential, $v_s(\rho(\underline{r}); \underline{r})$, is a function of the electron density itself (3.22a), they have to be solved self consistently in an iterative procedure. An initial estimate for the electron density is used to calculate the local external potential with equation (3.22a). In a next step, the equation (3.22) can be solved yielding the Kohn-Sham orbitals φ_i that generate a new density with equation (3.22b). This density is used as input for the next iteration. The procedure is repeated until self consistency is achieved, i.e., until the difference between the input and the resulting density of an iteration step is below a certain convergence threshold. In the present calculations, the convergence criteria are set to be 10^{-6} H (= 2.7211×10^{-5} eV) for the total energy and 10^{-5} e/Bohr³ (= 6.7483×10^{-5} e/Å³) for the electron density.

In the StoBe code [18] the Kohn-Sham orbitals, $\varphi_{i,0}(\underline{r})$, are expanded as a linear combination of analytic basis functions χ_μ with expansion coefficients c_μ ,

$$\varphi_{i,0}(\underline{r}) = \sum_{\mu} c_{\mu i} \chi_{\mu}(\underline{r}). \quad (B.1)$$

Thus the operators in equation (3.22) can be represented by matrices leading to a nonlinear coupled eigenvalue problem,

$$\sum (H_{nl}(c_{il}) - \varepsilon_i S_{nl}) c_{il} = 0 \quad (\text{B.2})$$

with the Kohn-Sham Hamiltonian matrix,

$$H_{nm}(c_{il}) = \left\langle \chi_n \left| -\frac{1}{2} \Delta + v_{s,0}(\underline{r}) \right| \chi_m \right\rangle \quad (\text{B.3})$$

and the overlap matrix

$$S_{nm} = \int d^3 r \chi_n^*(\underline{r}) \chi_m(\underline{r}). \quad (\text{B.4})$$

While the functions χ_μ refer to a fixed basis set only the expansion coefficients c_μ need to be varied to solve the eigenvalue problem. Therefore the quality of the solution strongly depends on the choice of basis functions, which is always a compromise between accuracy, computational cost, and transferability.

A prominent approach is to construct the basis from linear combinations of atomic orbitals (LCAO), whereas in the early days of quantum chemistry, Slater type orbitals [184] (STO) were initially used as basis functions:

$$STO(\zeta, n, l, m, r, \theta, \phi) = a r^{n-1} e^{-\zeta r} Y_l^m(\theta, \phi), \quad (\text{B.5})$$

where a is a normalization factor, ζ is the screened charge of the nuclei, n , l , and m are the quantum numbers, and $Y_l^m(\theta, \phi)$ being spherical harmonics. These functions have the correct asymptotic form for atomic orbitals near the atom origin and for very large distances from the origin. However, STO's have the disadvantage that most of the required integrals have to be solved numerically. Therefore, often Gaussian type orbitals (GTO) are used instead. It has been shown that with GTO's in Cartesian coordinates, i.e.,

$$GTO(\underline{r}, \underline{\alpha}, \underline{n}, \underline{R}) = (x - R_x)^{n_x} (y - R_y)^{n_y} (z - R_z)^{n_z} r^{n-1} e^{-\alpha(r-\underline{R})^2}, \quad (\text{B.6})$$

many of the required integrals can be solved analytically which makes their calculation highly efficient [185, 186]. In order to combine the advantage of STO's and the efficient integration for GTO's, so-called Gaussian contraction are used:

$$\chi_\mu(\underline{r}) = \sum_i \kappa_{i\mu} GTO(\underline{r}, \alpha_i, \underline{n}, \underline{R}). \quad (\text{B.7})$$

Here a contraction of GTO's, as represented by coefficients κ_i and α_i , is defined such that the contraction approximates a favorable function, e.g., STO. Thus, the resulting

basis set includes more analytic functions. However, this is outweighed by the faster integration properties of GTO's. Further, it has been shown that it is expedient to use auxiliary basis sets for the expansion of the electron density and the exchange-correlation potential (XCP), since it avoids the necessity to calculate expensive four-center integrals [187]. The orbital and the auxiliary basis sets with the corresponding coefficients that have been used in this work are listed in the Tables B.1 - B.7 at the end of this section.

In the Kohn-Sham scheme [83], an external potential $v_s(\rho(\mathbf{r});\mathbf{r})$ is introduced (3.22a), such that the solution for a system of non-interacting electrons yields the same density as the system of interacting electrons (see Section 3.1.3). There the complexity of the many-particle problem is condensed in the exchange-correlation potential v_{xc} . A crucial task in applying the Kohn-Sham scheme is to find density functionals that provide a good approximation of the exchange-correlation energy (see Section 3.1.4). The StoBe package [18] provides various exchange-correlation functionals. In the present work, a variation of the Perdew-Burke-Ernzerhof (PBE) [94, 97, 98] functional is used, the RPBE functional, introduced by Hammer et al. [101]. It is known to significantly improve the description of the chemisorption energies of atomic and molecular bonding to surfaces [101].

As already stated in Section 3.2, an evaluation of the full multi-dimensional PES is not possible for computational reasons. However, certain regions of the Born-Oppenheimer potential energy surface (PES) are of special interest: the minima, minimum energy paths (MEP) that connect these minima, and the saddle points of the MEP's. These points and paths can be located by applying efficient optimization algorithms. In the present work, the Broyden-Fletcher-Goldfarb-Shanno (BFGS) optimization scheme [103-106] (see Section 3.2.1) is used to find stable structures that are local minima of the PES. The BFGS scheme relies on first-order partial derivatives, and a detailed derivation of the gradients used in StoBe [18] can be found in [188]. The convergence criterion for a relaxed structure is set to be 10^{-4} H/Bohr ($=5.1422 \times 10^{-3}$ eV/Å) for the maximum force acting on an atom. As discussed in Sections 3.2.2 and 3.2.3, transition states have been located with the NEB [21, 108, 109] or the dimer [22] scheme. There the convergence criterion for force is set to be 10^{-3} H/Bohr ($=5.1422 \times 10^{-2}$ eV/Å). As both methods (NEB and dimer) rely on the forces, but not second order partial derivatives, it is possible that converged geometries results in a local minimum instead of a transition state. Therefore vibrational properties of each transition state are calculated to confirm the transition state character by the presence of an imaginary frequency. In StoBe [18], the vibrational properties are evaluated based on a harmonic approximation as implemented by C. Friedrich. A detailed discussion can be found in [24].

B1. Basis set tabulation

The details of basis sets that are used in the present work are listed below in the Tables B.1 - B.7. Table B.1 can be read as follows: The notation for orbital basis is $(n_{1s}, n_{2s}, \dots, n_{Ks} / n_{1p}, n_{2p}, \dots, n_{Lp} / n_{1d}, n_{2d}, \dots, n_{Md})$, where K, L, and M refer to the number of s-, p-, and d- type Gaussian contractions respectively. The individual entries, n_{ij} , indicate how many primitive GTO's are used for the specific contraction (see Table B.1). This means for example, that vanadium is described by six s-, three p-, and two d- type Gaussian contractions. Where the first s- type contraction contains six GTO's, and the second three GTO's, and so on. The notation for the auxiliary basis sets is $(n_{s(\text{CD})}, n_{\text{spd}(\text{CD})}; n_{s(\text{XC})}, n_{\text{spd}(\text{XC})})$. Here, $n_{s(\text{CD})}$ is the number of s-type GTO's used to fit the charge density (CD), and $n_{\text{spd}(\text{CD})}$ is the number of s-, p- and d- type GTO's (sharing the same exponent). $n_{s(\text{XC})}, n_{\text{spd}(\text{XC})}$ are defined similar to $n_{s(\text{CD})}, n_{\text{spd}(\text{CD})}$, but refer to GTO's used to fit the exchange-correlation potential.

Table B.1: Overview of the orbital and the auxiliary basis sets used for the different elements (see text).

Atom	Orbital basis	Auxiliary basis
V	(63321/531/41)	(5,5;5,5)
Si	(6321/521/1)	(5,4;5,4)
O	(7111/411/1)	(4,3;4,3)
N	(7111/411/1)	(4,3;4,3)
H	(3111/111)	(3,1;3,1)
terminal H	(311/1)	(3,1;3,1)

In the Tables B.2 - B.7, the basis set contractions for the different elements are listed. This includes the contraction coefficients, κ , and the exponential coefficients, α , of the Gaussian contractions used for the orbital basis set (see equations (B.6) and (B.7)), as well as the exponential coefficients, α , of the GTO's used in the auxiliary basis for the electron density, and the auxiliary basis for the exchange-correlation potential (XPC).

Table B.2: Basis set contraction of the vanadium atom (see text).

Orbital basis			Density basis	
l	α	κ	l	α
s	49145.2580000	0.00170490	s	42600.000
	7366.10090000	0.01306850		8500.000
	1669.95980000	0.06540440		2120.000
	468.43959000	0.22592860		532.000
	150.82100000	0.47044030		133.000
	51.25277600	0.36702730	s,p,d	42.000
s	99.48018000	-0.10271690		8.320
	11.21326400	0.60769800		2.080
	4.47782520	0.46607310	0.520	
s	7.99133500	-0.21478090	0.130	
	1.24681580	0.71090440	XPC basis	
	0.48739340	0.41627090	l	α
s	0.69088900	-0.14902600	s	14100.000
	0.09698660	0.63308970		2830.000
s	0.03676400	1.00000000		707.000
	p	595.12707000		0.00915890
140.00397000		0.06796570		44.000
43.94137700		0.25889920	s,p,d	14.00
15.52695200		0.50501160		2.800
5.59921580	0.34734430	0.690		
p	2.88927230	0.31914860	0.170	
	1.09088840	0.55183650	0.043	
	0.39812970	0.25524260		
p	0.09510000	1.00000000		
	d	16.22047300		
4.25474240		0.26686080		
1.26177140		0.48444430		
d	0.33151450	0.51113550		
	0.06400000	1.00000000		

Table B.3: Basis set contraction of the silicon atom (see text).

Orbital basis			Density basis	
l	α	κ	l	α
s	17268.57700000	0.00179740	s	9830.000
	2586.65090000	0.01379700		1966.000
	585.63641000	0.06878070		492.000
	163.77364000	0.23525080		123.000
	52.26702800	0.47661940		30.720
	17.54168100	0.35077260	s,p,d	9.600
s	35.12413900	-0.09021370		1.920
	3.56542270	0.57225480		0.480
	1.25914740	0.50455370		0.120
s	1.94701440	-0.15083520	XPC basis	
	0.23675730	0.67455940	l	α
s	0.08589660	1.00000000	s	3277.000
p	159.68174000	0.01239320		655.000
	37.25817200	0.08508000		164.000
	11.43825300	0.29055130		41.000
	3.82783360	0.49855880		10.000
	1.26790030	0.33256240	s,p,d	3.200
p	0.53440950	0.22643690		0.640
	0.18290310	0.55530350		0.160
p	0.06178730	1.00000000		0.040
d	0.45000000	1.00000000		

Table B.4: Basis set contraction of the oxygen atom (see text).

Orbital basis			Density basis	
l	α	κ	l	α
	10814.40200000	0.00078090	s	2000.000
	1623.75320000	0.00601020		400.000
	370.18274000	0.03052220		100.000
	104.97475000	0.11400890		25.000
	33.98442200	0.30195740	s,p,d	7.800
	11.98431200	0.45711070		1.560
	4.38597040	0.24324780		0.390
s	10.63003400	1.00000000	XPC basis	
s	0.93985260	1.00000000	l	α
s	0.27662130	1.00000000	s	667.000
p	61.54421800	0.00662380		133.000
	14.27619400	0.04646420		33.300
	4.33176790	0.17442290		8.300
	1.47660430	0.36661150	s,p,d	2.600
p	0.49598570	1.00000000		0.520
p	0.15448360	1.00000000		0.130
d	0.80000000	1.00000000		

Table B.5: Basis set contraction of the nitrogen atom (see text).

Orbital basis			Density basis	
l	α	κ	l	α
s	8104.17610000	0.00079690	s	1640.000
	1217.31380000	0.00612890		328.000
	277.73993000	0.03104710		82.000
	78.84759800	0.11536820		20.500
	25.53716100	0.30257380	s,p,d	6.400
	9.00457110	0.45579130		1.280
	3.28352780	0.24302080		0.320
s	7.84935730	1.00000000	XPC basis	
s	0.68622390	1.00000000	l	α
s	0.20350260	1.00000000	s	550.000
p	49.01460800	0.00590070		110.000
	11.31667100	0.04164440		27.000
	3.40340530	0.16102490	6.830	
	1.16111070	0.35835380	s,p,d	2.100
p	0.39533580	1.00000000		0.430
p	0.12689810	1.00000000		0.110
d	0.70000000	1.00000000		

Table B.6: Basis set contraction of the hydrogen atom (see text).

Orbital basis			Density basis	
l	α	κ	l	α
s	33.86500000	0.02549380	s	45.000
	5.09479000	0.19037300		7.500
	1.15879000	0.85216100		0.300
s	0.32584000	1.00000000	s,p,d	1.500
s	0.10274100	1.00000000	XPC basis	
s	0.03600000	1.00000000	l	α
p	3.00000000	1.00000000	s	15.000
p	0.75000000	1.00000000		2.500
p	0.18750000	1.00000000		0.100
			s,p,d	0.500

Table B.7: Basis set contraction of the terminal hydrogen atom (see text).

Orbital basis			Density basis	
l	α	κ	l	α
s	50.99917800	0.00966050	s	45.000
	7.48321810	0.07372890		7.500
	1.77746760	0.29585810		0.300
s	0.51932950	1.00000000	s,p,d	1.500
s	0.15411000	1.00000000	XPC basis	
p	0.75000000	1.00000000	l	α
			s	15.000
				2.500
				0.100
			s,p,d	0.500

C. Cluster models for diffusion calculations

For the simulation of diffusion processes at the $V_2O_5(010)$ surface, such as vacancy, hydrogen, or NH_4 diffusion, additional surface cluster models are created. This is motivated by the fact that for the calculation of a diffusion path and the corresponding energy barrier the model cluster has to simultaneously describe initial and final states, as well as the connecting path itself. To avoid edge effects, larger clusters may be needed and larger areas have to be considered in the geometry optimization in order to account for the surface relaxation. In the following, the different diffusion cluster models will be discussed.

C1. Vacancy diffusion clusters

Table C.1 lists cluster correction energies E_{corr} and vacancy formation energies $E_{\text{D}}(\text{O})$, as obtained for the diffusion cluster models. The latter indicate how the description of the oxygen vacancy compares to the results presented in Section 4.2. In addition, the corresponding diffusion barriers that are already discussed in Section 4.3 are repeated.

Table C.1: Cluster correction energy E_{corr} and oxygen vacancy formation energy $E_{\text{D}}^{1,2}(\text{O})$ as well as the diffusion energy barriers $E_{\text{barr}}^{1,2}$ for oxygen vacancy diffusion at the $V_2O_5(010)$ surface layer (in [eV]). The indices 1, 2 refer to the left, right vacancy of each pair.

	E_{corr}	$E_{\text{D}}^1(\text{O})$	$E_{\text{D}}^2(\text{O})$	$E_{\text{barr}}^1 \rightarrow$	$E_{\text{barr}}^2 \leftarrow$
$\text{O}(1)_{\text{vac}} \leftrightarrow \text{O}(2')_{\text{vac}}$	-0.15	4.82	6.22	~1.40	~0.00
$\text{O}(1')_{\text{vac}} \leftrightarrow \text{O}(2)_{\text{vac}}$	-0.23	5.69	6.54	0.93	0.08
$\text{O}(1')_{\text{vac}} \leftrightarrow \text{O}(3')_{\text{vac}}$	-0.22	5.87	6.31	1.38	0.94
$\text{O}(3)_{\text{vac}} \leftrightarrow \text{O}(2)_{\text{vac}}$	-0.36	6.30	6.34	0.61	0.57
$\text{O}(3)_{\text{vac}} \leftrightarrow \text{O}(3')_{\text{vac}}$	-0.27	6.14	6.14	0.44	0.44

The cluster models for vacancy diffusion will be discussed following the order of Table C.1. In general, the vacancy formation energies obtained for the diffusion models are in good agreement with the results presented in Table 4.5, with deviations that are smaller than 0.22 eV.

The cluster used for the diffusion step between the $O(1)_{\text{vac}}$ and the $O(2')_{\text{vac}}$ site is the same $V_{12}O_{40}H_{20}$ cluster as used for modeling the $O(1)$ vacancy (Section 4.2), but more atoms have been considered in the geometry optimization, as shown in Figure C.1, yielding a slightly larger cluster correction energy of -0.15 eV compared to the $O(1)_{\text{vac}}$ cluster model, $E_{\text{corr}} = -0.07$ eV.

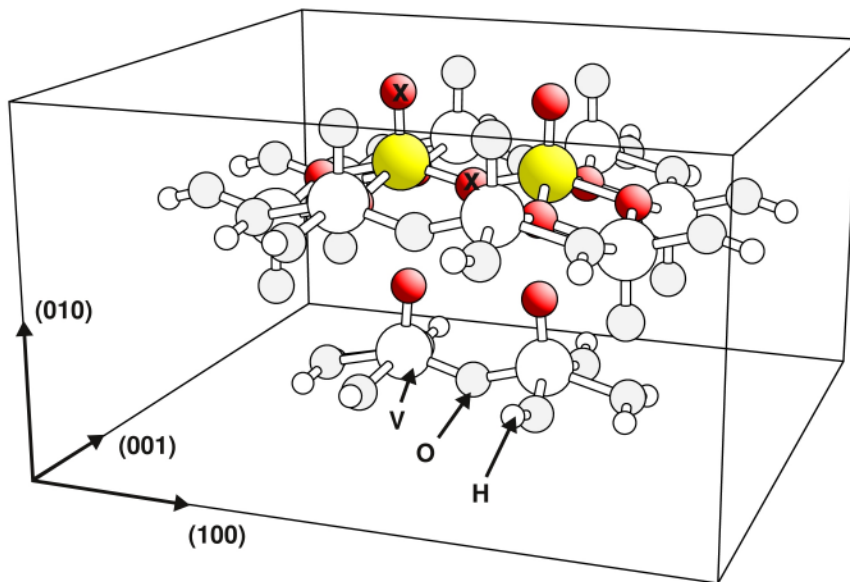


Figure C.1: Cluster model, $V_{12}O_{40}H_{20}$, for vacancy diffusion step $O(1)_{\text{vac}}$ to $O(2')_{\text{vac}}$ (marked by x). Vanadium centers are shown by large yellow balls, oxygen centers by red balls, and small balls refer to hydrogen centers. Sections that have been considered to be flexible are emphasized with shading

The model used to describe the $O(1')_{\text{vac}}$ contains the same $V_{10}O_{31}H_{12}$ surface cluster that is used for the $O(2)_{\text{vac}}$ site, plus an additional $V_2O_9H_8$ unit to account for interactions with the second layer (see Section 4.2.1). Obviously, this model also provides an accurate description of the $O(2)$ vacancy, and is therefore used to model this diffusion process between the $O(1')_{\text{vac}}$ and the $O(2)_{\text{vac}}$ site.

For the diffusion step between the $O(1')_{\text{vac}}$ and the $O(3')_{\text{vac}}$ site, the same surface cluster model as for the $O(3')_{\text{vac}}$ sites is used (see Section 4.2).

Furthermore, a $V_{14}O_{42}H_{14}$ cluster models the $V_2O_5(010)$ surface for the diffusion between the $O(3)_{vac}$ and the $O(2)_{vac}$ site, where a central V_4O_{16} unit accounts for surface relaxation, see Figure C.2.

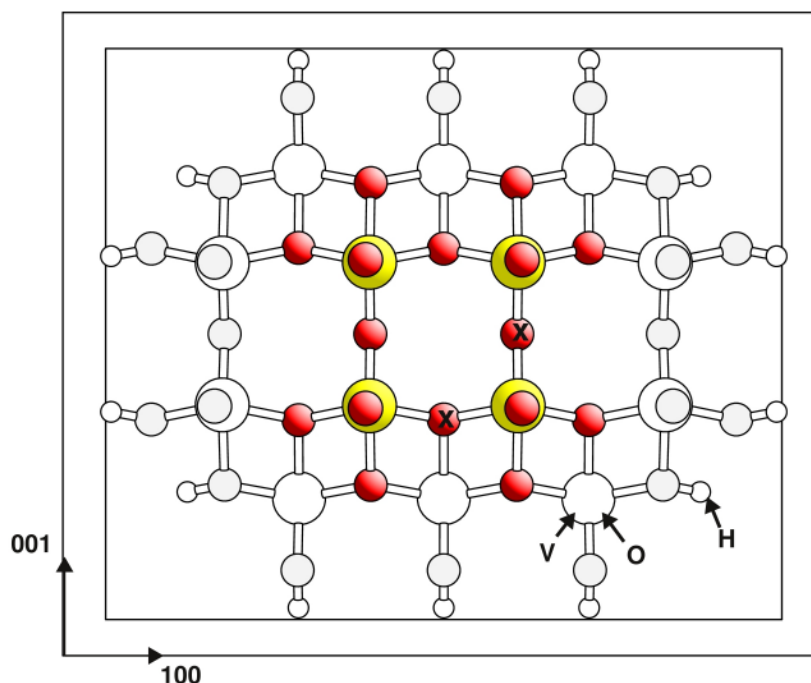


Figure C.2: Cluster model, $V_{14}O_{42}H_{14}$, for vacancy diffusion step $O(3)_{vac}$ to $O(2)_{vac}$ (marked by x). Vanadium centers are shown by large yellow balls, oxygen centers by red balls, and small balls refer to hydrogen centers. Sections that have been considered to be flexible are emphasized with shading.

For the last diffusion step in Table C.1, between an $O(3)_{vac}$ and the adjacent $O(3')_{vac}$ site a $V_{16}O_{53}H_{24}$ cluster is used (Figure C.3). The nearest and next nearest neighbors of both the $O(3)_{vac}$ and the $O(3')_{vac}$ sites are considered in order to account for surface relaxation. The vacancy formation energy $E_D(O(3)) = 6.14$ eV differs only by 0.04 eV from the corresponding energy obtained for the smaller $V_{14}O_{46}H_{22}$ cluster (see Table 4.5).

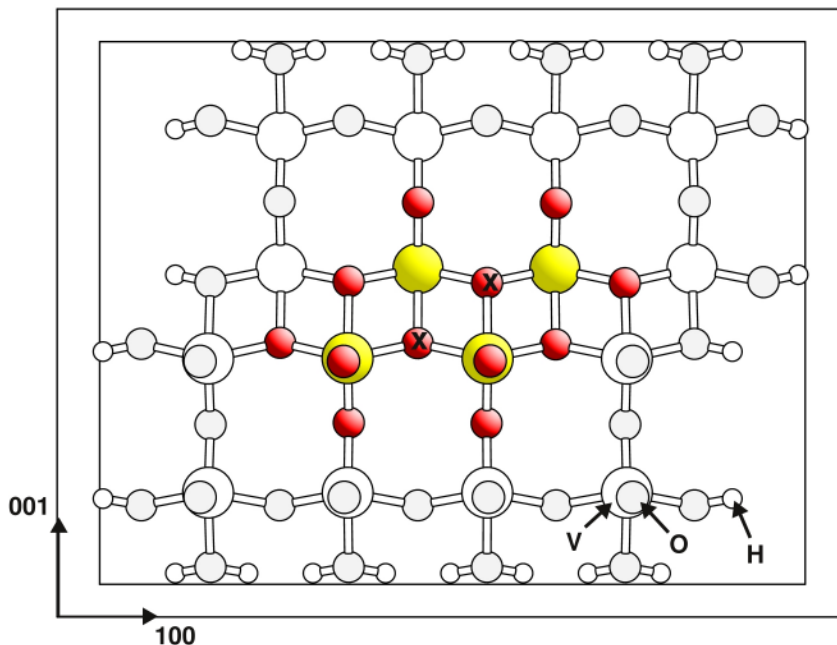


Figure C.3: Cluster model, $V_{16}O_{52}H_{24}$, for vacancy diffusion step $O(3)_{vac}$ to $O(3')_{vac}$ (marked by x). Vanadium centers are shown by large yellow balls, oxygen centers by red balls, and small balls refer to hydrogen centers. Sections that have been considered to be flexible are emphasized with shading.

C2. Hydrogen diffusion clusters

Cluster correction energies E_{corr} and hydrogen adsorption energies $E_{ads}(H)$ obtained for the diffusion clusters are listed in Table C.2. The latter indicate how the surface hydrogen as described by the diffusion models compares with the surface models used in Section 5.1.1 (see Table 5.1). In addition, the corresponding diffusion energy barriers that are already discussed in Section 6.1.1 are repeated.

Table C.2: Cluster correction energy E_{corr} and hydrogen adsorption energies $E_{\text{ads}}^{1,2}(\text{H})$ as well as the diffusion energy barriers $E_{\text{barr}}^{1,2}$ for hydrogen diffusion between oxygen sites at the $\text{V}_2\text{O}_5(010)$ surface (in [eV]). The indices 1, 2 refer to the left, right oxygen site of each pair.

	E_{corr}	$E_{\text{ads}}^1(\text{H})$	$E_{\text{ads}}^2(\text{H})$	$E_{\text{barr}}^1 \rightarrow$	$E_{\text{barr}}^2 \leftarrow$
O(1) \leftrightarrow O(1) (001)	-0.31	-2.74	-2.74	0.43	0.43
O(1) \leftrightarrow O(1) (100)	-0.18	-2.69	-2.69	0.16	0.16
O(1) \leftrightarrow O(2')	-0.18	-2.69	-2.62	1.14	1.08
O(1) \leftrightarrow O(3')	-0.22	-2.61	-2.36	1.25	1.00
O(3') \leftrightarrow O(3)	-0.35	-2.35	-2.54	1.34	1.52
O(1) \leftrightarrow O(3)	-0.22	-2.63	-2.52	1.20	1.09
O(3) \leftrightarrow O(2)	-0.55	-2.63	-2.83	0.64	0.83
O(2) \leftrightarrow O(2)	-0.31	-2.81	-2.81	0.80	0.80

In general, the hydrogen adsorption energies obtained for the diffusion model clusters are in good agreement with the results presented in Chapter 5 (Table 5.1), with deviations that are smaller than 0.11 eV.

For the hydrogen diffusion step between two O(1) sites along the (001) direction, and for the diffusion step between two neighboring O(2) sites, the $\text{V}_{14}\text{O}_{42}\text{H}_{14}$ cluster considering relaxation of central region defined by the nearest and next nearest neighbors of the two central O(2) sites is used. This is the same cluster that was discussed in Section 4.1.2 for modeling the adsorption at two neighboring O(2) sites (see Figure 4.3 and 4.4)

The cluster model as defined for a single O(2) site is used for the hydrogen diffusion step between two O(1) sites along the (100) direction, and the diffusion between the O(1) and the O(2') sites (see Figures 4.3 and 4.4). For the diffusion step between the O(1) and the O(3') sites, as well as the diffusion step between the O(1) and the O(3) sites, the cluster model as defined for the O(3) sites of the perfect surface has been used (see Section 4.1.2).

Two new cluster models are created for hydrogen diffusion between the O(3) and the O(3') sites, as well as diffusion between the O(2) and the O(3) sites. They are presented in Figure C.4 and Figure C.5, respectively. As can be seen in Table C.2, although the cluster correction energies are rather large, the hydrogen adsorption energies are in excellent agreement with the findings presented in Section 5.1.1.

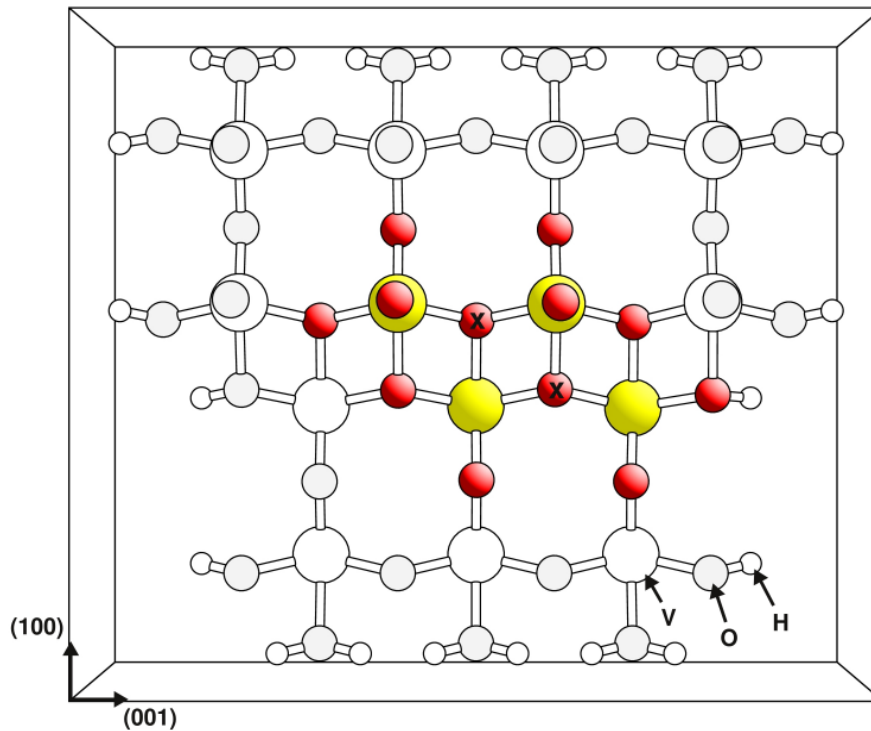


Figure C.4: Cluster model, $V_{14}O_{46}H_{22}$, for hydrogen diffusion step: $O(3) \leftrightarrow O(3')$ (oxygen sites marked by x). Vanadium centers are shown by large yellow balls, oxygen centers by red balls, and small balls refer to hydrogen centers. Sections that have been considered to be flexible are emphasized with shading.

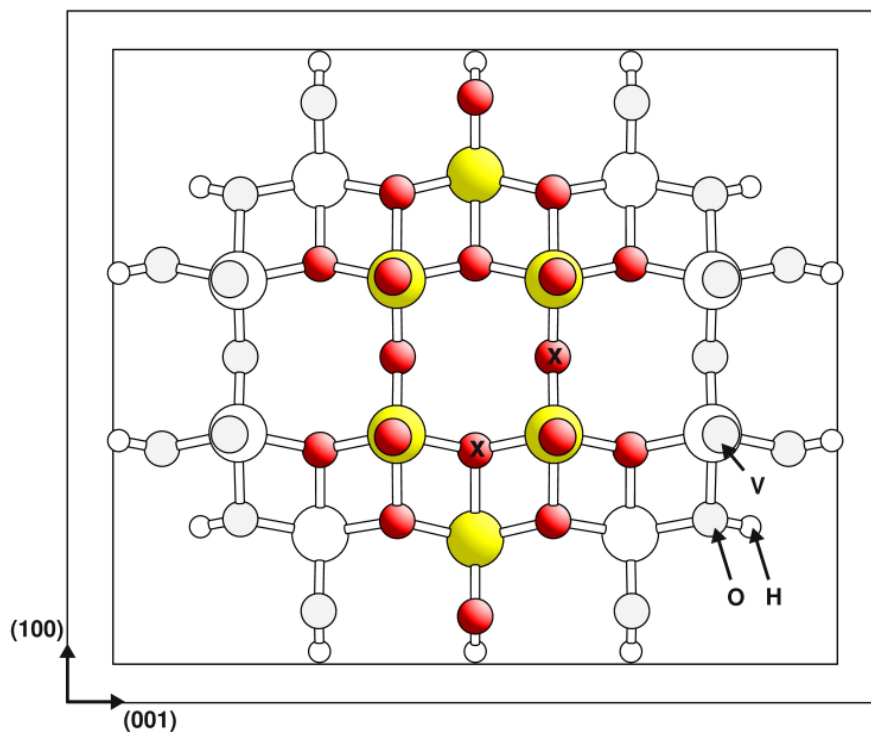


Figure C.5: Cluster model, $V_{14}O_{42}H_{14}$, for hydrogen diffusion step: $O(2) \leftrightarrow O(3)$ (oxygen sites marked by x). Vanadium centers are shown by large yellow balls, oxygen centers by red balls, and small balls refer to hydrogen centers. Sections that have been considered to be flexible are emphasized with shading.

In addition to hydrogen diffusion also the water formation and desorption is discussed in Chapter 6. As can be seen Section 6.1.2 starting point are two neighboring O(1)H groups at the surface. Therefore a cluster model is needed that includes relaxation of the next-nearest neighbors of the two neighboring vanadyl sites. Furthermore, after water desorption an O(1) vacancy is formed. Hence, it is important to consider the interaction with vanadyl oxygen from the lower layer as well (see Section 4.2.1). As can be seen in Figure C.1 the cluster that is used to describe the oxygen vacancy diffusion between the O(1)_{vac} and the O(2')_{vac} fulfills these requirements and therefore is used as a surface model for the surface water formation and diffusion.

C3.NH₄ diffusion clusters

Table C.3 lists cluster correction energies E_{corr} and NH₄ adsorption energies $E_{\text{ads}}(\text{NH}_4)$ as obtained for the diffusion clusters, and the corresponding diffusion barriers that are already discussed in Section 6.2 are repeated.

Table C.3: Cluster correction energy E_{corr} and NH₄ adsorption energies $E_{\text{ads}}^{1,2}(\text{NH}_4)$ as well as the diffusion energy barriers $E_{\text{barr}}^{1,2}$ for NH₄ diffusion between different sites at the V₂O₅(010) surface (in [eV]). The indices 1, 2 refer to the left, right adsorption site of each pair.

	E_{corr}	$E_{\text{ads}}^1(\text{NH}_4)$	$E_{\text{ads}}^2(\text{NH}_4)$	$E_{\text{barr}}^1 \rightarrow$	$E_{\text{barr}}^2 \leftarrow$
O(1) ↔ O(1) tumble	-0.58	-3.70	-3.70	0.17	0.17
O(1) ↔ O(1) twist	-0.17	-3.90	-3.90	0.0002	0.001
V₁₄O₄₅H₂₀ cluster with large relaxation area (Fig. C.7)					
O(1) ↔ V		-3.78	-3.52	0.30	0.04
V ↔ O(2)	-0.96	-3.51	-3.45	0.14	0.07
O(2) ↔ O(2)		-3.45	-3.45	0.10	0.10
V₁₄O₄₅H₂₀ cluster with small relaxation area (Fig. C.8)					
O(1) ↔ V		-3.69	-3.39	0.34	0.04
V ↔ O(2)	-0.12	-3.39	-3.36	0.08	0.05
O(2) ↔ O(2)		-3.36	-3.36	0.08	0.08

The diffusion path for the tumbling over two neighboring O(1) sites was calculated using an V₁₀O₃₁H₁₂ cluster, where the six neighboring vanadyl groups are considered flexible to account for surface relaxation, see Figure C.6.

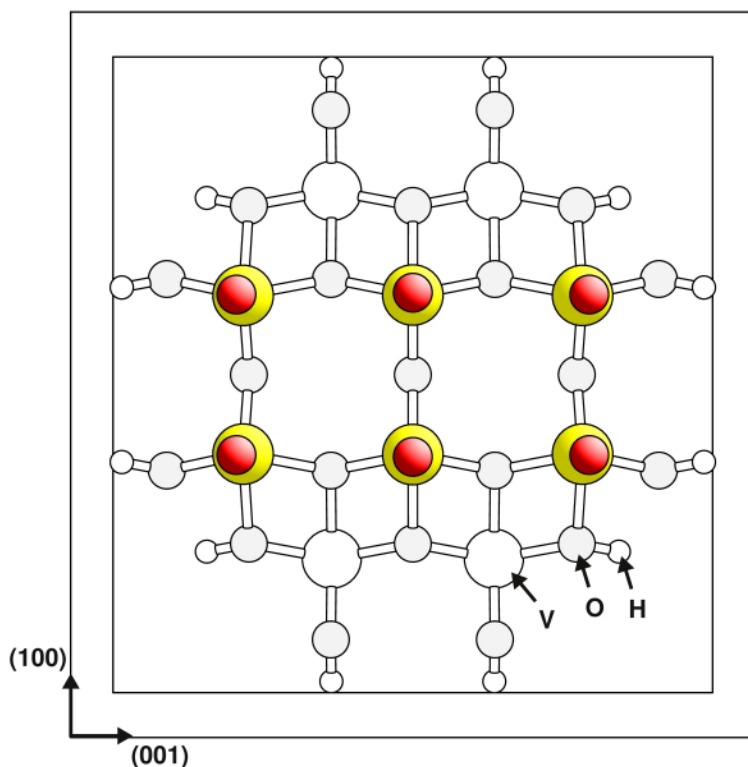


Figure C.6: Cluster model, $V_{10}O_{31}H_{12}$, for NH_4 diffusion step: $O(1) \leftrightarrow O(1)$ tumble. Vanadium centers are shown by large yellow balls, oxygen centers by red balls, and small balls refer to hydrogen centers. Sections that have been considered to be flexible are emphasized with shading.

The second part of the tumble-twist diffusion path, the twist of the NH_4 molecule (see Section 6.2.1), is calculated on the same model cluster as used for NH_4 adsorption on top of four neighboring $O(1)$ sites (see Figures 4.3 and 4.4).

In order to model the surface for the diffusion steps between the $O(1)$ ridge and the valley, as well as diffusion steps in the valley, the $V_{14}O_{45}H_{20}$ cluster as shown in Figure C.7 is used. Since NH_4 is interacting with many surface atoms simultaneously (see Section 5.1.4), 34 atoms were considered to be flexible in order to account for surface relaxation (Figure C.7, large relaxation area). This yields a cluster correction energy of -0.96 eV. In order to verify that even if the cluster correction energy is large, this surface model provides reasonable results, the diffusion paths have been also calculated using a constrained model. There, only relaxation of the 13 surface oxygen atoms is considered (see Figure C.8, small relaxation area), resulting in a relaxation energy of only -0.12 eV. As can be seen in Table C.3, the adsorption energies obtained with these two cluster models vary by less than 0.13 eV and the diffusion energy barriers by less than 0.06 eV.

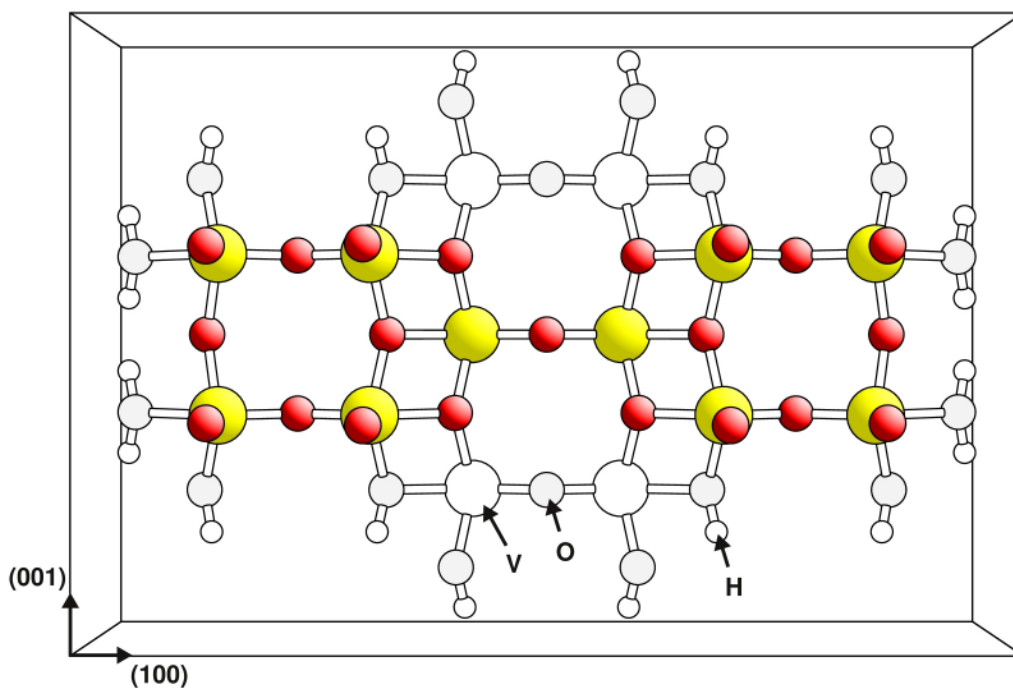


Figure C.7: Cluster model, $V_{14}O_{45}H_{20}$, for NH_4 diffusion steps: $O(1) \leftrightarrow V$, $V \leftrightarrow O(2)$ and $O(2) \leftrightarrow O(2)$ including large area of relaxation. Vanadium centers are shown by large yellow balls, oxygen centers by red balls, and small balls refer to hydrogen centers. Sections that have been considered to be flexible are emphasized with shading.

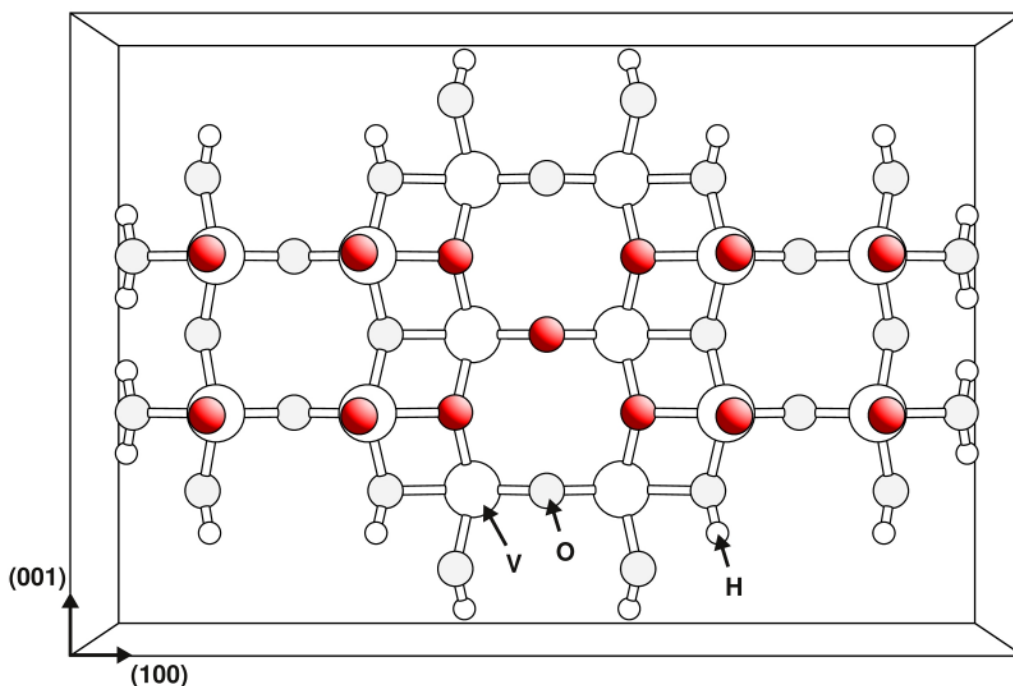


Figure C.8: Cluster model, $V_{14}O_{45}H_{20}$, for NH_4 diffusion steps: $O(1) \leftrightarrow V$, $V \leftrightarrow O(2)$ and $O(2) \leftrightarrow O(2)$ including a small area of relaxation. Vanadium centers are shown by large yellow balls, oxygen centers by red balls, and small balls refer to hydrogen centers. Sections that have been considered to be flexible are emphasized with shading.

D. SCR reaction path at the particle and the small cluster

All SCR reaction paths calculated for the reaction at the $V_2Si_6O_{14}H_6$ particle, simulating a local section of the $VO_x/SBA-15$ catalyst, and at the small $V_2O_9H_8$ cluster are presented below.

D1.SCR reaction at Brønsted acid site

In general, the intermediates and transition states for the reaction at the Brønsted sites of the particle (Figure D.1) and the small cluster (Figure D.2) are consistent with the findings for the surface model (see Section 8.3.1). NH_3 adsorbs at the surface OH group, yielding NH_4^+ (**B2**), which further reacts with NO to form a weakly-bound precursor intermediate (**B3**). Next, NH_2NO is formed by a double-dehydrogenation step. In the transition state (**B4^{TS}**), one hydrogen is fully transformed, and the second hydrogen is located between the surface O(1) site and the emerging NH_2 species. Simultaneously, the nitrogen atom of the NO molecule starts to interact with the nitrogen atom of the emerging NH_2 . Going beyond the transition state (**B4^{TS}**) results in NH_2NO being adsorbed at the catalyst surface (**B5**).

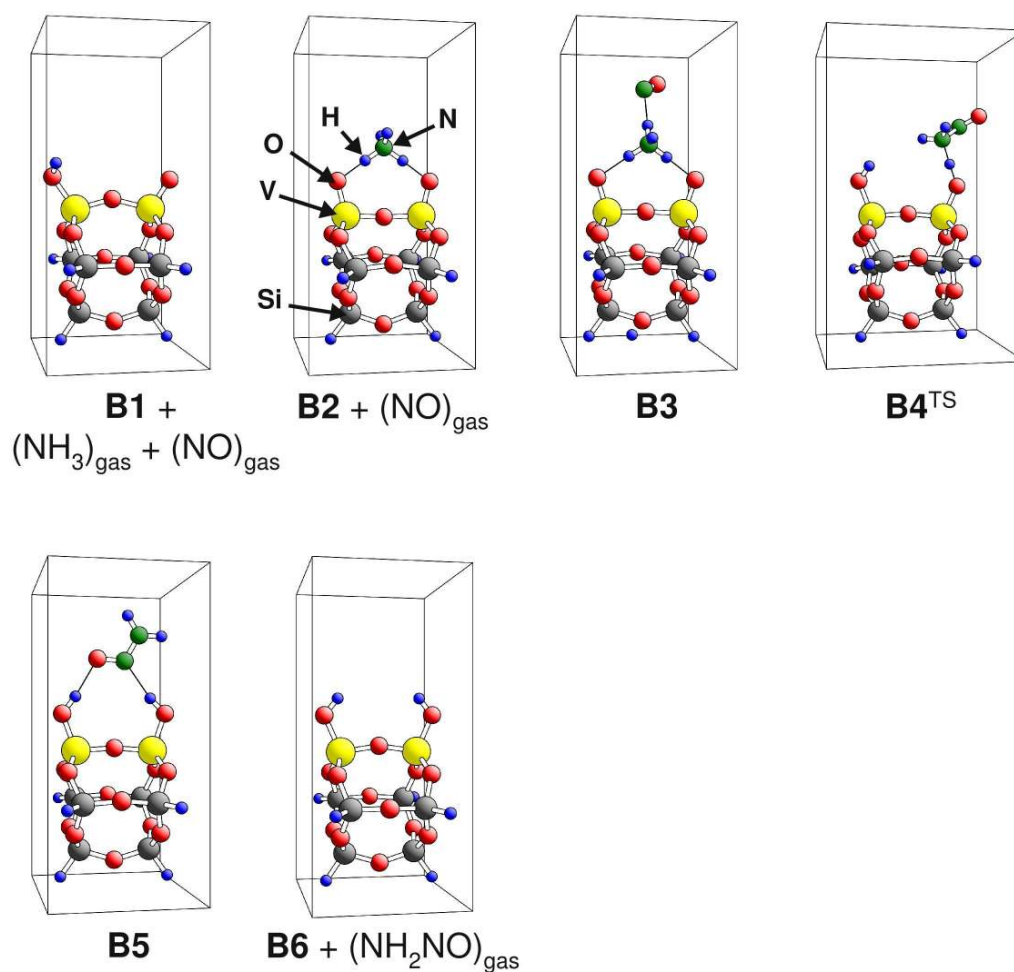


Figure D.1: Intermediates and transition states for the path of the SCR reaction near Brønsted acid sites of the $V_2Si_6O_{14}H_6$ particle. Vanadium centers are shown by large yellow balls, oxygen centers by red balls, nitrogen centers by green balls, silicon centers by dark gray, hydrogen centers by small blue balls, and saturation hydrogen by small light gray balls.

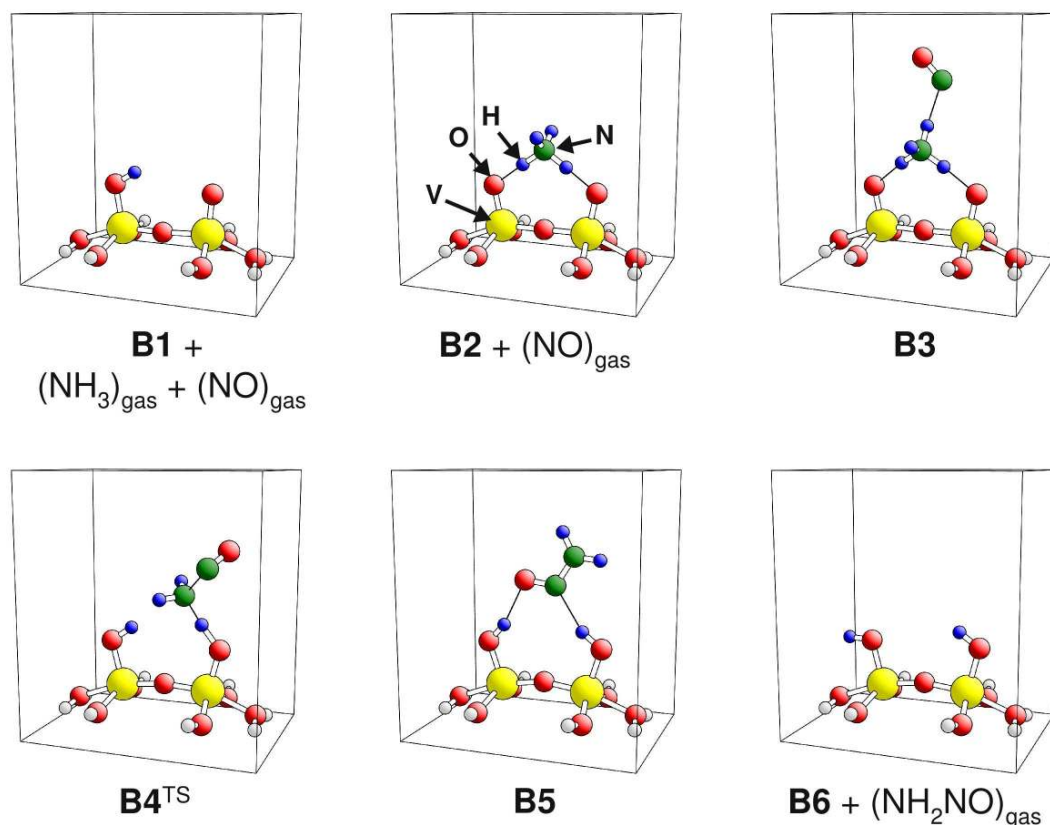


Figure D.2: Intermediates and transition states for the path of the SCR reaction path near Brønsted acid sites of the $\text{V}_2\text{O}_9\text{H}_8$ cluster. Vanadium centers are shown by large yellow balls, oxygen centers by red balls, nitrogen centers by green balls, hydrogen centers by small blue balls, and saturation hydrogen by small light gray balls.

In contrast to the surface model, the particle and the small cluster only provide two vanadyl oxygen sites. Therefore, the surface NH_4 species that is formed at these model clusters after ammonia adsorption (**B2**) has a different geometry where the NH_4 points with two hydrogen atoms towards the two O(1) sites (Figures D.1 and D.2). The difference in geometry is also accompanied by a noticeable drop in adsorption energy by 0.5 eV compared to the surface model (Table 8.1). The lack of additional vanadyl sites also affects the intermediate, after the nitrosamide formation (**B5**) and further decomposition into N_2 and H_2O . At the surface model, the molecule swings around such that it stabilizes on top of one of the OH groups and the neighboring O(1) site (Figure 8.2), which represent an active site for decomposition. On the particle and the small cluster, the adsorbed NH_2NO stabilizes on top of the two OH groups with the NO part pointing towards the hydrogen atoms. Since both O(1) sites are covered by hydrogen and no other O(1) site is available, no direct decomposition as proposed for the surface model is possible.

D2.SCR reaction at Lewis acid site

The reaction steps identified for NH_2NO formation at the surface model are shown below. Ammonia adsorbs at the reduced vanadium site (**L2**), where it gets dehydrogenated (**L3**). The remaining NH_2 species reacts with NO , from a weakly adsorbed intermediate (**L5**). The NH_2NO formation occurs via two steps, where first NO co-adsorbs next to NH_2 at the vanadium site (**L7**) and then pushes itself between the NH_2 adsorbate and the vanadium atom (**L9**).

In the case of reaction at the $\text{V}_2\text{Si}_6\text{O}_{14}\text{H}_6$ particle, the NH_2NO formation is a three-step process, since the NO can dock towards the more open vanadium site, avoiding a direct interaction with the adsorbed NH_2 molecule (**L5.2**) (see Section 8.3.2). An interesting difference was found for the transition state of the NH_3 dehydrogenation (**L2^{TS}**). As discussed in Section 8.3.2, on the extended surface model the hydrogen is already transferred in the transition state, as indicated by the corresponding distances, $d(\text{NH}_2\text{-H}) = 2.42 \text{ \AA}$ and $d(\text{O}(1)\text{-H}) = 0.98 \text{ \AA}$. At the particle surface in the transition state geometry (**L2^{TS}**), a bridge is formed between NH_2 , hydrogen, and $\text{O}(1)$, $d(\text{NH}_2\text{-H}) = 1.63 \text{ \AA}$ and $d(\text{H-O}(1)) = 1.07 \text{ \AA}$ (Figure D.3). This does not really affect the energy barrier for dehydrogenation (Table 8.3), but the resulting intermediate (**L3**) is stabilized by -0.51 eV with respect to (**L2^{TS}**), compared to only -0.08 eV as found for the surface model. However, besides the additional intermediate, the reaction path found for the particle is similar to the reaction path as found for the surface model (Figures D.3 and D.4). As can be seen in Figures D.5 and D.6, the reaction path found for the NH_2NO formation at the small $\text{V}_2\text{O}_9\text{H}_8$ cluster mimics in all steps the path as found for the surface model.

For both models, the particle and the small clusters, nitrosamide desorption and re-adsorption at a Brønsted site has been considered to reach the active site for decomposition into N_2 and H_2O .

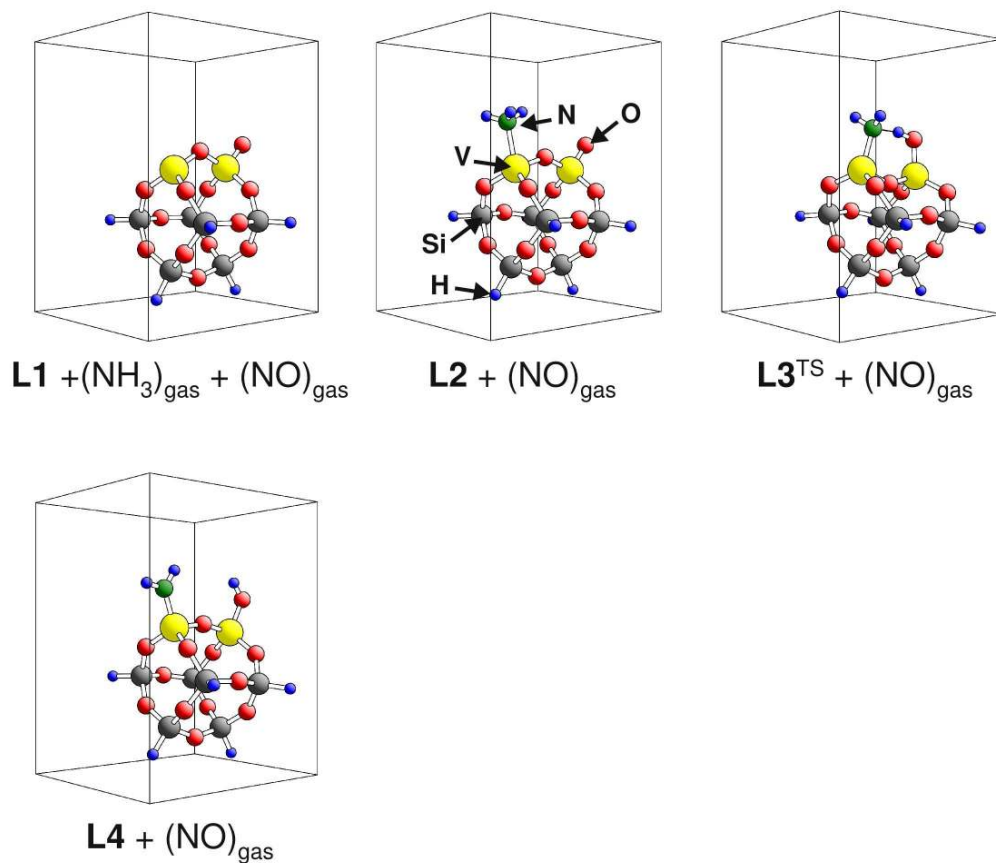


Figure D.3: Intermediates and transition states for SCR reaction steps (**L1**) \rightarrow (**L4**) (initial NH_3 adsorption and dehydrogenation) near Lewis acid sites of the $V_2Si_6O_{14}H_6$ particle. Vanadium centers are shown by large yellow balls, oxygen centers by red balls, nitrogen centers by green balls, silicon centers by dark gray, hydrogen centers by small blue balls, and saturation hydrogen by small light gray balls.

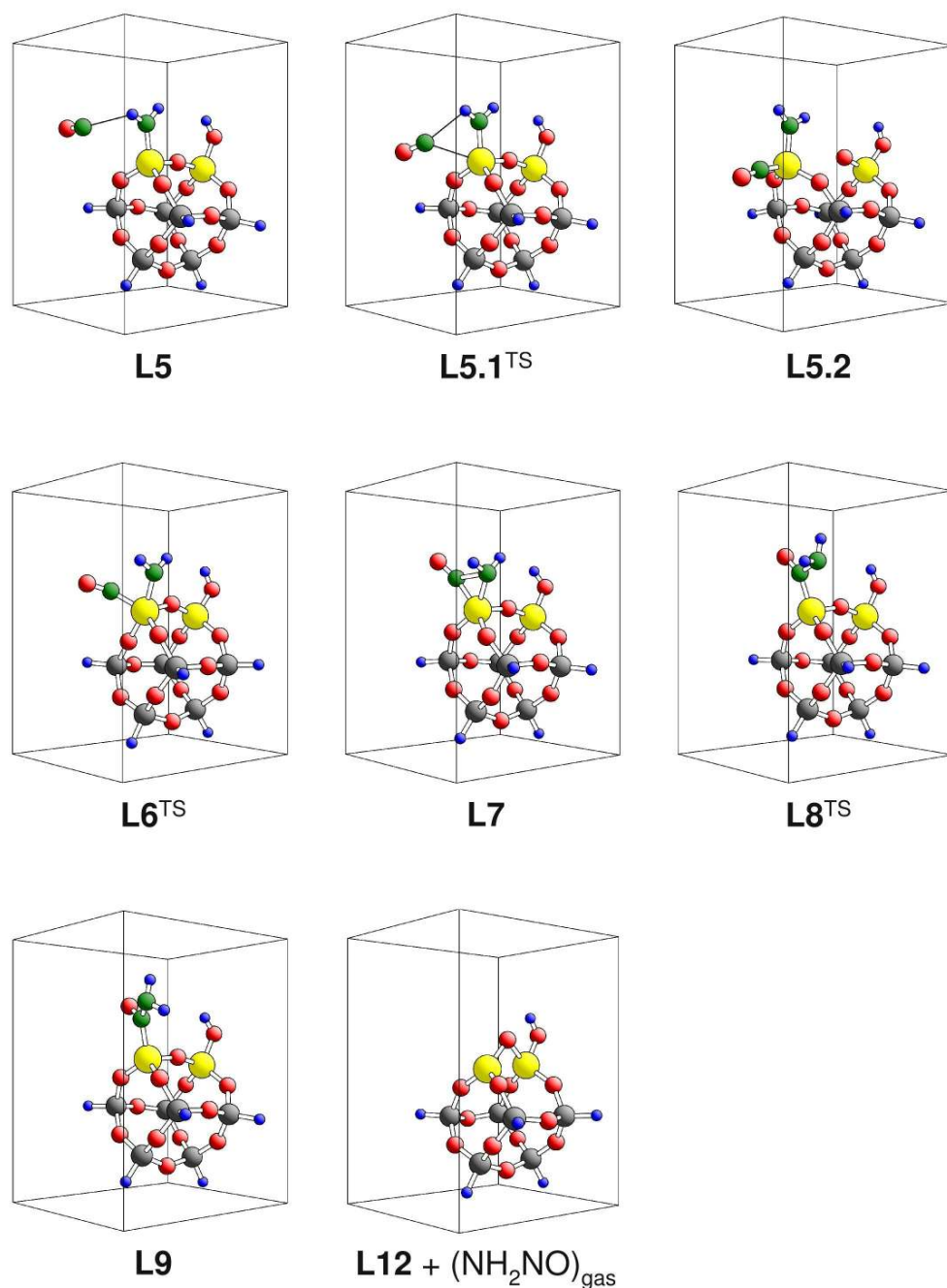


Figure D.4: Intermediates and transition states for SCR reaction steps (**L5**) → (**L12**) (reaction with NO, NH₂NO formation and desorption) near Lewis acid sites of the V₂Si₆O₁₄H₆ particle. Vanadium centers are shown by large yellow balls, oxygen centers by red balls, nitrogen centers by green balls, silicon centers by dark gray, hydrogen centers by small blue balls, and saturation hydrogen by small light gray balls.

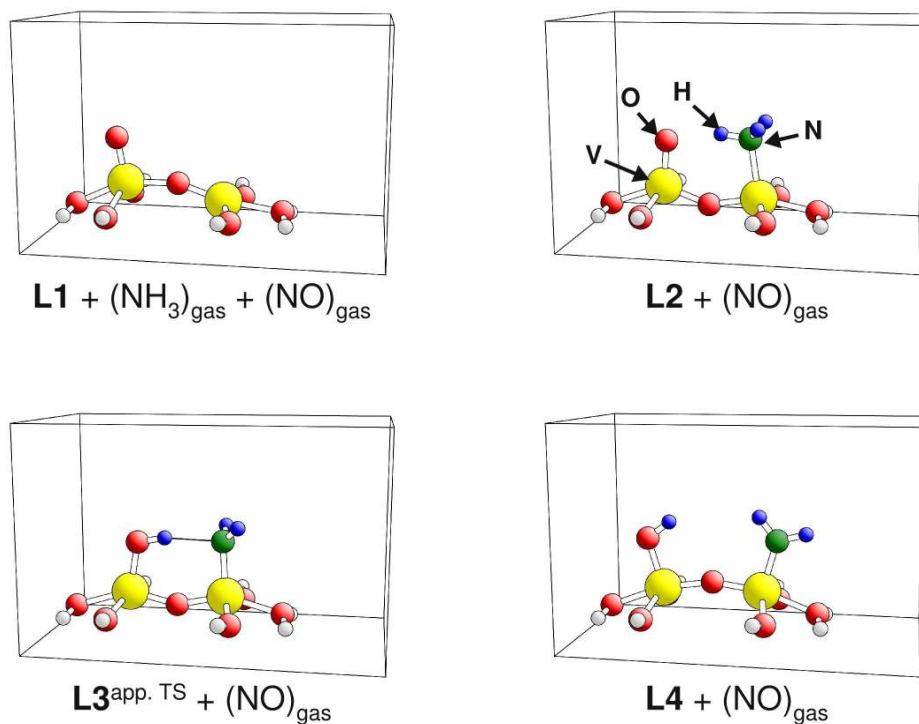


Figure D.5: Intermediates and transition states for SCR reaction steps (L1) \rightarrow (L4) (initial NH_3 adsorption and dehydrogenation) near Lewis acid sites of the $V_2O_8H_8$ cluster. Vanadium centers are shown by large yellow balls, oxygen centers by red balls, nitrogen centers by green balls, hydrogen centers by small blue balls, and saturation hydrogen by small light gray balls.

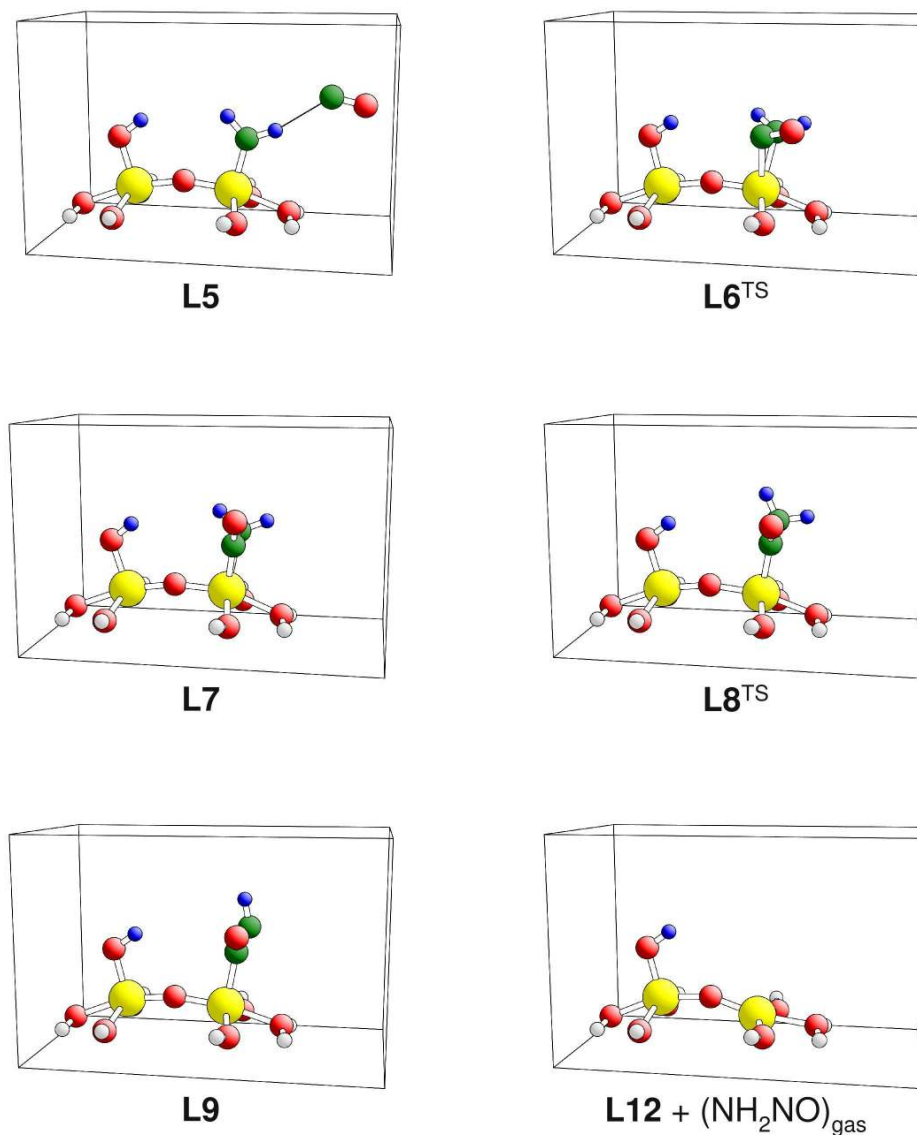


Figure D.6: Intermediates and transition states for SCR reaction steps (L5) \rightarrow (L12) (reaction with NO, NH₂NO formation and desorption) near Lewis acid sites of the V₂O₈H₈ cluster. Vanadium centers are shown by large yellow balls, oxygen centers by red balls, nitrogen centers by green balls, hydrogen centers by small blue balls, and saturation hydrogen by small light gray balls.

Abstract

The Selective Catalytic Reduction (SCR) of NO_x by NH_3 is one of the most effective NO_x reduction processes. It is widely employed in units of industrial scale where vanadium based metal oxides, VO_x , act as catalysts. The SCR reaction has been studied experimentally in great detail. However, details of the reaction mechanism at an atomic scale are still under debate. Ammonia adsorption, NH_x (de)hydrogenation, reaction with NO , surface water formation, and diffusion processes at the VO_x catalyst are found to contribute elementary steps [17]. In this work these elementary steps of the SCR reaction are examined in theoretical studies applying density functional theory (DFT) together with gradient corrected functionals (cluster code StoBe [18]). The VO_x catalyst substrate is modeled by clusters that are cut out from the ideal $\text{V}_2\text{O}_5(010)$ surface with the peripheral oxygen bonds saturated by hydrogen atoms. A Mars and van Krevelen mechanism [57] where the catalyst surface gets reduced and oxygen vacancies are formed, was proposed for the SCR reaction [17]. In this work, geometric, energetic, and electronic properties of the perfect and the reduced $\text{V}_2\text{O}_5(010)$ surface as well as the diffusion of oxygen vacancies will be discussed.

Based on surface cluster models the adsorption of H , NH_x , ($x = 0, \dots, 4$), and NO at the perfect and the reduced surface are studied. It is found that all adsorbates can stabilize at the surface and that except for, hydrogen and NH_4 , adsorption at the reduced surface sites is more favorable. In order to understand the surface mobility of adsorbates, diffusion properties of H and NH_4 at the $\text{V}_2\text{O}_5(010)$ surface are discussed, presenting detailed reaction paths and corresponding energy barriers. Hydrogen with its small mass can diffuse more easily compared to other adsorbates and hydrogen diffusion may participate in the water formation during the SCR reaction. NH_4 is an interesting example as it adsorbs at the $\text{V}_2\text{O}_5(010)$ surface with strong electrostatic binding contributions.

The reaction mechanism that have been suggested most often for the SCR process [17] include either hydrogenation or dehydrogenation of NH_3 . Therefore, a Born-Haber cycle is applied to calculate the (de)hydrogenation reaction energies, at the catalyst surface, based on surface adsorption and gas phase binding energies. It is shown that the surface supports both the hydrogenation and the dehydrogenation of NH_3 and that surface reduction lowers the energies for dehydrogenation even more. In experiment the adsorption of ammonia has been identified as the initial reaction step of the SCR reaction. Based on the analysis of infrared (IR) data where two strongly adsorbed NH_3 species at the $\text{V}_2\text{O}_5(010)$ surface have been found [17]. In contrast, theoretical studies could verify only one adsorption site so far. In the present work, two active sites for NH_3 adsorption are identified which can explain the experimental results. First, NH_3 is found to bind with the $\text{V}_2\text{O}_5(010)$ surface in the presence of OH groups (Brønsted acid sites) where it can form a rather stable surface NH_4^+ species. Second, NH_3 can bind at vanadium centers of lower coordination (Lewis acid sites) as provided by the reduced surface. (Vanadium sites at the perfect surface do not serve as adsorption sites for ammonia, in agreement with previous work.) Accordingly, the initial NH_3 adsorption leads to two different SCR scenarios where all reaction steps can be described by corresponding reaction paths and intermediates as is discussed in detail. In addition, silica supported vanadia particles are considered as catalysts by corresponding clusters, yielding quite similar results compared with those of the extended $\text{V}_2\text{O}_5(010)$ system.

Zusammenfassung

Die selektive katalytische Reduktion (Selective Catalytic Reduction, SCR) von NO_x durch Ammoniak ist einer der effizientesten Prozesse um Stickoxide zu reduzieren. Diese Technik wird häufig in Anlagen von industriellem Maßstab angewendet, wobei Katalysatoren auf Vanadiumoxidbasis, VO_x , eingesetzt werden. Obwohl die SCR-Reaktion in einer Vielzahl von experimentellen Arbeiten untersucht wurde, sind die mikroskopischen Details der Reaktionsabläufe nach wie vor nicht vollends verstanden. Diese schließen die Adsorption und (De)Hydrierung von NH_3 , die Reaktion mit NO sowie die Bildung von Wasser und Diffusionsprozesse an der VO_x -Katalysatoroberfläche als elementare Reaktionsschritte ein [17]. In der Arbeit werden die elementaren Schritte der SCR-Reaktion mit Hilfe von dichtefunktionaltheoretischen (DFT) Methoden unter Anwendung der generalisierten Gradienten-näherung (Cluster Code StoBe [18]) untersucht.

Als Modell für die Oberfläche des VO_x -Katalysatorsubstrats dienen Cluster, die aus der idealen $\text{V}_2\text{O}_5(010)$ Oberfläche herausgeschnitten und deren periphere Sauerstoffbindungen mit atomarem Wasserstoff abgesättigt werden. Für die SCR-Reaktion [17] wurde ein Mars-van-Krevelen-Mechanismus vorgeschlagen [57], bei dem die Katalysatoroberfläche reduziert und Sauerstoffleerstellen gebildet werden. Zunächst werden daher die geometrischen, energetischen und elektronischen Eigenschaften der perfekten und der reduzierten $\text{V}_2\text{O}_5(010)$ Oberfläche untersucht.

Im Anschluss wird die Adsorption von H , NH_x ($x = 0, \dots, 4$) und NO an den Clustermodellen für die perfekte und die reduzierte Oberfläche diskutiert. Es zeigt sich, dass außer für H und NH_4 , die Adsorption an der reduzierten Oberfläche verglichen mit Adsorption an der perfekten Oberfläche energetisch günstiger ist. Um die Mobilität der Adsorbate besser zu verstehen, werden die Diffusionseigenschaften von atomarem Wasserstoff und Oberflächen- NH_4 genauer untersucht. Wasserstoff mit seiner kleinen Masse kann leichter diffundieren. Zusätzlich können seine Diffusionseigenschaften wichtig für das Verständnis der Bildung von Oberflächenwasser sein. Andererseits ist NH_4 aufgrund der starken elektrostatischen Beiträge zur Adsorption an der $\text{V}_2\text{O}_5(010)$ -Oberfläche besonders interessant.

Die am häufigsten vorgeschlagenen Reaktionsmechanismen für die SCR-Reaktion [17] beinhalten als Reaktionsschritte entweder die Hydrierung oder die Dehydrierung von NH_3 . Mit Hilfe eines Born-Haber-Kreisprozesses kann die Reaktionsenergie für die (De)Hydrierung an der Katalysatoroberfläche durch Adsorptions- und Gasphasenbindungsenergien bestimmt werden. Durch die Präsenz der Katalysatoroberfläche wird sowohl die Hydrierung als auch die Dehydrierung erleichtert. Für die Dehydrierung wird dieser Effekt durch Reduktion der Oberfläche weiter verstärkt. In Experimenten zur SCR-Reaktion wurde die Adsorption von Ammoniak als der erste Reaktionsschritt identifiziert. Die Analyse von Infrarot-(IR)-Daten nach Adsorption von NH_3 an der $\text{V}_2\text{O}_5(010)$ -Oberfläche zeigt die Existenz von zwei stark adsorbierte Spezies [17]. In Gegensatz dazu konnte in theoretischen Untersuchungen nur eine stark gebundene Spezies auf der perfekten $\text{V}_2\text{O}_5(010)$ -Oberfläche gefunden werden. Die vorliegende Arbeit schlägt zwei unterschiedliche reaktive Adsorptionsplätze vor, anhand derer die experimentellen Daten erklärt werden können. Zum einem kann NH_3 an Oberflächen-OH-Gruppen (Brønsted-Säureplätze) adsorbieren und stabiles Oberflächen- NH_4^+ bilden. Zum anderen kann NH_3 mit niedriger koordinierten Vanadiumatomen (Lewis-Säureplätze), wie man sie auf der reduzierten Oberfläche findet, reagieren. (Vanadiumatome der perfekten Oberfläche können keine starke Bindung mit NH_3 eingehen wie schon in früheren Arbeiten gezeigt wurde.) Als Ergebnis führt die NH_3 -Adsorption an zwei unterschiedlichen Plätzen zu zwei unterschiedlichen SCR Reaktionsszenarien, deren Reaktionspfade und Intermediate im Detail besprochen werden. Zuletzt wird die Reaktion für Vanadiumoxidpartikel auf Silikatsubstrat untersucht. Die sich hieraus ergebenden Reaktionspfade sind ähnlich zu denen an der $\text{V}_2\text{O}_5(010)$ -Oberfläche.

Danksagung

An dieser Stelle möchte ich meinem Doktorvater Prof. Dr. Klaus Hermann für seine fachliche Unterstützung und sein Interesse an meiner Arbeit danken.

Ganz besonders bedanke ich mich bei meinen Eltern Hiltrud und Horst die mich bei meiner Ausbildung unterstützt und somit den Grundstein für diese Arbeit gelegt haben.

Weiters möchte ich mich auch bei meinen Kollegen, den Sekretärinnen und Prof. Dr. Matthias Scheffler für die freundschaftliche und produktive Atmosphäre in der Theorie Abteilung des Fritz-Haber-Instituts bedanken.

Diese Arbeit wurde durch ein Stipendium der International Max Planck Research School “Complex Surfaces in Material Science” und im Rahmen des Sonderforschungsbereich 546 “Struktur, Dynamik und Reaktivität von Übergangsmetalloxid-Aggregaten” von der Deutschen Forschungsgemeinschaft finanziell unterstützt.

Eidesstattliche Versicherung

Ich versichere hiermit alle Hilfsmittel und Hilfen angegeben und auf dieser Grundlage die Arbeit selbstständig verfasst zu haben. Die Arbeit ist weder in einem früheren Promotionsverfahren angenommen noch als ungenügend beurteilt worden.

Lebenslauf

Der Lebenslauf ist in der
Online-Version aus Gründen des Datenschutzes nicht enthalten.

For reasons of data protection,
the curriculum vitae is not included in the online version.

Bibliography

- [1] V.E. Henrich and P.A. Cox, *The Surface Science of Metal Oxides*, Cambridge University Press, Cambridge, 1994.
- [2] J.A. Bergwerff and B.M. Weckhuysen, *Oxide–Support Interactions*, in: Handbook of Heterogeneous Catalysis, Wiley-VCH, Weinheim, 2008.
- [3] H.H. Kung, *Transition Metal Oxides*, in: B. Delmon and J.T. Yates (Eds.) Studies in Surface Science and Catalysis, Elsevier, Amsterdam, 1989.
- [4] E.R. Braithwaite and J. Haber, *Molybdenum: An Outline of its Chemistry and Uses*, Elsevier, Amsterdam Lausanne New York Oxford Shannon Tokyo, 1994.
- [5] B. Grzybowska-Świerkosz, F. Trifiro, and J.C. Verdine, *Vanadia catalysts for selective oxidation of hydrocarbons and their derivatives*, Elsevier, Amsterdam Lausanne New York Oxford Shannon Tokyo, 1997.
- [6] W. Brückner, H. Oppermann, W. Reichelt, J. I. Terukow, F. A. Tschudnowski, and E. Wolf, *Vanadiumoxide: Darstellung, Eigenschaften, Anwendungen*, Akademie-Verlag, Berlin, 1983.
- [7] D. Adler, Rev. Mod. Phys., 40 (1968) 714.
- [8] F.J. Morin, Phys. Rev. Lett., 3 (1959) 34.
- [9] S. Lu, L. Hou, and F. Gan, Adv. Mater., 9 (1997) 244.
- [10] K. Kato, P.K. Song, H. Okada, and Y. Shigesato, Jpn. J. Appl. Phys., (2003) 6523.
- [11] K. Hermann and M. Witko, *Theory of physical and chemical behavior of transition metal oxides: vanadium and molybdenum oxides*, in: D.P. Woodruff (Ed.) The Chemical Physics of Solid Surfaces, Elsevier, 2001, pp. 136.
- [12] S.F. Håkonsen and A. Holmen, *Oxidative Dehydrogenation of Alkanes*, in: Handbook of Heterogeneous Catalysis, Wiley-VCH, Weinheim, 2008.
- [13] F. Näumann and M. Schulz, *Oxidation of Sulfur Dioxide*, in: Handbook of Heterogeneous Catalysis, Wiley-VCH, Weinheim, 2008.
- [14] R.K. Grasselli and M.A. Tenhover, *Amoxidation*, in: Handbook of Heterogeneous Catalysis, Wiley-VCH, Weinheim, 2008.
- [15] R.K. Grasselli, J.D. Burrington, D.J. Buttrey, P. DeSanto, C.G. Lugmair, A.F. Volpe, and T. Weingand, Top. Catal., 23 (2003) 5.
- [16] P. Gabrielsson and H.G. Pedersen, *Flue Gases from Stationary Sources*, in: Handbook of Heterogeneous Catalysis, Wiley-VCH, Weinheim, 2008.
- [17] G. Busca, L. Lietti, G. Ramis, and F. Berti, Appl. Catal., B, 18 (1998) 1.

-
- [18] K. Hermann, L.G.M. Pettersson, M.E. Casida, C. Daul, A. Goursot, A. Koester, E. Proynov, A. St-Amant, D.R. Salahub, V. Carravetta, H. Duarte, C. Friedrich, N. Godbout, J. Guan, C. Jamorski, M. Leboeuf, M. Leetmaa, M. Nyberg, S. Patchkovskii, L. Pedocchi, F. Sim, L. Triguero, and A. Vela, *StoBe-deMon version 3.0*, 2009, see <http://www.fhi-berlin.mpg.de/KHsoftware/StoBe/index.html>
- [19] R.M. Dreizler and E.K.U. Gross, *Density functional theory: An approach to the quantum many-body problem*, Springer Verlag, Berlin and New York, 1990.
- [20] W. Koch and M.C. Holthausen, *A Chemist's Guide to Density Functional Theory*, 2nd ed., Wiley-VCH, Weinheim, 2001.
- [21] H. Jónsson, G. Mills, and K.W. Jacobson, *Nudged elastic band method for finding minimum energy paths and transitions*, in: B.J. Berne, G. Ciccotti, and D.F. Coker (Eds.) *Classical and Quantum Dynamics in Condensed Phase Simulations*, World Scientific Publishing Company, 1998.
- [22] G. Henkelman and H. Jónsson, *J. Phys. Chem.*, 111 (1999) 7010.
- [23] R. Družinić, *Strukturelle und elektronische Eigenschaften von Vanadiumpentoxid: Clustermodell-Untersuchungen*, PhD thesis, Freie Universität Berlin, 1999.
- [24] C. Friedrich, *Geometrische, elektronische und vibronische Eigenschaften der reinen und defektbehafteten $V_2O_5(010)$ -Oberfläche und deren Wechselwirkung mit Adsorbaten: Theoretische Untersuchungen*, PhD thesis, Freie Universität Berlin, 2004.
- [25] Y.V. Belokopytov, K.M. Kholyavenko, and S.V. Gerei, *J. Catal.*, 60 (1979) 1.
- [26] G. Ramis, L. Yi, and G. Busca, *Catal. Today*, 28 (1996) 373.
- [27] F. Haber, *Verhandlungen der Deutschen Physikalischen Gesellschaft*, 21 (1919) 750.
- [28] H.C. Frey, *Engineering-Economic Evaluation of SCR NO_x Control Systems for Coal-Fired Power Plants*, in: *American Power Conference*, Illinois, Institute of Technology, Chicago, 1995, pp. 1583.
- [29] M. Calatayud, B. Mguig, and C. Minot, *Surf. Sci. Rep.*, 55 (2004) 169.
- [30] Q. Liu, Z. Liu, and C. Li, *Chin. J. Cat.*, 27 (2006) 636.
- [31] L.J. Alemany, F. Berti, G. Busca, G. Ramis, D. Robba, G.P. Toledo, and M. Trombetta, *Appl. Catal., B*, 10 (1996) 299.
- [32] H. Bosch and F.J. Janssen, *Catal. Today*, 2 (1988) 369.
- [33] S.M. Cho, *Chem. Eng. Prog.*, 90 (1994) 39.
- [34] P. Forzatti and L. Lietti, *Heterogen. Chem. Rev.*, 3 (1996) 33.
- [35] F.J.J.G. Janssen, in: G. Ertl, H. Knözinger, and J. Weitkamp (Eds.) *Handbook of Heterogeneous Catalysis*, Wiley-VCH, Weinheim, 1997.
- [36] S.C. Wood, *Chem. Eng. Prog.*, 90 (1994) 33.
- [37] D.J. Cole, C.F. Cullis, and D.J. Hucknall, *J. Chem. Soc., Faraday Trans.*, 72 (1976) 2185.

-
- [38] G. Oliveri, G. Ramis, G. Busca, and V.S. Escribano, *J. Mater. Chem.*, 3 (1993) 1239.
- [39] G. Ramis, G. Busca, C. Cristiani, L. Lietti, P. Forzatti, and F. Bregani, *Langmuir*, 8 (1992) 1744.
- [40] C. Cristiani, M. Bellotto, P. Forzatti, and F. Bregani, *Journal of Materials Research*, 8 (1993) 2019.
- [41] J.M.G. Amores, V.S. Escribano, and G. Busca, *J. Mater. Chem.*, 5 (1995) 1245.
- [42] M. Takagi, T. Kawai, M. Soma, T. Onishi, and K. Tamaru, *J. Catal.*, 50 (1977) 441.
- [43] M. Inomata, A. Miyamoto, and Y. Murakami, *J. Catal.*, 62 (1980) 140.
- [44] M. Inomata, A. Miyamoto, T. Ui, K. Kobayashi, and Y. Murakami, *Ind. Eng. Chem. Prod. Res. Dev.*, 21 (1982) 424.
- [45] A. Miyamoto, K. Kobayashi, M. Inomata, and Y. Murakami, *J. Phys. Chem.*, 86 (1982) 2945.
- [46] H. Bosch, F.J.J.G. Janssen, F.M.G. van den Kerkhof, J. Oldenziel, J.G. van Ommen, and J.R.H. Ross, *Appl. Catal.*, 25 (1986) 239.
- [47] I.-S. Nam, *J. Catal.*, 119 (1989) 269.
- [48] E.T.C. Vogt, A.J. van Dillen, J.W. Geus, F.J.J.G. Janssen, and F. van den Kerkhof, *J. Catal.*, 119 (1989) 270.
- [49] F.J.J.G. Janssen, F.M.G. Van den Kerkhof, H. Bosch, and J.R.H. Ross, *J. Phys. Chem.*, 91 (1987) 5921.
- [50] F.J.J.G. Janssen, F.M.G. Van den Kerkhof, H. Bosch, and J.R.H. Ross, *J. Phys. Chem.*, 91 (1987) 6633.
- [51] B.L. Duffy, H.E. Curry-Hyde, N.W. Cant, and P.F. Nelson, *J. Phys. Chem.*, 98 (1994) 7153.
- [52] U.S. Ozkan, Y. Cai, and M.W. Kumthekar, *J. Phys. Chem.*, 99 (1995) 2363.
- [53] U.S. Ozkan, Y.P. Cai, and M.W. Kumthekar, *J. Catal.*, 149 (1994) 375.
- [54] U.S. Ozkan, Y.P. Cai, and M.W. Kumthekar, *J. Catal.*, 149 (1994) 390.
- [55] M. Koebel, G. Madia, and M. Elsener, *Catal. Today*, 73 (2002) 239.
- [56] P. Forzatti, *Appl. Catal., A*, 222 (2001) 221.
- [57] P. Mars and D.W. van Krevelen, *Chem. Eng. Sci.*, 3 (1954) 41.
- [58] L. Lietti and P. Forzatti, *J. Catal.*, 147 (1994) 241.
- [59] R.A. Rajadhyaksha and H. Knözinger, *Appl. Catal.*, 51 (1989) 81.
- [60] T.Z. Srnak, J.A. Dumesic, B.S. Clausen, E. Törnqvist, and N.Y. Topsøe, *J. Catal.*, 135 (1992) 246.

- [61] G.T. Went, L.J. Leu, S.J. Lombardo, and A.T. Bell, *J. Phys. Chem.*, 96 (1992) 2235.
- [62] G. Ramis, G. Busca, F. Bregani, and P. Forzatti, *Appl. Catal.*, 64 (1990) 259.
- [63] H. Miyata, N. Yoshiro, O. Takehiko, and K. Yukata, *Chem. Lett.*, 12 (1938) 1141.
- [64] M.S. Went and J.A. Reimer, *J. Am. Chem. Soc.*, 114 (1992) 5768.
- [65] L. Lietti, I. Nova, S. Camurri, E. Tronconi, and P. Forzatti, *AIChE Journal*, 43 (1997) 2559.
- [66] E. Tronconi, L. Lietti, P. Forzatti, and S. Malloggi, *Chem. Eng. Sci.*, 51 (1996) 2965.
- [67] M. Anstrom, N.-Y. Topsøe, and J.A. Dumesic, *J. Catal.*, 213 (2003) 115.
- [68] T. Homann, T. Bredow, and K. Jug, *Surf. Sci.*, 515 (2002) 205.
- [69] S. Soyer, A. Uzun, S. Senkan, and I. Onal, *Catal. Today*, 118 (2006) 268.
- [70] X. Yin, H. Han, I. Gunji, A. Endou, S.S. Cheettu Ammal, M. Kubo, and A. Miyamoto, *J. Phys. Chem. B*, 103 (1999) 4701.
- [71] R.-M. Yuan, G. Fu, X. Xu, and H.-L. Wan, *PCCP*, 13 (2011) 453.
- [72] F. Gilardoni, J. Weber, and A. Baiker, *Int. J. Quantum Chem*, 61 (1997) 683.
- [73] V.Y. Borovkov, E.P. Mikheeva, G.M. Zhidomirov, and O.B. Lapina, *Kinet. Catal.*, 44 (2003) 710.
- [74] T. Bredow, T. Homann, and K. Jug, *Res. Chem. Intermed.*, 30 (2004) 65.
- [75] K. Jug, T. Homann, and T. Bredow, *J. Phys. Chem. A*, 108 (2004) 2966.
- [76] A. Vittadini, M. Casarin, and A. Selloni, *J. Phys. Chem. B*, 109 (2005) 1652.
- [77] N.Y. Topsøe, J.A. Dumesic, and H. Topsøe, *J. Catal.*, 151 (1995) 241.
- [78] N.Y. Topsøe, H. Topsøe, and J.A. Dumesic, *J. Catal.*, 151 (1995) 226.
- [79] G.T. Went, L.-j. Leu, and A.T. Bell, *J. Catal.*, 134 (1992) 479.
- [80] G.T. Went, L.-J. Leu, R.R. Rosin, and A.T. Bell, *J. Catal.*, 134 (1992) 492.
- [81] M. Born and R. Oppenheimer, *Annalen der Physik*, 389 (1927) 457.
- [82] P. Hohenberg and W. Kohn, *Phys. Rev.*, 136 (1964) B864.
- [83] W. Kohn and L.J. Sham, *Phys. Rev.*, 140 (1965) A1133.
- [84] F. Bloch, *Z. Phys. A: Hadrons Nucl.*, 57 (1929) 545.
- [85] P.A.M. Dirac, *Math. Proc. Cambridge*, 26 (1930) 376.
- [86] J.C. Slater, *Phys. Rev.*, 81 (1951) 385.
- [87] D.M. Ceperley and B.J. Alder, *Phys. Rev. Lett.*, 45 (1980) 566.

-
- [88] S.H. Vosko, L. Wilk, and M. Nusair, *Can. J. Phys.*, 58 (1980) 1200.
- [89] J.P. Perdew and A. Zunger, *Phys. Rev. B: Condens. Matter*, 23 (1981) 5048.
- [90] J.P. Perdew and Y. Wang, *Phys. Rev. B: Condens. Matter*, 46 (1992) 12947.
- [91] J.P. Perdew, *Phys. Rev. Lett.*, 55 (1985) 1665.
- [92] J.P. Perdew, *Phys. Rev. Lett.*, 55 (1985) 2370.
- [93] O. Gunnarsson and B.I. Lundqvist, *Phys. Rev. B: Condens. Matter*, 13 (1976) 4274.
- [94] J.P. Perdew, K. Burke, and Y. Wang, *Phys. Rev. B: Condens. Matter*, 54 (1996) 16533.
- [95] J.P. Perdew, J.A. Chevary, S.H. Vosko, K.A. Jackson, M.R. Pederson, D.J. Singh, and C. Fiolhais, *Phys. Rev. B: Condens. Matter*, 46 (1992) 6671.
- [96] J.P. Perdew, J.A. Chevary, S.H. Vosko, K.A. Jackson, M.R. Pederson, D.J. Singh, and C. Fiolhais, *Phys. Rev. B: Condens. Matter*, 48 (1993) 4978.
- [97] J.P. Perdew, K. Burke, and M. Ernzerhof, *Phys. Rev. Lett.*, 77 (1996) 3865.
- [98] J.P. Perdew, K. Burke, and M. Ernzerhof, *Phys. Rev. Lett.*, 78 (1997) 1396.
- [99] G.L. Oliver and J.P. Perdew, *Physical Review A*, 20 (1979) 397.
- [100] Y. Zhang and W. Yang, *Phys. Rev. Lett.*, 80 (1998) 890.
- [101] B. Hammer, L.B. Hansen, and J.K. Nørskov, *Phys. Rev. B: Condens. Matter*, 59 (1999) 7413.
- [102] J.M. Bofill, *Int. J. Quantum Chem*, 94 (2003) 324.
- [103] C.G. Broyden, *IMA J. App. Math.*, 6 (1970) 222.
- [104] R. Fletcher, *Comp. J.*, 13 (1970) 317.
- [105] D. Goldfarb, *Math. Comput.*, 24 (1970) 23.
- [106] D.F. Shanno, *Math. Comput.*, 24 (1970) 647.
- [107] J. Nocedal and S.J. Wright, *Numerical Optimization*, 2nd ed., Springer 2000.
- [108] G. Mills, H. Jónsson, and G.K. Schenter, *Surf. Sci.*, 324 (1995) 305.
- [109] G. Mills and H. Jónsson, *Phys. Rev. Lett.*, 72 (1994) 1124.
- [110] R.E. Gillilan and K.R. Wilson, *J. Phys. Chem.*, 97 (1992) 1757.
- [111] G. Henkelman and H. Jónsson, *J. Phys. Chem.*, 113 (2000) 9978.
- [112] G. Henkelman, B.P. Uberuaga, and H. Jónsson, *J. Phys. Chem.*, 113 (2000) 9901.
- [113] G.M. Crippen and H.A. Scheraga, *Arch. Biochem. Biophys.*, 144 (1971) 462.
- [114] R.L. Hilderbrandt, *Comput. Chem. (Oxford)*, 1 (1977) 179.

- [115] A.F. Voter, Phys. Rev. Lett., 78 (1997) 3908.
- [116] A. Heyden, A.T. Bell, and F.J. Keil, J. Phys. Chem., 123 (2005) 224101.
- [117] J. Kästner and P. Sherwood, J. Phys. Chem., 128 (2008) 014106.
- [118] H.G. Bachmann, F.R. Ahmed, and W.H. Barnes, Z. Kristallogr., 115 (1961) 110.
- [119] A. Byström, K.-A. Wilhemi, and O. Brotzen, Acta Chem. Scand., 4 (1950) 1119.
- [120] R. Enjalbert and J. Galy, Acta Crystallogr. Sect. C: Cryst. Struct. Commun., 42 (1986) 1467.
- [121] R.W.G. Wyckoff, *Crystal Structures*, Interscience, Wiley, New York, 1965.
- [122] L. Fiermans and J. Vennik, Surf. Sci., 9 (1968) 187.
- [123] R.L. Smith, W. Lu, and G.S. Rohrer, Surf. Sci., 322 (1995) 293.
- [124] R.L. Smith, G.S. Rohrer, K.S. Lee, D.K. Seo, and M.H. Whangbo, Surf. Sci., 367 (1996) 87.
- [125] A.D. Costa, C. Mathieu, Y. Barbaux, H. Poelman, G. Dalmai-Vennik, and L. Fiermans, Surf. Sci., 370 (1997) 339.
- [126] H. Poelman, J. Vennik, and G. Dalmai, J. Electron. Spectrosc. Relat. Phenom., 44 (1987) 251.
- [127] J.S. Braithwaite, C.R.A. Catlow, J.D. Gale, and J.H. Harding, Chem. Mater., 11 (1999) 1990.
- [128] V. Brázdová, M.V. Ganduglia-Pirovano, and J. Sauer, Phys. Rev. B: Condens. Matter, 69 (2004) 165420.
- [129] A. Chakrabarti, K. Hermann, R. Družinić, M. Witko, F. Wagner, and M. Petersen, Phys. Rev. B: Condens. Matter, 59 (1999) 10583.
- [130] V. Eyert and K.-H. Höck, Phys. Rev. B: Condens. Matter, 57 (1998) 12727.
- [131] G. Kresse, S. Surnev, M.G. Ramsey, and F.P. Netzer, Surf. Sci., 492 (2001) 329.
- [132] X. Yin, A. Fahmi, A. Endou, R. Miura, I. Gunji, R. Yamauchi, M. Kubo, A. Chatterjee, and A. Miyamoto, Appl. Surf. Sci., 130-132 (1998) 539.
- [133] X. Yin, A. Endou, R. Miura, A. Fahmi, I. Gunji, R. Yamauchi, M. Kubo, K. Teraishi, and A. Miyamoto, Computational Materials Science, 14 (1999) 114.
- [134] H. Chiba, K. Nishidate, M. Baba, N. Kumagai, T. Sato, and K. Nishikawa, Solid State Commun., 110 (1999) 497.
- [135] K. Hermann, M. Witko, and R. Družinić, Faraday Discuss., 114 (1999) 53.
- [136] K. Hermann, M. Witko, R. Družinić, and R. Tokarz, Top. Catal., 11-12 (2000) 67.
- [137] K. Hermann, M. Witko, R. Družinić, and R. Tokarz, Appl. Phys. A, 72 (2001) 429.

-
- [138] N.V. Hieu and D. Lichtman, *J. Vac. Sci. Technol.*, 18 (1981) 49.
- [139] S.F. Cogan, N.M. Nguyen, S.J. Perrotti, and R.D. Rauh, *J. Appl. Phys.*, 66 (1989) 1333.
- [140] A.Z. Moshfegh and A. Ignatiev, *Thin Solid Films*, 198 (1991) 251.
- [141] K. Hermann, M. Witko, R. Družinić, A. Chakrabarti, B. Tepper, M. Elsner, A. Gorschlüter, H. Kuhlenbeck, and H.J. Freund, *J. Electron. Spectrosc. Relat. Phenom.*, 98-99 (1999) 245.
- [142] Q. Wu, A. Thissen, W. Jaegermann, M. Schuz, and P. Schmidt, *Chem. Phys. Lett.*, 430 (2006) 309.
- [143] R.F.W. Bader, *Atoms in Molecule, A Quantum Theory*, Clarendon Press, Oxford, 1990.
- [144] R.S. Mulliken, *J. Phys. Chem.*, 23 (1955) 1841.
- [145] B. Weckhuysen, *Catal. Today*, 78 (2003) 25.
- [146] M.E. Harlin, V.M. Niemi, and A.O.I. Krause, *J. Catal.*, 195 (2000) 67.
- [147] G. Silversmit, J.A. van Bokhoven, H. Poelman, A.M.J. van der Eerden, G.B. Marin, M.-F. Reyniers, and R. De Gryse, *Appl. Catal., A*, 285 (2005) 151.
- [148] K. Chen, E. Iglesia, and A.T. Bell, *J. Catal.*, 192 (2000) 197.
- [149] K. Chen, A. Khodakov, J. Yang, A.T. Bell, and E. Iglesia, *J. Catal.*, 186 (1999) 325.
- [150] R.K. Grasselli, *Top. Catal.*, 21 (2002) 79.
- [151] J. Haber, *Fundamentals of Hydrocarbon Oxidation*, in: *Handbook of Heterogeneous Catalysis*, Wiley-VCH, Weinheim, 2008.
- [152] B. Tepper, B. Richter, A.C. Dupuis, H. Kuhlenbeck, C. Hucho, P. Schilbe, M.A. bin Yarmo, and H.J. Freund, *Surf. Sci.*, 496 (2002) 64.
- [153] M.N. Colpaert, P. Clauws, L. Fiermans, and J. Vennik, *Surf. Sci.*, 36 (1973) 513.
- [154] Q. Wu, *Appl. Surf. Sci.*, 236 (2004) 473.
- [155] E.R.S. Winter, *J. Chem. Soc. A*, (1968) 2889.
- [156] T. Oshio, Y. Sakai, and S. Ehara, *Scanning tunneling microscopy/spectroscopy study of V_2O_5 surface with oxygen vacancies*, in, *AVS*, 1994, pp. 2055.
- [157] K. Devriendt, H. Poelman, L. Fiermans, G. Creten, and G.F. Froment, *Surf. Sci.*, 352-354 (1996) 750.
- [158] M. Ganduglia-Pirovano and J. Sauer, *Phys. Rev. B: Condens. Matter*, 70 (2004).
- [159] M.V. Ganduglia-Pirovano, A. Hofmann, and J. Sauer, *Surf. Sci. Rep.*, 62 (2007) 219.
- [160] J. Goclon, R. Grybos, M. Witko, and J. Hafner, *Phys. Rev. B: Condens. Matter*, 79 (2009) 075439.
- [161] J. Sauer and J. Dobler, *Dalt. Trans.*, (2004) 3116.

-
- [162] D.O. Scanlon, A. Walsh, B.J. Morgan, and G.W. Watson, *J. Phys. Chem. C*, 112 (2008) 9903.
- [163] S. Laubach, P.C. Schmidt, A. Thißen, F.J. Fernandez-Madrigo, Q.-H. Wu, W. Jaegermann, M. Klemm, and S. Horn, *PCCP*, 9 (2007) 2564.
- [164] N.E. Quaranta, L.A. Gambaro, and H.J. Thomas, *J. Catal.*, 107 (1987) 503.
- [165] X. Yin, H. Han, A. Endou, M. Kubo, K. Teraishi, A. Chatterjee, and A. Miyamoto, *J. Phys. Chem. B*, 103 (1999) 1263.
- [166] *Structure of free molecules in the gas phase*, in: W.M.M. Haynes (Ed.) *CRC handbook of chemistry and physics*, CRC Taylor and Francis, 2011, pp. 9.
- [167] A.A. Tsyganenko, D.V. Pozdnyakov, and V.N. Filimonov, *J. Mol. Struct.*, 29 (1975) 299.
- [168] F. Gilardoni, J. Weber, and A. Baiker, *J. Phys. Chem. A*, 101 (1997) 6069.
- [169] J.A. Dumesic, G.W. Huber, and M. Boudart, *Rates of Catalytic Reactions*, in: *Handbook of Heterogeneous Catalysis*, Wiley-VCH, Weinheim, 2008.
- [170] H. Fu, Z.-P. Liu, Z.-H. Li, W.-N. Wang, and K.-N. Fan, *J. Am. Chem. Soc.*, 128 (2006) 11114.
- [171] R. Catani, G. Centi, F. Trifiro, and R.K. Grasselli, *Ind. Eng. Chem. Res.*, 31 (1992) 107.
- [172] G. Centi and S. Perathoner, *J. Catal.*, 142 (1993) 84.
- [173] G. Ertl, in: J.R. Anderson and M. Boudart (Eds.) *Catalysis Science and Technology Vol. 4*, Springer, Berlin, 1983, pp. 209.
- [174] L.V. Gurvich, I.V. Veyts, C.B. Alcock, and V.S. Iorish, *Thermodynamic Properties of Individual Substances*, 4th ed., Hemisphere, New York, 1991.
- [175] M. Farber and S.P. Harris, *J. Phys. Chem.*, 88 (1984) 680.
- [176] E.W.-G. Diau and S.C. Smith, *J. Phys. Chem.*, 106 (1997) 9236.
- [177] X. Duan and M. Page, *J. Mol. Struct. TEOCHEM*, 333 (1995) 233.
- [178] D. Zhao, J. Feng, Q. Huo, N. Melosh, G.H. Fredrickson, B.F. Chmelka, and G.D. Stucky, *Science*, 279 (1998) 548.
- [179] D. Zhao, Q. Huo, J. Feng, B.F. Chmelka, and G.D. Stucky, *J. Am. Chem. Soc.*, 120 (1998) 6024.
- [180] Y. Segura, L. Chmielarz, P. Kustrowski, P. Cool, R. Dziembaj, and E.F. Vansant, *Appl. Catal., B*, 61 (2005) 69.
- [181] M. Hävecker, M. Cavalleri, R. Herbert, R. Follath, A. Knop-Gericke, C. Hess, K. Hermann, and R. Schlögl, *Phys. Status Solidi B*, 246 (2009) 1459.
- [182] M. Cavalleri, K. Hermann, A. Knop-Gericke, M. Hävecker, R. Herbert, C. Hess, A. Oestereich, J. Döbler, and R. Schlögl, *J. Catal.*, 262 (2009) 215.

- [183] J. Li and S. Li, PCCP, 9 (2007) 3304.
- [184] J.C. Slater, Phys. Rev., 36 (1930) 57.
- [185] R. McWeeny, Acta Crystallogr., 6 (1953) 631.
- [186] S.F. Boys, Proc. R. Soc. London, Ser. A, 200 (1950) 542.
- [187] H. Sambe and R.H. Felton, J. Phys. Chem., 62 (1975) 1122.
- [188] R. Fournier, J. Andzelm, and D.R. Salahub, J. Phys. Chem., 90 (1989) 6371.